

ARCHITECTURE-DEPENDENT VIBRATIONAL ENERGY TRANSPORT IN  
MOLECULAR CHAINS

AN ABSTRACT

SUBMITTED ON THE FIFTH DAY OF DECEMBER 2018

TO THE DEPARTMENT OF CHEMISTRY

OF THE SCHOOL OF SCIENCE AND ENGINEERING

OF TULANE UNIVERSITY

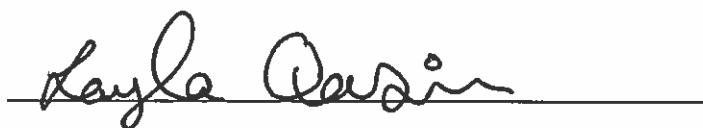
IN PARTIAL FULFILLMENT OF THE REQUIREMENTS

FOR THE DEGREE

OF

DOCTOR OF PHILOSOPHY

BY



LAYLA NEDAL QASIM

APPROVED:

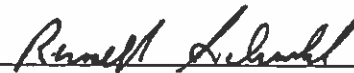


IGOR V. RUBTSOV, PH.D.

CHAIR OF DISSERTATION COMMITTEE



BRENT KOPLITZ, PH.D.



RUSSELL SCHMEHL, PH.D.



JANARTHANAN JAYAWICKRAMARAJAH, PH.D.

## **Abstract**

The development of nanocomposite materials with desired heat management properties, including nanowires, layered semiconductor structures, and self-assembled monolayer (SAM) junctions, attracts broad interest. Such materials often involve polymeric/oligomeric components and can feature high or low thermal conductivity, depending on their design. For example, in SAM junctions made of alkane chains sandwiched between metal layers, the thermal conductivity can be very low, whereas the fibers of ordered polyethylene chains feature high thermal conductivity, exceeding that of many pure metals.

Generally, there are two classes of vibrational energy transport regimes which have been identified in molecules. There is diffusive energy transport, which involves hopping of vibrational energy between localized states in the Brownian-like style or motion, and ballistic transport, which involves free propagation of a vibrational wave packet through delocalized vibrational modes. Previous studies demonstrated fast vibrational energy transport in a variety of oligomer chains, including 3.9 Å/ps speed in perfluoroalkanes, 5.5 Å/ps in PEGs, and 14.4 Å/ps in polyethylene oligomers. The fast speeds suggest that the observed transport regime was ballistic to significant distances. Although the speeds of transport observed were impressive, an in-depth explanation for the different speeds was not provided.

The work in the present dissertation is aimed at understanding the fundamental reasons as to why different speeds of vibrational energy transport can be achieved through structurally complex chains. Relaxation assisted two-dimensional infrared spectroscopy is used to investigate experimentally the energy transport in a variety of molecular chains. In these experiments, the transport in a molecule is initiated by exciting an IR-active group (a tag) and recorded by another mode in the molecule (a reporter) via the influence of the excess energy on its frequency. The energy transport time can be measured from the tag to the reporter, and the transport speed through the molecule is evaluated. Experiments on a series of alkane chains with different tag modes showed that different speeds of ballistic transport could be achieved using different methods of initiation. To understand why different speeds of transport occur, a detailed analysis of the vibrational chain states and the intramolecular vibrational relaxation pathways of the tag modes were performed. It was concluded that different tags populate different chain bands, which support different speeds of energy transport. Similar experiments were performed on PEG oligomers and, interestingly, the speed of transport was the same in several case of initiation. The detailed analysis of the transport showed that the presence of oxygen heteroatoms in the backbone weakens the site coupling of the PEG chain states, leading to localization of the vibrational modes. Detailed analysis of the energy transport between the PEG chain states along with modeling based on solving the quantum Liouville equation for a system of coupled states demonstrated that a switch from ballistic to directed diffusive transport occurs in PEG chains for longer chains. To better understand the role of mode localization on the transport mechanism and to see if ballistic transport across an alien molecular group in otherwise uniform chain is possible,

vibrational energy transport was studied in a series of alkane chains infused with different small functional groups. The functional group which disrupts the chain state delocalization was shown to disrupt the ballistic transport, and the one which preserves the delocalization appears to not disrupt the transport. The studies presented in this dissertation provides an in-depth description of the vibrational energy transport in a variety of different molecular chains. Such information can be useful in the development of materials with customized energy transport properties.



ARCHITECTURE-DEPENDENT VIBRATIONAL ENERGY TRANSPORT IN  
MOLECULAR CHAINS

A DISSERTATION  
SUBMITTED ON THE FIFTH DAY OF DECEMBER 2018  
TO THE DEPARTMENT OF CHEMISTRY  
OF THE SCHOOL OF SCIENCE AND ENGINEERING  
OF TULANE UNIVERSITY  
IN PARTIAL FULFILLMENT OF THE REQUIREMENTS  
FOR THE DEGREE  
OF  
DOCTOR OF PHILOSOPHY  
BY

  
LAYLA NEDAL QASIM

APPROVED:   
IGOR V. RUBTSOV, PH.D.  
CHAIR OF DISSERTATION COMMITTEE

  
BRENT KOPLITZ, PH.D.

  
RUSSELL SCHMEHL, PH.D.

  
JANARTHANAN JAYAWICKRAMARAJAH, PH.D.

## **Acknowledgments**

When I enrolled in this doctoral program, I was prepared to be challenged intellectually and to experience highs and lows in my academic progress. What I hadn't anticipated as much was the myriad of personal challenges and fluctuations one experiences from their early 20's to their late 20's. When these two dynamic processes are coupled, the results can be overwhelming at times, but ultimately very rewarding. I am grateful for this opportunity to thank those who have helped me in this journey.

First and foremost, I want to express my extreme gratitude to my research advisor, Professor Igor Rubtsov. The amount of effort Professor Rubtsov puts into personally training each graduate student in our lab individually is remarkable. Coming into the lab, I possessed almost none of the technical skills needed to conduct research in a laser spectroscopy group, but with his open-door policy, I was able to develop many skill sets that I never thought I was capable of attaining. It is impossible to express the extent of appreciation I feel for him in writing, but I'd like to address the most important lessons I learned from Professor Rubtsov, which are how to work independently and to not give up on problems too quickly.

I'd also like to thank my committee members, Professors Russell Schmehl, Janan Jayawickramarajah, and Brent Koplitz for their time and for providing valuable insights on my dissertation work. I would like to thank Professor Alex Burin for his many helpful

discussions and his substantial collaborative work. Without his theoretical insights, the conclusions made from my experimental work would not be nearly as rich. I would also like to acknowledge Dr. Arkady Kurnosov, who was the graduate student from Professor Burin's lab with whom I worked with most closely. I'd like to thank my synthetic collaborators Berk Atuk and Xiao Zhou, who I worked with closely as well.

The members of my group have been very helpful personally and in research. I'd like to thank former and current group members Dr. Yuankai Yue, Dr. Natalia Rubtsova, Dr. Joel Leger, Clara Nyby, Clyde Varner, Robert Mackin, Xiao Li, Furman Marshall, Zowie Saxman, and Junhan Zhou. I'd like to especially thank Yuankai, who spent a substantial amount of time training me and for being a role model to me, Natalia for her friendship and encouragement, and Robert, for his comradery and for being my closest friend at Tulane.

I have been fortunate to have made many close friends in the chemistry department at Tulane who have offered me their chemical expertise at one point or another. Here I would like to acknowledge Dr. Matthew Hillyer, Nick Ernst, Ross Zaenglein, Kristina Martinez, Rebecca Dupre, Molly Payne, and Yonglong Xiao. I'd like to also thank Andrii Maksymov, not just for his friendship but for also his assistance when we were taking coursework together.

I want to thank my parents for their unwavering support, and my sister, who inspired me to pursue the sciences in the first place. Finally, and with the most emotional sentiment, I want to express my gratitude to Ryan Vik. Ever since my matriculation into this program, Ryan has been a constant source of support, comfort, and companionship for me.

## Table of Contents

<b>Acknowledgments .....</b>	<b>i</b>
<b>List of Tables .....</b>	<b>viii</b>
<b>List of Figures .....</b>	<b>x</b>
<b>Chapter 1. Introduction</b>	
1.1 Measuring thermal energy transport from the mesoscopic to the molecular level: overview of the field .....	1
1.2. Diffusive transport in molecules: principles and examples .....	3
1.3. Ballistic energy transport: principles and examples .....	7
1.4. Dissertation Outline .....	11
<b>Chapter 2. Principles and Methods of 2DIR Spectroscopy</b>	
2.1. Introduction .....	14
2.2. Nonlinear optical spectroscopy: introduction .....	16
2.3. Fundamentals of 2DIR spectroscopy .....	19
2.3.1. 2DIR spectrum of a single oscillator .....	21
2.3.2. 2DIR spectrum of coupled oscillators .....	23
2.4. Frequency domain 2DIR spectroscopy .....	25
2.5. Time-domain dual-frequency 2DIR spectroscopy .....	25
2.6. Relaxation-assisted 2DIR spectroscopy .....	29
2.7. Details of the fully-automated 2DIR spectrometer .....	32

2.8. Measurement details.....	37
-------------------------------	----

## **Chapter 3. Ballistic Vibrational Energy Transport in Optical Alkane**

### **Chain Bands**

3.1. Overview.....	38
3.2. Experimental Details.....	39
3.2.1. Experimental method.....	39
3.2.2. Sample preparation .....	39
3.2.3. Quantum-chemistry calculations .....	40
3.3. Results and Discussion .....	40
3.4. Conclusions.....	59
3.5. Theoretical Methods .....	59
3.5.1. Calculations of the band structure for alkane chains.....	59
3.5.2. Group velocity calculations.....	61
3.5.3. Vibrational relaxation dynamics calculations.....	62
3.5.4. Mode coupling evaluation by scanning masses.....	63
3.6. Acknowledgments.....	64

## **Chapter 4. Energy Transport in PEG Oligomers: Contributions of**

### **Different Optical Bands**

4.1. Overview.....	65
4.2. Experimental Details.....	66
4.2.1. Experimental method.....	67
4.2.2. Sample preparation.....	67
4.2.3. Quantum-chemistry calculations.....	67

4.3. Results.....	68
4.3.1. End group to end group energy transport.....	69
4.3.2. End group to chain energy transfer.....	71
4.3.3. Energy transfer among the chain states.....	76
4.3.4. Dispersion relations for regular PEG chains .....	80
4.3.5. Relaxation pathways of the chain states .....	84
4.3.6. Relaxation pathways of the end-group tags .....	90
4.4. Discussion .....	93
4.4.1. Transport regimes in PEGs: from ballistic transport to directed diffusion.....	93
4.4.2. Properties of various PEG chain bands .....	95
4.4.3. Delocalization extent in chains with alternating coupling strength.....	97
4.4.4. Energy transport modeling.....	99
4.5. Conclusions.....	109
4.6. Theoretical Methods.....	111
4.6.1. Modeling of the dispersion relations of the optical bands in the all-anti PEG conformation .....	111
4.6.2. Group velocity calculations.....	112
4.6.3. Mode coupling evaluation for CH <sub>2</sub> modes of the alkane and PEG unit cell.....	113
4.6.4. Calculating mode centers for normal modes of a PEG chain ....	114

## Chapter 5. Ballistic transport of vibrational energy through an amide group bridging alkyl chains

5.1. Introduction .....	115
5.2. Experimental details.....	118
5.2.1. Experimental method.....	118
5.2.2. Sample preparation and characterization.....	118
5.2.3. DFT calculations.....	118
5.3. Results.....	119
5.3.1. Energy transport from $\nu_{N3}$ to the amide moiety.....	119
5.3.2. Energy transport from $\nu_{N3}$ to the ester moiety.....	122
5.3.3. Energy transport from $\nu_{C=O}$ to the amide group.....	123
5.3.4. Energy transport from $\nu_{C=O}$ to the azido group.....	124
5.3.5. Energy transport from am-I to the azido group.....	124
5.3.6. Lifetimes of the involved modes.....	125
5.4. Discussion.....	126
5.4.1. Energy transport through a homogeneous alkane chain.....	126
5.4.1.1. Transport from the azido group to the amide.....	126
5.4.1.2. Transport from am-I to the azido group.....	128
5.4.1.3. Transport from $\nu_{C=O}$ to the amide.....	130
5.4.2. Transport across the amide.....	131
5.4.2.1. Transport from $\nu_{N3}$ to the ester group.....	131
5.4.2.2. Transport from $\nu_{C=O}$ to the azido group.....	134
5.4.3. Mode delocalization.....	136

5.4.4. Ballistic transport initiation.....	138
5.5. Conclusions.....	142
5.6. Kinetic modeling.....	143
<b>Chapter 6. Vibrational Energy Transport in Electronically Conjugated Systems</b>	
6.1. Introduction .....	143
6.2. Experimental details .....	146
5.2.1. Experimental method .....	147
5.2.2. Sample preparation .....	147
5.2.3. Quantum-chemistry calculations .....	147
6.3. Results and discussion.....	147
6.4. Conclusions.....	158
<b>List of references</b> .....	159

## List of Tables

### Chapter 3. Ballistic Vibrational Energy Transport in Optical Alkane Chain Bands

**Table 3.1.** Chain band frequencies at  $q = 0$  and  $\pi$  ( $\omega(0)$  and  $\omega(\pi)$ ) and the group velocities computed for each band,  $\langle |V| \rangle$ , and for the specific frequency regions,  $\langle |V_b| \rangle$ , indicated in Figure 3.4(a)

**Table 3.2.** Comparison of the DFT computed frequencies for different chain bands with experimentally reported values for polyethylene.<sup>16</sup> The experimental frequencies are presented based on individual peak assignment.

### Chapter 4. Energy Transport in PEG Oligomers: Contributions of Different Optical Bands

**Table 4.1.**  $T_{\max}$  values (in ps) obtained from the waiting-time dependences of the  $\nu(\text{N}\equiv\text{N}) / \text{C1-C4}$  and  $\nu_{\text{as}}(\text{C=O}) / \text{C1-C4}$  cross peaks in azPEG4, 8, and 12.

**Table 4.2.** Results of the fit of the diagonal chain-state (C2-C4) waiting-time dependences with a double exponential function,  $S(T) = A_1 \exp(-T / \tau_1) + A_2 \exp(-T / \tau_2)$ . The relative contribution of the slowly decaying component ( $\tau_2$ ) is given in parentheses ( $\gamma = A_2 / (A_1 + A_2) \times 100\%$ ).

**Table 4.3.**  $T_{\max}$  values (in ps) obtained from the waiting-time dependences of cross peaks among C1 – C4 states in azPEG8 and azPEG12.

**Table 4.4.** PEG chain band frequencies at  $q = 0$  and  $\pi$  ( $\omega(0)$  and  $\omega(\pi)$ ) and the group velocities computed for each band,  $\langle |V| \rangle$ , for the all-anti PEG conformation.

**Table 4.5.** Coupling constants computed for the neighboring  $\text{CH}_2$  groups,  $\beta_1$ , and  $\text{CH}_2$  groups across the oxygen atom,  $\beta_2$ , in PEG chains for the relevant anti and gauche conformations. The site energies for the gauche and anti-conformations at the C-C bond are given ( $\omega_g$  and  $\omega_a$ ).

## Chapter 6. Vibrational energy transport in electronically conjugated systems

**Table 6.1.** Results of the fit of the diagonal  $\nu_{\text{as}}(\text{NO}_2)$  waiting-time dependences with a double exponential function,  $S(T) = A_1 \exp(-T/\tau_1) + A_2 \exp(-T/\tau_2)$ . The relative contribution of the slowly decaying component ( $\tau_2$ ) is given in parentheses ( $\gamma = A_2/(A_1 + A_2) \times 100\%$ ).

**Table 6.2.** Parameters of the IVR computed lifetimes of the  $\nu_{\text{as}}(\text{NO}_2)$  mode (Figure 6.3(a,b)). The decays were fit with a double exponential function,  $S(T) = A_1 \exp(-T/\tau_1) + A_2 \exp(-T/\tau_2)$ . The relative contribution of the slowly decaying component ( $\tau_2$ ) is given in parentheses ( $\gamma = A_2/(A_1 + A_2) \times 100\%$ ).

**Table 6.3.** DFT computed tag-reporter distances and coupling constants in DBA and 6-nitrohexanoic acid.

## List of Figures

### Chapter 1. Introduction

**Figure 1.1.** Structure of PBN with the energy transport time between various modes. The transport times between  $\nu(\text{C}\equiv\text{N})$  to Am-I,  $\nu(\text{C}\equiv\text{N})$  to Am-II, and  $\nu(\text{C}\equiv\text{N})$  to  $\nu(\text{C}=\text{O})$  are indicated in orange, green, and blue, respectively.

**Figure 1.2.** Structure of CH<sub>3</sub>-s with the tag ( $\nu(\text{N}\equiv\text{N})$ ) and reporter modes indicated. Energy transport times between the tag and different reporter groups are indicated.

### Chapter 2. Principles and Methods of 2DIR Spectroscopy

**Figure 2.1.** Molecular structures and simulated 2DIR spectrum for coupled acetone dimers

**Figure 2.2. (a)** Morse potential energy surface describing an anharmonic oscillator with energy levels and dipole transitions indicated. The ground-state bleach and stimulated emission are indicated in red, and the excited-state absorption is indicated by the blue arrow. **(b)** The resulting 2DIR spectrum. The positive response is indicated in blue and the negative response is indicated in red.

**Figure 2.3.** 2DIR spectrum of two coupled oscillators with frequencies of fundamental transitions  $\omega_1$  and  $\omega_2$ . The diagonal anharmonicities for the transitions are indicated as  $\Delta_{11}$  and  $\Delta_{12}$ , and the cross-peak anharmonicities are labeled as  $\Delta_{12}$ .

**Figure 2.4.** (a) An energy diagram for vibrational modes  $\omega_1$  and  $\omega_2$  showing coherence and population states accessed by the pulse sequence. The spectra of the IR pulses are shown on the left. (b) Delays between the pulses are shown in dual-frequency 2DIR measurements.  $\tau$  is the delay between  $k_1$  and  $k_2$ ,  $T$  is the delay between  $k_2$  and  $k_3$ , and  $t$  is the delay between the local oscillator and the 3<sup>rd</sup>-order signal. (c) Schematic of the three-pulse dual-frequency 2DIR experiment. (d) Example of dual frequency 2DIR spectrum correlating the  $\nu(\text{N}\equiv\text{N})$  and  $\nu_{\text{as}}(\text{C}=\text{O})$  modes of CH5-a (bottom).

**Figure 2.5.** (a) Depiction of direct coupling and relaxation-assisted coupling, respectively, between vibrational modes  $\omega_1$ ,  $\omega_2$ , and  $\omega_x$ . (b) and (e) reflect the cross peaks generated in the direct coupling and relaxation-assisted coupling cases, respectively. (c, d) An energy diagram of the energy transport process is illustrated. (f) Waiting-time kinetics curve generated from the intensity of the cross peak as a function of  $T$ .

**Figure 2.6.** (a) Structure of CH3-s with tag ( $\nu(\text{N}\equiv\text{N})$ , 2100  $\text{cm}^{-1}$ ) and reporter mode at 1205  $\text{cm}^{-1}$  indicated. (b) Atomic displacements of various reporter modes. (c) Waiting time dependence between  $\nu(\text{N}\equiv\text{N})$  and various reporter modes. (d) The normalized 1-D waiting time kinetics for the indicated cross peaks.

**Figure 2.7.** Schematic of the dual-frequency 2DIR instrument. (a) Essential functional components. (b) Detailed optical schematic. Here, Q is an MCT quad detector, D is an

optical delay stage, T is a translation stage, PR is a parabolic reflector, Pr is a right-angled prism reflector, PZ is a gold mirror equipped with a piezo actuator, BS is a beam splitter, WP is a waveplate – wire-grid polarizer or two wire-grid polarizers assembly, GP is a wire-grid polarizer, W is a phase modulator (wobbler), F is a mechanical flipper, OM is an optical mask, PD is a Si photodiode, SC is a sample cell, IS an image spectrometer, and MCD is an MCT array detector. BS1 is a 50/50 beam splitter with separate regions for m-IR and HeNe beams. Standard mirrors are omitted to increase legibility.

### Chapter 3. Ballistic Vibrational Energy Transport in Optical Alkane Chain Bands

**Figure 3.1.** (a) Diagram illustrating the principles of RA 2DIR spectroscopy. An example of the cross peak between  $\nu(\text{C=O})$  and  $\nu(\text{N}\equiv\text{N})$  in CH5-a, measured at  $T = 1$  ps (b) and its waiting time dependence (c) obtained by integrating the individual 2DIR spectra along  $\omega_\tau$  axis from 1650 to 1780  $\text{cm}^{-1}$ . The tag excitation pulses in this measurement were centered at 1710  $\text{cm}^{-1}$ , while the tag probing pulses were centered at 2100  $\text{cm}^{-1}$ . (d) Structures of the CHn-a and CHn-s compounds with indicated combinations of tags and reporters. (e) Linear absorption spectra of CH5-a, CH15-a, and CH5-s in  $\text{CDCl}_3$  at 120, 120, and 40 mM concentrations, respectively. The modes used as tags and reporters are indicated.

**Figure 3.2.** (a) Waiting time dependence of the  $\nu(\text{C=O})/\nu(\text{N}\equiv\text{N})$  cross-peak amplitude for the indicated CHn-a compounds. The fit with a two-exponential function is shown (red lines); the  $T_{\text{max}}$  values obtained from the fit are indicated by arrows. (b) Waiting time dependence of the  $\nu_{\text{as}}(\text{C=O})/\nu(\text{N}\equiv\text{N})$  cross-peak amplitude for the indicated CHn-s compounds at  $\sim 40$  mM concentration. The fit with a two-exponential function is

shown (red lines). (c)  $T_{\max}$  values plotted as a function of the tag–reporter distance for the CHn-a and CHn-s compounds for the transport initiated by  $\nu(\text{C=O})$ ,  $\nu_{\text{as}}(\text{C=O})$ , and  $\nu(\text{N}\equiv\text{N})$  modes. The linear fit (red lines) resulted in the transport speed of  $8.0 \pm 0.3$  and  $8.0 \pm 0.2$  Å/ps for the transport in CHn-a and CHn-s series initiated by  $\nu(\text{C=O})$  and  $\nu_{\text{as}}(\text{C=O})$  tags, respectively. The transport speed in CHn-a, initiated by  $\nu(\text{N}\equiv\text{N})$ , was  $14.4 \pm 2$  Å/ps.

**Figure 3.3.** Rates of all relaxation channels of the  $\nu(\text{N}\equiv\text{N})$  tag (a) in CH5-a, the  $\nu_{\text{as}}(\text{C=O})$  tag (b) in CH5-a, and  $\nu(\text{C=O})$  tag (c) in CH3-s, normalized in each case by the sum of all respective rate constants ( $k_i / \sum_i k_i$ ), where  $k_i$  is the rate of an individual third-order IVR pathway. (d) DFT computed energy states of CH15-a (filled symbols) and CH5-a (opened symbols), both in the all-anti conformation, plotted in the order of ascending energy for each motion type. There are 15 chain states of each motion type for CH15-a, except for  $\nu(\text{CC})$ , for which it is 14, which are equally spaced along abscissa. The x-axis for CH5-a was constructed the same way. The energies of the azido-group modes,  $\nu(\text{N=N})$  and  $\nu(\text{N-C})$ , are also shown (orange). The boxes, centered at the  $\nu(\text{N=N})$  and  $\nu(\text{N-C})$  mode frequencies, are 150 and 15  $\text{cm}^{-1}$  high, respectively, to indicate the chain states which fall within the full width at 1/e of the maximum of the respective azido-group transition. (e) Linear absorption spectra for CH5-a in KBr pellet (blue line) and 1,3,4,6-tetra-O-acetyl-2-azido-2-deoxy- $\alpha$ -D-glucopyranose ( $\alpha$  anomer, red line) in deuterated chloroform.

**Figure 3.4.** (a) Structure of 10 lowest-energy optical bands for the alkane chain (labeled) as a function of a normalized wavevector. The boxes match the width of the azido-group stretching modes,  $\nu(\text{N=N})$  and  $\nu(\text{N-C})$  (similar to that in Figure 3.3(d)) and

the  $\nu(\text{NOC})$  of the succinimide ester (violet). (b) Change of the population numbers at indicated delays after excitation of  $\nu_{\text{as}}(\text{C=O})$  in CH3-s.

**Figure 3.5.** (a) DFT computed potential energy surface for CH3-s along the C–C–C–O dihedral angle ( $\theta$ ); see inset. Mean square couplings strength of the ester stretching modes to the C–C stretching and CH<sub>2</sub> rocking states (b) and their values weighted by the Boltzmann factor (c). The ratio of the integrals under the curves in panel c equals 4.4; multiplication by the density of states ratio ( $\sim 3$ ) results in  $\sim 13$ -fold dominance of the relaxation rates into C–C stretching vs CH<sub>2</sub> rocking modes of the chain.

**Figure 3.6.** Linear absorption spectra of the CH5-s (blue) and reference (CH5-s-ref, black) compounds in the fingerprint region, normalized for the  $\nu(\text{CO})$  mode, and the difference between them (red). The region corresponding to the  $\nu(\text{N=N})$  mode in CH5-s is shaded.

**Figure 3.7.** (a) Waiting time dependence of the  $\nu(\text{N=N})/\nu_{\text{as}}(\text{C=O})$  cross-peak amplitude for the CHn-s compounds at  $\sim 45$  mM concentration. The fit with a two-exponential function is shown (red). (b) Dependence of  $T_{\text{max}}$  vs the tag–reporter distance measured for the CHn-s compounds for the energy transport initiated by the  $\nu(\text{N=N})$  tag and recorded with the  $\nu_{\text{as}}(\text{C=O})$  reporter. The linear fit (red) resulted in the transport speed of  $11 \pm 4$  Å/ps.

**Figure 3.8.** Dependences of the  $\nu(\text{C=O})/\nu(\text{N}\equiv\text{N})$  and  $\nu_{\text{as}}(\text{C=O})/\nu(\text{N}\equiv\text{N})$  cross-peak amplitudes for the CHn-a and CHn-s compounds, respectively. The fits with exponential decay function (red line) resulted in the characteristic decay distances,  $R_0$ , indicated in the inset.

## Chapter 4. Energy Transport in PEG Oligomers: Contributions of Different Optical Bands

**Figure 4.1.** Linear absorption spectra of the azPEG $n$  compounds and their structure. The arrows indicate different energy transport experiments performed in this study.

**Figure 4.2.** (a) 2DIR  $\nu_{\text{as}}(\text{C}=\text{O})/\nu(\text{N}\equiv\text{N})$  cross-peak ( $1740/2100\text{ cm}^{-1}$ ) of azPEG4 in  $\text{CDCl}_3$  measured at  $T = 10.2\text{ ps}$ . (b) Waiting time dependences of the  $\nu_{\text{as}}(\text{C}=\text{O})/\nu(\text{N}\equiv\text{N})$  cross-peak amplitude for azPEG0, 4, and 8. The curves are fitted with a double exponential function and the  $T_{\text{max}}$  values are indicated by arrows. (c) Tag-reporter distance dependence of  $T_{\text{max}}$  for the indicated compounds. Note that the tag-reporter distance was calculated as a through-bond distance. The fit with a linear function (red line), resulted in a transport speed of  $5.4 \pm 0.4\text{ Å/ps}$ .

**Figure 4.3.** Linear absorption spectrum of azPEG8 in  $\text{CDCl}_3$  (blue) in the frequency region from  $1010$  to  $1170\text{ cm}^{-1}$ . A fit with six Gaussian components (orange) and the resulting individual components (red, green) are shown. Whereas two narrow transitions, labeled as  $\nu(\text{NOC})$  and  $\nu(\text{CO})$ , belong to the NHS ester end group (green), the four components shown with red lines belong to the chain states. Note that the central frequencies of the C1-C4 peaks are  $1050\text{ cm}^{-1}$  (C1),  $1091\text{ cm}^{-1}$  (C2),  $1122\text{ cm}^{-1}$  (C3), and  $1147\text{ cm}^{-1}$  (C4).

**Figure 4.4.** (a) 2DIR magnitude spectrum of azPEG8 focusing at the cross-peaks between  $\nu(\text{N}\equiv\text{N})$  and C1-C4 chain states recorded at  $T = 2.2\text{ ps}$ . The linear absorption spectrum of azPEG4 is shown in the attached panels. (b-d) Waiting time dependences of the  $\nu(\text{N}\equiv\text{N}) / \nu(\text{C1-C4})$  cross-peak amplitudes for (b) azPEG4, (c) azPEG8, and (d)

azPEG12 obtained by integration of individual 2DIR spectra within specific cross-peak regions. Integration regions along the  $\omega_t$  axis were 1055-1075, 1090-1105, 1115-1130, and 1140-1155  $\text{cm}^{-1}$  for C1\*, C2, C3, and C4, respectively, and 2080-2125  $\text{cm}^{-1}$  along  $\omega_\tau$ . Note that C1 overlaps in frequency with the local  $\nu(\text{N-O-C})$  mode on the succinimide ester. All kinetics were fitted in the vicinity of their maxima with a double exponential function (red lines); the  $T_{\text{max}}$  values determined from the fit are shown in Table 4.1.

**Figure 4.5.** (a) 2DIR magnitude spectrum of azPEG8 focusing on the cross peaks between  $\nu_{\text{as}}(\text{C=O})$  and C1-C4 measured at  $T = 7$  ps. Waiting time dependences of the  $\nu_{\text{as}}(\text{C=O}) / \nu(\text{C1-C4})$  cross-peak amplitudes for (b) azPEG4, (c) azPEG8, and (d) azPEG12. The integration region along  $\omega_\tau$  was 1730-1760  $\text{cm}^{-1}$ ; the integration regions for C1-C4 peaks along the  $\omega_t$  axis are given in the Figure 4.4 caption. The kinetics were fitted in the vicinity of their maxima with a double exponential function (red lines); the  $T_{\text{max}}$  values determined from the fit are shown in Table 4.1.

**Figure 4.6.** (a) 2DIR spectrum of the chain band region (1050–1170  $\text{cm}^{-1}$ ) for azPEG8 at  $T = 3.0$  ps. The diagonal peak at about 1210  $\text{cm}^{-1}$  belongs to a localized  $\nu(\text{C-N-C})$  mode of the NHS ester. Waiting time dependences of (b) C3 and (c) C2 diagonal peaks of azPEGn. The kinetic traces were fitted with a double exponential function (see Table 4.2 for the results averaged over 3–5 measurements).

**Figure 4.7.** Waiting time dependences of various cross peaks among indicated chain states of azPEG8. The kinetics with a clear rise were fitted by a double exponential function and the  $T_{\text{max}}$  values were determined from the fit (see Table 4.3 for the  $T_{\text{max}}$  results averaged over 3-5 measurements).

**Figure 4.8.** PEG chain dispersion curves for the (a) all-anti and (b) anti-anti-gauche helical conformations. The graph b is reproduced with permission from ref.<sup>2</sup> All computed band frequencies in graph a were scaled by a factor of 0.97. Essential end-group states,  $\nu(\text{N}\equiv\text{N})$ ,  $\nu(\text{NOC})$ ,  $\nu(\text{OC})$ , and  $\nu(\text{NC})$ , are shown in panel a with horizontal bars; represented by their experimental frequencies, except for  $\nu(\text{NC})$ , given by the calculated frequency.

**Figure 4.9.** (a). DFT optimized structure of azPEG3a in the helical conformation, used for the relaxation dynamics analysis shown in this figure. (b,c) Graphically presented relaxation pathways for two excited bright chain states of (b) 1120  $\text{cm}^{-1}$  and (c) 1104  $\text{cm}^{-1}$  frequencies. For every product of the  $i \rightarrow j + k$  reaction, occurring with the rate constant of  $k_{i/jk}$ , where mode  $i$  is the initially excited mode, the bars of the length  $k_{i/jk}(1+n_k)(1+n_j)$  were added at  $\omega_j$  and  $\omega_k$ , where  $n_m$  is the thermal population of mode  $m$ . For every relaxation channel  $i + k \rightarrow j$ , having a rate constant  $k_{ik/j}$ , where  $i$  is the initially excited mode, the bars of the length  $n_k * k_{ik/j}$  were added at  $\omega_j$  and  $-\omega_k$ . The states of different chain bands are color coded and labeled in the inset. The percent numbers by the band labels are the total rates in percent that lead to populating the states of the selected group of states (bands),  $(\sum_{\text{within group}} k / \sum_{\text{all pathways}} k) \times 100\%$ , where  $k$  is the rate of a relaxation pathway involving the tag mode. d&e). Relaxation dynamics in azPEG3a followed excitation of the states at (d) 1120  $\text{cm}^{-1}$  and (e) 1104  $\text{cm}^{-1}$ . Population excess of the initially excited modes (red), and their fit with a double-exponential function (d) 0.8 ps (96%) and 10 ps (4%) components and (e) 0.8 ps (96%) and 10 ps (4%) components) are shown. The sum of the population excesses of all states of the indicated band(s) are shown separately. Thick black line shows the

population excess dynamics of all states of the  $\nu_5 - \nu_{15}$  bands; thin black line shows the population excess of all states within these bands except the initially excited state.

**Figure 4.10.** Population excess dynamics of four states of the  $\nu_{15}$  band of azPEG3a at 866, 834, 822, and 795  $\text{cm}^{-1}$  followed excitation of each state. The relaxation of the state at 1104  $\text{cm}^{-1}$  is shown for comparison (grey line). The fast components of the double-exponential fit, attributed to the mode lifetimes, are 1.2, 2.5, 2.9, and 1.4 ps for the kinetics at 866, 834, 822, and 795  $\text{cm}^{-1}$ , respectively; the amplitude of the fast component exceeds 87% for all kinetics. The inset shows population excess dynamics in the same four states of the  $\nu_{15}$  band following excitation of the 1104  $\text{cm}^{-1}$  state.

**Figure 4.11.** Simulated diagonal- and cross- peak amplitude waiting time dependences for chain states of azPEG3a for two chain-state tags at (a) 1120  $\text{cm}^{-1}$  and (b) 1104  $\text{cm}^{-1}$ . Both diagonal signals (blue lines) were fitted with a double exponential function, resulting in essentially the same component: the fast component of ca. 1.6 ps and slow component of ca. 13.7 ps with a contribution of ca. 42%. Some cross-peak kinetics show just decays (magenta), whereas others show a growth (cyan, green) followed by the decay with a peak at ca. 1-3 ps.

**Figure 4.12.** Modeled IVR pathways of azPEG3s and azCH3s. (A) All IVR pathways from the  $\nu_{\text{as}}(\text{C}=\text{O})$  between both azCH3s and azPEG3s are very similar. (B) All IVR channels from  $\nu(\text{N}\equiv\text{N})$  (into  $\text{N}=\text{N}$  and  $\text{C}-\text{N}$ ) are the same between azPEG3s and azCH3s.

**Figure 4.13.** Graphically presented relaxation pathways for (a) the excited  $\nu(\text{N}=\text{N})$  and (b) the excited  $\nu(\text{N}-\text{C})$  mode in azPEG3a. See the caption of Figure 4.9 for details of computations. The states of different chain bands are color coded and labeled in

the inset; the percent numbers by the band labels are the total rates in percent that lead to populating the states of the selected group (bands).

**Figure 4.14.** Graphically presented frequencies and delocalization for a linear chain of 12 states coupled with site energies of  $1000 \text{ cm}^{-1}$  (green squares) and nearest-neighbor coupling strength alternating between  $\beta_1$  and  $\beta_2$ , as shown in panel A. A uniform next-neighbor coupling  $\chi$  is applied. The values in wavenumbers for  $\beta_1$ ,  $\beta_2$ , and  $\chi$  used for each calculation are shown in the insets. The length of the error bars for each state equals to  $\pm(\text{PN}-1)/2$ , where PN is the participation number for the state.

**Figure 4.15. (a)** Dependences of  $T_{\text{max}}$  vs. chain length for the end group to end group (main panels) and end group to chain state (top panels) energy transport computed for  $N = 2 - 19$ ,  $W = (0.81 \text{ ps})^{-1}$ ,  $\gamma = 0.19 \text{ ps}^{-1}$ , and  $\Delta = 6.5 \text{ cm}^{-1}$ . A linear fit over the range with  $N = 3 - 19$  is shown with a red line resulting in the inverse slope of  $5.5 \text{ \AA/ps}$ . Inset shows the length dependence of the transported energy,  $P_{\text{max}}$ . Best fit with an exponential function,  $P_{\text{max}}(L) = P_{\text{max}}(0)\exp(-L/L_0)$ , is shown with red line and resulting  $L_0$  value is indicated. To match the experimental tag-reporter distances, the length was calculated as  $L = 13 \text{ \AA} + a(N - 1)$ . **(b)** Same dependences as in (a) computed for the transport through the  $\nu_{15}$  band using the following parameters:  $N = 2 - 19$ ,  $W = (4.5 \text{ ps})^{-1}$ ,  $\gamma = 0.22 \text{ ps}^{-1}$ , and  $\Delta = 4.3 \text{ cm}^{-1}$ . Linear fits over the range with  $N = 1 - 9$  and  $N = 12 - 20$  are shown with red lines having the inverse slopes of  $5.6$  and  $5.7 \text{ \AA/ps}$ , respectively.

**Figure 4.16. (a-c)** Location and delocalization extent for the DFT-computed  $\nu_{11}$ - $\nu_{15}$  normal modes of PEG-8 for three chain conformations. (a) all-anti chain conformation; (b) single gauche kink at a C-C bond at the all-anti conformation; (c) two gauche kinks at the all-anti conformation. The positions of the kinks are shown with red lines.

Delocalization for each mode, characterized by a participation number, is shown with error bars of  $\pm (PN-1)/2$  length. (d) Cartoon, illustrating different delocalization scenarios for coupled eigenstates of a chain of eight sites by showing their centers and participation numbers, PN (error bars of  $\pm (PN-1)/2$  length). (left) Fully delocalized states in the chain featuring no structural inhomogeneity; (middle) Type I structural kink; (right) Type II structural kink. The positions of the kinks are shown with red lines.

## Chapter 5. Ballistic transport of vibrational energy through an amide group bridging alkyl chains

**Figure 5.1.** (A) Structure of Amn-4,  $n = 4, 7, 11$ . The ovals represent different vibrational modes which were used as tag or reporter modes:  $\nu_{N3}$  (blue), am-I (cyan), am-II (orange), and  $\nu_{C=O}$  (magenta). (B) Solvent subtracted linear infrared spectra of Amn-4,  $n = 4, 7, 11$ . The arrows indicate the types of energy transport RA 2DIR measurements performed in this study.

**Figure 5.2.** (A) 2DIR magnitude spectrum of Am7-4 at  $T = 4.3$  ps. From left to right:  $\nu_{N3} / \text{am-II}$ ,  $\nu_{N3} / \text{am-I}$ , and  $\nu_{N3} / \nu_{C=O}$  cross peaks are seen. (B) 2D waiting time dependence of  $\nu_{N3} / \text{am-II}$ ,  $\nu_{N3} / \text{am-I}$ , and  $\nu_{N3} / \nu_{C=O}$  (bottom to top) obtained by integrating  $\omega_t$  from 2080 to 2120  $\text{cm}^{-1}$ . (C) Waiting time dependence of the  $\nu_{N3} / \text{am-I}$  cross-peak amplitude for Am4-4 (black line), Am7-4 (green line), and Am11-4 (blue line). The 1-D kinetic traces were fitted with a double exponential function (red lines). The area of integration over the cross peak consisted of  $\omega_t$  from 1650 – 1685  $\text{cm}^{-1}$  and  $\omega_\tau$  from 2090 – 2110  $\text{cm}^{-1}$ . The  $T_{\text{max}}$  is determined for each trace from the fitting. (D) Waiting time dependence of the  $\nu_{N3} / \text{am-II}$  cross-peak amplitude for Am4-4, Am7-4, and Am11-4. The area of integration over the cross peak consisted of  $\omega_t$  from 1520 – 1540  $\text{cm}^{-1}$  and  $\omega_\tau$  from

2090 – 2110  $\text{cm}^{-1}$ . The fitting of the kinetic traces and  $T_{\text{max}}$  consideration is the same as that for panel C. (E)  $T_{\text{max}}$  values plotted as a function of tag-reporter distance for the Am $n$ -4 compounds for the transport initiated by  $\nu_{\text{N3}}$  and detected at am-I (green circles) and am-II (magenta triangles). The energy transport speed was calculated as 1/slope of the linear fit (red lines) and resulted in speeds of 13.8 and 13.9 Å/ps for the am-I and am-II reporters, respectively.

**Figure 5.3.** (A) Waiting time dependence of the  $\nu_{\text{N3}} / \nu_{\text{C=O}}$  cross-peak amplitude for Am $n$ -4 compounds. The area of integration over the cross peak consisted of  $\omega_{\text{r}}$  from 1725 - 1755  $\text{cm}^{-1}$  and  $\omega_{\text{r}}$  from 2090 – 2110  $\text{cm}^{-1}$  (see Figure 5.2A). (B) The averaged over three or more measurements  $T_{\text{max}}$  values for  $\nu_{\text{N3}} / \nu_{\text{C=O}}$  all Am $n$ -4 compounds and plotted as a function of tag-reporter distance (blue stars). The linear dependence (red line) poorly describes the data.

**Figure 5.4.** Waiting time traces of the  $\nu_{\text{C=O}} / \text{am-I}$  (green) and  $\nu_{\text{C=O}} / \text{am-II}$  (blue) cross and  $\nu_{\text{C=O}}$  diagonal (grey) peaks in Am4-4. The inset zooms in on the early portion of the dynamics. The decay times found from the fit of both the  $\nu_{\text{C=O}}$  diagonal and  $\nu_{\text{C=O}} / \text{am-I}$  cross peaks is  $1.0 \pm 0.1$  ps; the slow components of 11 ps (1.4%) and 5.2 ps (10%) were involved in the fit of the respective traces.

**Figure 5.5.** (A) Waiting time traces of the  $\nu_{\text{C=O}} / \nu_{\text{N3}}$  cross-peak. The area of integration over the cross peak consisted of  $\omega_{\text{r}}$  from 1725 – 1745  $\text{cm}^{-1}$  and  $\omega_{\text{r}}$  from 2090 – 2110  $\text{cm}^{-1}$  (see Figure 5.6A). (B) Tag-reporter distance dependence of the  $\nu_{\text{C=O}} / \nu_{\text{N3}}$  cross-peaks Am $n$ -4 (mauve circles) and the  $\nu_{\text{C=O}} / \text{am-II}$  cross-peak (blue square).

**Figure 5.6.** (A) 2DIR spectrum of Am4-4 at  $T = 6.0$  ps focusing on the am-I /  $\nu_{\text{N3}}$  ( $\omega_{\tau} = 1660 \text{ cm}^{-1}$ ) and  $\nu_{\text{C=O}} / \nu_{\text{N3}}$  ( $\omega_{\tau} = 1750 \text{ cm}^{-1}$ ) cross peaks. The 1D waiting time kinetics in (B) were constructed from the am-I /  $\nu_{\text{N3}}$  cross peaks RA2DIR spectra. The  $T_{\text{max}}$  plotted as a function of tag-reporter distance yielded a speed of  $4.2 \pm 0.3 \text{ \AA/ps}$  (C) and is described well by a linear fit.

**Figure 5.7.** The dispersion relations of the  $\text{CH}_2$  rocking, twisting, wagging, scissoring, and C-C stretching bands for an alkane chain. The orange boxes match the width of the  $\nu_{\text{N=N}}$  and  $\nu_{\text{N-C}}$  modes of the azide. The group velocity for a narrow range of frequencies centered at  $\nu_0(q_0)$  is determined as  $V_{\text{gr.}}(q_0) = (\partial\omega/\partial q)|_{q=q_0}$ , and the mean group velocity over a selected range of wavevectors from  $q_1$  to  $q_2$  was computed as  $\langle V_{\text{box}} \rangle = (q_2 - q_1)^{-1} \int_{q_1}^{q_2} |V(q)| dq$ . The transport speeds supported by different portions of the dispersion curves are indicated as insets.

**Figure 5.8.** Extent of delocalization for the DFT computed chain-states in (A) methyl 11-azidoundecanoate (CH10-ester), (B) Am4-4 and (C) Am7-4. The state shown are of the  $\text{CH}_2$  rocking (black circle), twisting (magenta stars), wagging (green diamonds), scissoring (blue hexagons), and C-C stretching (cyan triangles) states. The positions of the azide, amide, and methyl ester functional groups are shown by the orange dotted lines. The center of amplitude for each state is plotted with error bars as  $\pm(\text{PN}-1)/2$  length, where PN is the participation number, showing the extent of mode amplitude delocalization within the molecule.

**Figure 5.9.** Rates of all relaxation channels for am-I (A) and  $\nu_{\text{C=O}}$  (B). The DFT calculated structures used for the analysis is shown above their respective graphs. The relaxation channels into the optical bands for am-I (A) are 0.1% in scissoring, 8.0% in

wagging, 8.4% into twisting, and 13.3% into CC stretching bands. There is a single dominating IVR channel for  $\nu_{\text{C=O}}$  (B) into the O-C-CH<sub>2</sub> mode on the ester at 911 cm<sup>-1</sup>.

**Figure 5.10.** Dependences of the  $\nu_{\text{N3}} / \nu_{\text{C=O}}$  and  $\nu_{\text{N3}} / \text{am-I}$  cross-peak amplitudes in the Amn-4 compounds. The amplitudes were fitted with an exponential decay function resulting in a characteristic decay distances,  $L_0$ , indicated in the figure.

**Figure 5.11.** Experimental points from Figures 5.2E (red and blue) and 5.3B (green) are shown with symbols. The lines represent the results of the kinetic modeling.

## Chapter 6. Vibrational energy transport in electronically conjugated systems

**Figure 6.1.** Structures of (a) BA and (b) DBA. (c) Solvent-subtracted infrared absorption spectra of BA and DBA in DMSO.

**Figure 6.2.** (b) Waiting time dependence of the  $\nu_{\text{as}}(\text{NO}_2)$  diagonal-peak amplitude for BA and DBA. The fit with a double-exponential function is shown (red lines). (a) 2DIR spectrum at  $T = 3$  ps of the  $\nu_{\text{as}}(\text{NO}_2)$  diagonal (1530 cm<sup>-1</sup> diagonal),  $\nu(\text{C=O})$  diagonal (1700 cm<sup>-1</sup> diagonal), and the  $\nu_{\text{as}}(\text{NO}_2) / \nu(\text{C=O})$  cross peak (1710 cm<sup>-1</sup>, 1530 cm<sup>-1</sup>).

**Figure 6.3.** (a) Relaxation dynamics in BA and DBA of  $\nu_{\text{as}}(\text{NO}_2)$  with harmonic frequencies of 1584 and 1572 cm<sup>-1</sup>, respectively. The decay is fit with a double-exponential function (red lines). (b,c) Graphically presented relaxation pathways for the  $\nu_{\text{as}}(\text{NO}_2)$  normal mode in (b) BA and (c) DBA.

**Figure 6.4.** Waiting time dependence of the  $\nu_{\text{as}}(\text{NO}_2)$  diagonal-peak amplitude for BA and DBA. The fit with a double-exponential function is shown (red lines). The 2DIR spectrum of the  $\nu(\text{C=O})$  diagonal can be seen in Figure 6.2(a).

**Figure 6.5.** DFT computed harmonic frequencies and atomic displacements in BA for (a) the CH<sub>2</sub> wagging mode at 1473 cm<sup>-1</sup>, (b)  $\nu_{\text{as}}(\text{NO}_2)$  at 1536 cm<sup>-1</sup>, (c)  $\nu(\text{C}=\text{C})$  at 1590 cm<sup>-1</sup>, (d)  $\nu(\text{C}=\text{C})$  at 1600 cm<sup>-1</sup>, and (e)  $\nu(\text{C}=\text{O})$  at 1711 cm<sup>-1</sup>. All DFT computed harmonic frequencies are scaled by 0.97. All vibrational modes between 1470 and 1711 cm<sup>-1</sup> are presented here.

**Figure 6.6.** 2DIR spectrum showing the (a)  $\nu_{\text{as}}(\text{NO}_2) / \nu(\text{C}=\text{O})$  and (b)  $\nu(\text{C}=\text{O}) / \nu_{\text{as}}(\text{NO}_2)$  cross peaks in BA at  $T = 3$  ps. (c) Waiting time dependence of the  $\nu_{\text{as}}(\text{NO}_2) / \nu(\text{C}=\text{O})$  and (d)  $\nu(\text{C}=\text{O}) / \nu_{\text{as}}(\text{NO}_2)$  cross-peak amplitude for the BA and DBA compounds. The fit with a two-exponential fit is shown (red lines). (e)  $T_{\text{max}}$  values plotted as a function of the tag-reporter distance for the BA and DBA compounds for the transport initiated by  $\nu(\text{C}=\text{O})$  (magenta) and  $\nu_{\text{as}}(\text{NO}_2)$  (gray). The DFT computed tag-reporter distances for BA and DBA are 5.73 and 10.0 Å, respectively.

**Figure 6.7.** DFT calculated structures of (a) DBA and (b) 6-nitrohexanoic acid.

## Chapter 1

### Introduction

#### **1.1. Measuring thermal energy transport from the mesoscopic to the molecular level: overview of the field**

It has long been known that the flow of vibrational energy in molecules is an omnipresent driving force for most chemical phenomena, although an understanding of the intricate mechanistic details of such vibrational energy transport is still needed. Such energy transfer plays an important role in any process involving barrier crossing. For example, for a peptide to undergo a conformational change additional vibrational energy is needed to overcome the barrier; when the new conformation is achieved, the excess vibrational energy need to be removed to make the process irreversible.<sup>1-3</sup> The importance of the excess energy for chemical reactions is also apparent: the breaking and reforming of chemical bonds in reagents to generate the required products require overcoming the potential energy barriers in such chemical rearrangements by fluctuations of excess energy between the reactants and the environment.<sup>4-7</sup> In the developing field of molecular electronics, implementing efficient methods of heat dissipation is important for the performance and longevity of devices.<sup>8-9</sup> Attractive candidates for this purpose include systems which are light weight and can dissipate large quanta of energy efficiently.

The most widely-used methods for studying energy transport and thermal conductivity in mesoscopic materials are  $3\omega$  modulation and time-domain thermoreflectance approaches. Such techniques introduce a temperature gradient in the sample via resistive heating or a laser pulse, and the thermal conductance can be derived by measuring physical changes in the material.<sup>10-13</sup> Various regimes of energy transport were observed in such materials, such as ballistic and diffusive regimes. In addition, a switch between transport mechanisms, for example from diffusive to ballistic, occurs with a decrease of a sample thickness and is recorded experimentally by a change in the thermal conductivity coefficient.

One of the limitations of such measurements is that the smallest threshold sample sizes need to be in the hundreds of nanometers, which limit the types of systems which can be studied. As a result, information specific to individual components of the studied material is not accessible, but only the bulk material as a whole. For example, nanostructured materials which can be measured using these techniques often consist of several components, and the energy transport within and between each component must be understood to optimize such systems. Consider self-assembled monolayer junctions with alkane chains sandwiched between metal layers -- both the energy transport across the metal-chain interface and through the chain determine the overall heat conductivity;<sup>14-</sup><sup>15</sup> however, it is difficult to separately measure these contributions, which limits the understanding of the overall energy transport process. In such measurements, which requires two dimensions to be macroscopic, the system temperature was typically near room temperature, resulting in the transport being governed by acoustic phonons.

Molecules offer exciting opportunities to transfer energy efficiently due to strong covalent bonds in the backbones. On the molecular level, different methods employing ultrafast laser spectroscopy have been used to measure vibrational energy transport. The molecular systems in such cases are designed to have a chromophore (tag) which is excited. Upon relaxation, the tag introduces excess energy into the molecule and initiates energy transport. The transport can be probed using a variety of transitions, called reporters, which have to be sensitive to the excess energy arrival. Various tag moieties can be used for this purpose including those which require vibrational excitation,<sup>16-17</sup> electronic excitation,<sup>18-20</sup> and the flash-heating of a metal surface of which the molecules are attached to.<sup>15</sup> The latter two methods release a large amount of energy into or near by the molecule, thus initiating numerous transport pathways, whose individual contributions to the overall transport are difficult to separate.

More delicate sources of excess energy can be provided by vibrational tag excitation using mid-IR laser pulses. Such tags can be designed to feature localized and spectrally isolatable high-frequency vibrational modes, such that the amount of excess energy provided to the molecular system is known. Several model molecular systems designed in this way have been interrogated by in two-dimensional infrared spectroscopy (2DIR) permitting one to track energy transport and to elucidate the transport mechanism in molecules with varying architecture.<sup>21-24</sup>

## **1.2. Diffusive transport in molecules: principles and examples**

Thermal conductivity of matter of different sizes and dimensionalities is an important parameter to understand, as it has significant implications in many fields of science and engineering. In 1822, Joseph Fourier formulated the empirical relationship

describing the relation between the conduction heat flux to the direction of the temperature gradient in a material. The most general equation describing multidimensional conduction is

$$\vec{q} = -k\vec{\Delta}T$$

Where  $\vec{q}$  is the heat flow rate by conduction ( $\frac{W}{m^2}$ ),  $k$  is the thermal conductivity of the material ( $\frac{W}{m \cdot K}$ ), and  $\vec{\Delta}T$  is the temperature gradient ( $\frac{K}{m}$ ). This equation is known as Fourier's law. One important implication of this equation is that the heat transfer propagates in the direction of decreasing temperature. Although initially controversial, Fourier's law is now highly regarded and forms the basis of thermal conductivity and heat diffusion in materials.<sup>25</sup> After its conceptualization, Fourier's law was applied to describe the thermal conductivity in many classes of materials including fluids, solid metals, polymeric materials, and nanostructures.<sup>25-26</sup>

Advances in studying the thermal conductivity in materials resulted in the discovery of two primary regimes of energy transport: diffusive and ballistic.<sup>27</sup> In the diffusive regime, energy propagates by random hopping between spatially separated and localized vibrational modes. Such a regime of energy transport is governed by Fourier's law. It has been observed that this transport regime occurs not only in bulk materials, but also at the molecular level in systems ranging from ionic liquids<sup>28</sup> and electrolyte solutions<sup>29</sup>, to biologically relevant compounds such as peptides<sup>30-31</sup>, DNA<sup>32-33</sup>, and amino acids<sup>18, 34-35</sup>. In molecules, diffusive energy transport occurs through a process known as intramolecular vibrational redistribution (IVR). In an IVR process, the population of an initially excited vibrational state of a polyatomic molecule is

redistributed between different quantum states of the molecule. The secondary populated states may also relax into other vibrational modes as well, and so on. The IVR process is driven by the anharmonicity between the involved modes, meaning that vibrational states which are well-coupled will experience faster rates of IVR.

Consider a 3<sup>rd</sup>-order IVR process involving exchange between an initially populated vibrational mode  $i$ , dissipating energy into lower-frequency modes  $j$  and  $k$  which are coupled anharmonically. These anharmonic interactions lead to transitions which change the population numbers  $n_i, n_j, n_k \leftrightarrow n_i - 1, n_j + 1, n_k + 1$ . The energy of the IVR process must be conserved, such that  $\omega_i = \omega_j + \omega_k$ , however a mismatch in energy can be compensated by the surrounding medium within  $k_B T$ . In the case that tag mode  $i$  is delocalized well, upon relaxation energy can travel efficiently to large distances by the diffusive mechanism.

Energy transfer experiments have shown that IVR rates between tag and reporter modes can be useful as a “molecular ruler” – that is the energy transfer kinetics can be correlated to the distance traveled with nearly angstrom sensitivity. Condensed-phase dual-frequency 2DIR experiments reported by Naraharisetty et. al. performed on 4-(4-oxo-piperidine-1-carbonyl)-benzonitrile (PBN) demonstrate this concept well. (Figure 1.1A). The PBN molecule is an ideal model compound to elucidate this concept, as there are many IR-active vibrational modes which are separated both spatially and energetically, meaning they can be excited or probed selectively. The distance between  $\nu(\text{C}\equiv\text{N})$  of the cyano group and Am-I of the amide moiety is 6.5 Å, while the  $\nu(\text{C}\equiv\text{N})$ -to- $\nu(\text{C}=\text{O})$  distance is 11 Å. The energy arrival time from the  $\nu(\text{C}\equiv\text{N})$  mode to the Am-I

vibrational mode is 7.5 ps, and the transport time from  $\nu(\text{C}\equiv\text{N})$  to  $\nu(\text{C}=\text{O})$  is 10.6 ps. The differences in energy transport time correlate to the distance between the respective groups.

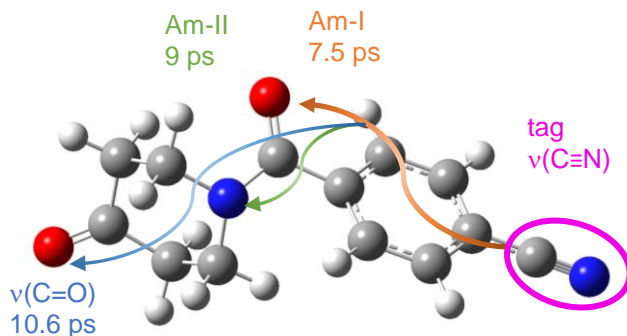


**Figure 1.1.** Structure of PBN with the energy transport time between various modes. The transport times between  $\nu(\text{C}\equiv\text{N})$  to Am-I,  $\nu(\text{C}\equiv\text{N})$  to Am-II, and  $\nu(\text{C}\equiv\text{N})$  to  $\nu(\text{C}=\text{O})$  are indicated in orange, green, and blue, respectively.

A similar trend was observed in the compound referred to as CH3-s (Figure 1.2), featuring an azide tag moiety and N-hydroxysuccinimide ester reporter group (NHS).<sup>36</sup> Similar to PBN, the succinimide ester end group features reasonably located modes suitable to serve as reporters. The energy transport was initiated by excitation of  $\nu(\text{N}\equiv\text{N})$  of the azide ( $2100\text{ cm}^{-1}$ ) and the energy transport arrival was measured to a variety of reporter modes on the succinimide ester tag moiety (Figure 1.2). A trend was observed between energy transport time and location of the reporter: the energy transport time was larger for the reporter modes located farther away from the  $\nu(\text{N}\equiv\text{N})$  tag. Such behavior was attributed to extra IVR steps needed to reach the reporter.

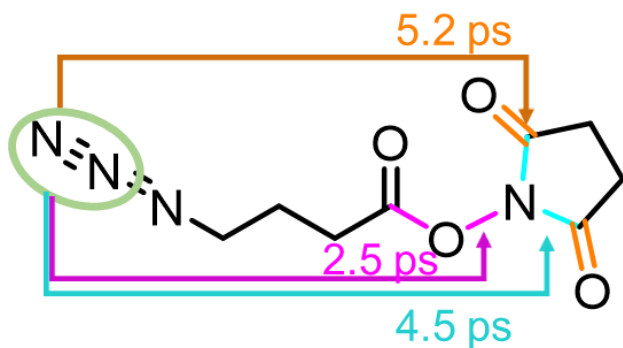


**Figure 1.2.** Structure of CH<sub>3</sub>-s with the tag ( $\nu(\text{N}\equiv\text{N})$ ) and reporter modes indicated. Energy transport times between the tag and different reporter groups are indicated.

In both systems a diffusive energy transport mechanism was proposed. The dependence of the time of energy transport on the intermodal distance was found to be linear, resulting in an approximate speed of  $1.2 \text{ \AA/ps}$ .<sup>36-38</sup> It is important to note that diffusive transport generally does not result in a constant speed regime, and instead a quadratic dependence of the inter-site distance.<sup>39-40</sup> A constant speed regime for diffusive energy transfer can occur in cases where there are large energy losses from the molecule into the solvent. In this case, only the IVR steps in the forward direction will deliver energy to the reporter by the smallest number of IVR steps needed, resulting in a constant speed.<sup>41</sup> Such regime is called directed diffusion.

### 1.3. Ballistic energy transport: principles and examples

Unlike the diffusive transport regime, which is slow and occurs through IVR between localized states, ballistic transport can be very fast and occurring as a wave packet through highly delocalized states. A widely used principle to distinguish diffusive from ballistic transport is that diffusive transport occurs when the mean free path (MFP) of the phonons is much smaller than the transport length, where as in ballistic transport the

phonon MFP is exceeds the length of transport. In the ballistic regime, Fourier's law does not apply as the transport is affected by both phonon-boundary and internal scattering.<sup>26,</sup>

42

Because ballistic energy transport must occur through delocalized states, molecular systems supporting such transport have to be highly periodic in nature. The translational symmetry of these structures results in bands, represented as dispersion curves, which are made up of delocalized vibrational modes that are characterized by their energy and wavevector. For ballistic transport to occur, a superposition of the delocalized vibrational states for any particular band(s) form a wave packet (WP) which propagates freely in the substance. The speed of the WP is determined by the coupling of the neighboring sites from which it is formed – the stronger the coupling, the faster the transport can be. One of the requirements of the ballistic regime is that the vibrational modes which make up the band must be delocalized throughout the entire length of the transport. Another requirement is that the duration of the transport cannot exceed the dephasing time of the WP, which is determined by the total dephasing time of the individual states of the band.

Many mesoscopic materials with periodic motifs such as nanowires,<sup>13, 43-45</sup> lattice structures,<sup>46-47</sup> and nanotubes<sup>48</sup> have exhibited ballistic thermal conductance; often it is proposed that acoustic phonons are responsible for the thermal transport. Several ultrafast spectroscopic studies have demonstrated ballistic transport occurring in molecules.

Ballistic energy transport in molecules for the first time was reported by Troe and co-workers in one-dimensional alkane chains of varying length, bridging an azulene chromophore and anthracene moiety.<sup>19</sup> Upon UV-excitation of the azulene S<sub>1</sub> band (400 nm), rapid internal conversion led to making that part of the molecule hot. The

vibrationally populated  $S_0$  vibrational states of the azulene delivered energy to the alkane chains. The cooling dynamics of the azulene moiety was measured as a function of the bridge length, and infinitely high speed was observed.

An exciting experiment using sum frequency generation (SFG) spectroscopy was reported by Dlott and co-workers, demonstrating intramolecular transport through self-assembled thiolated alkane monolayers chemisorbed to a gold surface in response to a flash heating of the gold at 800K. The experiments showed as a fast speed of transport through the alkane chains of 9.5 Å/ps was achieved.

Further investigation of ballistic transport in oligomers was performed utilizing the dual-frequency 2DIR technique. In these studies, various oligomer chains were terminated by end groups featuring high-energy vibrational states which could be selectively excited with m-IR laser pulses to initiate energy transport. In these studies, the transport speed dependence on the chain-type along with energy-transport initiator was assessed. The specific type of 2DIR spectroscopy used to measure vibrational energy transfer between spatially separated modes is called relaxation-assisted two-dimensional infrared spectroscopy (RA 2DIR). Details of the method will be provided in Section 2 of the dissertation.

Lin et. al. reported the observation of fast vibrational energy transport in PEG oligomers studied by RA 2DIR spectroscopy.<sup>49</sup> In these experiments, PEG chains of varying length (0, 4, 8, and 12 PEG units) were terminated by azide and NHS groups.<sup>49-50</sup> By initiating energy transport via excitation of  $\nu(\text{N}\equiv\text{N})$  of the azide, it was found that the transport occurred with a constant speed of 5.5 Å/ps. Initially, the energy transport was assumed to be ballistic suggested by the high transport speed. As mentioned before, one

of the criteria for ballistic energy transport is that the duration of the transport cannot exceed the dephasing time of the WP. The constant-speed regime in PEGs was observed through 12 PEG units, which exceeds 60 Å through-bond distance and taking over 9 ps. The question was raised: is it possible for the energy transport in PEGs to be truly ballistic for such a large duration of travel? This question is addressed in Chapter 4 of the present dissertation.

Following the PEG experiments, RA 2DIR spectroscopy was used to study vibrational energy transport through other types of oligomer chains with various end groups. For example, energy transport measurements were performed on perfluoroalkane chains terminated by carboxylic acid and CHF<sub>2</sub> moieties.<sup>51-52</sup> The transport initiated by excitation of the carbonyl stretching of the carboxylic acid was found to occur with a constant speed of 3.9 Å/ps. Then the energy transport experiments were performed on alkane chains of varying length (CH<sub>n</sub>-s, n = 3, 5, 10, 15 methylene units) terminated by an azide and NHS ester. The transport initiated by  $\nu(\text{N}\equiv\text{N})$  resulted in a constant speed of transport of 14.4 Å/ps, which was the fastest observed energy-transport speed yet observed in such compounds.<sup>36</sup>

The observation of vibrational energy transport through these molecular chains was exciting as the speeds were fast and the transport efficiency was high. The difference in speeds and efficiency among different types of chains was also compelling; expanding on the observations could allow the design of molecular systems which can exhibit desired thermal conductive properties. However, these observations raised many questions:

- Can we identify the properties of molecular chains which dictate the speeds that they can support?

- Does the method of transport initiation play a role in the observed speeds? If so, how is it related to the properties of the chain?
- What is the extent of which true ballistic transport can occur in these molecular chains? If the ballistic portion occurs for a length which is shorter than the length of the compound, does a switch in the mechanism occur? If so, how do we describe it?

These key questions are addressed in the scope of the present dissertation. To provide answers to these questions, dual-frequency 2DIR experiments were performed on a variety of different molecular chains and varying energy-transport initiators. In addition to experiment, computational methods such as density functional theory and various theoretical models were implemented in addressing these questions. A combination of the experimental results with the modeling resulted in the description of the energy transport in molecular chains at the mechanistic level.

#### **1.4. Dissertation Outline**

Chapter 2 of the dissertation describes the spectroscopic methods used to perform experiments which are discussed in the present work. The chapter encompasses the theoretical principles of non-linear spectroscopy, a description of the RA 2DIR spectroscopic method, and details of the specific 2DIR spectrometer used in the interrogation of the mentioned molecular systems.

Chapter 3 describes the RA 2DIR study of the energy transport via alkane chains initiated by a variety of end-group modes. It was found that the speed of transport was highly dependent on the vibrational mode used as the initiator. The IVR and ballistic

energy transport processes occurring in the studied systems were modeled. Combining the experimental results with the modeled results describe the energy transport mechanism throughout the entire molecule in each case of initiation. The energy transport is described as being fully ballistic, occurring through different chain-bands depending on the case of initiation. These models were developed by Dr. Alexander Burin and Dr. Arkady Kurnosov.

Chapter 4 describes a detailed RA 2DIR study of energy transport in varying length PEG oligomers in different cases of transport initiation. Unlike in the alkanes, the speed of transport via PEG chains was found to be the same in different cases of energy transport initiation. The presence of the heteroatom in the PEG backbone allowed the chain-state dynamics to be probed, shedding light on the energy transfer dynamics between the states. IVR modeling along with solving the quantum Liouville equation for a system of coupled states was performed to describe the energy transport in PEGs. The energy transport through the PEG chain through various chain-bands is described as being initially diffusive, and a switch to directed diffusion occurs. These models used were developed by Dr. Alexander Burin and Dr. Arkady Kurnosov.

Chapter 5 describes RA 2DIR experiments performed on alkane chains containing a different type of perturbing functional groups (carbonyl and amide) groups intersecting the chain at various places. These studies were aimed at understanding the impact that functional groups which intersect the chain have on the through-chain energy transport. It was observed that the initially formed wave packet loses coherence upon its arrival to the amide moiety, but then reforms a wave packet after passing the amide which can travel ballistically. The impact of the perturber on the chain-state delocalization is thought

to affect the transport regime, as the amide impacts the chain state delocalization.

Theoretical modeling was capable of explaining the through-chain energy transport in the compounds featuring the amide.

Chapter 6 describes RA 2DIR experiments on compounds featuring electronic delocalization. It was discovered that vibrational energy transport in polyphenyl chains can be fast and possibly ballistic. It was also demonstrated that the electronically conjugated bridge can result in substantial initial coupling between the tag and reporter groups. This is an ongoing study.

## Chapter 2

### Principles and Methods of 2DIR Spectroscopy

#### 2.1. Introduction

The root of the word “spectroscopy” is the word “spectre”, which is latin for “ghost” or “appartition”. Because spectroscopy probes the influence of light on matter without ever actually seeing the molecules, the etymology of the term “spectroscopy” is very appropriate. Spectroscopy has been a powerful tool in interrogating molecular properties by using light sources spanning nearly all regions of the electromagnetic (EM) spectrum. For example, nuclear magnetic resonance (NMR) spectroscopy is based on the absorption of EM radiation in the radio frequency range (0.5 – 75 m), measuring the energy transfer between nuclear spins to gain information regarding the chemical structure. On the higher-energy end of the EM spectrum, ultraviolet-visible (UV-vis) spectroscopy employs significantly shorter-wavelength radiation (200 – 700 nm) to interrogate the electronic transitions of molecules.

The scope of this dissertation pertains to mid-infrared spectroscopy. The mid-infrared (m-IR) region of the EM spectrum is in between the microwave and visible regions, ranging from 3 to 30  $\mu\text{m}$ . When interacting with EM radiation in the m-IR, molecular vibrations can be excited. m-IR spectroscopies can interrogate the oscillations of molecular bonds, gaining information pertaining to the structure and dynamics of molecules. Generally, there are two classes of molecular vibrations: stretching, in which a

bond which is made up of two or more atoms periodically increases and decreases, and bending, in which the bond angles between different atoms within a molecule change. To be IR-active, a vibration must induce a change in dipole within the molecule.

In 1957, Perkin-Elmer developed the first low-cost infrared spectrometer using sodium chloride as a dispersive element.<sup>53</sup> It was not until 1969 that Digilab produced the first commercial IR spectrometer using a Michelson Interferometer.<sup>54</sup> Since then, Fourier-transform infrared spectroscopy (FTIR) which uses optical interferometry is the standard in steady-state infrared spectroscopy, typically using a heated silicon carbide radiation source.

Advances in the development of lasers producing ultrashort pulses have generated great opportunity for developing vibrational spectroscopies which can deliver dynamic information regarding molecular vibrations on ultrafast timescales. With the development of Kerr-optics and mode locking lasers, laser pulses with temporal widths as short as tens of femtoseconds were generated. Since its development in 1986, Ti:Sapphire lasers have become the standard light source in the application of ultrafast spectroscopy.<sup>55</sup> Since then, many methods of ultrafast laser spectroscopy have been developed including transient absorption spectroscopy and 2DIR spectroscopy, which are capable of measuring the interactions of different vibrational modes.

2DIR spectroscopy was the main experimental tool used in the studies described in this present dissertation. It is a non-linear, third-order spectroscopic technique. The next subsection in this chapter describes the fundamentals of linear and non-linear spectroscopy. The descriptions follow the principles detailed in “Nonlinear Optics” by

Robert Boyd, third edition, Academic Press, 2008 and "Concepts and Methods of 2D Infrared Spectroscopy", by Peter Hamm and Martin Zanni, first edition, 2011.

## 2.2. Nonlinear optical spectroscopy: introduction

In spectroscopy, an incident electric field,  $E(t)$ , with a frequency,  $\omega$ , interacts with a molecular sample to induce a dipole moment. In linear spectroscopy, the sample response reflects the interaction of a single electric field,  $E = E_0 \cos(\omega t - kx)$ . The resulting macroscopic polarization,  $P(t)$ , is expressed as

$$P(t) = \chi(\omega)E(t) \quad (2.1)$$

Where  $\chi(\omega)$  is a second-ranked tensor describing the first-order response of the system, also known as the linear susceptibility.

In microscopic systems, the first-order polarization is expressed as

$$\mu = \alpha E \quad (2.2)$$

where  $\mu$  is the induced dipole moment,  $\alpha$  is the linear polarizability, and  $E$  is the interacting electric field.

If the intensity of the oscillating field is sufficiently strong, a nonlinear response from the sample can be observed. Pulsed laser light sources, for example, can provide sufficient power to generate nonlinear responses. In such a case, the resulting non-linear polarization of the medium is a function of multiple electric fields. It is expressed as a power series in the following form

$$P^{(n)}(t) = \sum_n \chi^{(n)}(\omega) E^n(t) \quad (2.3)$$

The first term ( $n = 1$ ) describes the 1<sup>st</sup>-order linear polarization, while the  $n > 1$  terms describe the  $n^{\text{th}}$ -order non-linear polarizations. The non-linear susceptibility  $\chi^{(n)}$  is a tensor of  $n + 1$  rank. The non-linear susceptibility can be a function of many different frequencies. Consider the second-order nonlinear response, expressed as

$$P^{(2)}(t) = \chi^{(2)} E^{(2)} \quad (2.4)$$

Suppose the interacting electric field has two distinct frequency components, described as

$$E(t) = E_1 e^{-i\omega_1 t} + E_2 e^{-i\omega_2 t} + c. c. \quad (2.5)$$

where  $c. c.$  is the complex conjugate. Using this expression of the electric field, the second-order polarization can be expressed as

$$P^{(2)}(t) = \chi^{(2)} [E_1^2 e^{-2i\omega_1 t} + E_2^2 e^{-2i\omega_2 t} + 2E_1 E_2 e^{-i(\omega_1 + \omega_2)t} + 2E_1 E_2^* e^{-i(\omega_1 - \omega_2)t} + c. c.] + 2\chi^{(2)} [E_1 E_1^* + E_2 E_2^*] \quad (2.6)$$

As apparent by eq 2.6, a variety of frequency components of the second-order nonlinear polarization are present:

$$P(2\omega_1) = \chi^{(2)} E_1^2 \text{ (second harmonic generation)}$$

$$P(2\omega_2) = \chi^{(2)} E_2^2 \text{ (second harmonic generation)}$$

$$P(\omega_1 + \omega_2) = 2\chi^{(2)} E_1 E_2 \text{ (sum frequency generation)}$$

$$P(\omega_1 - \omega_2) = 2\chi^{(2)} E_1 E_2^* \text{ (difference frequency generation)}$$

$$P(0) = 2\chi^{(2)} (E_1 E_1^* + E_2 E_2^*) \text{ (optical rectification)}$$

Note that even-ordered non-linear susceptibilities have symmetry restrictions such that only non-centrosymmetric media will generate even-order responses. Many molecular systems, such as solutions, studied by spectroscopy display inversion symmetry and the even-ordered contributions to the signal from the bulk normally vanish.

It is apparent that with increasing order of non-linearity, additional frequency components contribute to the polarization and the description of such polarization becomes increasingly complicated. Consider third-order non-linear polarization, which is a function of three different electric field interactions

$$P^{(3)}(t) = \chi^{(3)}E^3(t) \quad (2.7)$$

Suppose the expression for the electric field,  $E(t)$ , has three distinct spectral components

$$E(t) = E_1 e^{-i\omega_1 t} + E_2 e^{-i\omega_2 t} + E_3 e^{-i\omega_3 t} + c. c. \quad (2.8)$$

Substituting equation 2.8 into equation 2.7 results in 44 different frequency components for the third-order polarization, oscillating at  $\omega_1, \omega_2, \omega_3, 3\omega_1, 3\omega_2, 3\omega_3, (\omega_1 + \omega_2 + \omega_3), (-\omega_1 + \omega_2 + \omega_3), (\omega_1 - \omega_2 + \omega_3), (\omega_1 + \omega_2 - \omega_3), (2\omega_1 \pm \omega_2), (2\omega_1 \pm \omega_3), (2\omega_2 \pm \omega_1), (2\omega_2 \pm \omega_3), (2\omega_3 \pm \omega_1), (2\omega_3 \pm \omega_2)$  frequencies, in addition to their negative counterparts.

In non-linear spectroscopy, laser sources tuned to specific frequencies spatially overlap in the sample to generate a desired non-linear response. The emitted signal, generated by any particular polarization component, travels in a well-defined direction, determined by the wavevectors ( $k_i$ ) of the electric fields interacting with the sample. The non-linear polarization can be measured with a spectrograph and information pertaining

to the molecular structure and dynamics of the sample can be obtained. In general, nonlinear spectroscopy involving more than one frequency can give considerably richer information about the sample than linear spectroscopy.

### 2.3. Fundamentals of 2DIR spectroscopy

2DIR spectroscopy is a third-order non-linear spectroscopic technique which correlates vibrational modes in molecular systems. In this technique, multiple (two or three) ultrafast m-IR laser beams are tuned to resonate with molecular vibrations of interest. The beams are focused onto a sample so that they are spatially overlapping in it. The time delays between the m-IR pulses are precisely controlled. The nonlinear signal emitted by the molecular system is dispersed spectrally by a spectrometer and measured using a mid-IR array detector, most often via heterodyned or homodyned detection approach.

In 2DIR spectroscopy, we consider couplings of vibrational modes. To illustrate this concept, consider the carbonyl stretches ( $\nu(\text{C=O})$ ) of a pair of acetone molecules which form a dimer, just a few angstroms apart (Figure 2.1). In such a scenario, the molecules are close enough to feel each other's electrostatic potential, altering their molecular orbitals, and ultimately causing their vibrational frequencies to shift. The molecular vibrations in this case are described as being coupled, and the interaction energy of the two vibrational states,  $\beta_{12}$ , is calculated as

$$\beta_{12} = \frac{1}{4\pi\epsilon_0} \left[ \frac{\vec{\mu}_1 \cdot \vec{\mu}_2}{r_{12}^3} - 3 \frac{(\vec{r}_{12} \cdot \vec{\mu}_1)(\vec{r}_{12} \cdot \vec{\mu}_2)}{r_{12}^5} \right] \quad (2.9)$$

where the vector  $\vec{\mu}_{1,2}$  is the dipole direction,  $\vec{r}_{12}$  is the vector which points from transition dipoles 1 to 2, and  $\epsilon_0$  is the vacuum permittivity. Note that this expression breaks down in the case that the distance between the transition dipoles is too close. Suppose the unperturbed frequency of each acetone molecule was  $1710\text{ cm}^{-1}$ . However, since the dimer pair is strongly interacting, for example such that  $\beta_{12} = 5\text{ cm}^{-1}$ , the states are split such that  $\Delta\omega = 2\beta_{12} = 10\text{ cm}^{-1}$ , resulting in new coupled states with energies  $1705\text{ cm}^{-1}$  and  $1715\text{ cm}^{-1}$ . In the 2DIR spectrum, each of the coupled states generates a pair of peaks around the diagonal of the spectrum – they are called the diagonal peaks (Figure 2.1). One peak is directly on the diagonal, laying exactly on the fundamental frequency of the state with a positive sign, while the other is shifted off diagonal and has a negative sign; the origins of the signs will be detailed in the next section. The anharmonicity of the vibrational mode (known as the diagonal anharmonicity) causes the shift in the off-diagonal peak. The x and y axes of the 2D spectrum are labeled  $\omega_{\text{probe}}$  and  $\omega_{\text{pump}}$ , respectively; the naming of the axes will be described within this chapter.

Because the carbonyl stretches are coupled, they will generate a pair of cross peaks with negative and positive peaks. The cross peaks contain information regarding the interaction strength between the two molecules. The pair of cross peaks will appear approximately at (x,y) coordinates ( $\omega_{\text{probe}} = 1705\text{ cm}^{-1}$ ,  $\omega_{\text{pump}} = 1715\text{ cm}^{-1}$ ) and ( $\omega_{\text{probe}} = 1715\text{ cm}^{-1}$ ,  $\omega_{\text{pump}} = 1705\text{ cm}^{-1}$ ), however the anharmonic shift between the negative and positive peaks (known as the off-diagonal anharmonicity) will cause the center of the peaks to be slightly shifted off resonance with the fundamental frequencies (Figure 2.1).

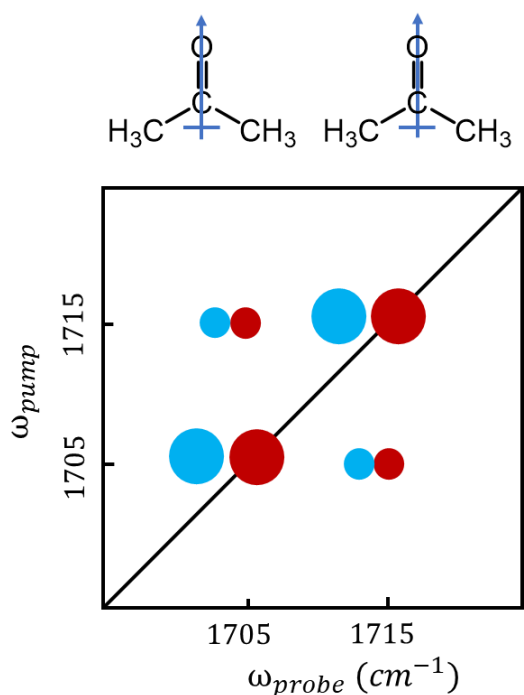


**Figure 2.1.** Molecular structures and simulated 2DIR spectrum for coupled acetone dimers

The example of the coupled acetone molecules serves to give a qualitative description of how coupling affects vibrational frequencies of the coupled molecules and how such coupling can result in cross peaks. The following section will describe more in detail how 2DIR can describe the potential energy surface of such oscillators.

### 2.3.1. 2DIR spectrum of a single oscillator

In this section, we will consider the simplest case of how a 2DIR spectrum will look like for a single vibrational state. The potential energy surfaces of molecular vibrations can be represented by the Morse oscillator

$$V(x) = D(1 - e^{-ax})^2 \quad (2.10)$$

where  $D$  is the depth of the well,  $x$  is the interatomic distance, and  $\alpha$  is the curvature of the potential well. Solving the Schrodinger equation for the harmonic oscillator results in the exact solution for vibrational eigen states

$$E_n = \hbar\omega \left(n + \frac{1}{2}\right) - x \left(n + \frac{1}{2}\right)^2 \quad (2.11)$$

where  $\omega$  is the harmonic frequency,  $n$  is the quantized eigenstate of the oscillator, and  $x$  is the anharmonicity.

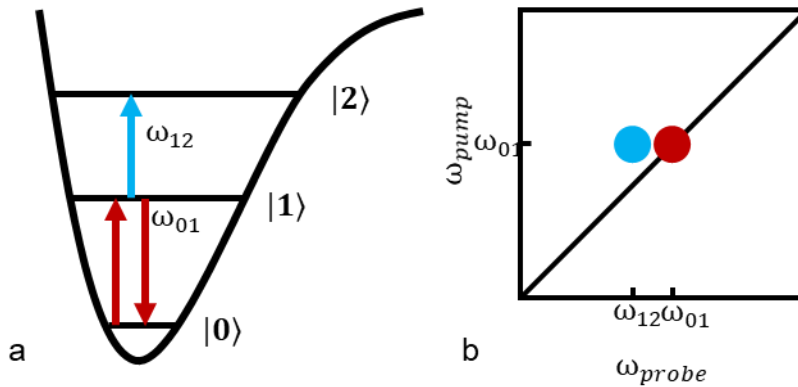


**Figure 2.2.** (a) Morse potential energy surface describing an anharmonic oscillator with energy levels and dipole transitions indicated. The ground-state bleach and stimulated emission are indicated in red, and the excited-state absorption is indicated by the blue arrow. (b) The resulting 2DIR spectrum. The positive response is indicated in blue and the negative response is indicated in red.

The most straight forward 2DIR technique is the pump-probe method, and so the following description of the correlation spectrum in Figure 2.2(b) will be described in the context of a pump-probe experiment. In such an experiment, two laser pulses interact with the sample. The first narrow-band pulse (known as the pump pulse) tuned to frequency  $\omega_{01}$  ( $\omega_{01} = \hbar\omega - 2x$ ) excites the molecules from vibrational ground state  $|0\rangle$  to the first excited vibrational state  $|1\rangle$ . The second broad-band pulse (probe) follows the pump, causing some fraction of molecules in the vibrationally excited state to undergo

either stimulated emission back to the ground state, or to be promoted into the second vibrational excited state  $|2\rangle$  by excited state absorption. The third-order signal coincides with the probe beam and is always in phase with it. The difference spectrum is normally plotted, which results from the difference in the probe signal with vs. without the pump pulse. This results in a pair of peaks, one positive in amplitude and one negative. The negative peak amplitude is caused by the depletion of the ground state (ground state bleach) and the stimulated emission, as both these contributions to result in less absorption (Figure 2.2). The excited state absorption, however, gives a positive contribution as it results in a new absorption induced by the pump pulse. The signal from this process appears at frequency  $\omega_{12}$  ( $\omega_{12} = \omega_{01} - 2x$ ), which is redshifted from  $\omega_{01}$  due to the anharmonicity of the potential, shown in Figure 2.2(b) as the blue peak. The magnitude of the anharmonic shift is  $\omega_{12} - \omega_{01} = 2x = \Delta$ , which is known as the diagonal anharmonicity. Note that the amplitudes of the positive and negative peaks will be similar, even though the negative peak results from two processes and the positive peak results from only one. This is because the harmonic oscillator dipole transition moment scales as  $\mu_{12}^2 = 2\mu_{01}^2$ .

### 2.3.2. 2DIR spectrum of coupled oscillators

The 2DIR spectrum of coupled oscillators contains substantial information on the interaction strength of two vibrational states due to their transition dipoles, including information linked to the distance between the two modes. Consider two transition dipoles, 1 and 2, which are sufficiently far apart.

The potential describing these two coupled oscillators is calculated as

$$V(r_1, r_2) = V_1(r_1) + V_2(r_2) + \beta_{12}r_1r_2 \quad (2.12)$$

Because the two oscillators are coupled and interacting, they no longer behave as isolated oscillators and their combination band is shifted from the  $\omega_1 + \omega_2$  value, where  $\omega_1$  and  $\omega_2$  are the harmonic frequencies of the vibrational modes 1 and 2, respectively. As a result, along with an anharmonic shift being observed in the diagonal peaks ( $\Delta_{11}$  and  $\Delta_{22}$  are the diagonal anharmonicity terms for transitions 1 and 2, respectively), the combination band will be shifted by the off-diagonal anharmonicity  $\Delta_{12}$  as demonstrated in Figure 2.3.

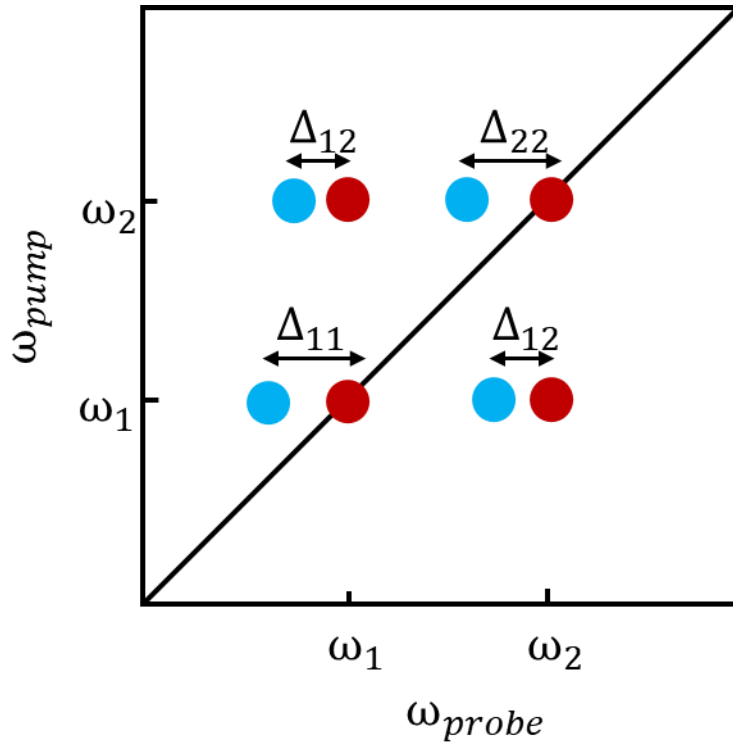


**Figure 2.3.** 2DIR spectrum of two coupled oscillators with frequencies of fundamental transitions  $\omega_1$  and  $\omega_2$ . The diagonal anharmonicities for the transitions are indicated as  $\Delta_{11}$  and  $\Delta_{12}$ , and the cross-peak anharmonicities are labeled as  $\Delta_{12}$ .

Thus, transition dipoles which interact strongly will have large off-diagonal anharmonicities, resulting in a greater off-diagonal frequency shift in comparison to a pair of dipoles which interact weakly.

#### **2.4. Frequency domain 2DIR spectroscopy**

As stated earlier, the simplest 2DIR spectroscopy method is the single-frequency pump-probe method collected in the frequency domain. When using this method, a two-photon interaction between one beam of light and the sample is used to excite the vibrational modes. The center frequency of the spectrally narrow IR pulse is scanned across the frequency region of interest; when resonance with the vibrational mode of interest is achieved, absorption occurs. A spectrally broad probe pulse is focused on the sample to generate the third-order signal which is collected by a spectrograph. Although this 2DIR method is the most simple to implement, there are several drawbacks. One of the drawbacks is that the signal-to-noise is small. Because the third-order signal co-propagates with the probe pulse, the noise from the much stronger probe is reflected in the measurements. Another disadvantage of this measurement style is broadening of the time profile of the pump pulse, resulting in the narrowing of the spectral width. The typical pulse duration in such measurements is about 1 ps. The temporal broadening of the pump pulse limits the time resolution of the measurements.

#### **2.5. Time-domain dual-frequency 2DIR spectroscopy**

Time-domain 2DIR spectroscopy is a more complicated experiment, however it is a more sensitive technique which results in much higher signal-to-noise. In the frequency domain experiments, a narrow-band pump pulse is used, and the center frequency is

scanned. In time domain experiments, the pump consists of two femtosecond broad-band pulses with a set time delay between them ( $\tau$ ), and the delay is scanned instead of the central frequency. By scanning  $\tau$ , the excited vibrational modes are being brought in-and-out of resonance with the pump. This results in a sinusoidal spectrum as a function of time. By performing a Fourier transform of the resulting sinusoid, the frequency components of the obtained signal can be separated.

The development of dual-frequency 2DIR spectroscopy, using a heterodyned detection method, has dramatically increased the sensitivity of the measurements. In this method, two independently-tunable m-IR beams are split into two parts each: the splitting of the first beam forms the pump pulses with wavevectors  $k_1$  and  $k_2$  tuned to resonate with the selected vibrational state (“tag”) with a frequency of  $\omega_1$ , while the split of the second beam forms the  $k_3$  probe pulse and local oscillator, tuned to resonate with a second oscillator (reporter) with a frequency of  $\omega_2$  (Figure 2.4). Consider a molecular system featuring two vibrational modes,  $|01\rangle$  and  $|10\rangle$ , which are spatially close and interact significantly. The first pump pulse  $k_1$  prepares the system in a particular vibrational coherence state,  $|01\rangle\langle 00|$ . The dipoles oscillate and dephase during a time period,  $\tau$ , before the second pump pulse,  $k_2$ , interacts with the sample to generate a population state,  $|01\rangle\langle 01|$ . In experimental implementation, the time delay  $\tau$  between  $k_1$  and  $k_2$  is controlled by a delay stage. After a waiting time between the 2<sup>nd</sup> and 3<sup>rd</sup> pulses,  $T$ , the probe pulse  $k_3$  interacts with the system generating another coherence,  $|11\rangle\langle 01|$  which emits radiation. This radiation is directed to overlap with the local oscillator, spectrally dispersed by a spectrograph, and then detected with an MCT array detector via the approach called spectral interferometry.

Because the thickness of the sample for 2DIR measurements is much larger than the wavelength of the m-IR pulses, the third-order signal is generated in a specific direction. The three phase-locked infrared laser pulses with wave vectors of  $k_1$ ,  $k_2$ , and  $k_3$  interact with the sample at a specific geometry to satisfy the phase matching conditions:  $\omega_s = -\omega_1 + \omega_2 + \omega_3$  and  $k_s = -k_1 + k_2 + k_3$ , where  $\omega_s$  and  $k_s$  are the frequency and wavevector of the third-order signal, respectively (Figure 2.4(b)). Figure 2.4(d) is an example of a resulting dual-frequency 2DIR spectrum showing the correlation between  $\nu(\text{N}\equiv\text{N})$  of an azide moiety and the carbonyl stretching vibrational mode of a carboxylic acid group ( $\nu_{\text{as}}(\text{C}=\text{O})$ ) in a compound referred to as CH5-a (Figure 2.4(d), bottom). The  $\nu(\text{N}\equiv\text{N})$  was initially excited by  $k_1$  and  $k_2$  and the  $\nu_{\text{as}}(\text{C}=\text{O})$  was detected by  $k_3$ . Corresponding to the pulse sequence, the y-axis is labeled  $\omega_\tau$  and the x-axis is labeled  $\omega_t$ . Such a cross peak would be labeled as the  $\nu(\text{N}\equiv\text{N})/\nu_{\text{as}}(\text{C}=\text{O})$  peak.

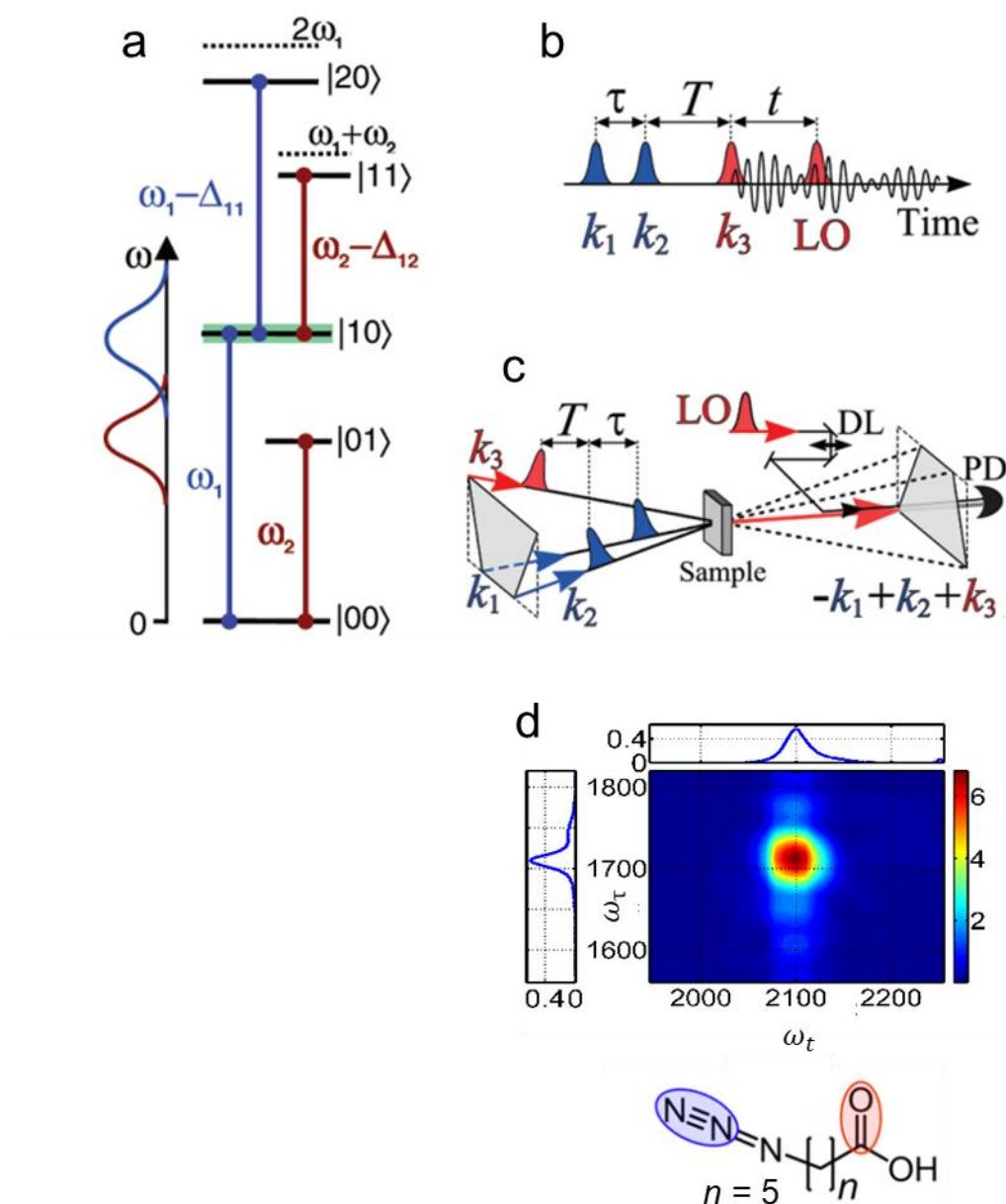


**Figure 2.4.** (a) An energy diagram for vibrational modes  $\omega_1$  and  $\omega_2$  showing coherence and population states accessed by the pulse sequence. The spectra of the IR pulses are shown on the left. (b) Delays between the pulses are shown in dual-frequency 2DIR measurements.  $\tau$  is the delay between  $k_1$  and  $k_2$ ,  $T$  is the delay between  $k_2$  and  $k_3$ , and  $t$  is the delay between the local oscillator and the 3<sup>rd</sup>-order signal. (c) Schematic of the three-pulse dual-frequency 2DIR experiment. (d) Example of dual frequency 2DIR spectrum correlating the  $\nu(\text{N}\equiv\text{N})$  and  $\nu_{\text{as}}(\text{C}=\text{O})$  modes of CH5-a (bottom).

## 2.6. Relaxation-assisted 2DIR spectroscopy

The technique used in the studies within the scope of this dissertation is coined relaxation assisted 2DIR (RA 2DIR) spectroscopy, which is a flavor of time-domain dual-frequency 2DIR. RA 2DIR relies on the observation that upon the relaxation of the excited tag, a substantial amount of energy is deposited within the molecule. Following this, the excess energy starts to propagate through the molecule in all directions, including the direction towards the reporter. When the excess energy reaches the vicinity of the reporter, low-frequency vibrational modes with frequencies  $\omega_x$  become excited (Figure 2.5(a,c)). Because the mode(s) with frequency  $\omega_x$  have substantial spatial overlap with the reporter mode, many of them are well coupled to the reporter and a cross peak will be present in the 2DIR spectrum. At small delay times, the energy has not had the chance to reach the reporter vicinity. Because of this, the cross peak reflects the direct coupling of  $\omega_1$  and  $\omega_2$  as demonstrated in Figure 2.5(b). The overall cross-peak amplitude in this case is small, so the anharmonicity  $\Delta_{12}$  is small. This leads to the negative and positive portions of the real signal to overlap, resulting in amplitude cancellation. At larger waiting times, however, the excess energy can reach the reporter site, exciting  $\omega_x$  and leading to a larger anharmonic shift reflecting  $\Delta_{x2}$ . This scenario means that less cancellation will occur between the negative and positive peaks, which gives a larger cross-peak amplitude.

Integrating the cross-peak area as a function of  $T$  results in a characteristic curve, as shown in Figure 2.5(f). With increasing  $T$ , the energy travels towards the reporter site and reaches a maximum at the waiting time denoted as  $T_{\max}$ . At  $T > T_{\max}$ , the cross-peak amplitude decays due to relaxation of the molecule to the surrounding medium. At  $T_{\max}$ ,

the cross-peak amplitude reaches a plateau caused by an overall increase in sample temperature.  $T_{\max}$  describes the time needed to deliver the largest amount of energy from the tag to the reporter site; it is referred to as the energy transport time. Note that the cooling times for different molecules and reporters were found to be similar, affecting the peak position similarly.

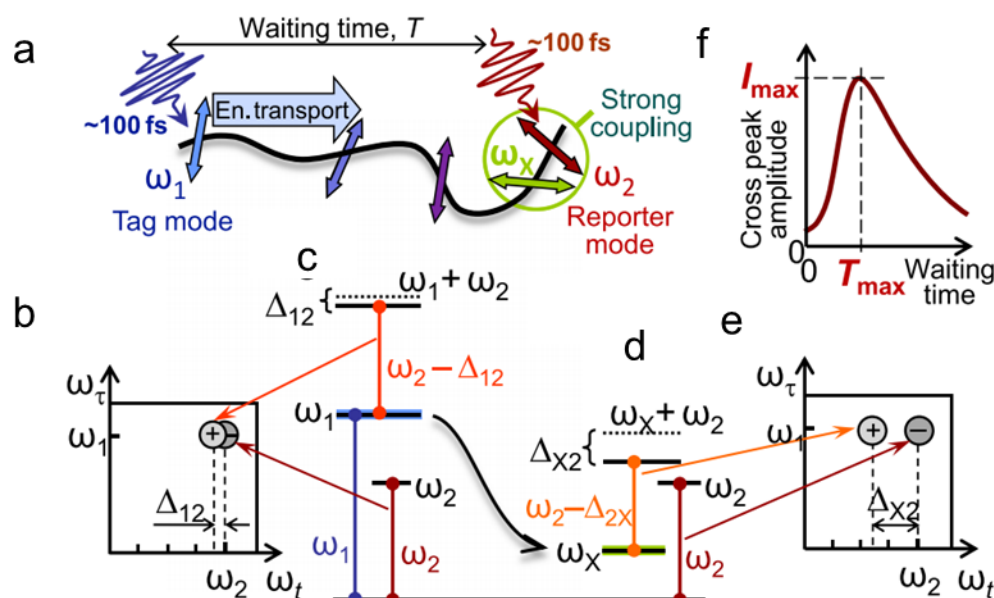


**Figure 2.5.** (a) Depiction of direct coupling and relaxation-assisted coupling, respectively, between vibrational modes  $\omega_1$ ,  $\omega_2$ , and  $\omega_x$ . (b) and (e) reflect the cross peaks generated in the direct coupling and relaxation-assisted coupling cases, respectively. (c, d) An energy diagram of the energy transport process is illustrated. (f) Waiting-time kinetics curve generated from the intensity of the cross peak as a function of  $T$ .

The principles of RA 2DIR which were just described will be illustrated in Figure 2.6, using an energy transport study which was reported by Rubtsova et. al.<sup>36</sup> In these experiments, the transport between two spatially separated functional groups, an azide moiety and N-hydroxysuccinimide (NHS), was studied. The studied compound is shown

in Figure 2.6(a). Numerous IR active modes of the NHS ester were used as reporters; some of the reporter frequencies and displacements are shown in Figure 2.6(b). The energy transport was initiated by excitation of  $\nu(\text{N}\equiv\text{N})$  of the azide ( $2100\text{ cm}^{-1}$ ) with a short m-IR pulse, and the energy transport arrival to a variety of reporter modes on the NHS tag moiety was measured. The reporter  $\nu(\text{N}-\text{O})$  mode at  $1070\text{ cm}^{-1}$  is closest to the azide, the  $\nu(\text{C}-\text{N}-\text{C})$  of the succinimide ring at  $1205\text{ cm}^{-1}$  is the next-closest to the tag, and the  $\nu_{\text{as}}(\text{C}=\text{O})$  of the carbonyls on the succinimide ring at  $1742\text{ cm}^{-1}$  is the furthest spatially from the azide. The cross peaks between the  $\nu(\text{N}\equiv\text{N})$  and these reporters were measured, and the time-dependence of the 2D cross-peak amplitudes is shown in Figure 2.6(c). It is apparent from this projection of the cross peaks that each peak reaches a maximum at different waiting times; the  $\nu(\text{N}-\text{O})$ ,  $\nu(\text{C}-\text{N}-\text{C})$ , and  $\nu_{\text{as}}(\text{C}=\text{O})$  reporters reach the maximum peak amplitudes at 2.5, 4.5, and 5.1 ps, respectively. Clearly, a dependence between the tag-reporter distance and the energy arrival time exists as the vibrational modes which are more deeply embedded into the NHS have larger  $T_{\text{max}}$  values. The cross-peak areas were integrated as a function of time to yield the 1-D waiting curves shown in Figure 2.6(d).

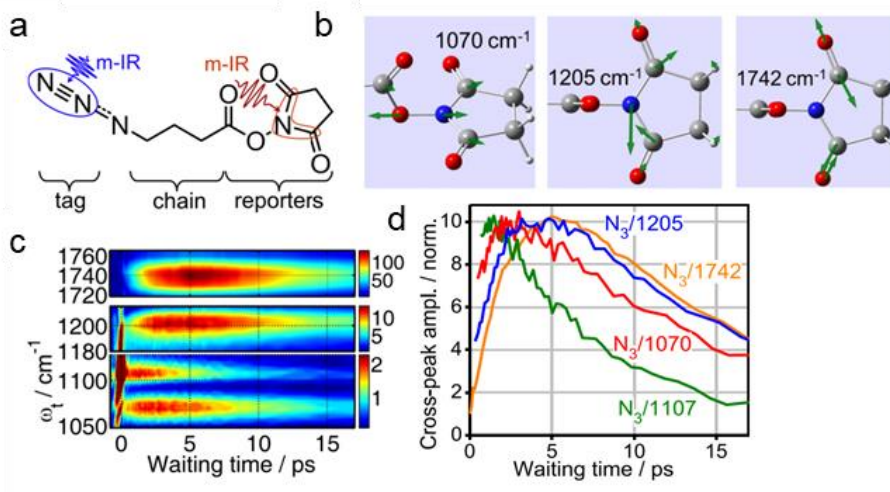


**Figure 2.6.** (a) Structure of CH3-s with tag ( $\nu(\text{N}\equiv\text{N})$ ,  $2100\text{ cm}^{-1}$ ) and reporter mode at  $1205\text{ cm}^{-1}$  indicated. (b) Atomic displacements of various reporter modes. (c) Waiting time dependence between  $\nu(\text{N}\equiv\text{N})$  and various reporter modes. (d) The normalized 1-D waiting time kinetics for the indicated cross peaks.

## 2.7. Details of the fully-automated 2DIR spectrometer

The research group of Professor Rubtsov designed and built the first fully automated dual-frequency three-pulse 2DIR spectrometer, accessing a spectral range from 800 to 4000 wavenumbers. This instrument, of which I participated in the construction, has over 20 computer-controlled elements and was used in the experiment described in this dissertation. The in-depth description of this novel user-friendly 2DIR spectrometer was reported by Leger et. al.<sup>56</sup>

A block diagram of the essential components of the instrument is illustrated in Figure 2.7 (a). A Ti:Sapphire laser, producing 1.5 W of power at 1 kHz repetition rate, 800 nm wavelength,  $\sim 14\text{ nm}$  bandwidth (fwhm), and 80 fs pulse duration (Libra, Coherent), was used to pump a fully computer-controlled dual optical parametric amplifier (OPA, Palitraduo, Quantronix). Two pairs of Signal and Idler OPA outputs

were directed into two noncollinear difference-frequency generation (DFG) units, also computer-controlled (nIR-A and nIR-B, Quantronix), each featuring two interchangeable DFG crystals, AgGaS<sub>2</sub> and AgGaSe<sub>2</sub>, to cover a broader range of m-IR frequencies. The m-IR pulse energy produced by each DFG unit varies from 1.5 to 10  $\mu$ J, depending on the central wavelength. First, each m-IR beam passes through a schematic that stabilizes its direction. The schematic uses a single HgCdTe (MCT) quad detector as a position sensitive element and provides beam direction stabilization accuracy of better than 50  $\mu$ rad over the whole spectral range.<sup>56</sup> Next, beam A is split into two equal parts and a small part of beam B is taken for use as the local oscillator (LO). The time delays between the four pulses are controlled by translation stages. Finally, a user-selected beam geometry at the sample is set, the pulses are focused into the sample, and the third-order signal is measured by an image spectrometer with an array detector via heterodyned detection.

A detailed schematic of the instrument is illustrated in Figure 2.7(b). After direction stabilization by units Bst A, beam A passes a phase modulator (W1) and a 10 cm long delay stage (D0, Newport), and then split into two equal parts using a broadband 50/50 beam splitter (BS1, Tydex) to serve as pulses 1 and 2 for 2DIR measurements. Each pulse, 1 and 2, is delayed by a short delay stage (D1 and D2, Newport), reflected from the right-angled prism reflector (Pr), and directed at the parabolic reflector (PR1) that focuses them into the sample. Another mIR beam, B, is directed by Bst B and split into two uneven parts, taking ~90% for pulse 3 and ~10% for the LO. Beam 3 passes through a phase modulator (W2) and is directed at the parabolic reflector (PR1). Interferometric measurements require precise knowledge on the delays at which an

interferogram is measured. Moreover, the Fourier transformation methods used to generate the spectra from interferograms work best with the data measured on a constant-step delay grid. A schematic that uses a Helium Neon laser (HeNe) interferometer is built for accurately measuring the delays between pulses 1 and 2. A co-propagating HeNe beam is introduced with beam A before the D0 stage (Figure 2.7(b), dashed line). The HeNe beam is then split at BS1 into two equal parts and each follows the respective mIR beam. Just before the parabolic reflector, the two HeNe beams are reflected and set to interfere using a pair of lenses, as shown in the box “HeNe phase meas.” at the bottom-left corner of Figure 2.6(b).

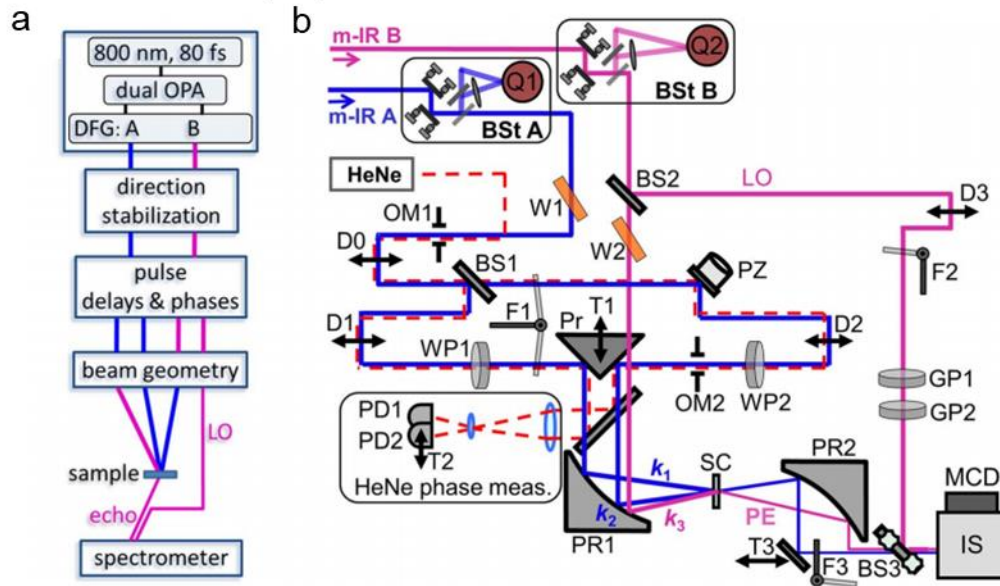


**Figure 2.7.** Schematic of the dual-frequency 2DIR instrument. **(a)** Essential functional components. **(b)** Detailed optical schematic. Here, Q is an MCT quad detector, D is an optical delay stage, T is a translation stage, PR is a parabolic reflector, Pr is a right-angled prism reflector, PZ is a gold mirror equipped with a piezo actuator, BS is a beam splitter, WP is a waveplate – wire-grid polarizer or two wire-grid polarizers assembly, GP is a wire-grid polarizer, W is a phase modulator (wobbler), F is a mechanical flipper, OM is an optical mask, PD is a Si photodiode, SC is a sample cell, IS an image spectrometer, and MCD is an MCT array detector. BS1 is a 50/50 beam splitter with separate regions for m-IR and HeNe beams. Standard mirrors are omitted to increase legibility.

The interference pattern is directed by two Si photodiodes (PD1, PD2), which measure the delay changes with an accuracy of  $\sim 10$  nm. To be able to measure m-IR interferograms on a constant-step grid and to provide active delay stabilization, a piezo-actuator was attached to one of the mirrors (PZ) in the beam 2 path.<sup>57</sup> The piezo-actuator range of motion of  $\sim 14$   $\mu\text{m}$  and the response time of  $\sim 0.5$  ms are sufficient to work efficiently in the closed-loop mode; the delay stabilization accuracy of  $\sim 60$  as is achieved. Moreover, for largest third-order signal strength, the m-IR beams must be directed onto the sample at angles determined by the frequencies of the m-IR pulses and

must satisfy the phase-matching conditions. The required beam geometry is set by a right-angled prismatic mirror (Pr), which is mounted on a translation stage (T1) and placed before the parabolic reflector PR1. The beam geometry at the sample is set so that the direction of the third-order signal is preserved. After re-collimation by the second parabolic reflector (PR2), the third-order signal is focused at the entrance slit of the image spectrometer (IM, Triax-190, Jobin Yvon). The LO beam passes through a delay stage (D3); a BaF<sub>2</sub> window (BS3) fixed in a Gimbal mount is used to combine it collinearly with the third-order signal. An MCT array detector (IR-6400, Infrared Associates) records the interference of the third-order signal and LO, measured in a heterodyned fashion using a double phase-cycling regime with wobblers W1 and W2 implemented on beams A and k<sub>3</sub>. Two wire-grid polarizers (GP1 and GP2) are placed on the LO beam for adjusting its intensity. The polarization directions of beams 1 and 2 are controlled by waveplate-polarizer pairs (WP1 and WP2), allowing for polarization-sensitive measurements. The instrument is controlled by three specially designed computer programs, named Beam Stabilization, HeNe Position, and Data Acquisition. Upon request, the Beam Stabilization program performs beam direction stabilization for both m-IR beams in the automatic mode. The HeNe Position program measures the delays between the m-IR pulses, controls the piezo-actuator, and exchanges data with the Data Acquisition program, which executes various regimes of spectral measurements, such as heterodyned and integrated third-order signal spectral measurements, recording the spectra of the m-IR pulses, pump-probe measurements, etc. Automatic switching between these regimes is performed using mechanical flippers (F1-F3), which permit blocking individual or multiple beams at a time. The instrument has outstanding

sensitivity, capable of measuring anharmonic shifts smaller than  $10^{-4} \text{ cm}^{-1}$ . This superior sensitivity is reached by implementing a background-free three-pulse third-order signal scheme and using spectral interferometry and phase cycling. The instrument covers a broad spectral range from 800 to  $4000 \text{ cm}^{-1}$  in a fully automated fashion and features high time resolution limited only by the duration of the m-IR pulses. The schematic design permits measuring anisotropy of the 2DIR peaks. The instrument is modular and compact, built on a  $2 \times 3 \text{ ft}$  breadboard.

## **2.8. Measurement details**

Typically, each 2DIR spectrum contained  $\sim 300$  points along  $\tau$  with a total acquisition time of 2–4 min. RA 2DIR measurements were performed by recording 2DIR spectra at different waiting times, which were scanned with a nonconstant step, ranging from 200 fs at short waiting times to 10 ps at longer waiting times. A typical RA 2DIR experiment was recorded with 30–40 points along  $T$ , with an acquisition time of  $\sim 2.5 \text{ h}$ . For stronger cross peaks, an approximately 8-fold under sampling was implemented, which reduced the time for the full RA 2DIR experiment to about 20 minutes. Waiting time kinetics for a particular diagonal or cross peak were obtained by integrating each 2DIR spectrum within a rectangular region centered at the peak.

## Chapter 3

### Ballistic Vibrational Energy Transport in Optical Alkane Chain Bands

The work detailed in this chapter has been published in the following paper: **Yue, Y.;** Qasim, L. N.; Kurnosov, A. A.; Rubtsova, N. I.; Mackin, R. T.; Zhang, H.; Zhang, B.; Zhou, X.; Jayawickramarajah, J.; Burin, A. L.; Rubtsov, I. V., Band-Selective Ballistic Energy Transport in Alkane Oligomers: Towards Controlling the Transport Speed. *J. Phys. Chem. B* **2015**, *119*, 6448-6456

#### 3.1. Overview

Ordered polyethylene fibers are attractive candidates for energy dissipation in molecular electronics as they are low density, yet they exhibit thermal conductivity which exceed that of many metals.<sup>58</sup> The ability to control thermal conductivity properties can result in the development of new materials for thermal management and efficient elements for molecular electronics.

As described in detail in Chapters 1.2. and 1.3, two encompassing mechanisms, ballistic and diffusive, describe the limiting regimes of the vibrational energy transport. Diffusive energy transport involves Brownian-like energy exchange steps, whereas ballistic energy transport involves free propagation of the vibrational wave packet and can be very fast and efficient. It requires vibrational states delocalized over the region of transport; thus, it benefits from having an ordered oligomeric molecular structure.<sup>1</sup> Ballistic energy transport initiated by a heat gradient, which is typically rather small, occurs via low-

frequency acoustic vibrational bands capable of transporting small quanta of energy at a time.<sup>59-60</sup> The ability of optical phonon bands to efficiently transfer energy has been first predicted in the 1960's, and has since been well developed.<sup>27, 61-63</sup> This work focuses on experimental studies of energy transport via oligomeric molecular chains.

The dynamics of the energy transport via oligomeric chains in a series of CHn-a and CHn-s (Figure 3.1(d)) compounds were recently measured using the RA 2DIR technique.<sup>36</sup> In those studies, the NN stretching mode of the azido moiety ( $\nu(\text{N}\equiv\text{N})$ ) attached to one end of the chain was used as a tag to initiate the energy transport, and a number of vibrational modes, located at the opposite end of the chain, were used as reporters for the energy arrival. It was found that the energy transport via alkane chains initiated by the  $\nu(\text{N}\equiv\text{N})$  tag proceeds ballistically with a speed of 14.4 Å/ps, while the energy transport within the succinimide ester end-group moiety occurs diffusively with the effective speed of 1.3 Å/ps.<sup>36</sup> This study is directed at identifying the nature of the chain bands predominantly contributing to the energy transport via alkane chains, initiated by various tags in the series of the CHn-a and CHn-s compounds (Figure 3.1(d)).

## **3.2. Experimental details**

### **3.2.1. Experimental method**

A detailed description of the fully-automated 2DIR spectrometer is presented in Chapter 2.7.

### **3.2.2. Sample preparation**

Two series of compounds (CHn-a and CHn-s), featuring alkane chains of different length were studied (Figure 3.1). The CHn-a and CHn-s compounds with  $n = 5, 10, 15$

were synthesized according to the reported procedures.<sup>36</sup> The CH3-s compound was purchased from Quanta BioDesign and used as received. For spectroscopic measurements, the CHn-a and CHn-s compounds were dissolved in deuterated chloroform at 120 and 40 mM concentration, respectively, and placed into a 100  $\mu$ m thick optical cell with CaF<sub>2</sub> or BaF<sub>2</sub> windows.

### 3.2.3. Quantum-chemistry calculations

The ground state structures of the CHn compounds, their normal modes, and anharmonicities were calculated using the density functional theory (DFT) with B3LYP hybrid functional and 6-311++G(d,p) basis sets, as implemented in a Gaussian 09 software package.<sup>64</sup>

## 3.3. Results and Discussion

The end-group vibrational modes, such as  $\nu(\text{N}\equiv\text{N})$  and  $\nu(\text{N}=\text{N})$  of the azido moiety and carbonyl stretches of the carboxylic acid and succinimide ester that were tested as tags initiating the energy transport via the alkane chain are shown in Figure 3.1(d). The tags and respective reporters are indicated in Figure 3.1(d); their infrared absorption peaks are shown in Figure 3.1(e). Figure 3.1(c) shows that the C=O/N $\equiv$ N cross-peak amplitude increases with the waiting time due to the energy transport from the tag ( $\nu(\text{C}=\text{O})$ ) to the  $\nu(\text{N}\equiv\text{N})$  reporter site and reaches maximum at  $\sim 4.2$  ps. The subsequent decay of the cross peak is associated with dissipation of the excess energy to the solvent.<sup>49</sup>

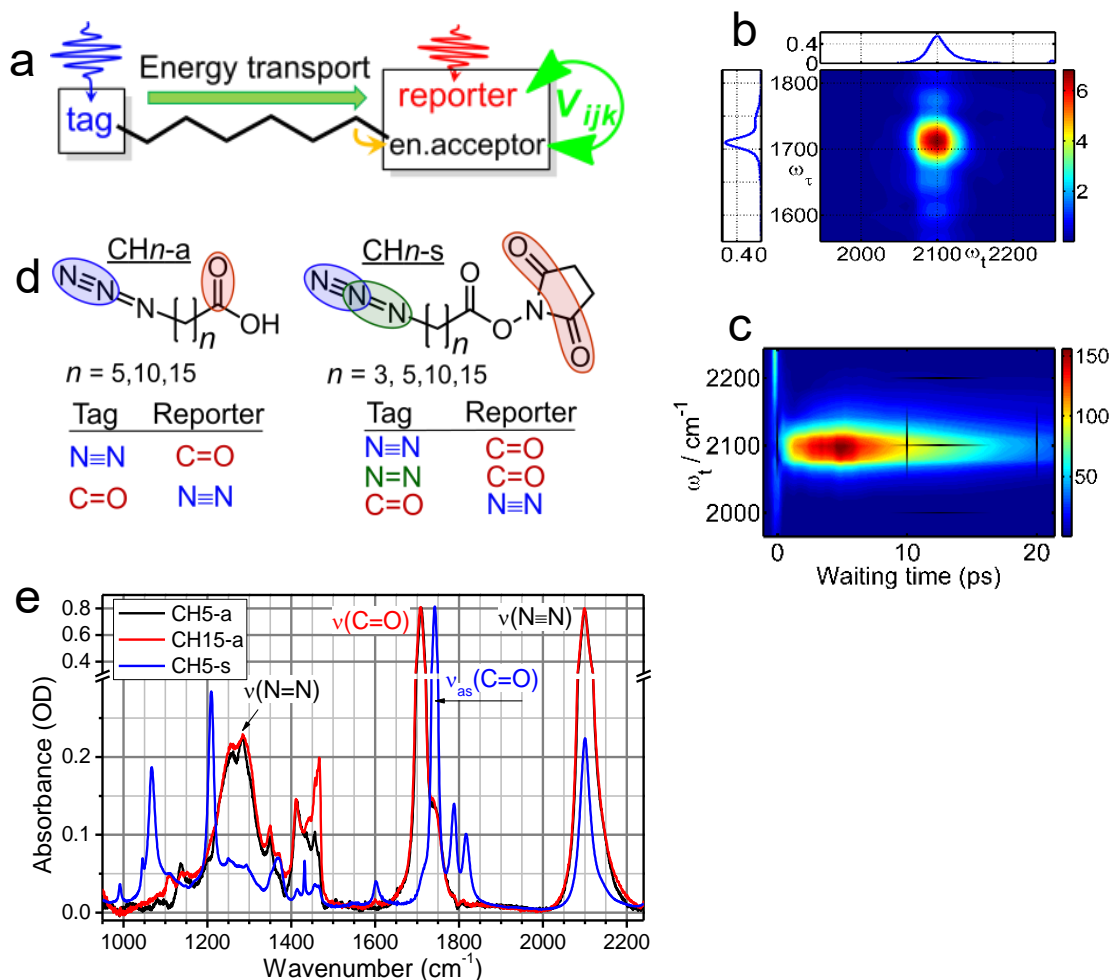


**Figure 3.1.** (a) Diagram illustrating the principles of RA 2DIR spectroscopy. An example of the cross peak between  $\nu(\text{C}=\text{O})$  and  $\nu(\text{N}\equiv\text{N})$  in CH5-a, measured at  $T = 1$  ps (b) and its waiting time dependence (c) obtained by integrating the individual 2DIR spectra along  $\omega_\tau$  axis from 1650 to 1780  $\text{cm}^{-1}$ . The tag excitation pulses in this measurement were centered at 1710  $\text{cm}^{-1}$ , while the tag probing pulses were centered at 2100  $\text{cm}^{-1}$ . (d) Structures of the CHn-a and CHn-s compounds with indicated combinations of tags and reporters. (e) Linear absorption spectra of CH5-a, CH15-a, and CH5-s in  $\text{CDCl}_3$  at 120, 120, and 40 mM concentrations, respectively. The modes used as tags and reporters are indicated.

The one-dimensional waiting-time kinetics were constructed from the 2DIR data (Figure 3.2(a,b)) and fitted with a double-exponential function (Figure 3.2(a), red lines) to evaluate the  $T_{\text{max}}$  value (marked with arrows). Averaged over three measurements per compound, the  $T_{\text{max}}$  values were plotted as a function of the tag–reporter distance (Figure

3.2(c)). The dependence can be fitted well by a linear function, and the energy transport speed, calculated as  $1/\text{slope}$ , was obtained at  $8.0 \pm 0.3 \text{ \AA/ps}$ . Such a high transport speed via the chain suggests that the transport is ballistic.<sup>24</sup>

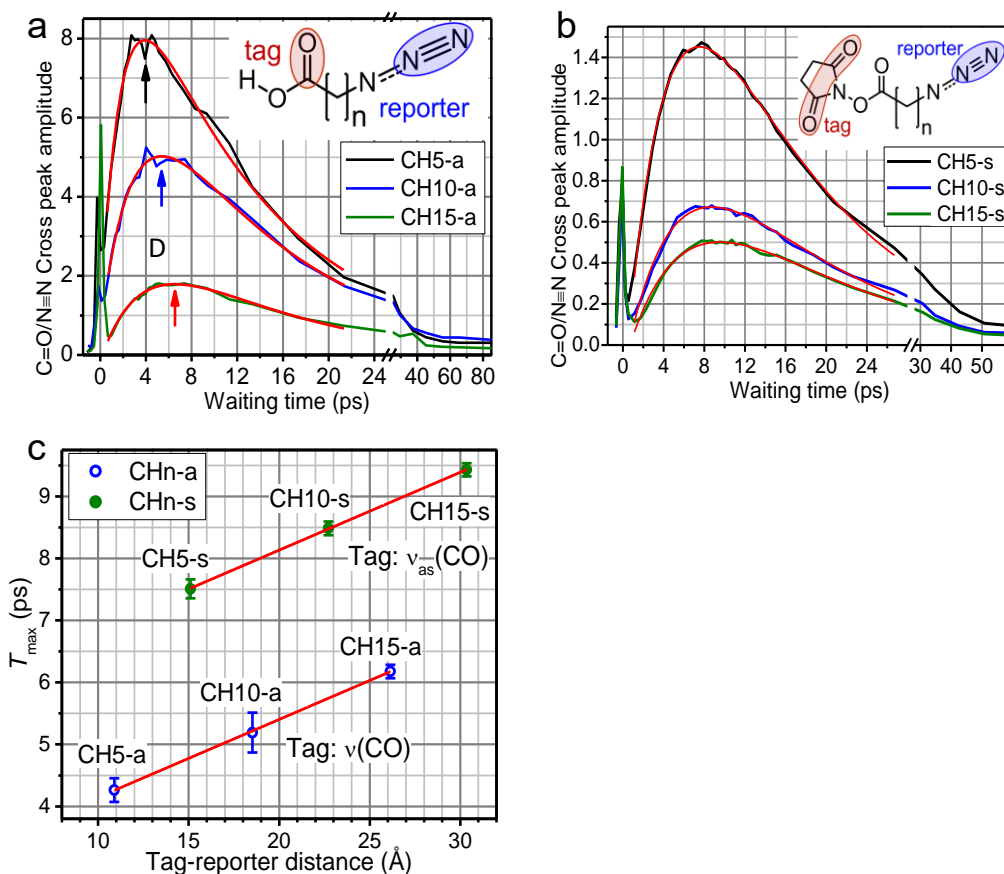


**Figure 3.2.** (a) Waiting time dependence of the  $\nu(\text{C=O})/\nu(\text{N}\equiv\text{N})$  cross-peak amplitude for the indicated CHn-a compounds. The fit with a two-exponential function is shown (red lines); the  $T_{\text{max}}$  values obtained from the fit are indicated by arrows. (b) Waiting time dependence of the  $\nu_{\text{as}}(\text{C=O})/\nu(\text{N}\equiv\text{N})$  cross-peak amplitude for the indicated CHn-s compounds at  $\sim 40 \text{ mM}$  concentration. The fit with a two-exponential function is shown (red lines). (c)  $T_{\text{max}}$  values plotted as a function of the tag-reporter distance for the CHn-a and CHn-s compounds for the transport initiated by  $\nu(\text{C=O})$ ,  $\nu_{\text{as}}(\text{C=O})$ , and  $\nu(\text{N}\equiv\text{N})$  modes. The linear fit (red lines) resulted in the transport speed of  $8.0 \pm 0.3$  and  $8.0 \pm 0.2 \text{ \AA/ps}$  for the transport in CHn-a and CHn-s series initiated by  $\nu(\text{C=O})$  and  $\nu_{\text{as}}(\text{C=O})$  tags, respectively. The transport speed in CHn-a, initiated by  $\nu(\text{N}\equiv\text{N})$ , was  $14.4 \pm 2 \text{ \AA/ps}$ .<sup>36</sup>

Note that the C=O group in the CHn-a compounds is directly attached to the alkane chain, so the wave packet in the chain can be initiated rapidly by the  $\nu(\text{C=O})$  tag relaxation. This relaxation has to occur through anharmonic interactions, as the energy gap between the  $\nu(\text{C=O})$  and the closest chain band states is substantial ( $>230\text{ cm}^{-1}$ ). The intercept corresponding to a zero-chain length for the  $\nu(\text{C=O})$  initiation is  $\sim 2.3\text{ ps}$  larger than that for the  $\nu(\text{N}\equiv\text{N})$  initiation (Figure 3.2(c)). The additional time found for the case of  $\nu(\text{C=O})$  initiation may be needed for the excess energy to reach the  $\nu(\text{N}\equiv\text{N})$  reporter site and/or for additional IVR steps at the carboxylic acid site. Note that the  $\nu(\text{C=O})$  excited-state lifetime measured at  $1.2\text{ ps}$ , is similar to that for the  $\nu(\text{N}\equiv\text{N})$  group.

Similar RA 2DIR experiments were performed for the CHn-s compounds where the  $\nu_{\text{as}}(\text{C=O})$  of the succinimide ester served as a tag to initiate the transport and  $\nu(\text{N}\equiv\text{N})$  served as a reporter (Figure 3.2(b)). The  $\nu_{\text{as}}(\text{C=O})$  mode ( $1742\text{ cm}^{-1}$ , Figure 3.1(e)) involves asymmetric motion of the two carbonyls of the succinimide group and thus is spatially separated from the chain by three bonds. As a result, additional IVR steps following the initial tag relaxation are expected to occur before the excess energy reaches the chain. Indeed, the  $T_{\text{max}}$  values for all three CHn-s samples are significantly larger (by  $3.3\text{ ps}$ ) than the respective  $T_{\text{max}}$  values for the CHn-a samples (Figure 3.2(a,b)). However, the speed of the energy transport via the chain in CHn-s,  $8.0 \pm 0.2\text{ \AA/ps}$ , appears to be the same as the speed in CHn-a (Figure 3.2(c)). Interestingly, this speed is different from the speed of transport via alkane chains initiated by the  $\nu(\text{N}\equiv\text{N})$  tag ( $14.4 \pm 2\text{ \AA/ps}$ ).<sup>36</sup>

The difference in speed indicates that different chain bands are involved in the energy transport for different types of transport initiation. Theoretical analysis of the vibrational relaxation channels, based on a recently developed Marcus-type theory for the

vibrational relaxation rates via anharmonic transitions,<sup>41, 65</sup> was performed for the three tags,  $\nu(\text{N}\equiv\text{N})$ ,  $\nu(\text{C}=\text{O})$ , and  $\nu_{\text{as}}(\text{C}=\text{O})$ , to help identify the most probable chain states involved in the transport. The method uses the mode coupling constants evaluated for the molecule in question by anharmonic calculations within the DFT method (see Chapter 3.5.4). Note that the DFT calculations were performed for the isolated molecule and its low-frequency modes serve as a bath in the theoretical treatment. The relaxation dynamics calculations show that the  $\nu(\text{N}\equiv\text{N})$  mode decays predominantly into the combination band of the  $\nu(\text{N}=\text{N})$  and  $\nu(\text{N}-\text{C})$  modes at the azido moiety (Figure 3.3(a)); the rate of the second fastest decay channel is over 10-fold smaller. The dominance of essentially a single decay channel occurs due to a small number of degrees of freedom at the azido moiety.

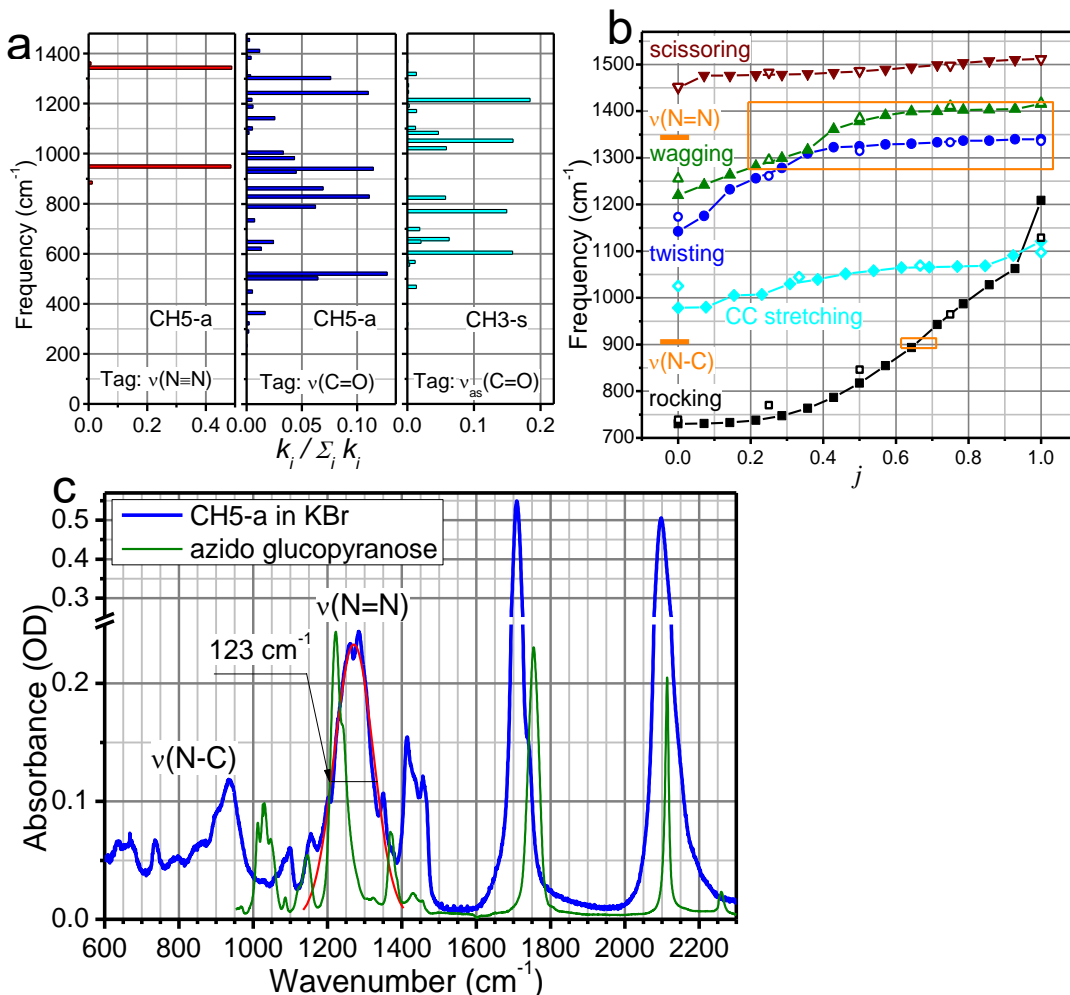


**Figure 3.3.** Rates of all relaxation channels of the  $v(N \equiv N)$  tag (a) in CH5-a, the  $v_{as}(C=O)$  tag (b) in CH5-a, and  $v(C=O)$  tag (c) in CH3-s, normalized in each case by the sum of all respective rate constants ( $k_i / \sum_i k_i$ ), where  $k_i$  is the rate of an individual third-order IVR pathway. (d) DFT computed energy states of CH15-a (filled symbols) and CH5-a (opened symbols), both in the all-anti conformation, plotted in the order of ascending energy for each motion type. There are 15 chain states of each motion type for CH15-a, except for  $v(CC)$ , for which it is 14, which are equally spaced along abscissa. The x-axis for CH5-a was constructed the same way. The energies of the azido-group modes,  $v(N=N)$  and  $v(N-C)$ , are also shown (orange). The boxes, centered at the  $v(N=N)$  and  $v(N-C)$  mode frequencies, are  $150$  and  $15 \text{ cm}^{-1}$  high, respectively, to indicate the chain states which fall within the full width at  $1/e$  of the maximum of the respective azido-group transition. (e) Linear absorption spectra for CH5-a in KBr pellet (blue line) and 1,3,4,6-tetra-O-acetyl-2-azido-2-deoxy- $\alpha$ -D-glucopyranose ( $\alpha$  anomer, red line) in deuterated chloroform.

To inspect if the  $\nu(\text{N}=\text{N})$  and  $\nu(\text{N}-\text{C})$  modes energy-match any chain bands, the chain modes were plotted in the energy ascending order within each motion type for the CH15-a and CH5-a compounds (Figure 3.3(d)). The  $\nu(\text{N}=\text{N})$  mode frequency falls within two chain bands, corresponding to the  $\text{CH}_2$  wagging and twisting motions (Figure 3.3(d)). The  $\nu(\text{N}-\text{C})$  mode frequency matches the  $\text{CH}_2$  rocking band of the chain. Importantly, the width of the  $\nu(\text{N}=\text{N})$  transition is very large (Figure 3.1(e) and Figure 3.3(e)) with the full width at half-maximum (fwhm) of  $123 \text{ cm}^{-1}$ . As a result, there are many dark chain states within its bandwidth, which provide a large number of relaxation channels (Figure 3.3(d), box). Assuming that short excited state lifetime is the reason for the large  $\nu(\text{N}=\text{N})$  line width, it can be evaluated as  $T_1 = (2\pi c\sigma)^{-1}$ , where  $\sigma$  is the fwhm of the transition in wavenumbers and  $c$  is the speed of light, resulting in the lifetimes of 44 fs. Note that the  $\nu(\text{N}=\text{N})$  peak in azido-substituted  $\alpha$ -D-glucopyranose ( $\alpha$  anomer) is much narrower ( $43 \text{ cm}^{-1}$ , Figure 3.3(e)), confirming the importance of the alkane chain states for the broadening. The width of the  $\nu(\text{N}-\text{C})$  transition is small,  $\sim 12 \text{ cm}^{-1}$ , resulting in much fewer resonances with the chain states.

In addition to the energy match, the symmetry affects the coupling between the energy receiving modes and the chain bands. DFT calculations showed that the conformer gauche at the  $\text{N}_3$ -chain connection has a slightly lower energy than the all-anti conformer by  $86 \text{ cm}^{-1}$ . Taking into account the Boltzmann factor and twice higher statistical weight for the gauche conformation, we obtain that the gauche conformers at the azido-group site are  $\sim 3$ -fold more abundant than the anti, which makes the twisting band a major contributor to the  $\nu(\text{N}=\text{N})$  mode relaxation.

Additional refinement for the involvement of different chain bands can be obtained from the comparison of the group velocities supported by each chain band with the experimental transport speeds. Previously the band structure was evaluated for alkane chains using semiempirical force field methods,<sup>66</sup> and these results are consistent with our DFT analysis, as detailed in Chapter 3.2.3. The Hessian matrix of force constants for the alkane chain was obtained from the DFT normal-mode analysis for CH15-a. The optical bands, shown in Figure 3.4(a), appear in pairs and are represented by the lines of the same color. For example, the two rocking modes are shown with black lines, where the first band spans from 733 to 804  $\text{cm}^{-1}$  and the second band spans from 804 to 1082  $\text{cm}^{-1}$ . It is sufficient to plot the band in the wavevector ( $q$ ) region from 0 to  $\pi/a$ ; for the finite chain length, this portion of the band contains the number of states equal to the number of unit cells. Due to central symmetry of the unit cell, the two bands of the same motion nature have the same energy at  $q = \pi/a$  and continuous derivative. Thick lines are used in Figure 3.4(a) to identify the bands of the same motion type. Each thick line comprises two optical bands, one in the wavevector region from 0 to  $\pi/a$ , another from  $\pi/a$  to  $2\pi/a$  (Figure 3.4(a), Table 3.1).

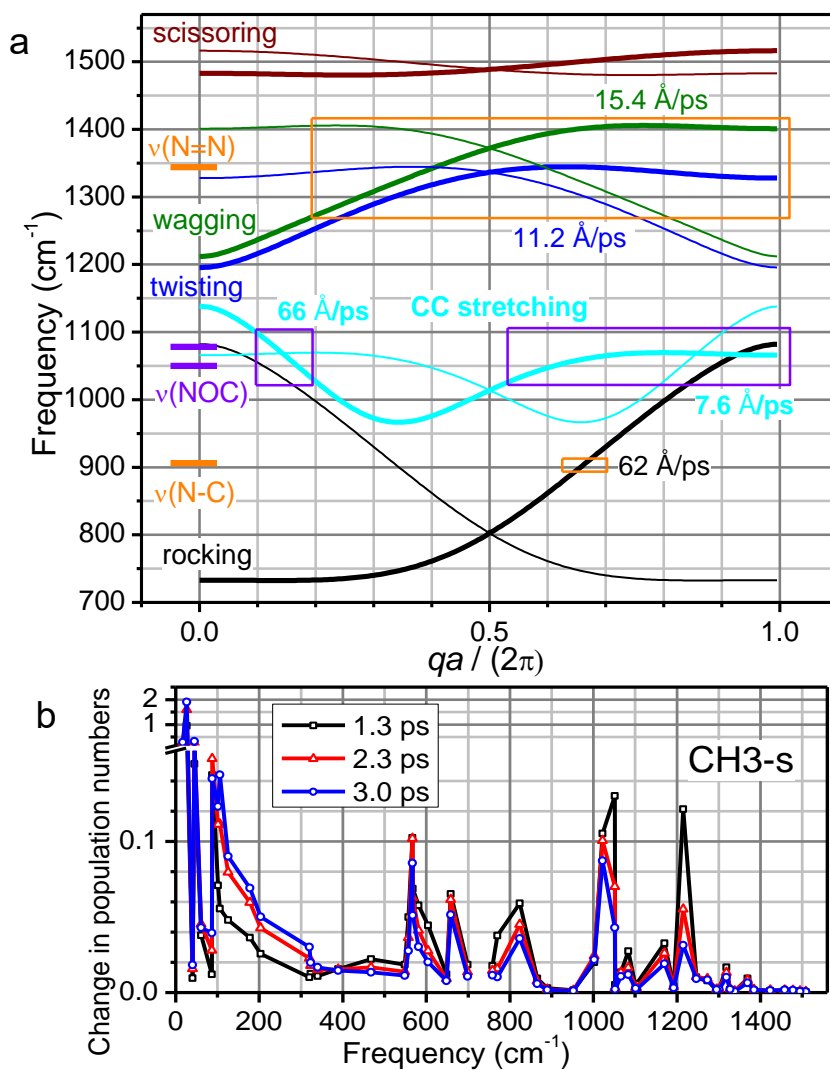


**Figure 3.4.** (a) Structure of 10 lowest-energy optical bands for the alkane chain (labeled) as a function of a normalized wavevector. The boxes match the width of the azido-group stretching modes,  $\nu(\text{N}=\text{N})$  and  $\nu(\text{N}-\text{C})$  (similar to that in Figure 3.3(d)) and the  $\nu(\text{NOC})$  of the succinimide ester (violet). (b) Change of the population numbers at indicated delays after excitation of  $\nu_{\text{as}}(\text{C}=\text{O})$  in CH3-s.

**Table 3.1.** Chain band frequencies at  $q = 0$  and  $\pi$  ( $\omega(0)$  and  $\omega(\pi)$ ) and the group velocities computed for each band,  $\langle |V| \rangle$ , and for the specific frequency regions,  $\langle |V_b| \rangle$ , indicated in Figure 3.4(a)

band no.	band type	$\omega(0)$ , $\text{cm}^{-1}$	$\omega(\pi)$ , $\text{cm}^{-1}$	$\langle  V  \rangle$ , $\text{\AA}/\text{ps}$	$\langle  V_b  \rangle$ , $\text{\AA}/\text{ps}$ in boxes
5	$\rho(\text{CH}_2)$	733	804	10.5	$32.8^a$
6	(black)	1082	804	42.7	$62^b$
7	$\nu(\text{CC})$	1138	1014	33.5	$66^a$
8	(cyan)	1067	1014	8.8	$7.6^a$
9	$\text{tw}(\text{CH}_2)$	1196	1337	21.5	$11.2^c$
10	(blue)	1328	1337	4.0	$11.2^c$
11	$\text{w}(\text{CH}_2)$	1212	1372	24.6	$15.4^c$
12	(green)	1401	1372	6.0	$15.4^c$
13	$\text{sc}(\text{CH}_2)$	1483	1489	1.5	
14	(wine)	1516	1489	4.3	

<sup>a</sup>The group velocities measured within the boxes matching the width of a the two  $\nu(\text{NOC})$  modes. <sup>b</sup>The group velocity measured within the boxes matching the width of the  $\nu(\text{N}-\text{C})$  mode. <sup>c</sup>The group velocity measured within the boxes matching the width of the  $\nu(\text{N}=\text{N})$  mode.

**Table 3.2.** Comparison of the DFT computed frequencies for different chain bands with experimentally reported values for polyethylene.<sup>67</sup> The experimental frequencies are presented based on individual peak assignment.

band	computed chain band frequencies ( $\text{cm}^{-1}$ )	experimental frequencies ( $\text{cm}^{-1}$ )
$\text{CH}_2$ Scissoring	1480.4 – 1516.4	1416, 1440, 1463, 1473
$\text{CH}_2$ Wagging	1211.9 – 1405.8	1175, 1370
$\text{CH}_2$ Twisting	1195.6 – 1344.7	1050, 1296
CC Stretching	996.5 – 1138.2	1067, 1133
$\text{CH}_2$ Rocking	733 – 1082.1	721, 734, 1170

The group velocity for a narrow range of frequencies centered at  $\omega_0(q_0)$  is determined as  $V(q_0) = \left( \frac{\partial \omega}{\partial q} \right) |_{q=q_0}$ . Because the velocity is different for different ranges of wavevectors (frequencies), the mean group velocity over a selected range of wavevectors from  $q_1$  to  $q_2$  is computed as

$$\langle V_b \rangle = (q_2 - q_1)^{-1} \int_{q_1}^{q_2} |V(q)| dq \quad (3.1)$$

The mean group velocity corresponding to the whole  $i^{\text{th}}$  band is defined as  $\langle V \rangle = \left(\frac{a}{\pi}\right) \int_0^{\pi/a} |\partial\omega_i/\partial q| dq$ . The mean group velocities computed for each optical band are given in Table 3.1.

The frequency width of the wave packet affects its group velocity (equation 3.1). Therefore, the group velocities were computed for each chain band for the frequency range corresponding to the  $1/e$  peak width of the two stretching transitions initiating the wave packet,  $\nu(\text{N}=\text{N})$  and  $\nu(\text{N}-\text{C})$ , and the results are given in Figure 3.4(a), inset and Table 3.1. The experimentally measured transport speed of 14.4 Å/ps is close to those calculated for the CH<sub>2</sub> wagging (15.4 Å/ps) and twisting (11.2 Å/ps) bands. The group velocity supported by the CH<sub>2</sub> rocking band is significantly larger than the experimental value. Small density of states in this band results in a low quality of the formed wave packet and reduces its throughput. To further discriminate which bands are involved in the transport, the mode coupling between the chain band and the azido end group was evaluated. The symmetry affects the coupling between the energy receiving modes and the chain bands. Alkane chains in solution can have anti or gauche conformations at every carbon site.<sup>49</sup> The DFT calculations used to evaluate the bands were computed for the molecules with all-anti conformation of the chain, which features a symmetry plane. As the nearest CH<sub>2</sub> group interactions are dominant (vide supra), the dependence of the band frequencies on the anti vs. gauche conformation is small and the all-anti conformation of the chain is expected to be representative for the chain bands in solution. Indeed, the computed bands match well the reported experimental bands (Table 3.2) and similar band frequencies were found for a variety of chain conformations. Because of the nearest group interaction dominance, the coupling of the end group modes

to the chain states is mostly affected by the conformation at the chain carbon closest to the end group. For example, if the azido group is in the anti-conformation, the azido group stretching modes ( $\nu(\text{N}=\text{N})$  and  $\nu(\text{N}-\text{C})$ ) are fully symmetric with the motion occurring within the symmetry plane. Therefore, they can only be coupled to the symmetric chain states, the  $\text{CH}_2$  wagging and C-C stretching, but not to the  $\text{CH}_2$  twisting, scissoring, or rocking. Thus, when the azido group is attached to the chain in the anti-conformation, the  $\nu(\text{N}=\text{N})$  mode relaxes predominantly into the wagging band while  $\nu(\text{N}-\text{C})$  can only relax into the C-C stretching band, which is though far in energy. When the azido group is gauche to the chain the  $\nu(\text{N}=\text{N})$  mode is also coupled to the  $\text{CH}_2$  twisting band, whereas the  $\nu(\text{N}-\text{C})$  mode is coupled to the  $\text{CH}_2$  rocking band. The DFT calculations show that the conformer gauche at the  $\text{N}_3$ -chain connection (all other sites were anti), has a slightly lower energy than the all-anti conformer by  $86 \text{ cm}^{-1}$ . Taking into account the Boltzmann factor and that two gauche conformations are possible, the ratio of the two conformers of gauche vs. anti of 3 is obtained at room temperature. So the gauche conformers at the azido-group site are ca. 3 times more abundant than the anti, which makes the twisting band a major contributor to the  $\nu(\text{N}=\text{N})$  mode relaxation. Thus, we conclude that the  $\text{CH}_2$  twisting and wagging bands contribute most to the transport initiated by the  $\nu(\text{N}=\text{N})$  mode.

Different from the  $\nu(\text{N}=\text{N})$  mode relaxation, there are many decay pathways with comparable rates for the carbonyl stretching mode relaxation, in both the  $\text{CHn-a}$  and  $\text{CHn-s}$  compounds (Figure 3.3(b,c)). Because of the presence of many relaxation channels for  $\nu(\text{C}=\text{O})$  in  $\text{CHn-a}$ , the energy transport through the chain may occur via several chain bands. However, the similarity of the speeds in the  $\text{CHn-a}$  and  $\text{CHn-s}$

compounds (8.0 Å/ps) suggests that the same chain bands are most important for the transport in both cases. While the tag in CHn-a is located right at the chain end, the tag in CHn-s,  $\nu_{\text{as}}(\text{C}=\text{O})$ , is buried deep in the succinimide ester end group, and several IVR steps are required for the excess energy to reach the chain. By the time the excess energy in CHn-s reaches the chain, which is  $\sim 3$  ps (Figure 3.2(c)), the mean energy for the succinimide ester modes bearing excess energy is expected to be much smaller than that in CHn-a after the first relaxation step, due to a much larger number of degrees of freedom at the succinimide ester moiety, compared to that at the carboxylic acid. Figure 3.4(b) shows the excess populations, compared to the thermal populations, for all modes below  $1550\text{ cm}^{-1}$  for CH3-s. The overall excess population in the modes with frequencies above  $730\text{ cm}^{-1}$ , which is the cutoff for the optical bands of the chain, after 3 ps of relaxation is substantial at 0.53 ( $\sum \Delta n$ ). To access those optical bands, the high-frequency modes at the ester site need to be used, as the ester spatially separates the end group from the chain. The highest frequency modes at the ester, except  $\nu(\text{C}=\text{O})$ , are associated with the N–O–C stretching motions ( $\nu_{\text{as}}(\text{NOC})$  at  $1083\text{ cm}^{-1}$  and  $\nu_{\text{ss}}(\text{NOC})$  at  $1052\text{ cm}^{-1}$ ). The population excess in these modes remains substantial at 3 ps delay (Figure 3.4(b)). Due to spatial proximity to the chain and high frequencies, the N–O–C stretching modes are the most probable candidates for the doorway modes for the energy transport to the optical bands of the chain.

The high-frequency doorway states at the ester,  $\nu_{\text{ss}}(\text{NOC})$  and  $\nu_{\text{as}}(\text{NOC})$ , frequency-match two regions of the C–C stretching bands and one region of the  $\text{CH}_2$  rocking band (Figure 3.4(a), violet boxes). The  $1/e$  width of the  $\nu_{\text{as}}(\text{NOC})$  absorption peak centered at  $1068\text{ cm}^{-1}$  was experimentally determined to be  $30\text{ cm}^{-1}$  (Figure 3.1(b)).

Assuming that the peak width of the  $\nu_{ss}(\text{NOC})$  transition is similar, the range of frequencies of the end-group doorway modes was taken from 1035 to 1093  $\text{cm}^{-1}$  (Figure 4(a), violet boxes). Dramatically different energy transport speeds are obtained for the three bands matching the doorway states: 66 and 7.6  $\text{\AA}/\text{ps}$  for the C–C stretching bands and 32.8  $\text{\AA}/\text{ps}$  for the rocking band (Figure 3.4(a), Table 3.1). The speed of 7.6  $\text{\AA}/\text{ps}$ , supported by the C–C stretching band, matches the experimental speed of 8.0  $\text{\AA}/\text{ps}$ , whereas the two other speeds do not. Note that the number of states of a band that are in resonance with the end-group states is inversely proportional to the group velocity; much higher transport efficiency is supported by the C–C stretching band featuring a small group velocity. The contribution to the  $T_{\text{max}}$  values associated with the groups of states featuring much higher speeds is expected to be small because of the small density of states and a cross-peak contribution at small waiting times. Thus, the transport speed calculations suggest that the C–C stretching band contributes the most to the ballistic transport initiated by  $\nu_{as}(\text{C=O})$  in the  $\text{CH}_n$ -s compounds.

The local symmetry at the chain–ester link provides additional arguments for evaluating the contributions of the two bands in question: the C–C stretch and  $\text{CH}_2$  rocking. With respect to the plane formed by the atoms of the ester ( $\text{C}-(\text{C=O})-\text{O}-\text{N}$ ) or the acid ( $\text{C}-(\text{C=O})-\text{O}-\text{H}$ ), the anti-conformation for the nearest  $\text{CH}_2$  group is the most stable with the dihedral angle  $\theta$  of  $180^\circ$  (Figure 3.5(a)). The atomic displacements associated with the two doorway states of the ester,  $\nu(\text{NOC})$ , occur in the ester plane. In the anti-conformation ( $\theta = 180^\circ$ ), the displacement of the two hydrogen atoms in the  $\text{CH}_2$  rocking modes, represented by the nearest  $\text{CH}_2$  group, is perpendicular to the ester plane, resulting in a zero coupling of the  $\nu(\text{NOC})$  with the  $\text{CH}_2$  rocking. However, the potential

energy surface is shallow and a range of conformations along  $\theta$  are thermally accessible at room temperature (Figure 3.5(a)). A mean coupling strength for the  $\nu_{\text{as}}(\text{NOC})$  with the two stretching modes and three rocking of the chain in the CH3-s compound was evaluated as a function of the dihedral angle  $\theta$  (Figure 3.5(b), as explained thoroughly in Chapter 3.2.6. Clearly, the  $\nu_{\text{as}}(\text{NOC})$  mode is coupled much more strongly to the stretching modes of the chain (Figure 3.5(b)). Taking into account the Boltzmann factor, the graph in Figure 3.5(c) is obtained. Considering the Boltzmann factor (Figure 3.5(c)), the difference in the density of states (inversely proportional to the group velocity) and using the Fermi Golden rule, the 13- fold faster rate was obtained for the  $\nu_{\text{as}}(\text{NOC})$  mode decay into the C–C stretching vs CH<sub>2</sub> rocking modes of the chain, confirming the importance of the former.

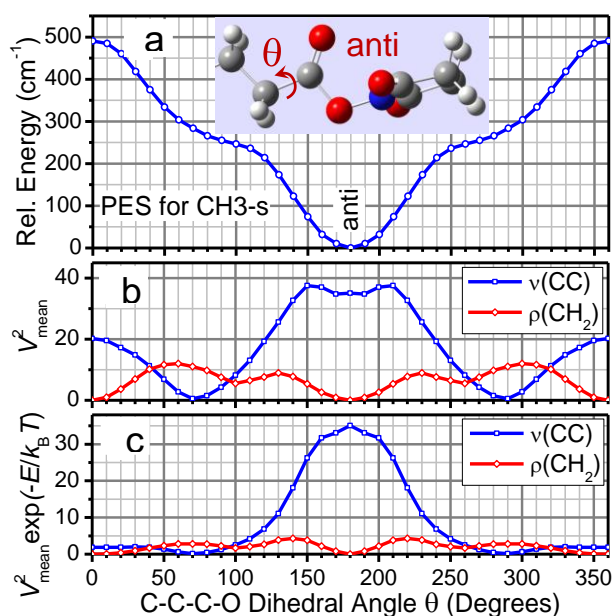


**Figure 3.5.** (a) DFT computed potential energy surface for CH3-s along the C–C–C–O dihedral angle ( $\theta$ ); see inset. Mean square couplings strength of the ester stretching modes to the C–C stretching and CH<sub>2</sub> rocking states (b) and their values weighted by the Boltzmann factor (c). The ratio of the integrals under the curves in panel c equals 4.4; multiplication by the density of states ratio ( $\sim 3$ ) results in  $\sim 13$ -fold dominance of the relaxation rates into C–C stretching vs CH<sub>2</sub> rocking modes of the chain.

An attempt to find similar doorway states in the CH<sub>n</sub>-a compounds following  $\nu(\text{C}=\text{O})$  relaxation was unsuccessful. The analysis of the relaxation channels of a range of CH<sub>5</sub>-a compounds differing by their conformations, anti or gauche, at different carbon sites showed the presence of a variety of decay channels which populate significantly the states below the  $1300\text{ cm}^{-1}$  frequency. The overall wave packet formed in the chain consists of many states from different bands. However, the bands featuring small group velocity (and large density of states) contribute mostly to the measured  $T_{\text{max}}$  values. There are only two regions in the optical bands below  $1300\text{ cm}^{-1}$  where the group velocity is relatively small: those are the C–C stretching band around  $1070\text{ cm}^{-1}$  (Figure 3.4(a), violet box) and the CH<sub>2</sub> rocking band around  $730\text{ cm}^{-1}$  (Table 3.1). The actual mean speed supported by the band depends on the frequency span (the bandwidth) of the wave packet. Importantly, the speed comparable with that observed experimentally, is supported by both these bands.

It is unlikely that acoustic bands are transporting vibrational energy efficiently within the molecule, as they are strongly coupled to the solvent.<sup>61</sup> They also have a much higher speed and low density of states; thus, the  $T_{\text{max}}$  values are not expected to be sensitive to their contribution.

The tags discussed above,  $\nu(\text{N}\equiv\text{N})$ ,  $\nu_{\text{as}}(\text{C}=\text{O})$ , and  $\nu(\text{C}=\text{O})$ , have frequencies that are substantially higher ( $>230\text{ cm}^{-1}$ ) than the frequencies of the closest chain band states, found at  $1470\text{ cm}^{-1}$  (Figure 3.3(d) and Figure 3.4(a)). It is expected that if the tag frequency falls within a chain band, the wave packet of this chain states can be initiated

without additional anharmonically driven relaxation steps.<sup>68-69</sup> Such a tag would allow selecting directly the chain band for the wave packet transport.

To test this prediction, the N=N stretching mode of the azido moiety (Figure 3.3(e)), which falls within the CH<sub>2</sub> wagging and CH<sub>2</sub> twisting chain bands (Table 3.1), was used as a tag with the  $\nu_{\text{as}}(\text{C}=\text{O})$  mode as a reporter (Figure 3.7(a)). The waiting time dependences for the CHn-s series were measured. Different from the  $\nu(\text{N}\equiv\text{N})$  and  $\nu(\text{C}=\text{O})$  initiations, the cross-peak amplitudes at early waiting times ( $T \approx 200$  fs) are already substantial for all compounds, indicating the existence of underlying weak succinimide ester transitions in the  $1300\text{ cm}^{-1}$  region with strong direct couplings to the  $\nu_{\text{as}}(\text{C}=\text{O})$  mode. Nevertheless, the infrared absorption in the  $1300\text{ cm}^{-1}$  region comes predominantly from the  $\nu(\text{N}=\text{N})$  mode, as seen from the comparison of the spectra of the CH5-s with the reference compound (CH5-s-ref), where the azido moiety is replaced by a hydrogen atom (Figure 3.6) ; the spatial closeness between the underlying succinimide ester transitions and the reporter site permits their direct coupling.

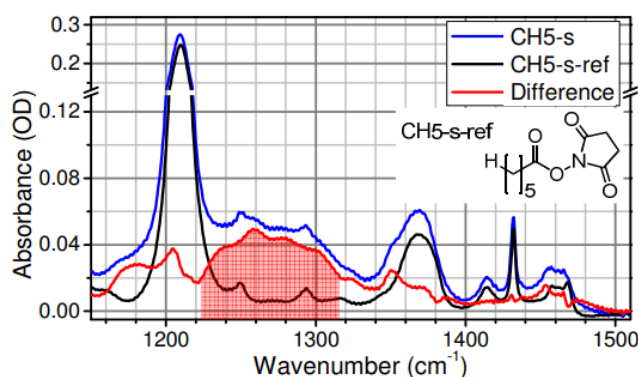


**Figure 3.6.** Linear absorption spectra of the CH5-s (blue) and reference (CH5-s-ref, black) compounds in the fingerprint region, normalized for the  $\nu(\text{CO})$  mode, and the difference between them (red). The region corresponding to the  $\nu(\text{N}=\text{N})$  mode in CH5-s is shaded.

This statement is further confirmed by the observation of a cross peak at the same frequencies from the reference compound. The kinetic behavior of this cross peak was measured and used as a baseline for all the CH<sub>n</sub>-s measurements. The transport speed evaluated from the linear fit is  $11 \pm 4$  Å/ps (Figure 3.7(b)).

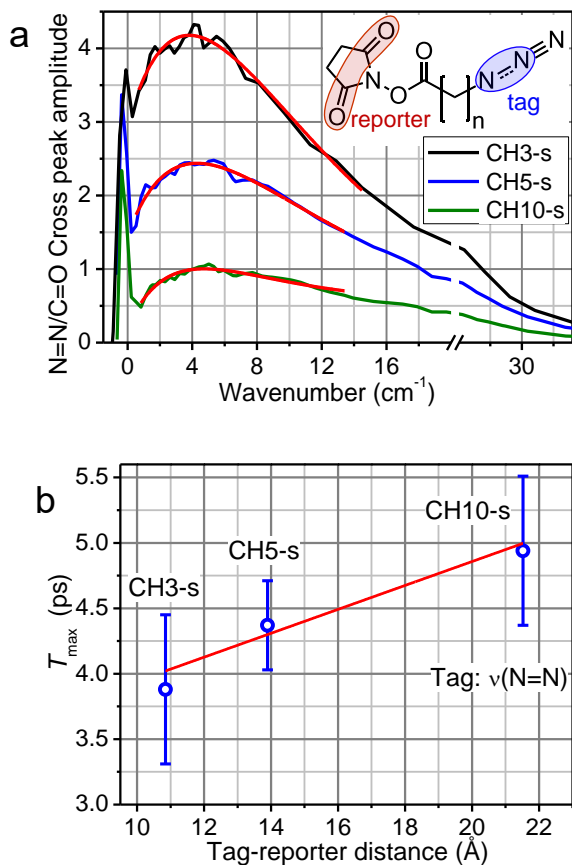


**Figure 3.7.** (a) Waiting time dependence of the  $\nu(\text{N}=\text{N})/\nu_{\text{as}}(\text{C}=\text{O})$  cross-peak amplitude for the CH<sub>n</sub>-s compounds at  $\sim 45$  mM concentration. The fit with a two-exponential function is shown (red). (b) Dependence of  $T_{\text{max}}$  vs the tag-reporter distance measured for the CH<sub>n</sub>-s compounds for the energy transport initiated by the  $\nu(\text{N}=\text{N})$  tag and recorded with the  $\nu_{\text{as}}(\text{C}=\text{O})$  reporter. The linear fit (red) resulted in the transport speed of  $11 \pm 4$  Å/ps.

The transport speed determined for the direct excitation on the  $\nu(\text{N}=\text{N})$  mode matches the speed calculated for the CH<sub>2</sub> twisting and CH<sub>2</sub> wagging band regions overlapping with the  $\nu(\text{N}=\text{N})$  spectrum, 15.4 and 11.2 Å/ps, respectively. It is also in

agreement with the speed of  $14.4 \text{ \AA/ps}$  measured for the transport initiated by the  $\nu(\text{N}\equiv\text{N})$  tag excitation, which was shown to be dominated by the pathway via the  $\nu(\text{N}=\text{N})$  mode. Excitation of the  $\nu(\text{N}=\text{N})$  mode with infrared pulses demonstrated that ballistic transport can be initiated directly, opening the opportunity of controlling the transport speed by selecting specific chain bands for the wave packet transport.

The cross-peak amplitudes measured for the CHn-a and CHn-s compounds were compared within each series (Figure 3.8). The distance dependence, approximated as exponential, resulted in characteristic decay distances,  $R_0$ , of  $14.6 \pm 3.5 \text{ \AA}$  for CHn-a and  $12 \pm 4 \text{ \AA}$  for CHn-s. These decay distances represent the mean free path distances for the intrachain optical-band wave packets. The  $R_0$  values are similar to those for the ballistic energy transport initiated by  $\nu(\text{N}\equiv\text{N})$  in alkane chains ( $14.4 \pm 2 \text{ \AA/ps}$ ),<sup>36</sup> PEG chains ( $15.7 \pm 1 \text{ \AA/ps}$ ),<sup>49</sup> and perfluoroalkane chains ( $16.4 \pm 2 \text{ \AA/ps}$ )<sup>52</sup> in solution at room temperature.

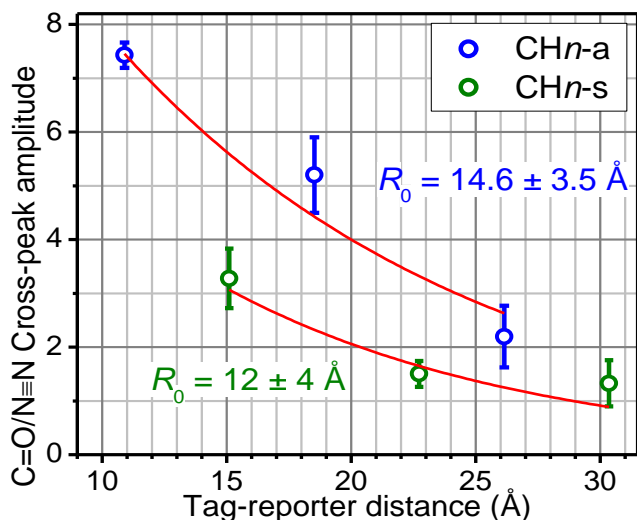


**Figure 3.8.** Dependences of the  $\nu(\text{C}=\text{O})/\nu(\text{N}\equiv\text{N})$  and  $\nu_{\text{as}}(\text{C}=\text{O})/\nu(\text{N}\equiv\text{N})$  cross-peak amplitudes for the CHn-a and CHn-s compounds, respectively. The fits with exponential decay function (red line) resulted in the characteristic decay distances,  $R_0$ , indicated in the inset.

### 3.4. Conclusions

To summarize, a combination of the experimental and theoretical studies permitted identifying the optical bands responsible for the ballistic transport in alkanes when initiated by four different tags. Different chain bands are found to be most important for different cases of transport initiation, thus demonstrating different energy transport speeds. For the transport initiated by  $\nu(\text{N}\equiv\text{N})$ , we found that the  $\text{CH}_2$  twisting and  $\text{CH}_2$  wagging chain bands contribute the most to the energy transport. For the  $\nu(\text{C}=\text{O})$  initiation, the  $\text{C}-\text{C}$  stretching and  $\text{CH}_2$  rocking chain bands were identified as the dominant energy transporters, in both the  $\text{CH}_n\text{-a}$  and  $\text{CH}_n\text{-s}$  compounds. In the case with the  $\nu(\text{N}\equiv\text{N})$  and  $\nu(\text{C}=\text{O})$  tags, the chain bands were far in energy from the tag and IVR relaxation steps were required to initiate the wave packet in the chain. Direct excitation of the local mode,  $\nu(\text{N}\equiv\text{N})$ , which is coupled directly to the chain states resulted in the transport speed characteristic for the matching optical bands,  $\text{CH}_2$  twisting and wagging. This study presents a consistent quantitative picture for describing the energy transport via alkane chains. Understanding the role different chain bands play in the energy transport will help in designing molecular systems with much higher energy transport speed and systems where the transport can be controlled.

### 3.5. Theoretical Methods

#### 3.5.1. Calculations of the band structure for alkane chains

Consider an alkane chain with  $\text{C}_2\text{H}_4$  as a unit cell. Introduce 18-dimensional displacement vector  $x_k$  for the atoms of the  $k$ -th unit cell ( $6 \text{ atoms} \times 3 \text{ Cartesian coordinates} = 18 \text{ degrees of freedom}$ ). The Hessian matrix of the system can be split into

blocks  $H(k, n)$ , 18-by-18 matrices corresponding to harmonic interaction between  $k$ -th and  $n$ -th unit cells. The assumption of translational symmetry leads to relations  $H(k + m, n + m) = H(k, n)$ . Assuming short-range interaction ( $H(k, k + 3) \approx 0$ ) we can represent the Hamiltonian as

$$H = \frac{1}{2} \sum_k \{ p_k^\dagger M^{-1} p_k + x_k^\dagger A x_k + x_k^\dagger B^\dagger x_{k-1} + x_k^\dagger B x_{k+1} + x_k^\dagger C^\dagger x_{k-2} + x_k^\dagger C x_{k+2} \} \quad (3.2)$$

where  $A = H(k, k)$ ,  $B = H(k, k + 1)$ ,  $C = H(k, k + 2)$ ,  $p_k$  is the momentum vector and  $M$  is the 18x18 diagonal matrix of atomic masses. The choice of the boundary conditions is not significant for the dispersion relations, so for the sake of simplicity we can choose the periodic boundary conditions.

**Dispersion Relations.** Introducing mass weighted vectors and matrices  $y_k =$

$M^{1/2} x_k$ ,  $\tilde{p}_k = M^{-1/2} p_k$ ,  $A_w = M^{-1/2} A M^{-1/2}$ , etc., we obtain the equation of motion for the  $k$ -th unit cell as

$$\ddot{y}_k = -A_w y_k - B_w^\dagger y_{k-1} - B_w y_{k+1} - C_w^\dagger y_{k-2} - C_w y_{k+2} \quad (3.3)$$

Applying Fourier transform  $y_k(t) = \sum_q u_k(q) \exp\{-i\omega(q)t\}$  and using the Bloch theorem  $u_k(q) = u(q) \exp\{iaqk\}$ , we obtain the equation

$$G(q)u = \omega^2(q)u \quad (3.4)$$

where

$$G(q) = A_w + (B_w + B_w^\dagger) \cos(aq) + i(B_w - B_w^\dagger) \sin(aq) + (C_w + C_w^\dagger) \cos(2aq) + i(C_w - C_w^\dagger) \sin(2aq) \quad (3.5)$$

and  $a$  is a lattice period. Using Eq. 3.4, the dispersion relations for each mode,  $\omega_i(q)$ ,  $i = 1 - 18$ , can be obtained expressing eigenmode frequencies as square roots of corresponding eigenvalues of the Hermitian matrix  $G(q)$ . Based on the symmetry properties of the Hessian matrix, it can be shown that the four lowest frequency bands,  $i = 1 - 4$ , are acoustic ( $\omega_i(0) = 0$ ), whereas other bands are optical as  $\omega_i(0) \neq 0$  for  $i = 5 - 18$ .

### 3.5.2. Group velocity calculations

The Hessian matrix for the alkane chain was obtained using the DFT normal mode analysis for CH15-a. To reduce the boundary effects, the matrices  $A, B, C$  were determined for the third and fourth cells in CH15-a and nearly identical results were obtained, as expected. The short-range approximation is justified by the relation:

$$||H(k, k \pm 3)|| / ||H(k, k \pm 1)|| \lesssim 6 \cdot 10^{-3}. \text{ The lattice period was taken as } a = 3.06 \text{ \AA}.$$

Practically, the Hessian matrix does not reveal an ideal translational and rotational symmetry; also the neglected non-zero elements increase the effect of violation of the  $G(q)$  matrix symmetry properties. The calculation error in the Hessian leads to the error in the calculated frequencies. The absolute value of the error,  $\delta\omega$ , is of the same order of magnitude for all bands, although the relative error,  $\delta\omega/\omega_i$ , increases for the bands with smaller frequencies. Therefore, the low-frequency modes, the acoustic bands, require more careful consideration, which will be a subject for further study. For the optical bands,  $\frac{\delta\omega}{\omega_i} \ll 1$ , the above-mentioned minor symmetry violation is negligible.

Figure 3.4(a) shows the lowest energy optical bands,  $i = 5 - 14$ . The bands appear in the graph in pairs represented by the lines of the same color. For example, the two rocking modes ( $i = 5, 6$ ) are shown with black lines, where the first rocking band spans from 730 to 802  $\text{cm}^{-1}$  and the second rocking band spans from 802 to 1075  $\text{cm}^{-1}$ . It is sufficient to plot the band in the wavevector region from 0 to  $\pi/a$ ; for the finite chain length, this portion of the band contains the number of states equal to the number of unit cells. Due to central symmetry of the unit cell, the two bands of the same motion type have exactly the same energy at  $q = \pi/a$  and continuous derivative. Thick lines are used to identify clearly the bands of the same motion type. Each thick line comprises two bands, one in the wavevector region from 0 to  $\pi/a$ , another from  $\pi/a$  to  $2\pi/a$  (Figure 3.4(a) and Table 3.1). The group velocity for a narrow range of frequencies centered at  $\omega_0(q_0)$  is determined as  $V(q_0) = \left(\frac{\partial \omega}{\partial q}\right)_{q=q_0}$  because it is different for different ranges of wavevectors (frequencies), the mean group velocity over a selected range of wavevectors from  $q_1$  to  $q_2$  is computed as:

$$\langle V_b \rangle = (q_2 - q_1)^{-1} \int_{q_1}^{q_2} |V(q)| dq \quad (3.6)$$

The mean group velocity corresponding to the whole  $i$ -th band is defined as  $\langle V \rangle = (a/\pi) \int_0^{\pi/a} \left| \frac{\partial \omega_i}{\partial q} \right| dq$ . The group velocities computed for each optical band ( $i = 5 - 14$ ) as a whole are given in Table 3.1.

### 3.5.3. Vibrational relaxation dynamics calculations

Vibrational relaxation dynamics was computed using a recently developed method based on a modification of the Marcus theory for electron transfer applied to

anharmonic transitions.<sup>41, 65</sup> The theory calculates the rates (Holstein)<sup>70</sup> of all IVR processes involving three modes ( $i \rightarrow j + k, i + j \rightarrow k$ ):

$$W_i^{jk} = 2\pi V_{ijk*}^2 \sqrt{\frac{\pi}{\lambda_{ijk} k_B T}} \exp \left\{ \frac{-(-\Delta_{ijk} + \lambda_{ijk})^2}{4\lambda_{ijk} k_B T} \right\} \quad (3.7)$$

where  $k_B$  is the Boltzmann constant,  $T$  is the temperature and the exact definitions of effective mode coupling constants  $V_{ijk*}^2$ , driving force  $\Delta_{ijk}$ , and reorganization energy  $\lambda_{ijk}$  can be found in the published work by Tesar et. al. “Theoretical Study of Internal Vibrational Relaxation and Energy Transport in Polyatomic Molecules.”<sup>41</sup> Required anharmonic frequencies, third-order anharmonic force constants, and the X-matrix of anharmonic couplings<sup>71</sup> were computed using the perturbative anharmonic treatment implemented in Gaussian 09. The initial population distribution for all modes was taken to be thermal at room temperature, except for the tag mode, whose initial population was increased by unity. The only free parameter in the calculations, the rate of energy dissipation to the solvent, was taken as (14 ps<sup>-1</sup>).<sup>72</sup>

### 3.5.4. Mode coupling evaluation by scanning masses

The potential energy surface concerning the succinimide ester orientation with respect to the chain is shallow and a range of conformations along  $\theta$  are thermally accessible at room temperature (Figure 3.5(a)). A coupling strength for the  $\nu_{as}(\text{NOC})$  with the two stretching modes and three rocking of the chain in the CH<sub>3</sub>-s compound was evaluated as a function of the dihedral angle  $\theta$ . The DFT normal-mode calculations with a fixed dihedral angle and optimized all other degrees of freedom were performed at different dihedral angles at a 10 degrees grid. To evaluate the coupling between  $\nu_{as}(\text{NOC})$

with the two stretching modes and three rocking of the chain in the CH<sub>3</sub>-s compound, the masses of the oxygen and nitrogen atoms at the ester were scanned using the mass-normalized Hessian and detecting the frequency jump of the  $\nu_{\text{as}}(\text{NOC})$  mode frequency when it passes the resonance with other normal mode in the molecule. A somewhat similar approach was used previously where an external electric field strength was varied to shift the energy of one state with respect to another.<sup>73</sup> The frequency jump equals to  $2\beta$ , where  $\beta$  is the coupling of the two modes. It was evaluated for the two C-C stretching modes at the chain and three rocking modes and the squares were averaged within each mode type (Figure. 3.5(b)).

### 3.6. Acknowledgements

The work was supported by the National Science Foundation (NSF, grant CHE1012371). Construction of the fully automated 2DIR instrument was supported by NSF grant, CHE-1040491, and the Louisiana Board of Regents grants (LEQSF(2011-12)-ENH-TR-29 and LEQSF-EPS(2014)-PFUND-377. The synthesis of the bifunctional linkers was supported by the NSF grant, CHE-1112091.

## Chapter 4

### Energy Transport in PEG Oligomers: Contributions of Different Optical Bands

The work detailed in this chapter has been published in the following paper: Layla N. Qasim, Arkady Kurnosov, Yuankai Yue, Zhiwei Lin, Alexander L. Burin, and Igor V. Rubtsov, Energy Transport in PEG Oligomers: Contributions of Different Optical Bands. *J. Phys. Chem. C* **2016**, 120, 26663 – 26677

#### 4.1. Overview

Chapter 3 of this dissertation described how the transport speed via alkane chains was found to be dependent on the way the excess energy is introduced into the chain. The difference in the speeds was attributed to the involvement of different optical chain bands. The group velocities, supported by various bands were computed; the experimental energy transport velocities of 14.4 (v(N≡N) mode initiation) and 8.0 Å/ps (v(C=O) mode initiation) were found to be in agreement with the group velocities of the wagging – twisting CH<sub>2</sub> bands and C-C stretching band, respectively. The assignment of the energy transporting bands was supported by theoretical investigations of the alkane band structure as well as the IVR pathways of the end group relaxation. The objective of the study described in this chapter is to understand the energy transport mechanism in polyethylene glycol (PEG) chains. Due to the presence of a heteroatom in its unit cell, PEG chains are more complex than alkane chains. The presence of the heteroatom results in an alternating coupling strength pattern along the chain, which greatly affects its energy transport properties. Previous reports indicate that the transport initiated by

excitation of  $\nu(\text{N}\equiv\text{N})$  of the azido end group results in a through-chain energy transport with a constant speed of  $5.5 \text{ \AA/ps}$ ,<sup>49</sup> although the chain bands responsible for the transport were not identified. To better understand and describe vibrational energy transport via PEG chains, RA 2DIR measurements were performed on a set of compounds featuring chains of 0, 4, 8, and 12 PEG units terminated by azido and succinimide ester end groups. Energy transport initiated by the excitation of the asymmetric carbonyl stretching mode of succinimide ester end group,  $\nu_{\text{as}}(\text{C}=\text{O})$ , was studied first and compared to the transport initiated by  $\nu(\text{N}\equiv\text{N})$ . As opposed to alkanes, PEG chains have IR-active vibrational modes in the fingerprint region. These states were directly interrogated in this study by measuring 2DIR diagonal and cross peaks among the chain states and the end-group states. To understand the factors determining the transport speed for the two types of transport initiations,  $\nu(\text{N}\equiv\text{N})$  and  $\nu_{\text{as}}(\text{C}=\text{O})$ , a theoretical modeling of the PEG chain bands (details are shown later) was performed; in addition, reported results for the  $7_2$ -helical conformation were used.<sup>74</sup> The modeling suggests involvement of several optical chain bands with  $800\text{--}1500 \text{ cm}^{-1}$  energies in the transport. Rates of vibrational relaxation pathways for end-group and chain states were computed leading to a better understanding of how energy is entering the chain from the end group and how it is redistributed within the chain. A theoretical model based on solving the quantum Liouville equation for a density matrix was implemented for a linear chain of coupled states. The model describes both ballistic and diffusive transport mechanisms and provides a range of parameters at which these transport regimes can occur in PEG chains.

## 4.2. Experimental Details

#### 4.2.1. Experimental method

A detailed accounting of the fully-automated 2DIR spectrometer is presented in Chapter 2.7.

#### 4.2.2. Sample preparation

A series of polyethylene glycol (PEG) oligomers of varying lengths featuring azido and succinimide ester (NHS ester) moieties terminating opposite ends of the PEG chains were studied (Figure 4.1). Compounds featuring 4, 8, and 12 PEG units (azPEG4, 8, and 12) were purchased from Quanta Biodesign Limited (Azido-dPEGnNHS ester). 4-Azidobutyrate-N-hydroxysuccinimide ester, denoted as azPEG0, was purchased from Synthonix. The chain length was taken as the through-bond distance between the nitrogen atom of the azido group closest to the chain and the carbon atom of the ester and is determined as 6.1, 22.1, 39.7, and 57.2 Å for  $n = 0, 4, 8$ , and 12, respectively. For linear absorption and 2DIR measurements the compounds were dissolved in deuterated chloroform ( $\text{CDCl}_3$ ) at about 80 mM concentration and placed in a sample cell featuring a 100  $\mu\text{m}$  Teflon spacer and 1 mm thick  $\text{BaF}_2$  windows. The experiments were performed at room temperature, which was  $22.5 \pm 0.3$  °C.

#### 4.2.3. Quantum-chemistry calculations

Geometry optimization and normal mode analysis were performed within Gaussian 09 suite using B3LYP functional and 6-311++G(d,p) basis sets. Harmonic normal-mode analysis in vacuum was performed on an azPEG8 compound and PEG-8 oligomer ( $\text{T}-(\text{CH}_2\text{-O-CH}_2)_8\text{-T}$ ), where T was a hydrogen atom with an artificial mass of 4 amu. The computed harmonic frequencies were scaled by a factor of 0.97. Anharmonic

DFT calculations were performed for azPEG3a in vacuum, where the NHS ester end group is replaced by a carboxylic acid group. Tight optimization conditions and ultrafine integration grid were used for calculating anharmonic force constants and anharmonicities. For calculating dispersion relations for PEG chains, normal-mode analysis was performed for azPEG8a chain in an all-anti conformation.

### 4.3. Results

Introduction of excess energy into one of the end groups (tags) of a molecule results in a nonequilibrium energy distribution within the molecule and with respect to the surrounding solvent. A complete local thermalization requires about 50 ps; during this time the system is under nonequilibrium conditions.<sup>75</sup> Thermalization of such system involves energy equilibration within the molecule as well as energy exchange with the solvent. For relaxation of high-energy states compared to the thermal energy (energies  $\gg k_B T$ ) the former process dominates when solvents weakly interact with the compound. Thermalization within the molecule can occur more or less rapidly, depending on the molecular structure. Thermalization within the molecule can be detected by observing the influence of the excess energy onto another vibrational mode, a reporter; such reporter can be placed at another end group or within the chain. In the former case, the waiting time dependence of the tag/reporter cross-peak amplitude reports on the energy transport properties of the molecular chain connecting the end groups.

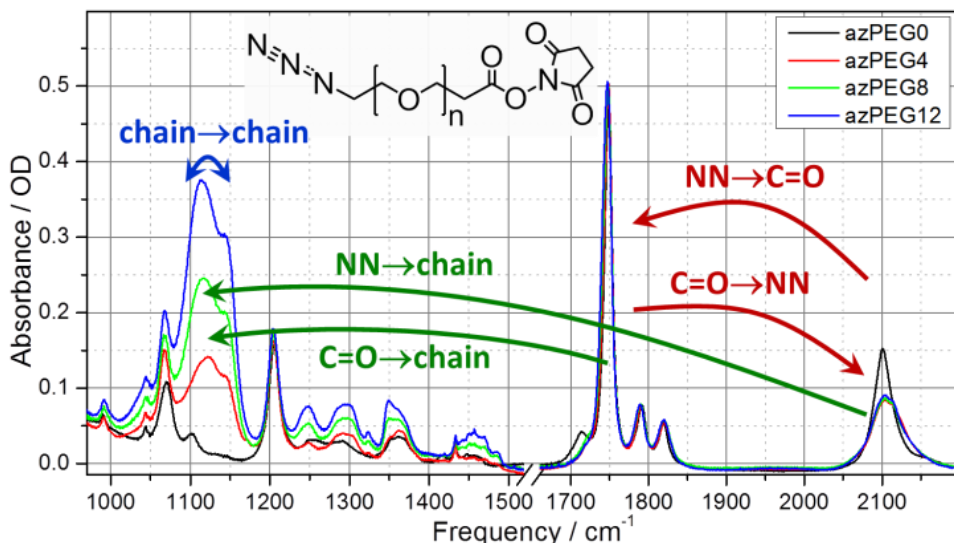


**Figure 4.1.** Linear absorption spectra of the azPEG $n$  compounds and their structure. The arrows indicate different energy transport experiments performed in this study.

#### 4.3.1. End group to end group energy transport

Dynamics of the energy transport between the end groups of the azPEG $n$  compounds dissolved in  $\text{CDCl}_3$  were studied using RA 2DIR spectroscopy. The excess energy was introduced by exciting the asymmetric carbonyl stretching mode of succinimide,  $\nu_{\text{as}}(\text{C}=\text{O})$  (the tag), with the first two mid-IR pulses. Energy arrival to the opposite end of the chain was monitored by probing the reporter mode, the stretching mode of the azido moiety,  $\nu(\text{N}\equiv\text{N})$ . Figure 4.2(a) shows the  $\nu_{\text{as}}(\text{C}=\text{O})/\nu(\text{N}\equiv\text{N})$  cross peak measured at the waiting time,  $T$ , of 10 ps. Examples of the waiting time dependences of the  $\nu_{\text{as}}(\text{C}=\text{O})/\nu(\text{N}\equiv\text{N})$  cross peak for the three indicated compounds (azPEG $n$ ,  $n = 0, 4, 8$ ) are shown in Figure 4.2(b). The waiting time at which the cross-peak amplitude reaches the maximum,  $T_{\text{max}}$ , was determined for each kinetics (arrows in Figure 4.2(b)). The mean  $T_{\text{max}}$  values, averaged over 3–5 independent measurements for each compound, were plotted as a function of the tag-reporter through-bond distance (Figure 4.2(c)). The

dependence can be well represented by a linear function (red line) resulting in the energy transport with a constant speed of  $5.4 \pm 0.4$  Å/ps.

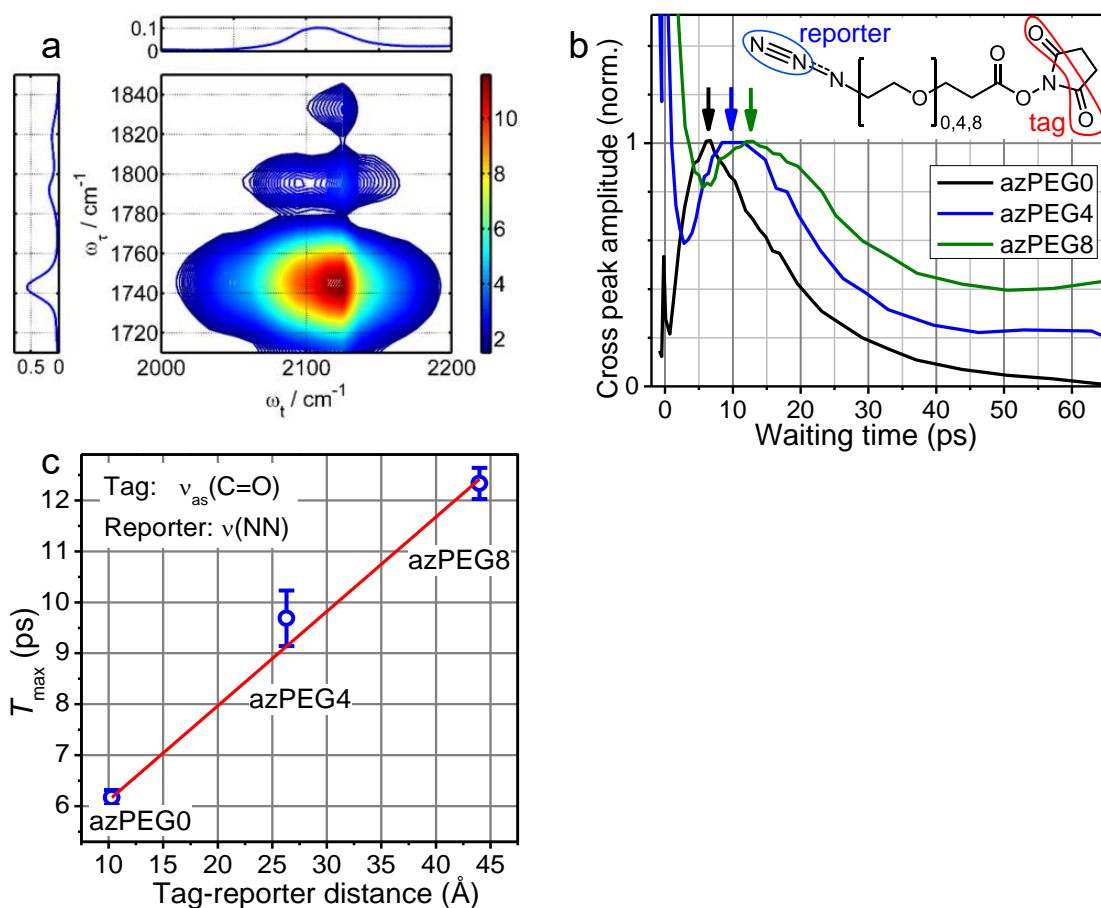


**Figure 4.2.** (a) 2DIR  $\nu_{\text{as}}(\text{C=O})/\nu(\text{N}\equiv\text{N})$  cross-peak ( $1740/2100 \text{ cm}^{-1}$ ) of azPEG4 in  $\text{CDCl}_3$  measured at  $T = 10.2$  ps. (b) Waiting time dependences of the  $\nu_{\text{as}}(\text{C=O})/\nu(\text{N}\equiv\text{N})$  cross-peak amplitude for azPEG0, 4, and 8. The curves are fitted with a double exponential function and the  $T_{\text{max}}$  values are indicated by arrows. (c) Tag-reporter distance dependence of  $T_{\text{max}}$  for the indicated compounds. Note that the tag-reporter distance was calculated as a through-bond distance. The fit with a linear function (red line), resulted in a transport speed of  $5.4 \pm 0.4$  Å/ps.

Interestingly, this speed is essentially the same as the speed of the transport initiated by  $\nu(\text{N}\equiv\text{N})$  tag in these compounds, reported to be about  $5.5$  Å/ps.<sup>49</sup> The results contrast with the data reported for alkane chains terminated with azido and NHS-ester moieties where the transport speed depends strongly on the way the transport is initiated

(8.0 and 14.4 Å/ps with  $\nu_{\text{as}}(\text{C}=\text{O})$  and  $\nu(\text{N}\equiv\text{N})$  tags, respectively).<sup>22</sup> To understand the differences in the energy transport properties of the two chains, alkane and PEG, 2DIR experiments directly involving PEG chain states were performed.

#### 4.3.2. End group to chain energy transfer

Relaxation of the end-group tag populates some chains states which participate in through-chain energy transport. To describe this initial step of the transport, the waiting time dependences of the cross peaks among end groups and different chain states were monitored.

Unlike alkanes, PEG chains feature oxygen heteroatoms resulting in IR active states (Figures 4.1 and 4.3) accessible via 2DIR spectroscopy, providing an opportunity to investigate the chain band involvement in the energy transport. The strongest chain transitions, found in the frequency region between 1030 and 1170  $\text{cm}^{-1}$  (Figures 4.1 and 4.3), gain their strength from the C–O stretching motion. The broadness of this optical signature is likely due to overlap of different chain band transitions. A good quality fit of this spectral region can be obtained with six Gaussian-shaped components. Four of them, centered at 1050, 1091, 1122, and 1147  $\text{cm}^{-1}$ , represent chain states and denoted as C1, C2, C3, and C4, respectively, and two, centered at 1067 and 1045  $\text{cm}^{-1}$ , represent the end-group-localized states of succinimide ester (Figures 4.1 and 4.3). Band structure calculations for PEG chains indicate that there are three chain bands in this frequency region, all involving different contributions of  $\nu(\text{C}-\text{O})$ ,  $\nu(\text{C}-\text{C})$ , and  $\rho(\text{CH}_2)$  transitions (vide infra).<sup>74</sup> 2DIR experiments were performed by initiating energy transport with the

end-group localized tags,  $\nu(\text{N}\equiv\text{N})$  or  $\nu_{\text{as}}(\text{C}=\text{O})$ , and probing the bright chain states, C1–C4.

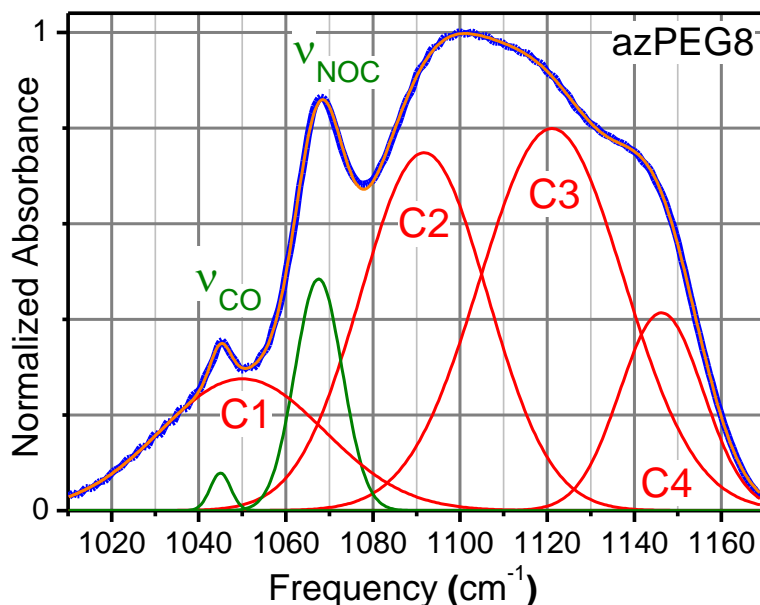


**Figure 4.3.** Linear absorption spectrum of azPEG8 in  $\text{CDCl}_3$  (blue) in the frequency region from 1010 to 1170  $\text{cm}^{-1}$ . A fit with six Gaussian components (orange) and the resulting individual components (red, green) are shown. Whereas two narrow transitions, labeled as  $\nu(\text{NOC})$  and  $\nu(\text{CO})$ , belong to the NHS ester end group (green), the four components shown with red lines belong to the chain states. Note that the central frequencies of the C1–C4 peaks are 1050  $\text{cm}^{-1}$  (C1), 1091  $\text{cm}^{-1}$  (C2), 1122  $\text{cm}^{-1}$  (C3), and 1147  $\text{cm}^{-1}$  (C4).

An example of a 2DIR spectrum of azPEG8, focusing at the cross peaks between the  $\nu(\text{N}\equiv\text{N})$  tag and C1–C4 reporters in the frequency region of 1050–1200  $\text{cm}^{-1}$ , is shown in Figure 4.4(a). Waiting time dependences for individual cross peaks for the azPEG4–12 compounds are shown in Figure 4.4(b–d). Note that the  $\omega_t$  region for C1 includes also a strong  $\nu(\text{NOC})$  peak; the asterisk, C1\*, indicates this overlap. Because of this complication, we first discuss the waiting time dependences involving the C2–C4 transitions.

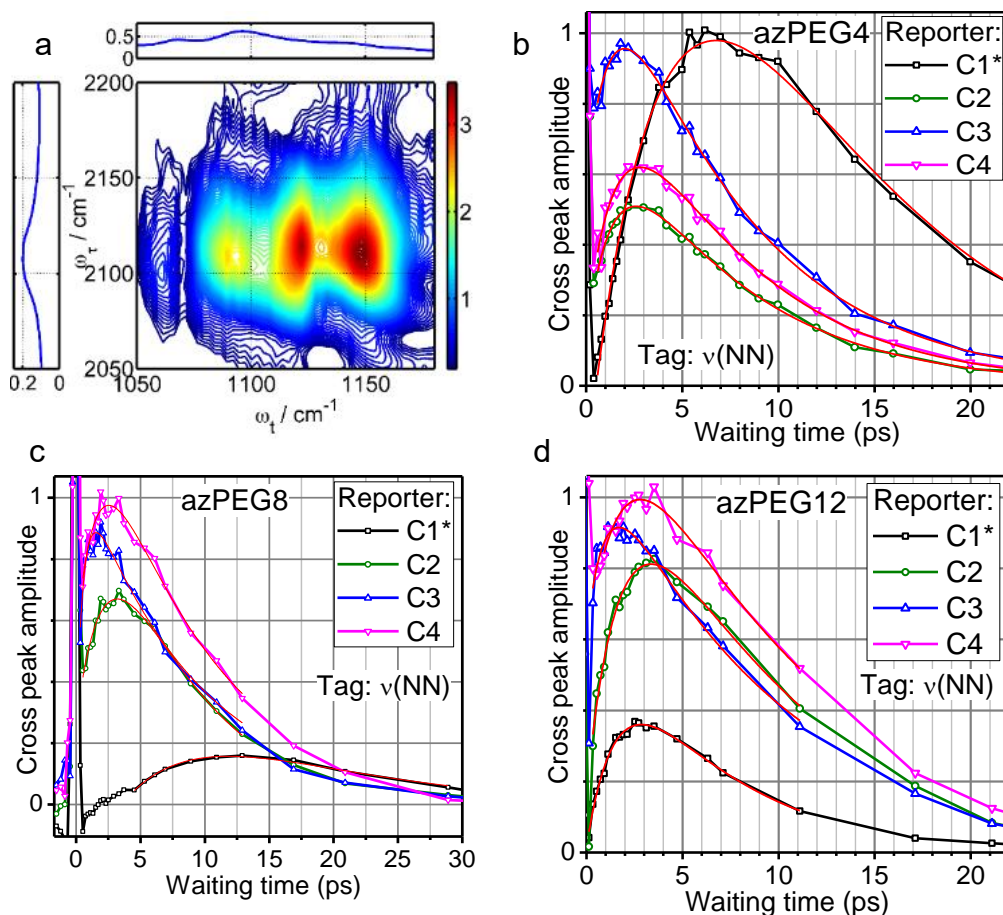


**Figure 4.4.** (a) 2DIR magnitude spectrum of azPEG8 focusing at the cross-peaks between  $\nu(\text{N}\equiv\text{N})$  and C1-C4 chain states recorded at  $T = 2.2$  ps. The linear absorption spectrum of azPEG4 is shown in the attached panels. (b-d) Waiting time dependences of the  $\nu(\text{N}\equiv\text{N})$  /  $\nu(\text{C1-C4})$  cross-peak amplitudes for (b) azPEG4, (c) azPEG8, and (d) azPEG12 obtained by integration of individual 2DIR spectra within specific cross-peak regions. Integration regions along the  $\omega_t$  axis were 1055-1075, 1090-1105, 1115-1130, and 1140-1155 cm<sup>-1</sup> for C1\*, C2, C3, and C4, respectively, and 2080-2125 cm<sup>-1</sup> along  $\omega_r$ . Note that C1 overlaps in frequency with the local  $\nu(\text{N-O-C})$  mode on the succinimide ester. All kinetics were fitted in the vicinity of their maxima with a double exponential function (red lines); the  $T_{\text{max}}$  values determined from the fit are shown in Table 4.1.

**Table 4.1.**  $T_{\text{max}}$  values (in ps) obtained from the waiting-time dependences of the  $\nu(\text{N}\equiv\text{N})$  / C1-C4 and  $\nu_{\text{as}}(\text{C}=\text{O})$  / C1-C4 cross peaks in azPEG4, 8, and 12.<sup>#</sup>

$\nu(\text{NN})$ tag, C1-C4 reporters				
	$\nu(\text{N3})/\text{C1}^*$	$\nu(\text{N3})/\text{C2}$	$\nu(\text{N3})/\text{C3}$	$\nu(\text{N3})/\text{C4}$
azPEG4	$6.7 \pm 0.2$	$2.5 \pm 0.4$	$2.0 \pm 0.5$	$2.4 \pm 0.5$
azPEG8	$11.8 \pm 0.6$	$3.0 \pm 0.5$	$1.5 \pm 0.3$	$2.2 \pm 0.4$
azPEG12	$3.1 \pm 0.5$	$3.2 \pm 0.5$	$1.4 \pm 0.3$	$2.9 \pm 0.4$

$\nu_{\text{as}}(\text{C}=\text{O})$ tag, C1-C4 reporters				
	$\nu_{\text{as}}(\text{C}=\text{O})/\text{C1}^*$	$\nu_{\text{as}}(\text{C}=\text{O})/\text{C2}$	$\nu_{\text{as}}(\text{C}=\text{O})/\text{C3}$	$\nu_{\text{as}}(\text{C}=\text{O})/\text{C4}$
azPEG4	--&	$7.8 \pm 0.6$	$7.3 \pm 0.6$	$7.4 \pm 0.5$
azPEG8	--&	$8.7 \pm 0.6$	$8.2 \pm 0.7$	$8.0 \pm 1$
azPEG12	--&	$7.5 \pm 0.7$	$6.8 \pm 0.5$	$7.8 \pm 0.5$

# The following frequency ranges were used for the cross peak integration: C1 ( $1055 - 1075 \text{ cm}^{-1}$ ), C2 ( $1090 - 1105 \text{ cm}^{-1}$ ), C3 ( $1115 - 1130 \text{ cm}^{-1}$ ), and C4 ( $1140 - 1155 \text{ cm}^{-1}$ ); & No rise in the waiting-time dependence was observed due to a dominating signal contribution from the end-group localized mode,  $\nu(\text{N-O-C})$ .

As apparent from Figure 4.4(b-d), the  $T_{\text{max}}$  values for different reporters (C2–C4) for a specific compound are similar. For example, for azPEG4, the three  $T_{\text{max}}$  values are 2.5, 2.0, and 2.4ps for C2, C3, and C4 reporters, respectively (Table 4.1). The spread of the  $T_{\text{max}}$  values is only slightly bigger for azPEG12 (Table 4.1). The  $T_{\text{max}}$  values are even more similar for a specific cross peak among different compounds indicating that the values are essentially chain-length independent.

The  $T_{\text{max}}$  values for the  $\nu(\text{N}\equiv\text{N})/\text{C1}^*$  cross peak are not monotonic with increasing chain length, which is explained by the presence of two competing contributions,  $\nu(\text{N}\equiv\text{N})/\text{C1}$  and  $\nu(\text{N}\equiv\text{N})/\nu(\text{NOC})$ . At small waiting times, the cross peaks for all three compounds are likely dominated by the  $\nu(\text{N}\equiv\text{N})/\text{C1}$  signal, even though it is rather weak in azPEG4 and azPEG8 due to a small extinction coefficient and large spectral width of the C1 peak. At larger waiting times, the signals in azPEG4 and 8 are dominated by the  $\nu(\text{N}\equiv\text{N})/\nu(\text{NOC})$  contribution, as the  $\nu(\text{NOC})$  transition is strong and narrow and the distance for energy transport from  $\nu(\text{N}\equiv\text{N})$  toward  $\nu(\text{NOC})$  is not very large. Therefore, the  $T_{\text{max}}$  values obtained for azPEG4 and 8 reflect the energy transport time to the NHS-ester end group across the whole chain. In azPEG12, the  $\nu(\text{N}\equiv\text{N})/\text{C1}$  cross peak becomes

dominant as its contribution increases with an increase of the chain length, while the contribution from  $\nu(\text{N}\equiv\text{N})/\nu(\text{NOC})$  decreases for longer chain lengths as the amount of energy delivered to the NHS ester is reduced. Therefore, only in azPEG12 the  $T_{\text{max}}$  for the  $\nu(\text{N}\equiv\text{N})/\text{C1}^*$  cross peak represents the chain state(s), C1, showing a comparable  $T_{\text{max}}$  time (3.1 ps) with other chain states (Table 4.1).

The energy transport initiated by the  $\nu_{\text{as}}(\text{C}=\text{O})$  excitation was studied by observing cross peaks between  $\nu_{\text{as}}(\text{C}=\text{O})$  and various chain states, C1–C4 (Figure 4.5(a)). The waiting time dependences for the  $\nu_{\text{as}}(\text{C}=\text{O})/\text{C2}–\text{C4}$  cross peaks appear to be very similar (Figure 4.5(b-d)), both among different bands within the same compound and among different compounds (Table 4.1); the measured  $T_{\text{max}}$  values fall between 6.8 and 8.7 ps. The larger  $T_{\text{max}}$  values obtained for the  $\nu_{\text{as}}(\text{C}=\text{O})$  initiation, compared to the  $\nu(\text{N}\equiv\text{N})$  initiation, are attributed to a substantially larger distance between the carbonyl groups of the succinimide and the chain (ca. 3 bonds).<sup>22, 24</sup> Note that the  $\nu_{\text{as}}(\text{C}=\text{O})/\text{C1}^*$  cross peak kinetics do not show a rise but only a decay (Figure 4.5(b-d)). This is because the cross-peak is dominated by the  $\nu_{\text{as}}(\text{C}=\text{O})/\nu(\text{NOC})$  contribution as  $\nu_{\text{as}}(\text{C}=\text{O})$  and  $\nu(\text{NOC})$  are strongly coupled ( $\Delta(\nu_{\text{as}}(\text{C}=\text{O})/\nu(\text{NOC})) = 1.03 \text{ cm}^{-1}$ ).

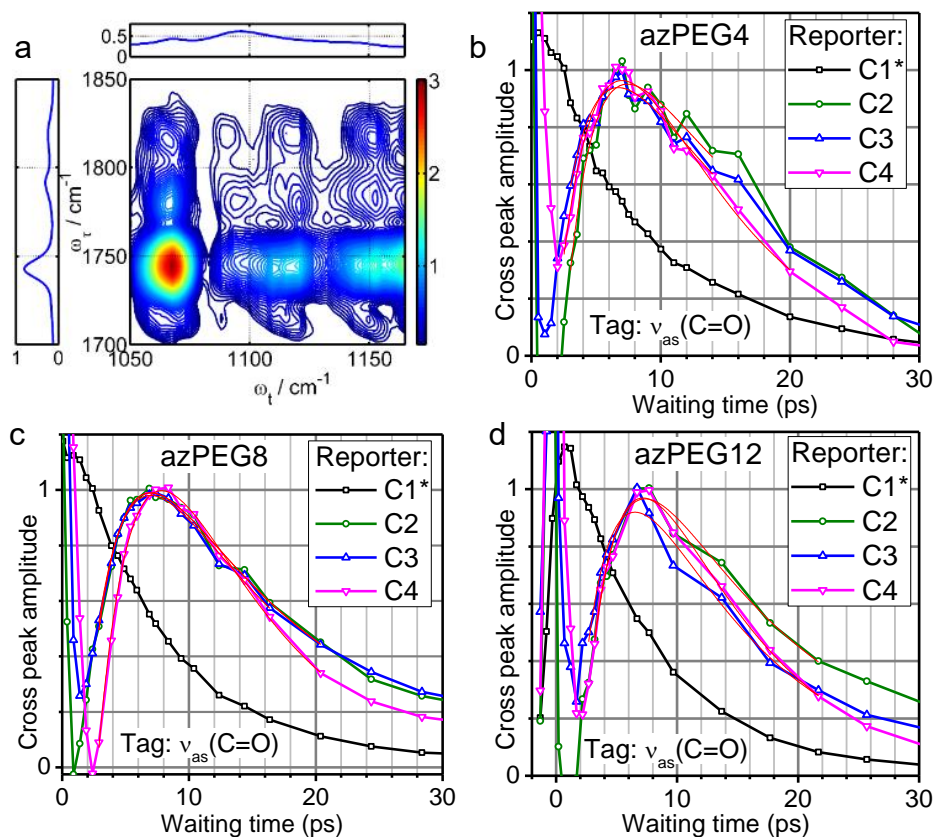


**Figure 4.5.** (a) 2DIR magnitude spectrum of azPEG8 focusing on the cross peaks between  $\nu_{\text{as}}(\text{C=O})$  and C1-C4 measured at  $T = 7$  ps. Waiting time dependences of the  $\nu_{\text{as}}(\text{C=O}) / \nu(\text{C1-C4})$  cross-peak amplitudes for (b) azPEG4, (c) azPEG8, and (d) azPEG12. The integration region along  $\omega_\tau$  was  $1730\text{--}1760 \text{ cm}^{-1}$ ; the integration regions for C1-C4 peaks along the  $\omega_t$  axis are given in the Figure 4.4 caption. The kinetics were fitted in the vicinity of their maxima with a double exponential function (red lines); the  $T_{\text{max}}$  values determined from the fit are shown in Table 4.1.

To summarize, the energy transport toward the chain initiated by  $\nu(\text{N}\equiv\text{N})$  takes about  $1.5\text{--}3$  ps, while it takes about  $7\text{--}8.5$  ps for energy to arrive at the chain from  $\nu_{\text{as}}(\text{C}\equiv\text{O})$ . In both cases of initiation, the transport time appears to be essentially chain-length independent.

### 4.3.3. Energy transfer among the chain states

*Dynamics of the diagonal chain peaks.* Chain state lifetimes and dephasing times are among the crucial parameters that determine the energy transport mechanism via the

respective chain band(s). The diagonal 2DIR spectra of the chain states were measured by exciting and detecting all of the chain states within the C1–C4 frequency region with a broadband pulse centered at  $1160\text{ cm}^{-1}$  (Figure 4.6(a)). The waiting time kinetics (Figure 4.6(b,c)), showing fast and slow decay components, were fitted with a double exponential function (Table 4.2). The fast component of about 1 ps is assigned to the lifetime of the excited chain state. The slow component reflects the coupling of the selected mode with other modes in the chain, which were populated from the tag relaxation.<sup>22</sup> The characteristic time of the slow component of about 6.5 ps describes the dynamics of energy flow away from those chain states, which are strongly coupled to the initially excited mode. Note that the slow decay component has a substantial amplitude, contributing to 22– 38% of the overall signal (Table 4.2).

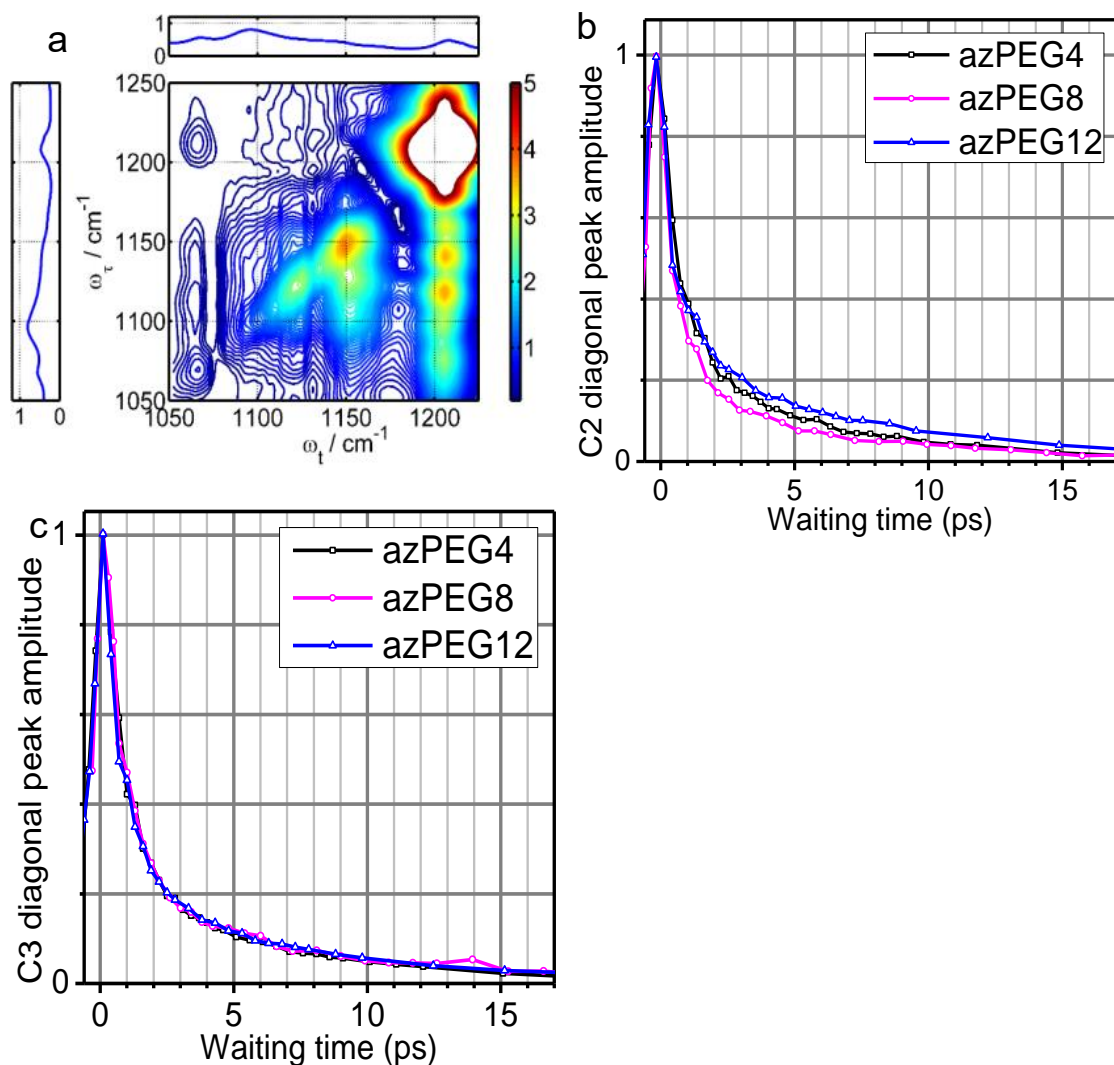


**Figure 4.6.** (a) 2DIR spectrum of the chain band region ( $1050\text{--}1170\text{ cm}^{-1}$ ) for azPEG8 at  $T = 3.0$  ps. The diagonal peak at about  $1210\text{ cm}^{-1}$  belongs to a localized  $\nu(\text{C}\text{--}\text{N}\text{--}\text{C})$  mode of the NHS ester. Waiting time dependences of (b) C3 and (c) C2 diagonal peaks of azPEG $_n$ . The kinetic traces were fitted with a double exponential function (see Table 4.2 for the results averaged over 3–5 measurements).

**Table 4.2.** Results of the fit of the diagonal chain-state (C2-C4)<sup>#</sup> waiting-time dependences with a double exponential function,  $S(T) = A_1 \exp(-T/\tau_1) + A_2 \exp(-T/\tau_2)$ . The relative contribution of the slowly decaying component ( $\tau_2$ ) is given in parentheses ( $\gamma = A_2/(A_1+A_2) \times 100\%$ ).

	C2		C3		C4	
	$\tau_1$ / ps	$\tau_2$ / ps ( $\gamma$ , %)	$\tau_1$ / ps	$\tau_2$ / ps ( $\gamma$ , %)	$\tau_1$ / ps	$\tau_2$ / ps ( $\gamma$ , %)
azPEG4	$1.0 \pm 0.4$	$6.1 \pm 0.6$ (28%)	$0.98 \pm 0.4$	$6.2 \pm 1.0$ (26%)	$0.93 \pm 0.3$	$6.6 \pm 0.8$ (29%)
azPEG8	$1.0 \pm 0.2$	$6.6 \pm 0.9$ (30%)	$0.92 \pm 0.3$	$6.7 \pm 0.4$ (22%)	$0.90 \pm 0.1$	$6.56 \pm 0.33$ (27%)
azPEG12	$1.2 \pm 0.4$	$7.13 \pm 0.9$ (35 %)	$0.92 \pm 0.3$	$6.8 \pm 1.0$ (23 %)	$0.85 \pm 0.3$	$6.2 \pm 0.5$ (38%)

<sup>#</sup> No data are given for the C1 peak as the diagonal v(NOC) peak dominates the C1 region (Fig. 6A).

**Dynamics of the cross peaks among chain states.** To investigate energy exchange

between different chain states, dynamics of the cross peaks among them were analyzed.

The waiting time dynamics for all chain-state cross peaks of azPEG8 are shown in Figure

4.7. Two distinctively different waiting time dependences were observed: one with a

clear growth of the cross-peak amplitude at short waiting times with a subsequent

maximum at  $T \neq 0$  and one with a maximum at  $T = 0$ . Kinetic traces which showed the

maxima at  $T \neq 0$  were fitted with a double exponential function to evaluate  $T_{\max}$ . The

other kinetic traces also show a clear indication of an underlined rise, masked however by

the decay contribution originating from the direct coupling of the two modes and a

nonresonant signal at  $T \sim 0$  (Figure 4.7). The  $T_{\max}$  values determined for azPEG8 and

azPEG12 compounds were found to be within a narrow range of 2.8–3.3 ps (Table 4.3).

Although no resolved peaks were observed for azPEG4, the shapes of the kinetics

indicated some signal growth, also peaking at about 3 ps. Therefore, we conclude that in

all three compounds the cross peaks between different chain states feature a rise with a

peak at about 3 ps.

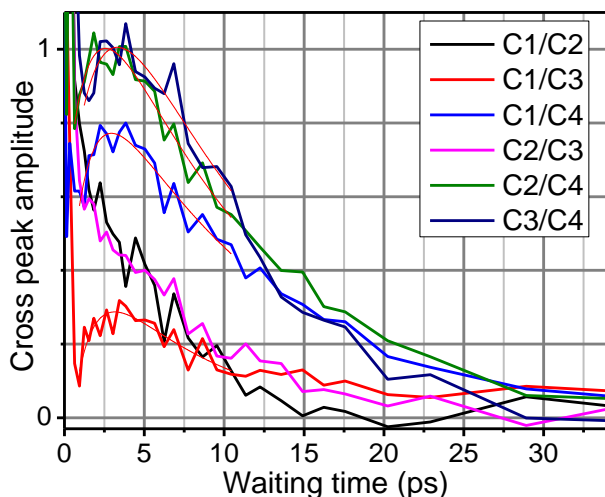


**Figure 4.7.** Waiting time dependences of various cross peaks among indicated chain states of azPEG8. The kinetics with a clear rise were fitted by a double exponential function and the  $T_{\max}$  values were determined from the fit (see Table 4.3 for the  $T_{\max}$  results averaged over 3-5 measurements).

**Table 4.3.**  $T_{\max}$  values (in ps) obtained from the waiting-time dependences of cross peaks among C1 – C4 states in azPEG8 and azPEG12.

	C1/C3	C1/C4	C2/C4	C3/C4
azPEG8	3.1	2.9	2.9	3.3
azPEG12	--#	--#	--#	2.8

# no rise was observed for these regions in azPEG12.

#### 4.3.4. Dispersion relations for regular PEG chains

In earlier sections, we discussed different chain states which are populated through end group relaxation and participate in the energy transport. To understand the character of these states, dispersion relations were computed for two PEG conformers. Chains with periodic structures result in fully delocalized states which can be characterized by dispersion relations. The dispersion relations provide information about the character of vibrational motion in different bands and about the width and shape of the bands. Although the structure of PEG chains in solution may not be fully regular

(periodic), the dispersion relations obtained for regular conformations provide a good starting point for discussing the chain states.

Two characteristic conformations were considered for the PEG chains, one with a gauche kink at every  $\text{H}_2\text{C}-\text{CH}_2$  bond resulting in the  $7_2$ -helical structure (anti-anti-gauche sequence) and the all-anti conformation leading to a planar chain. The dispersion relations for the helical conformation were reported previously; those results are used in this study (Figure 4.8(b)).<sup>74</sup> The chain dispersion curves in the all-anti conformation were performed in this study using the approach described previously (see Chapter 4.6.1).<sup>22</sup> Figure 4.8 presents the side-by-side comparison of the two computations. Despite the similarities of the two band structures, it is apparent that in the planar conformation the interactions (and band widths) vary much more than for the helical conformation. Indeed, some bands are very wide ( $\nu_{13}$ , wider than  $100\text{ cm}^{-1}$ ), while other are very narrow ( $\nu_9$ ,  $\sim 0.4\text{ cm}^{-1}$  wide). All bands in the helical conformation are narrower than  $65\text{ cm}^{-1}$ . Structural studies of PEG chains report that they form helices in the bulk and crystalline forms, and when dissolved in nonwater solvents.<sup>76-79</sup> For this reason, we are motivated to use the band structure of the helical conformation for quantitative assessment.

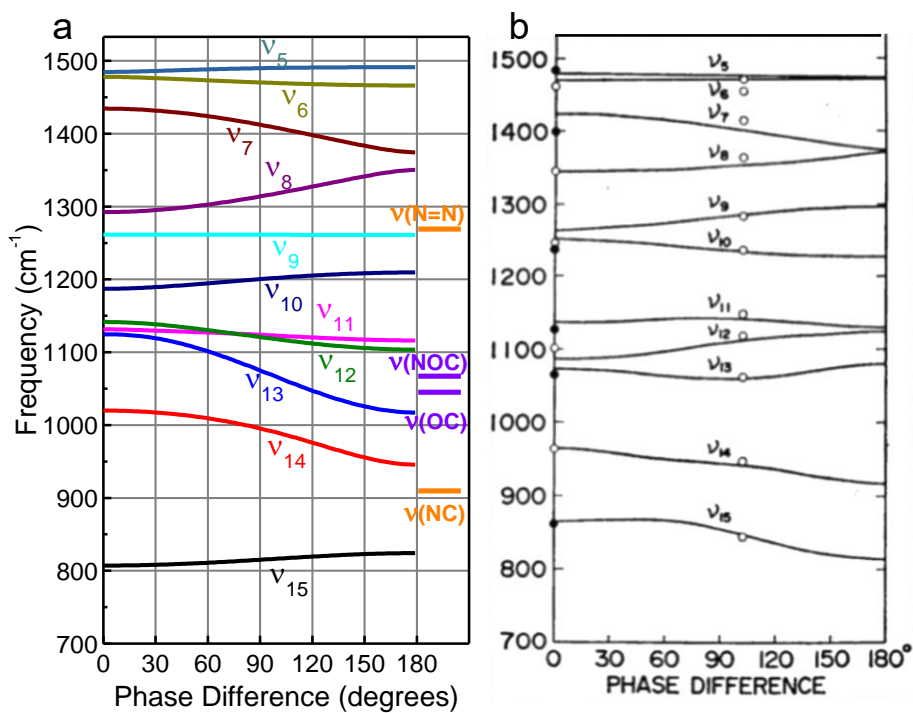


**Figure 4.8.** PEG chain dispersion curves for the (a) all-anti and (b) anti-anti-gauche helical conformations. The graph b is reproduced with permission from ref.<sup>74</sup> All computed band frequencies in graph a were scaled by a factor of 0.97. Essential end-group states,  $\nu(\text{N}=\text{N})$ ,  $\nu(\text{NOC})$ ,  $\nu(\text{OC})$ , and  $\nu(\text{NC})$ , are shown in panel a with horizontal bars; represented by their experimental frequencies, except for  $\nu(\text{NC})$ , given by the calculated frequency.

**Table 4.4.** PEG chain band frequencies at  $q = 0$  and  $\pi$  ( $\omega(0)$  and  $\omega(\pi)$ ) and the group velocities computed for each band,  $\langle |V| \rangle$ , for the all-anti PEG conformation.

Band	Band type	$\omega(0)$ , $\text{cm}^{-1}$	$\omega(\pi)$ , $\text{cm}^{-1}$	$\omega_{\text{center}}$ , $ \omega(0) - \omega(\pi) $	$\langle  V  \rangle$ , $\text{\AA}/\text{ps}$
$\nu_{15}$	$\rho(\text{CH}_2)^a$	806.4	823.5	17.1	3.1
$\nu_{14}$	$\nu(\text{CC})^a$	1019.0	944.7	74.3	13.6
$\nu_{13}$	$\nu(\text{CO})^a$	1123.7	1016.2	107.5	19.7
$\nu_{12}$	$\nu(\text{CO})^a$	1140.6	1102.4	38.2	7.0
$\nu_{11}$	$\rho(\text{CH}_2)^a$	1130.5	1115.2	14.8	2.8
$\nu_{10}$	$\text{tw}(\text{CH}_2)$	1186.0	1208.6	22.6	4.1
$\nu_9$	$\text{tw}(\text{CH}_2)$	1261.37	1260.97	0.4	0.073
$\nu_8$	$\text{w}(\text{CH}_2)$	1291.2	1349.1	57.9	10.6
Band	Band type	$\omega(0)$ , $\text{cm}^{-1}$	$\omega(\pi)$ , $\text{cm}^{-1}$	$\omega_{\text{center}}$ , $ \omega(0) - \omega(\pi) $	$\langle  V  \rangle$ , $\text{\AA}/\text{ps}$
$\nu_7$	$\text{w}(\text{CH}_2)$	1433.2	1373.1	60.1	11.0
$\nu_6$	$\text{sc}(\text{CH}_2)$	1476.7	1464.8	11.8	2.2
$\nu_5$	$\text{sc}(\text{CH}_2)$	1483.5	1490.0	6.5	1.2

<sup>a</sup> the most prominent contribution is shown, although both  $\nu(\text{C-O})$ ,  $\nu(\text{C-C})$ , and  $\rho(\text{CH}_2)$  motions are contributing.

In addition, the states populated upon  $\nu(\text{N}\equiv\text{N})$  and  $\nu_{\text{as}}(\text{C=O})$  tag relaxation, serving as doorway states, are shown in Figure 4.8(a) with orange and violet bars.<sup>22</sup> Their frequencies determine the chain bands that can contribute to the energy transport. The  $\nu_5$  and  $\nu_6$  bands associated with the  $\text{CH}_2$  scissoring motion (sc) and  $\nu_7$  and  $\nu_8$  bands due to  $\text{CH}_2$  wagging (w) are likely too high in energy to efficiently contribute to the transport in the PEG chains (Figure 4.8). The  $\nu_9$  and  $\nu_{10}$  bands associated with the  $\text{CH}_2$  twisting motion (tw) essentially overlap with  $\nu(\text{N}\equiv\text{N})$  and can contribute significantly to the energy transport originated from the  $\nu(\text{N}\equiv\text{N})$  tag excitation. The remaining five bands,  $\nu_{11}$ – $\nu_{15}$ , are expected to contribute to the transport initiated from either end of the

molecule. Each of these five bands involve a mixture of  $\nu(\text{C-O})$ ,  $\nu(\text{C-C})$  stretching and  $\text{CH}_2$  rocking ( $\rho$ ) motions in different proportions.<sup>74</sup>

The helical conformation provides a better match for the position of the IR active transitions (opened circles in Figure 4.8(b)) than the planar conformation. This observation suggests that gauche kinks often occur in PEG chains. Because the helical chain represents characteristic interactions involving gauche sites, it is likely that irregularities in the gauche site appearance will not affect much the general trends found in the helical conformation calculations. Therefore, even if the macroscopic chain structure is far from being an ideal  $7_2$  helix, its chain states are likely better represented by the helical conformation.

#### 4.3.5. Relaxation pathways of the chain states

To better understand energy exchange between the chain states, the relaxation pathways originating from various initially excited chain states were computed. A recently developed approach for modeling intramolecular vibrational energy redistribution (IVR) in molecules was used, which employs a Marcus-type Fermi-golden rule treatment for vibrational transitions, uses third-order anharmonic force constants, DFT-computed for the molecule in vacuum, and relies on low frequency modes of the molecule itself to serve as a bath.<sup>41, 65</sup> The computed IVR rates between modes  $i, j$ , and  $k$ ,  $i \rightarrow j + k$  and  $i + j \rightarrow k$ , were used to follow energy relaxation and transport. Details of this method can be found in Chapter 3.5.3.

A 3-unit PEG oligomer adopting a  $7_2$  helical conformation and terminated with azido and carboxylic acid moieties (azPEG3a, Figure 4.9(a)) was chosen for the task. The

calculated waiting time dependence of the excess population of one of the brightest chain modes,  $1120\text{ cm}^{-1}$ , is shown in Figure 4.9(d) (red). The population decay is dominated by a single exponential component of 0.74 ps, assigned to its lifetime, having about 97% contribution accompanied by a slow component of about 8.0 ps with 3% contribution (Figure 4.9(d)). The computed lifetime matches well the experimental lifetimes of the bright chain states, which are about 1 ps (Table 4.2,  $\tau_1$ ).

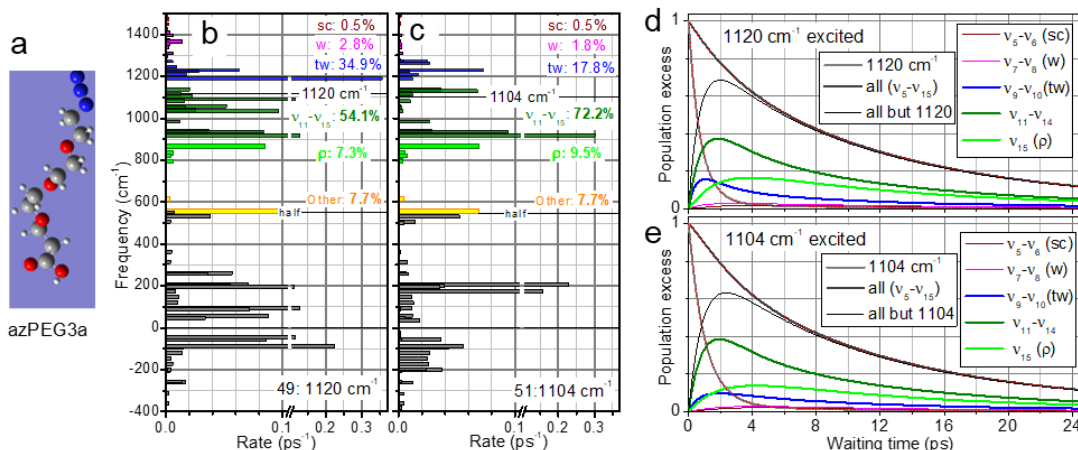


**Figure 4.9.** (a). DFT optimized structure of azPEG3a in the helical conformation, used for the relaxation dynamics analysis shown in this figure. (b,c) Graphically presented relaxation pathways for two excited bright chain states of (b) 1120 cm<sup>-1</sup> and (c) 1104 cm<sup>-1</sup> frequencies. For every product of the  $i \rightarrow j + k$  reaction, occurring with the rate constant of  $k_{i/jk}$ , where mode  $i$  is the initially excited mode, the bars of the length  $k_{i/jk}(1+n_k)(1+n_j)$  were added at  $\omega_j$  and  $\omega_k$ , where  $n_m$  is the thermal population of mode  $m$ . For every relaxation channel  $i + k \rightarrow j$ , having a rate constant  $k_{ik/j}$ , where  $i$  is the initially excited mode, the bars of the length  $n_k * k_{ik/j}$  were added at  $\omega_j$  and  $-\omega_k$ . The states of different chain bands are color coded and labeled in the inset. The percent numbers by the band labels are the total rates in percent that lead to populating the states of the selected group of states (bands),  $(\sum_{\text{within group}} k / \sum_{\text{all pathways}} k) \times 100\%$ , where  $k$  is the rate of a relaxation pathway involving the tag mode. d&e). Relaxation dynamics in azPEG3a followed excitation of the states at (d) 1120 cm<sup>-1</sup> and (e) 1104 cm<sup>-1</sup>. Population excess of the initially excited modes (red), and their fit with a double-exponential function (d) 0.8 ps (96%) and 10 ps (4%) components and (e) 0.8 ps (96%) and 10 ps (4%) components) are shown. The sum of the population excesses of all states of the indicated band(s) are shown separately. Thick black line shows the population excess dynamics of all states of the  $v_5 - v_{15}$  bands; thin black line shows the population excess of all states within these bands except the initially excited state.

All relaxation channels of the modes at 1120 and 1104 cm<sup>-1</sup> are shown graphically in Figure 4.9(b) and (c), respectively. The bar-length for a given mode represents the overall rate of all relaxation channels populating this mode as a result of relaxation of the tag (see details in the Figure 4.9 caption). All states of the same band, or group of bands, are colored the same and labeled in the inset. Relative contributions of the overall relaxation pathways populating the states of a specific group are shown with percent

numbers as inset. As apparent from the graphs, the tag relaxation predominantly populates the chain states, which are close in energy to that of the tag. For example, relaxation rates into bands  $\nu_9$  and  $\nu_{10}$  (tw) and  $\nu_{11}$ – $\nu_{15}$  ( $\nu_{C-O}$ ,  $\nu_{C-C}$ , and  $\rho_{CH_2}$ ) comprise 89 and 90% of all the rates for the 1120 and 1104  $\text{cm}^{-1}$  tags, respectively (Figure 4.9(b,c)). Only about 7.7% of all pathways lead to a loss of a population from the  $\nu_5$  to  $\nu_{15}$  bands. As a result, the overall excess population in all  $\nu_5$ – $\nu_{15}$  states  $Popul. excess(T) = \sum_{800 < \omega_j < 1500 \text{ cm}^{-1}} (n_j(T) - n_j^{eq})$ , where  $n_j(T)$  and  $n_j^{eq}$  are the populations of mode  $j$  at time delay,  $T$ , and at thermal equilibrium, decays much slower, showing a mean decay component of about 10 ps (Figure 4.9(d,e), black lines). Excess populations in different groups of states (bands) are shown in Figure 4.9(d,e). Dynamics originating from other chain state tags in the 900–1300  $\text{cm}^{-1}$  region yielded similar results.

The results indicate that even though the relaxation time of individual chain states of the  $\nu_9$ – $\nu_{14}$  bands is rather short, computed as 0.74 and 1.0 ps for the modes at 1120 and 1104  $\text{cm}^{-1}$ , respectively, the relaxation occurs predominantly into the states of the  $\nu_9$ – $\nu_{15}$  bands. The excitation equilibration within the  $\nu_5$ – $\nu_{15}$  bands requires several relaxation steps, each taking about 1 ps, and is largely completed by 3–4 ps (Figure 4.9(d,e)). Note that due to their high energy, the wagging and scissoring modes contribute little, with their overall excess population of less than 0.03.

Interestingly, the dynamics of the overall population excess for the two initially excited modes (Figure 4.9(b-e)) are very similar, despite different lifetimes of the two modes (0.74 and 1.0 ps) and different initial rate patterns (Figure 4.9(b,c)). This is explained by a prompt equilibration within the chain bands. The equilibration time, which can be taken as the waiting time at which the maximum population is observed, varies for

different bands (Figure 4.9(d,e)). The longest equilibration time is found for the rocking band ( $\sim 4$  ps), suggesting that the lifetimes of its states are also long. The relaxation dynamics of the individually excited rocking band states were calculated, confirming the prediction.

The calculations show that the lifetimes of the rocking states within azPEG3a vary substantially between 1.5 and 3.2 ps (Figure 4.10), such that the states with larger delocalization feature longer lifetimes, while more end-group localized states feature shorter lifetimes. Such end-group influence will be diminished with an increase in the chain length, and more states of the  $\nu_{15}$  band are expected to have long lifetimes of about 3 ps.

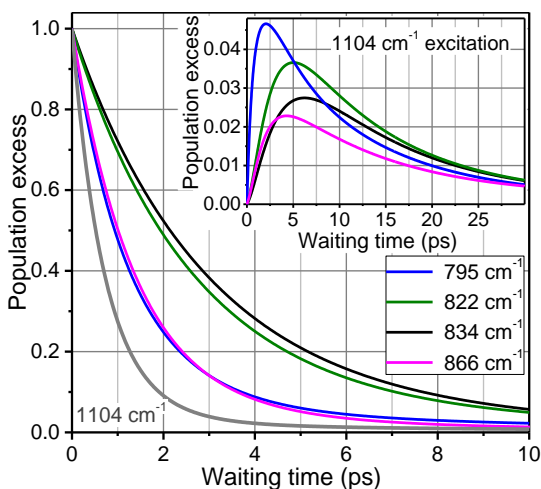


**Figure 4.10.** Population excess dynamics of four states of the  $\nu_{15}$  band of azPEG3a at 866, 834, 822, and 795  $\text{cm}^{-1}$  followed excitation of each state. The relaxation of the state at 1104  $\text{cm}^{-1}$  is shown for comparison (grey line). The fast components of the double-exponential fit, attributed to the mode lifetimes, are 1.2, 2.5, 2.9, and 1.4 ps for the kinetics at 866, 834, 822, and 795  $\text{cm}^{-1}$ , respectively; the amplitude of the fast component exceeds 87% for all kinetics. The inset shows population excess dynamics in the same four states of the  $\nu_{15}$  band following excitation of the 1104  $\text{cm}^{-1}$  state.

Next we will compare the computational predictions with the experimental diagonal and cross peak dynamics of the chain states. At a glance, the calculated chain

state dynamics are in agreement with the experiments on dynamics of the bright chain states (Figures 4.6 and 4.7). Indeed, the fast component of the chain state diagonal peaks dynamics ( $\sim 1$  ps, Figure 4.6(b,c)) matches the calculated lifetimes. The slow component of the diagonal peaks (Figure 4.6(b,c)) is about 10–15 ps, which matches the time for which the excess population survives within the  $\nu_9$ – $\nu_{15}$  bands (Figure 4.9(d,e)), thus, suggesting that the tail in the decay in Figure 4.6(b,c) is due to coupling of the studied mode with other modes within the  $\nu_9$ – $\nu_{15}$  bands. The maximum in the cross-peak dynamics of the chain states (Figure 4.7) is reached at about 3 ps (Table 4.3), which matches the computed mean equilibration times of 2–2.5 ps (Figure 4.9(d,e), thin black line).

To compare the calculations and the experiment, observed kinetics of diagonal- and cross-peak amplitudes were computed as  $S_r(T) = \sum_j (n_j(T) - n_j^{eq}) \Delta_{rj}$ , where  $n_j(T)$  is a population of mode  $j$  at time delay  $T$  after excitation of a tag mode  $i$ ,  $r$  is the reporter mode number, and summation is taken over all modes in the molecule.<sup>37, 41, 80</sup> Selected cross and diagonal peak kinetics originated from excitation of the tags at 1120 and 1104  $\text{cm}^{-1}$  are shown in Figure 4.11. The diagonal peaks (black lines) were fitted with the double-exponential function resulting in two components of 1.6 ps (58% contribution) and 13.7 ps (42%). The time constants and the contributions are comparable to the experimental values (Table 4.2), confirming that the slow component is originated from population of other states of the  $\nu_9$ – $\nu_{15}$  bands.

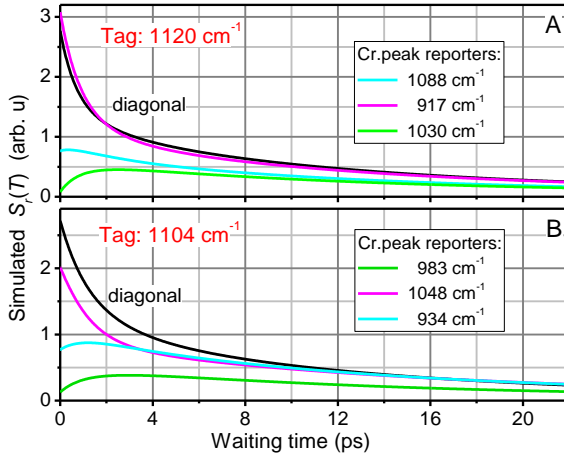


**Figure 4.11.** Simulated diagonal- and cross- peak amplitude waiting time dependences for chain states of azPEG3a for two chain-state tags at (a) 1120  $\text{cm}^{-1}$  and (b) 1104  $\text{cm}^{-1}$ . Both diagonal signals (blue lines) were fitted with a double exponential function, resulting in essentially the same component: the fast component of ca. 1.6 ps and slow component of ca. 13.7 ps with a contribution of ca. 42%. Some cross-peak kinetics show just decays (magenta), whereas others show a growth (cyan, green) followed by the decay with a peak at ca. 1-3 ps.

The cross-peak kinetics (Figure 4.11) also show at least two characteristic components. Although all modes except the tag itself experience a growth in population with time ( $n_j, j \neq i$ ), many of the computed kinetic traces,  $S_r(T)$ , show only a decay (Figure 4.11) originated from a strong coupling of the tag and reporter ( $\Delta_{ir}$ ). The reporters with weaker coupling to the tag,  $\Delta_{ir}$ , show a growth of the signal (Figure 4.11, cyan, green line) with  $T_{\text{max}}$  within the window of 1 - 3 ps, which matches the experiment.

The modeling of the chain state dynamics helped in deciphering the chain band properties, which determine the transport mechanisms supported by each band. To understand and describe the energy transport via the chain, it is essential to know how the excess energy enters the chain from the end groups.

#### 4.3.6. Relaxation pathways of the end-group tags

Relaxation pathways for the excited  $\nu(\text{N}\equiv\text{N})$  and  $\nu_{\text{as}}(\text{C}=\text{O})$  end-group tags were computed for azPEG3a, adopting a 7<sub>2</sub>- helical conformation. The  $\nu(\text{N}\equiv\text{N})$  mode decays predominantly ( $\sim 96\%$ ) into  $\nu(\text{N}\equiv\text{N})$  and  $\nu(\text{N}-\text{C})$  modes at 1269 and 910  $\text{cm}^{-1}$ , respectively (Figure 4.12(a)), with the computed rate of  $(0.51 \text{ ps})^{-1}$ , which is about 2-fold faster than the experimental value of  $(1.1 \text{ ps})^{-1}$ . Expectedly, the relaxation pathways are found to be essentially the same as those in the azido-terminated alkanes.<sup>22</sup> The  $\nu(\text{N}\equiv\text{N})$  and  $\nu(\text{N}-\text{C})$  mode frequencies are shown in Figure 4.8(a) with orange bars. The  $\nu(\text{N}\equiv\text{N})$  mode overlaps with the  $\text{CH}_2$  twisting band of the chain ( $\nu_9$ ) and is capable of generating a wave packet in this band.

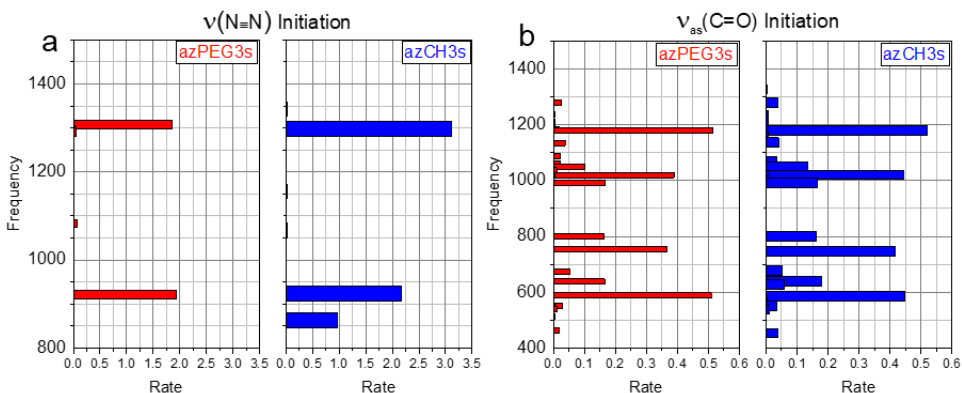


**Figure 4.12.** Modeled IVR pathways of azPEG3s and azCH3s. (A) All IVR pathways from the  $\nu_{\text{as}}(\text{C}=\text{O})$  between both azCH3s and azPEG3s are very similar. (B) All IVR channels from  $\nu(\text{N}\equiv\text{N})$  (into  $\text{N}=\text{N}$  and  $\text{C}-\text{N}$ ) are the same between azPEG3s and azCH3s.

The calculations based on third-order coupling (IVR) show efficient relaxation channels from  $\nu(\text{N}\equiv\text{N})$  into two modes of the twisting band,  $\nu_9$  and  $\nu_{10}$ , with the rates of 0.6 and 0.7  $\text{ps}^{-1}$  contributing 30% over all relaxation channels of  $\nu(\text{N}\equiv\text{N})$  (Figure

4.13(a)). The relaxation channels populating states of  $v_{11}-v_{15}$  contribute 31% over all relaxation channels of  $v(N\equiv N)$ , which includes the channels populating  $v_{15}$  at 2.1%.

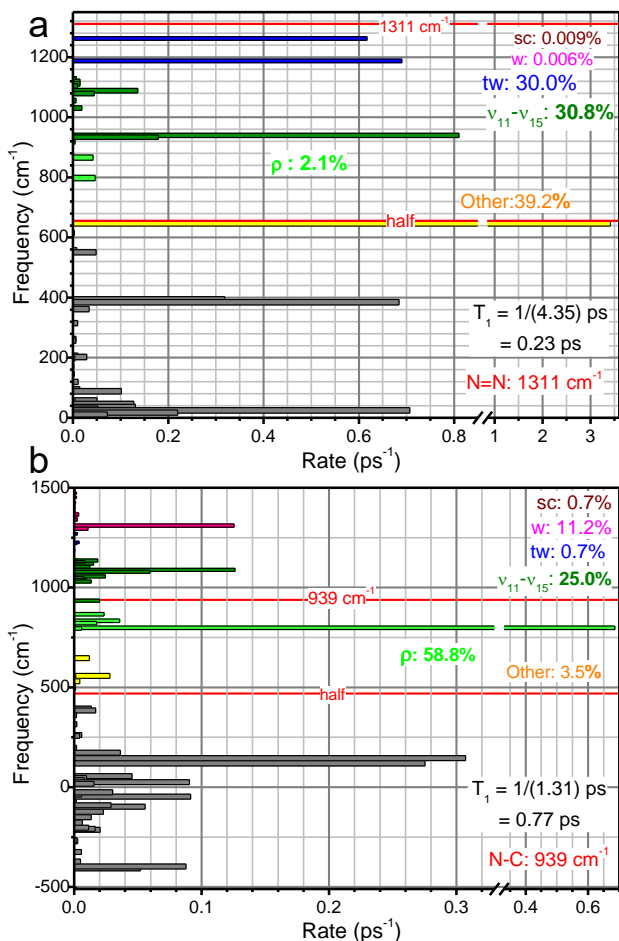


**Figure 4.13.** Graphically presented relaxation pathways for (a) the excited  $v(N\equiv N)$  and (b) the excited  $v(N-C)$  mode in azPEG3a. See the caption of Figure 4.9 for details of computations. The states of different chain bands are color coded and labeled in the inset; the percent numbers by the band labels are the total rates in percent that lead to populating the states of the selected group (bands).

The  $v(N-C)$  mode,  $939\text{ cm}^{-1}$ , overlaps partially with the  $v_{14}$  band, involving C–O and C–C stretching and  $\text{CH}_2$  rocking motion (Figure 4.8(b)). The relaxation IVR pathways of the  $v(N-C)$  mode lead to populating the  $v_{15}$  rocking band states (59%), the

states of  $\nu_{11}$ – $\nu_{14}$  bands (25%), and the wagging band states (11%, Figure 4.13(b)); all these bands may transfer energy ballistically.

The relaxation pathways of excited  $\nu_{as}(C=O)$  were found to be very similar to those determined for the alkane chains (Figure 4.12(b)), as they all are localized at the succinimide ester moiety and change little when the attached chain is modified.<sup>22</sup> The calculated  $\nu_{as}(C=O)$  lifetime of 0.75 ps matches the experiment well.

The analysis of the relaxation pathways in alkanes revealed that there are only two doorway states at the ester site which have sufficiently high energy to relax efficiently into the optical bands of the chain; those states are the stretching modes of the ester,  $\nu(NOC)$  and  $\nu(OC)$  (Figure 4.8(a)). It was concluded that for the ballistic transport in alkane chains, initiated by  $\nu_{as}(C=O)$ , the excess energy enters the chain via the two excited doorway states. The same main relaxation pathways into the attached PEG chains are expected in azPEGn. The  $\nu(NOC)$  and  $\nu(OC)$  modes overlap with the  $\nu_{13}$  chain band capable of generating a wave packet (Figure 4.8(b)).

#### 4.4. Discussion

There are many chain bands capable of transferring energy in PEG chains initiated by  $\nu(N\equiv N)$  or  $\nu_{as}(C=O)$  excitation. The twisting band,  $\nu_9$ , can be efficiently excited by the  $\nu(N\equiv N)$  relaxation. The  $\nu(C-O)$  containing bands,  $\nu_{11}$ – $\nu_{15}$ , can be efficiently excited by relaxation of both end groups. Energy exchange between the chain states can populate the wagging modes,  $\nu_7$  and  $\nu_8$ . Each band can transfer energy either ballistically or diffusively, depending on its properties. Next we discuss the requirements for the ballistic transport in PEG chains and features of the diffusive transport.

#### 4.4.1. Transport regimes in PEGs: from ballistic transport to directed diffusion

The energy transport through PEG features constant speed and exponential distance dependence of the transport efficiency.<sup>50</sup> There are two energy transport mechanisms satisfying such conditions, ballistic and directed diffusion regimes, which are discussed in this section.

Ballistic energy transport is a special transport regime that requires two conditions: the vibrational modes transporting energy should be delocalized over the whole region of the transport and the dephasing time of the chain states should be long enough to allow coherent wave packet propagation. The ballistic transport efficiency decays exponentially with the dephasing time,  $\tau_{\text{deph}}$ , proportionally to the fraction of wavepackets surviving dephasing,  $S(T) = S_0 \exp(-T/\tau_{\text{deph}})$ ; here  $S_0$  is the number of initially formed wave packets. If the transport time is shorter than the dephasing time, very small energy losses are observed as most wave packets remain phased and deliver energy ballistically. When the transport time is longer than the dephasing time (large transport distances), the efficiency of the transport is reduced as fewer wave packets reach the target. The transport mechanism can still be ballistic if the competing diffusive transport is even less efficient.

The transport efficiency in the ballistic regime decays exponentially as a function of transport distance,  $L$ , as  $S(L) = S_0 \exp(-L/L_0)$ , with the decay factor,  $L_0$ , given by the mean free path (MFP) distance. The transport efficiency in PEG chains decays exponentially with distance with  $L_0 = 15.7 \pm 1 \text{ \AA}$ .<sup>49</sup> If the transport is ballistic, the MFP distance is related to the dephasing time, as  $L_0 = \tau_{\text{deph}} v_{\text{gr}}$ , where  $v_{\text{gr}}$  is the group

velocity of the transport. Using the experimental transport speed of  $5.5 \text{ \AA/ps}$ , the dephasing time of  $2.9 \text{ ps}$  is obtained. Note also that the width of the chain band transferring energy ballistically with  $5.5 \text{ \AA/ps}$  speed should be no less than  $30 \text{ cm}^{-1}$ .<sup>50</sup>

The requirements for fully ballistic transport are very stringent and, as we will show, are not satisfied for all chain bands for all transport lengths up to azPEG12. Diffusive transport then occurs, which can have several flavors. If the chain states are fully delocalized across the transport region, but the dephasing time is too short to permit fully ballistic transport to the desired distance, the transport can be thought as involving multiple events of a wave packet scattering in the forward and backward directions which would result in diffusive nature of the overall transport. The transport speed under diffusive conditions, in general, decreases with distance and the transport efficiency does not decay exponentially. However, a directed diffusion regime can occur if losses from the chain are significant so that only forward scattering events would result in delivering a significant amount of energy to the end of the chain.<sup>81</sup> Under such conditions, the transport occurs with an approximately constant speed and the transport efficiency decays exponentially with distance, as observed experimentally. As we will discuss in detail in Chapter 4.4.4, the transport speed depends on the width of the chain band transferring energy, as well as on the rates of chain dephasing and cooling.

Another regime of energy transport can occur when the delocalization of the chain state is limited and does not cover the whole transport distance. Under conditions of partial delocalization, which can occur in chains with strong inhomogeneity, energy hopping between different regions of delocalized states is required to transfer energy over the whole chain length. Such transport can show ballistic character within each region of

delocalization, although as a whole it is diffusive. Again, directed diffusion can occur under conditions of substantial energy losses from the chain resulting in constant transport speed and exponential dependence of the transport efficiency over distance. The transport speed under such conditions will be affected by a hopping rate between the sites of partial delocalization as well as by the speed within delocalized regions.

#### 4.4.2. Properties of various PEG chain bands

The chain band properties, such as delocalization extent, chain-state lifetimes, and dephasing times, determine which transport regime can be supported by a given chain band. We discuss separately three relevant groups of PEG chain bands: twisting bands  $\nu_9$  and  $\nu_{10}$ ; experimentally accessed  $\nu(\text{C-O})$  containing bands  $\nu_{11}$ – $\nu_{14}$  and predominantly  $\text{CH}_2$ -rocking band,  $\nu_{15}$ .

***CH<sub>2</sub> twisting bands,  $\nu_9$  and  $\nu_{10}$ .*** These modes are considered separately, as one of them,  $\nu_9$ , is in resonance with the  $\nu(\text{N}\equiv\text{N})$  state of the azido moiety, populated via  $\nu(\text{N}\equiv\text{N})$  tag relaxation. The overall width of the  $\nu_9$  band is  $33\text{ cm}^{-1}$ , supporting a wave packet group velocity of  $6.0\text{ Å/ps}$ , in agreement with the experiment ( $5.5\text{ Å/ps}$ ). This match alone, however, is not a proof that energy is transported ballistically via  $\nu_9$ . The lifetimes, calculated for the  $\nu_9$  band states in the helical azPEG3a, range between 0.6 and 1.2 ps with a mean value of 1.03 ps. Even if the pure dephasing is small, the total dephasing time cannot exceed about 2 ps, which is capable of supporting ballistic transport in chain lengths not exceeding eight PEG units.

***$\nu(\text{C-O})$  containing bands,  $\nu_{11}$ – $\nu_{14}$ .*** Short lifetimes measured for selected states of the  $\nu_{11}$ – $\nu_{14}$  chain bands ( $\sim 1\text{ ps}$ ) and computed for other states of the bands (also  $\leq 1\text{ ps}$  for the

majority of the states) suggest that these states can support ballistic transport only to chain lengths substantially shorter than that of PEG12. Preliminary measurements of the total dephasing times for the C2–C4 chain states suggest that they are about 0.7–1 ps, which results in a pure dephasing time of 1.1–2 ps. These total dephasing time values are about 3-fold shorter than the time permitting the ballistic regime in PEG12 (2.9 ps). Thus, we conclude that, under the conditions of these experiments, the  $\nu_{11}$ – $\nu_{14}$  bands cannot support the ballistic regime for all studied chain lengths.

**Rocking band,  $\nu_{15}$ .** The lifetimes of the  $\nu_{15}$  rocking band states were computed and found to be rather long varying from 1.5 to 3.2 ps in azPEG3a. A correlation between the delocalization extent and the lifetime is found: the mean participation number for the two long-lived states (2.2 out of 3 in azPEG3) is much larger than the mean participation number for the two short-lived states (1.2). This result suggests that most states of the  $\nu_{15}$  band are long-lived in compounds with longer chains where the influence of the end groups is strongly reduced. It is conceivable that the pure dephasing time of the  $\nu_{15}$  states will also be long, correlating with its lifetime, analogous to that in other  $\nu(\text{C–O})$  containing bands ( $\nu_{11}$ – $\nu_{14}$ ). Therefore, these states can potentially transfer energy ballistically in chains even longer than PEG12. The speed of the ballistic transport supported by this band depends strongly on the chain conformation and can reach 17 Å/ps in the  $7_2$ - helical and 5.5 Å/ps in the planar conformations. Unfortunately, the frequencies of these states are too low to be accessed experimentally with the available 2DIR instrument.

#### 4.4.3. Delocalization extent in chains with alternating coupling strength

Delocalization extent is an important parameter for every chain state. It can be affected by chain disorder, including the disorder associated with variations in the chain conformation. In addition to a sufficiently long dephasing time of the energy transporting band, ballistic transport requires delocalization of the chain states over the region of the transport. Static disorder experienced by the chain can result in a reduced delocalization length.

The strength of the neighboring group interactions determines how broad the chain band is and how susceptible it is to disorder and localization. The bandwidth also determines the maximum group velocity supported by the band in the ballistic energy transport regime. As opposed to homogeneous chains, such as alkane chains consisting of groups of a single type ( $\text{CH}_2$ ), the PEG chain has a heteroatom in its unit cell, oxygen, which makes the couplings of two  $\text{CH}_2$  groups across the oxygen atom much smaller than that among the two neighboring  $\text{CH}_2$  groups. Therefore, the PEG chain bands associated with the  $\text{CH}_2$ -bending motion of different types (sc, w, tw, and  $\rho$ ) are characterized by an alternation of the coupling strength: strong-weak-strong and so on. For example, the  $\text{CH}_2$  twisting modes are characterized by the neighboring  $\text{CH}_2$  group coupling of about  $83 \text{ cm}^{-1}$ , while it is only about  $6 \text{ cm}^{-1}$  across the oxygen atom (both values are given for the all-anti conformation). The coupling constants between the neighboring  $\text{CH}_2$  groups for  $\text{CH}_2$  sc, w, tw, and  $\rho$  modes are listed in Table 4.5.

**Table 4.5.** Coupling constants computed for the neighboring CH<sub>2</sub> groups,  $\beta_1$ , and CH<sub>2</sub> groups across the oxygen atom,  $\beta_2$ , in PEG chains for the relevant anti and gauche conformations. The site energies for the gauche and anti-conformations at the C-C bond are given ( $\omega_g$  and  $\omega_a$ ).

	$\beta_1$ (cm <sup>-1</sup> ) H <sub>2</sub> C-CH <sub>2</sub> , anti	$\beta_1$ (cm <sup>-1</sup> ) H <sub>2</sub> C-CH <sub>2</sub> , gauche	$\beta_2$ (cm <sup>-1</sup> ) H <sub>2</sub> C-O-CH <sub>2</sub> , anti-anti	$\omega_a$ (cm <sup>-1</sup> ) anti	$\omega_g$ (cm <sup>-1</sup> ) gauche
CH <sub>2</sub> scissoring	5	6	12	1481	1480
CH <sub>2</sub> wagging	73	79	31	1284	1315
CH <sub>2</sub> twisting	83	113	6	1240	1208
CH <sub>2</sub> rocking	49	30	16	914	896

To understand the expectations for the chain bands with an alternating coupling pattern, we solved an eigen-value problem for a simple one-dimensional chain of  $N$  coupled states,  $N = 12$ , for which the nearest-neighbor coupling alternates along the chain between strong ( $\beta_1$ ) and weak ( $\beta_2$ ; Figure 4.14(a)). The eigen states of such a chain are split into two bands, with the splitting between the band centers of  $2\beta_1$  (Figure 4.14). The spread of the state energies in each band is determined by the coupling in the weaker pair,  $2\beta_2$ . Interestingly, if a next-nearest interaction,  $\chi$ , is introduced into the Hamiltonian, it causes asymmetry of the slopes in the two bands and can cause one of the bands to have a negligibly small width, while the other band will feature about  $4\beta_2$  bandwidth (Figure 4.14(c,d)). The presence of a weak link, a small  $\beta_2$  coupling, makes the chains more susceptible to disorder, which will be discussed in the next section.

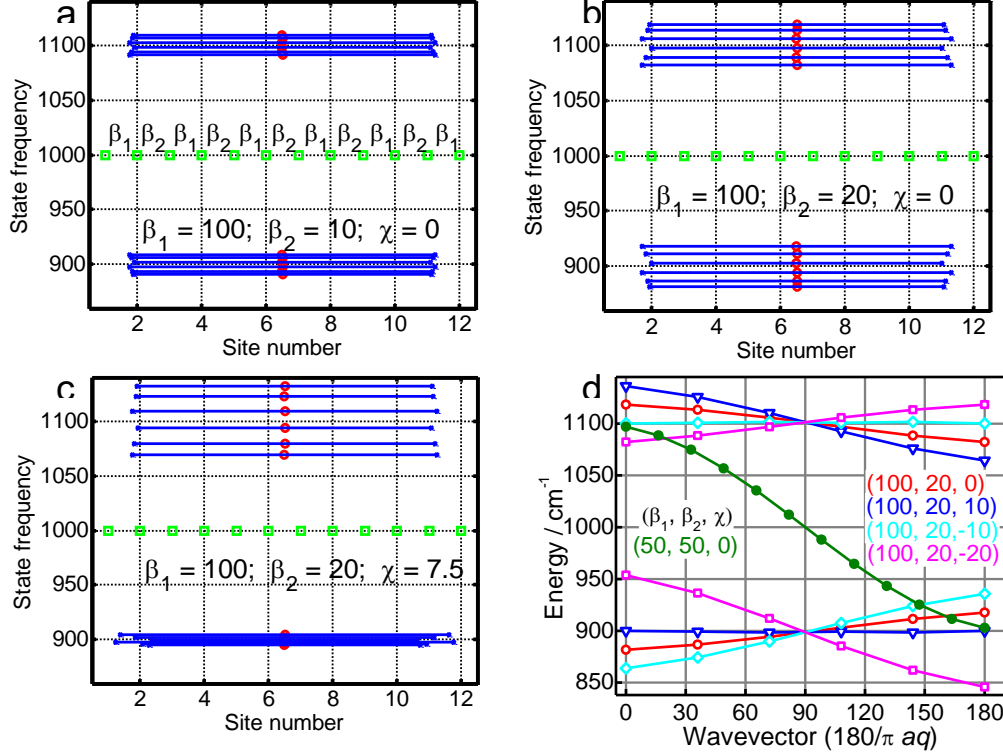


**Figure 4.14.** Graphically presented frequencies and delocalization for a linear chain of 12 states coupled with site energies of  $1000 \text{ cm}^{-1}$  (green squares) and nearest-neighbor coupling strength alternating between  $\beta_1$  and  $\beta_2$ , as shown in panel A. A uniform next-neighbor coupling  $\chi$  is applied. The values in wavenumbers for  $\beta_1$ ,  $\beta_2$ , and  $\chi$  used for each calculation are shown in the insets. The length of the error bars for each state equals to  $\pm(\text{PN}-1)/2$ , where PN is the participation number for the state.

#### 4.4.4. Energy transport modeling

Here we present a theoretical model for describing mixed ballistic and directed-diffusive energy transport mechanisms, which is then applied to the transport via  $\nu_9$  -  $\nu_{14}$  and  $\nu_{15}$  bands.

**Details of the model.** The vibrational energy transport was modeled by solving the quantum Bloch-Liouville equation for a density matrix,  $\hat{\rho}$ , for a linear chain of  $N$  coupled states:<sup>81</sup>

$$\frac{\partial \rho_{mn}}{\partial t} = \frac{i}{\hbar} [\hat{\rho}, \hat{H}]_{mn} - \gamma \rho_{mn} - W(1 - \delta_{mn}) \rho_{mn} - \frac{k}{2} (\delta_{mN} + \delta_{Nn}) \rho_{mn} \quad (4.1)$$

Here  $W$  is a decoherence rate due to dynamic disorder,  $\gamma$  is the relaxation time,  $k$  is the relaxation rate from the  $N$ -th site, and  $\delta_{mn}$  is a Kroneker symbol. The Hamiltonian,  $\hat{H}$ , is defined as:

$$\hat{H} = \sum_{m=1}^N \hbar \omega_m \hat{b}_m^\dagger \hat{b}_m + \frac{\hbar \Delta}{2} \sum_{m=1}^{N-1} (\hat{b}_m^\dagger \hat{b}_{m+1} + \hat{b}_m \hat{b}_{m+1}^\dagger) \quad (4.2)$$

where  $\omega_m$  are site energies,  $\Delta$  is the coupling, and  $\hat{b}_m^\dagger, \hat{b}_m$  are the creation and annihilation operators. The site energies are taken to be delta-correlated,  $\langle \delta \omega_m(0), \delta \omega_n(t) \rangle = \frac{W}{2} \delta(t) \delta_{mn}$  implying that the chain bandwidth,  $\Delta$ , is smaller than the thermal energy, so that  $\langle \omega_m \rangle = \omega$ .<sup>82</sup> Note that the Hamiltonian includes only harmonic terms and transitions associated with anharmonicity and interactions with the solvent are incorporated phenomenologically via relaxation coefficients  $\gamma, k$ , and  $W$ . An energy “trap” is introduced as an additional site, representing the end group and a reporter. It is populated irreversibly from the  $N^{\text{th}}$  state and relaxes as

$$\frac{\partial \rho_s}{\partial t} = k \rho_{NN} - \kappa \rho_s \quad (4.3)$$

Here  $\rho_s$  is the probability of finding excitation on the trap state and  $\kappa$  is its relaxation rate. The model implies the low temperature case,  $k_B T \ll \hbar \omega$ , such that the thermal excitations of vibrational states can be neglected and the only excitation in the chain is caused by the external laser pulse. The femtosecond laser pulse is assumed to be short on the time scale of the density matrix evolution, so the initial excitation is introduced by initial conditions:

$$\begin{aligned} \rho_s(0) &= \delta_{m1} \delta_{n1} \\ \rho_s(0) &= 0 \end{aligned} \quad (4.4)$$

The population at the  $m^{\text{th}}$  site is described by the diagonal element of the density matrix,  $\rho_{mm}(t)$ . The model was applied to describe the end group to end group and end group to chain state transports. For the latter, the cross-peak amplitude was associated with a collective population of all chain states:

$$P_{\text{br}}(t) = \sum_{m=2}^N \rho_{mm}(t) \quad (4.5)$$

This model can simultaneously describe ballistic and diffusive transport regimes; it can also indicate a transition between these limiting cases. To describe the transport via different chain bands, different sets of parameters,  $W$ ,  $\gamma$ ,  $\kappa$ ,  $k$ , and  $\Delta$ , need to be selected. Below we discuss separately the transport through  $v_9$ – $v_{14}$  and  $v_{15}$  bands.

**Transport via  $v_9$ – $v_{14}$  bands.** As detailed in chapter 4.3.3, the lifetimes of several  $\nu(\text{C-O})$  containing chain states were determined as about 1 ps. The calculations showed that their relaxation predominantly populates the states within the same band and the states of the bands close in energy (Figure 4.9(b,c)); only a small fraction of the excess population escapes the bands. These relaxation processes are treated within the model as dephasing,  $W$ , as different chain states, in addition to frequency, differ in wavevector and phase. The total dephasing time for selected chain states was evaluated to be about 1 ps as well. Therefore, the dephasing rate,  $W + \gamma$ , was fixed at  $(1 \text{ ps})^{-1}$ . The relaxation rate,  $\gamma$ , of the chain states describes how quickly the band loses energy. The value of  $\kappa$  was kept at  $(15 \text{ ps})^{-1}$  to match the overall cooling of the end group. The value to  $k$  was fixed at  $(1 \text{ ps})^{-1}$ , but the results are not very sensitive to this value. Therefore, only three parameters,  $\Delta$ ,  $W$ , and  $\gamma$ , remained to fit the experiments. The following experiments were modeled simultaneously: the chain length dependences of  $T_{\text{max}}(L)$  for the end group to end group (Figure 4.15(a,b), main panels) and end group to chain states (Figure 4.15(a,b), top panels),

as well as the chain length dependence of the transport efficiency between the end groups,  $P_{\max}$  (Figure 4.15, insets). The model showed a good agreement with all three experimental data sets for  $\Delta = 6.5 \text{ cm}^{-1}$  and  $\gamma = 0.19 \text{ ps}^{-1}$ , recovering the transport speed of  $5.5 \text{ Å/ps}$  and the decay parameter,  $L_0$ , of  $16 \text{ Å}$  (Figure 4.15(a)). The  $T_{\max}$  values for the end group to chain transport show minimal chain-length dependence with the value of about  $1.3 \text{ ps}$  (Figure 4.15(a), top panel). This value should be compared to the mean  $T_{\max}$  observed in the experiment ( $\sim 2.5 \text{ ps}$ ) minus the  $\nu(\text{N}\equiv\text{N})$  lifetime ( $1.1 \text{ ps}$ ), resulting in about  $1.4 \text{ ps}$ . Although the model is too simple to describe variations in  $T_{\max}$  for different bands (states), it predicts essentially no dependence of  $T_{\max}$  over the chain length, matching well the experiment. The width of a chain band can be approximated as  $4\Delta$ , resulting in  $26 \text{ cm}^{-1}$ , which matches the computed mean bandwidth for the  $\nu_9$ – $\nu_{14}$  bands of  $28.7 \text{ cm}^{-1}$ .<sup>74</sup>

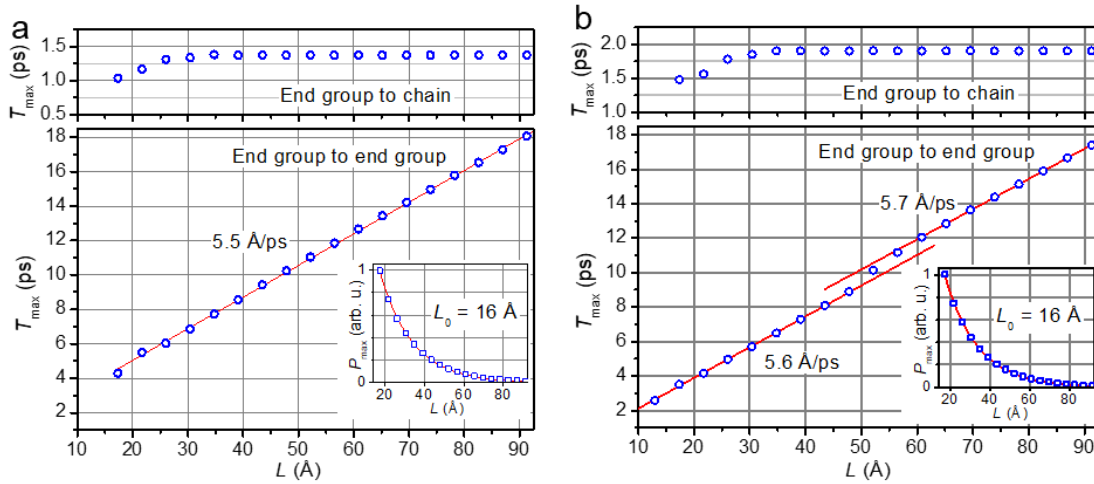


**Figure 4.15.** (a) Dependences of  $T_{\max}$  vs. chain length for the end group to end group (main panels) and end group to chain state (top panels) energy transport computed for  $N = 2 - 19$ ,  $W = (0.81 \text{ ps})^{-1}$ ,  $\gamma = 0.19 \text{ ps}^{-1}$ , and  $\Delta = 6.5 \text{ cm}^{-1}$ . A linear fit over the range with  $N = 3 - 19$  is shown with a red line resulting in the inverse slope of  $5.5 \text{ Å/ps}$ . Inset shows the length dependence of the transported energy,  $P_{\max}$ . Best fit with an exponential function,  $P_{\max}(L) = P_{\max}(0)\exp(-L/L_0)$ , is shown with red line and resulting  $L_0$  value is indicated. To match the experimental tag-reporter distances, the length was calculated as  $L = 13 \text{ Å} + a(N - 1)$ . (b) Same dependences as in (a) computed for the transport through the  $\nu_{15}$  band using the following parameters:  $N = 2 - 19$ ,  $W = (4.5 \text{ ps})^{-1}$ ,  $\gamma = 0.22 \text{ ps}^{-1}$ , and  $\Delta = 4.3 \text{ cm}^{-1}$ . Linear fits over the range with  $N = 1 - 9$  and  $N = 12 - 20$  are shown with red lines having the inverse slopes of  $5.6$  and  $5.7 \text{ Å/ps}$ , respectively.

**Transport via  $\nu_{15}$  band.** To model the transport via the  $\nu_{15}$  band, we first fixed the sum of  $W$  and  $\gamma$ , representing the dephasing at  $(3.0 \text{ ps})^{-1}$  and found, as expected, fully ballistic transport (see chapter 4.4.1). Here we present the results of calculations where the dephasing  $(W + \gamma)$  was set to  $(2.3 \text{ ps})^{-1}$ , which demonstrates clearly a switch between two regimes, ballistic and directed diffusion. The best match with the experiment was found with  $W = (4.5 \text{ ps})^{-1}$ ,  $\gamma = 0.22 \text{ ps}^{-1}$ , and  $\Delta = 4.3 \text{ cm}^{-1}$ . A clear kink in the  $T_{\max}$  versus  $L$  is seen for the end group to end group transport at about  $50 \text{ Å}$ , indicating a transition from the ballistic regime at smaller chain lengths to the directed diffusion regime at larger chain lengths. Interestingly, the transport speeds before and after the

transition are essentially the same (Figure 4.15(b), red fit lines in main panel), which is explained by the common nature of the transport with the transport rate determined by the same coupling,  $\Delta$ , and suppression of longer transport pathways, involving scattering, by the relaxation. The transport before the kink is characterized by free wave packet propagation with losses ( $\gamma$ ) but without scattering. The wave packet scattering introduces additional losses, but the speed remains the same as the wave packets scattered in the forward direction deliver most of the energy to the target (directed diffusion regime).

Interestingly, the computations with different decoherence rates  $W$  of  $(0.81 \text{ ps})^{-1}$  and  $(4.5 \text{ ps})^{-1}$ , resulted in different coupling values,  $\Delta$  (Figure 4.15(a,b)). We associate this effect with the difference between the mean group velocity for the band and its maximum group velocity. Indeed, the group velocities for different parts of the band are different as the dispersion relations are not linear (Figure 4.8). For example, the dispersion relations for a linear chain with only nearest neighbor interaction is described as  $\hbar\omega_i \sim \cos(q_i a)$ , where  $q_i$  is the mode  $i$  wavevector.<sup>83</sup> It seems that pure ballistic transport occurs at the group velocity close to the maximum, while the directed diffusion regime involves dephasing and relies on a group velocity better weighted across the band, the mean group velocity.

***Structural Inhomogeneity of PEG Chains.*** The effect of static disorder on mode localization is discussed in this section. There are three main contributions causing disorder for a molecule in the condensed phase: conformational disorder of the molecule, interactions with the solvent (matrix), and thermal fluctuations of populations of low-frequency modes of the molecule. In solution, the latter two often result in fluctuations that are fast on the time scale of the transport, contributing to dephasing. The disorder

associated with diversity of the PEG chain site conformations is truly static on the time scale of the transport. While for periodic conformations (all-anti, anti-anti-gauche, etc.), full delocalization of the chain states is expected, a state localization may occur in structurally disordered chains.

The above modeling assumes a fully periodic chain with no static disordering but with dynamic disorder across the transport region. Nevertheless, static disorder, including structural irregularities of the chain, can result in spatial localization of vibrational modes at sizes smaller than the chain length. Each backbone atom of a PEG chain (carbon or oxygen) is  $sp^3$  hybridized, resulting in a possibility of an anti or gauche conformation for every bond of the backbone. Preliminary analysis of mode localization in response to structural irregularity of the chains revealed several important points. First, we found that a gauche kink at the C–O bond introduced into an all-anti PEG chain results in energy raise,  $\Delta E_{CO}$ , of about  $520 \text{ cm}^{-1}$ , which is large and limits strongly the amount of such kinks. Introduction of the second C–O gauche kink caused about twice higher energy penalty. A persistence length of the chain without C–O kinks estimated as  $L_{C-O} = a/2 * \exp(\Delta E_{CO}/k_B T)$ , where  $a$  is the unit cell length ( $4.35 \text{ \AA}$ ), the factor of 2 reflects the presence of two C–O bonds per unit cell, and  $T$  is the temperature, results in  $L_{C-O} \sim 27 \text{ \AA}$ . At the same time a single gauche kink at a C–C bond costs only about  $78 \text{ cm}^{-1}$ , which suggests that such kinks can easily occur. The persistence length of the chain without C–C kinks  $L_{C-C} = a * \exp(\Delta E_{CC}/k_B T) \sim 6.5 \text{ \AA}$  is small, suggesting that they may occur more readily. Gauche kinks themselves can result in normal-mode localization, unless a periodic conformation is formed. For example all periodic structures, including  $7_2$  helical,

feature full delocalization (at least on the length scale of interest).<sup>84</sup> Nevertheless, some chain irregularities result in a substantial localization.

Our analysis performed on a limited set of conformations indicates that a single gauche kink at the C–O bond on an all-anti chain conformation causes a substantial localization for all modes related to the C–H bending motion but marginally affects the modes with significant  $\nu(\text{C–O})$  and  $\nu(\text{C–C})$  contributions,  $\nu_{11}$ – $\nu_{14}$ . A single gauche kink at the C–C bond, when placed not at the center of the oligomer, results in a substantial localization (Figure 4.16(b)). The localization increases further if an additional C–C kinks are introduced, in a fashion that no conformational regularity is formed in the short chain under question (Figure 4.16(c)). As expected, introduction of a single gauche kink precisely in the middle of an oligomeric chain does not reduce delocalization as a regular (pseudo periodic) type of structure is formed. Interestingly, the delocalization for some bands involving  $\nu(\text{C–O})$  and  $\nu(\text{C–C})$  ( $\nu_{11}$ – $\nu_{13}$ , Figure 4.16(b,c)) and for the  $\text{CH}_2$  wagging bands ( $\nu_7$  and  $\nu_8$ ) is affected little by the C–C kinks.<sup>23</sup> While the detailed analysis of structural distribution of the PEG chains is beyond the scope of this study, an additional observation on the localization style is essential.

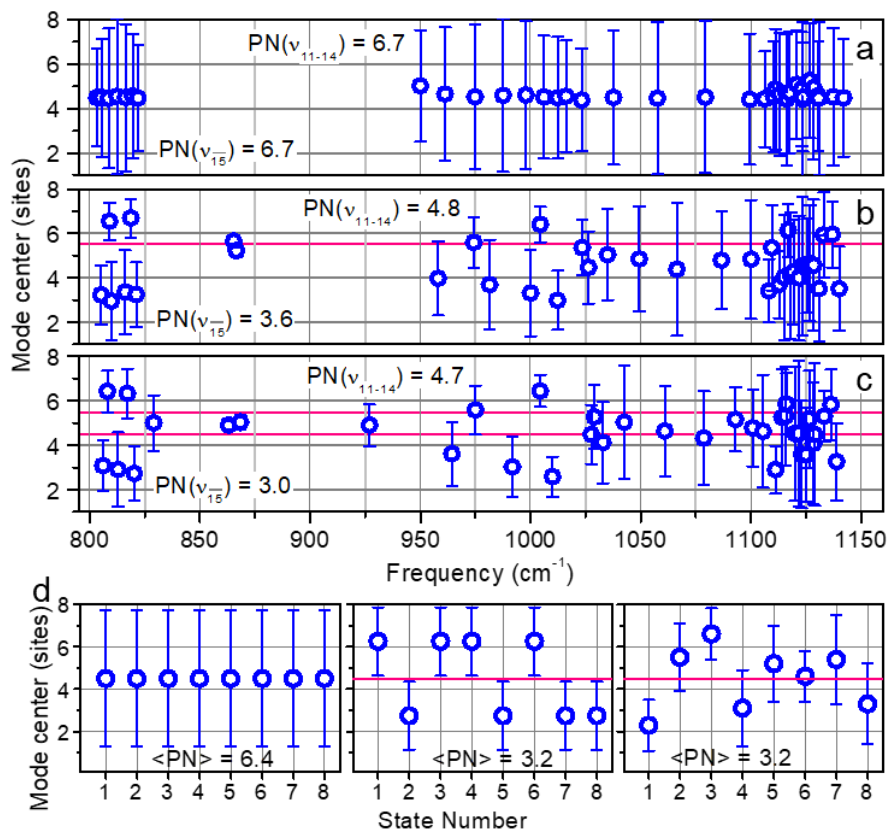


**Figure 4.16.** (a-c) Location and delocalization extent for the DFT-computed  $\nu_{11}$ -  $\nu_{15}$  normal modes of PEG-8 for three chain conformations. (a) all-anti chain conformation; (b) single gauche kink at a C-C bond at the all-anti conformation; (c) two gauche kinks at the all-anti conformation. The positions of the kinks are shown with red lines. Delocalization for each mode, characterized by a participation number, is shown with error bars of  $\pm (PN-1)/2$  length. (d) Cartoon, illustrating different delocalization scenarios for coupled eigenstates of a chain of eight sites by showing their centers and participation numbers, PN (error bars of  $\pm (PN-1)/2$  length). (left) Fully delocalized states in the chain featuring no structural inhomogeneity; (middle) Type I structural kink; (right) Type II structural kink. The positions of the kinks are shown with red lines.

One could imagine two types of localization in response to a single structural kink. The kink of the first type results in a full breakdown of delocalization so that all states are split into two groups; the states centered before the kink and those centered after the kink are delocalized within either side of the kink, and these groups of states do not overlap. The second type involves the states with reduced delocalization, but they

overlap heavily with no separation into two groups. A cartoon illustrating the two limiting cases is shown in Figure 4.16(d). Our calculations show that structural inhomogeneity of the PEG chain results in the states of the second type if they are considered collectively ( $\nu_7$ – $\nu_{15}$ ), as many states are delocalized across the kink(s). The energy transport would need to be modeled as hopping if the first type of delocalization prevails. The transport involving states of the second type can be modeled using the theoretical approach described above.

***Energy transport in the presence of inhomogeneity.*** In the presented theoretical model, the relaxation channels between different chain states were treated as dephasing ( $W$ ). The dephasing rate for the  $\nu_9$ – $\nu_{14}$  bands was taken at  $(1 \text{ ps})^{-1}$ . The distance passed by a wave packet moving with the speed of  $5.5 \text{ Å/ps}$  during 1 ps time is  $5.5 \text{ Å}$ , which is smaller than the persistence length for C–O kinks. Under such conditions, the chain inhomogeneity minimally affects the modeling results as the states dephase (relax to other chain states) more often than get scattered by inhomogeneity. The dephasing destroys the phase coherence and consequently leads to localization. Although in the model the normal modes are fully delocalized statically, they show dynamic localization on the distances that are either shorter or approaching the estimated persistence lengths for the PEG chain. This similarity suggests that the structural inhomogeneity contributes significantly to the state localization in PEGs; it results in constraining the distance for which the ballistic energy transport can occur.

The long-lived states of the  $\nu_{15}$  band are affected strongly by the structural inhomogeneity of the chain, as suggested by the calculations presented in Figure 4.16(b,c). If so, the ballistic transport, predicted by the modeling in Figure 4.15(b), will

be further suppressed by the inhomogeneity. Because this band will be more efficiently populated with the reduction of temperature one would expect that the transport rate should decrease with decreasing the temperature in contrast with the standard trend in regular systems. A low-temperature study is expected to be instrumental in probing the effect of static inhomogeneity.

#### 4.5. Conclusions

PEG chains belong to a large class of chains where the unit cell consists of at least two different backbone atoms and the coupling strength between the site states alternates along the chain. Peptide and protein chains also belong to this chain type.<sup>1</sup> In such molecules, high-frequency modes are localized at physiological temperatures and energy transport is diffusive<sup>85-86</sup> with the rate limited by IVR.<sup>87</sup> For example, recent calculations of the band structure in polyamides indicated a weak delocalization of high-frequency modes due to weak intersite mode coupling in comparison to the site inhomogeneity. The objective of this study is to understand the transport mechanism in PEG chains. Contrary to alkanes, the transport speed in PEG chains was found to be the same when initiated by the  $\nu(\text{N}\equiv\text{N})$  tag of the azido moiety or by  $\nu_{\text{as}}(\text{C}=\text{O})$  tag of the NHS ester. Several chain states were interrogated by RA 2DIR providing ample data on the involvement of the probed chain states in the transport. The results indicate that the probed chain states are capable of supporting the ballistic transport regime only within distances of about 10 Å at room temperature. The modeling, involving ballistic and diffusive mechanisms, results in a good match to the experimental observations for all studied chain lengths. The parameters of the transport are such that the directed diffusion regime dominates in longer chains. While this study shows with certainty that the chain states in the

1050–1160  $\text{cm}^{-1}$  region cannot support fully ballistic transport at room temperature, it is still not certain that such transport is not supported by other chain bands. In particular, computations show that the states of the  $\nu_{15}$  band, involving mostly  $\text{CH}_2$  rocking motion, have significantly longer lifetimes ( $\sim 3$  ps). Such long lifetimes are sufficient to support fully ballistic transport in chains up to PEG12, assuming that the dephasing times for these modes are long as well. While the lifetime values for the  $\nu_{15}$  band states are appropriate for transferring energy ballistically to large distances, inhomogeneity associated with chain conformation variations is found to be significant. Thorough structural analysis is required to quantitatively address the amount of conformational inhomogeneity and its influence on the chain band properties. It is certain that the very nature of the PEG chains, having a heteroatom in the unit cell and featuring alternating coupling strengths, results in higher sensitivity of their chain bands to the conformational inhomogeneity, compared to alkane chains, for example.

Low-temperature experiments can potentially clarify the contributions of different chain bands to the transport. The lifetimes of all chain band states, especially those of  $\nu_{15}$ , are expected to increase dramatically at low temperatures as the relaxation channels involving low frequency modes will be shut down. The pure dephasing time will also be longer at low temperatures. However, the presence of structural inhomogeneity may enhance chain state localization. Our preliminary calculations show that different bands are affected differently by structural inhomogeneity. It is conceivable that the transport regime may change at low temperatures, resulting in ballistic transport with higher speed and efficiency.

## 4.6. Theoretical Methods

### 4.6.1. Modeling of the dispersion relations of the optical bands in the all-anti PEG conformation

Consider a  $\text{H}_2\text{C-O-CH}_2$  unit cell of a PEG chain. A 21-dimensional displacement vector is introduced as  $\mathbf{x}_k$  for the atoms pertaining to the  $k^{\text{th}}$  unit cell (3 Cartesian coordinates  $\times$  7 atoms = 21 degrees of freedom). The Hessian matrix of this system is split into segments  $H(k, n)$ , 21-by-21 matrices corresponding to harmonic interaction between the  $k^{\text{th}}$  and  $n^{\text{th}}$  unit cells.

The Hamiltonian can be represented as

$$H = \frac{1}{2} \sum_k \left\{ \mathbf{p}_k^\dagger \mathbf{M}^{-1} \mathbf{p}_k + \mathbf{x}_k^\dagger \mathbf{A} \mathbf{x}_k + \mathbf{x}_k^\dagger \mathbf{B}^\dagger \mathbf{x}_{k-1} + \right. \\ \left. \mathbf{x}_k^\dagger \mathbf{B} \mathbf{x}_{k+1} + \mathbf{x}_k^\dagger \mathbf{C}^\dagger \mathbf{x}_{k-2} + \mathbf{x}_k^\dagger \mathbf{C} \mathbf{x}_{k+2} \right\} \quad (4.6)$$

where  $\mathbf{A} = H(k, k)$ ,  $\mathbf{B} = H(k, k + 1)$ ,  $\mathbf{C} = H(k, k + 2)$ ,  $\mathbf{p}_k$  is the momentum vector, and  $\mathbf{M}$  is the 21-by-21 diagonal matrix of atomic masses. Periodic boundary conditions were implemented for simplicity.

**Dispersion relations.** The chain band calculations for the all-anti conformer of PEG was performed using the Hessian matrix obtained from the DFT calculation of an all-anti PEG chain with 8 PEG units. The details of the calculation are presented in section 3.5.1. The symmetry properties of the Hessian are such that the four lowest frequency bands,  $i = 18 - 21$ , provides acoustic bands ( $\omega_i(0) = 0$ ), whereas other bands are optical ( $\omega_i(0) \neq 0$  for  $i = 1 - 17$ ). The lattice period was taken to be  $a = 4.35 \text{ \AA}$ .

Figure 4.8(a) of the main text shows optical bands for  $i = 5 - 15$ , labeled as  $\nu_{5-15}$ , and each band is represented by a different color. Each band contains vibrations of the same character, as outlined in Table 4.4. The bands are plotted as a function of the phase-difference, defined as  $qa$  times  $180/\pi$  and ranging between  $0 - 180^\circ$ .

#### 4.6.2. Group velocity calculations

Details of the group velocity calculations can be found in section 3.5.2. The mean group velocities, computed for whole bands, are given in Table 4.4.

#### 4.6.3. Mode coupling evaluation for CH<sub>2</sub> modes of the alkane and PEG unit cell

The strength of the nearest neighbor coupling,  $\beta_1$  and  $\beta_2$ , of the CH<sub>2</sub> rocking, wagging, twisting, and scissoring modes in a PEG chain was evaluated by DFT normal mode analysis of a quasi-alkane,  $H_{iso}H_2C-CH_2H_{iso}$  and a quasi-PEG ( $H_{iso}H_2C-O-CH_2H_{iso}$ ) unit cells. The coupling in the former structure is characteristic of  $\beta_1$ , the coupling of neighboring CH<sub>2</sub> groups in PEG, whereas the coupling of the latter structure is characteristic of  $\beta_2$ , the coupling among the CH<sub>2</sub> groups across the oxygen atom. Here an artificial hydrogen isotope of 300 amu,  $H_{iso}$ , was used to avoid additional vibrational modes in the frequency region of interest ( $800 - 1600\text{ cm}^{-1}$ ). For the two compounds in the all-anti conformations, the splitting among the normal modes of the same type provided the couplings: the splitting equals to the  $2\beta$ , where  $\beta$  is the coupling (Table 4.5). A gauche kink results in deviations of the two site energies and a more involved approach was used to determine the couplings.

The coupling was evaluated by simultaneously scanning the masses of two hydrogen atoms of the same CH<sub>2</sub> unit using the mass-normalized Hessian and detecting

the frequency jump of the  $\nu(\text{CH}_2)$  normal mode of the same type (rocking, twisting, etc.) as the two modes of the same type pass each other in resonance. Again, the frequency jump is equal to  $2\beta$ .<sup>88</sup> A similar approach was used previously where the strength of an external electric field was changed to shift the energy of one state with respect to another.<sup>89</sup> The results of the calculations are shown in Table 4.5.

#### 4.6.4. Calculating mode centers for normal modes of a PEG chain

The calculations are based on the normal-mode DFT calculations for the PEG molecule, providing displacements of each atom in the PEG backbone for every normal mode (Figure 4.14 and 4.16(a-c)). The mode center represents the “center of mass” for the motion at different sites along the chain. A molecular axis,  $\xi$ , was introduced along the chain that follows the C-C-O backbone.  $\xi$  coordinates of each backbone atom were evaluated using the DFT computed structure. The  $\xi$  coordinates for the hydrogen atoms of each methylene group were taken to be the same as the  $\xi$  coordinate of their carbon atom. The coordinate of the center of a selected mode was computed as:

$$\xi_C = \sum_i \xi_i (dx_i^2 + dy_i^2 + dz_i^2) / \sum_i (dx_i^2 + dy_i^2 + dz_i^2) \quad (4.7)$$

where,  $i$  runs over all atoms of the chain (not in the whole molecule),  $dx_i$ ,  $dy_i$ , and  $dz_i$  are the displacements for this normal mode.

## Chapter 5.

### **Ballistic transport of vibrational energy through an amide group bridging alkyl chains**

The work presented in this chapter has been submitted for publication: Layla N. Qasim, E. Berk Atuk, Andrii O. Maksymov, Janarthanan Jayawickramarajah, Alexander L. Burin, Igor V. Rubtsov

#### **5.1. Introduction**

The field of molecular electronics, conceptualized in the 1970's, has gained increasing interest in the recent years.<sup>90</sup> Continuous miniaturization of electronic circuits, as predicted by Moore's law, is expected to reach the transistor densities of  $10^{11}/\text{cm}^2$  by the year 2020, resulting in individual elements sizes of  $10\text{ nm}^2$ , making them comparable to molecular sizes. Although the miniaturization of such electronics has great potential in device processing speeds, memory capacity, and sensing ability, there are many practical issues that make it difficult to harness their maximum potential. One such difficulty is the heat management of such densely packed environments; effective heat dissipation is critical to the performance of such devices.<sup>8-9, 92-95</sup> Light-weight organic structures are attractive for heat management, including heat dissipation, although pure organic materials are generally poor thermal conductors.<sup>96-99</sup> However there are exceptions, for example ordered low density polyethylene fibers have shown to have very high thermal conductivity and they are most effective in conducting heat along the fibers.<sup>62, 100-101</sup> Other organic

polymeric structures demonstrate a strong dependence of the thermal conductivity on the structure.<sup>92, 102-106</sup> A fundamental understanding of the relationship between molecular structure and conductivity is necessary for developing polymeric materials for molecular electronics.

Numerous molecular systems were interrogated using the RA 2DIR technique, including molecules with dissimilar functional group along the molecular backbone,<sup>24, 107</sup> and molecules with oligomeric backbones. The transport via several oligomeric chains, PEG,<sup>23</sup> alkane,<sup>22, 36</sup> and perfluoroalkane,<sup>51-52</sup> was found to occur ballistically, although to different maximal chain length.<sup>38</sup> In addition, the energy transport speed was found to be dependent not only on the chain type but also on the way the energy is introduced into the chain. For example, when the transport via alkyl chain is introduced by exciting the  $\nu_{N3}$  mode at  $2100\text{ cm}^{-1}$  on the azido moiety, the speed of  $14.4 \pm 2\text{ Å/ps}$  results, where as a speed of  $8.0 \pm 0.3\text{ Å/ps}$  was obtained and by exciting the C=O of the carboxylic acid ( $1712\text{ cm}^{-1}$ ) or the asymmetric C=O stretching mode of the NHS ester ( $1740\text{ cm}^{-1}$ ).<sup>22</sup> The difference in speeds was associated with involvement of different optical bands of the chain, which support different group velocities.

Whereas the energy transport via purely periodic oligomeric chains was studied in detail for a number of chains, the transport via chains with incorporated perturber, an alien group placed in the middle of the chain, has not been studied. It is not known how such perturber group will change the regime of energy transport across the whole compound and under what conditions the ballistic transport regime across the perturber can be achieved. It is also not known how to preserve high transport efficiency and if the interaction at the perturber moiety can modify the transport speed and efficiency.

In this study an amide group was selected as a perturber linking two alkyls chains consisting of 4, 7, and 11  $\text{CH}_2$  units terminated by an azido group on one side and 4  $\text{CH}_2$  units terminated by the methyl ester moiety on another side ( $\text{Am}n\text{-}4$ ,  $n = 4, 7, 11$ , Figure 5.1 A). Various RA 2DIR measurements were performed to interrogate the energy transport across the whole molecule and between the end groups and the amide (Figure 5.1 B, arrows). A combination of theoretical analysis of the alkane chain bands and modeling of the intramolecular vibrational relaxation (IVR) pathways of the initially excited states permitted the identification of the energy transporting chain states. The experimental and computational methods used are described in Section 5.2. Section 5.3 separately describes the experimental data for each of the energy pathways studied (Figure 5.1B, arrows), which are then discussed and modeled in Section 5.4.

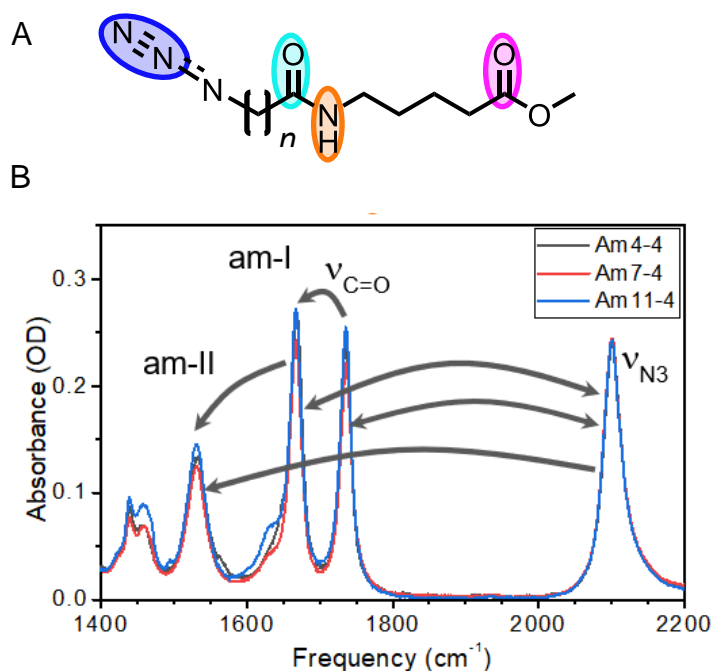


**Figure 5.1.** (A) Structure of  $\text{Am}n\text{-}4$ ,  $n = 4, 7, 11$ . The ovals represent different vibrational modes which were used as tag or reporter modes:  $\nu_{\text{N}_3}$  (blue), am-I (cyan), am-II (orange), and  $\nu_{\text{C=O}}$  (magenta). (B) Solvent subtracted linear infrared spectra of  $\text{Am}n\text{-}4$ ,  $n = 4, 7, 11$ . The arrows indicate the types of energy transport RA 2DIR measurements performed in this study.

## **5.2. Experimental details**

### **5.2.1. Experimental method**

A detailed accounting of the fully-automated 2DIR spectrometer is presented in Chapter 2.7.

### **5.2.2 Sample preparation and characterization.**

The series of alkyl amide compounds denoted as Am4-4, Am4-7, and Am4-11 (Figure 5.1A), were synthesized at Tulane University in collaboration with Dr. Jayawickramarajah. The solvent-subtracted linear absorption spectra of all compounds used in this study are shown in Figure 5.1B. For the spectroscopic measurement the compounds were dissolved in CD<sub>3</sub>CN at concentrations of 30 – 50 mM. The measurements were performed in a 100  $\mu$ m thick sample cell with 1 mm thick BaF<sub>2</sub> windows at room temperature (22.5 °C). The linear absorption spectra of the samples were measured with the Nexus 870 (Thermo Nicolet) FTIR spectrometer.

### **5.2.3. DFT Calculations.**

Geometry optimization, normal mode analysis, and third order anharmonicity calculations were performed using the Gaussian 09 suite using the B3LYP functional and 6-311G(d,p) basis sets. The calculated through-bond distance from the azide-to-amide-I was taken from the nitrogen atom of the azide closest to the alkane chain to the carbon of the amide carbonyl, while the azide-to-amide-II distance was taken to be the distance to the nitrogen of the amide moiety. The azide-to-ester distance was taken to be the distance from the azide to the carbon of the ester group. The calculations were performed in the gas phase.

### 5.3. Results

Figure 5.1B shows the solvent subtracted linear absorption spectra of the three compounds, Am $n$ -4 with  $n = 4, 7$ , and  $11$ , dissolved in CD<sub>3</sub>CN. The stretching mode of the azido moiety ( $\nu_{N_3}$ , 2100 cm<sup>-1</sup>) and the carbonyl stretching mode of the methyl ester ( $\nu_{C=O}$ , 1735 cm<sup>-1</sup>) were used as tags and reporters to study energy transport through the entire molecules, while the amide I (am-I, 1666 cm<sup>-1</sup>) and amide II (am-II, 1535 cm<sup>-1</sup>) modes of the amide group were used for initiating and observing the transport in the middle of the chain. The experiments with  $\nu_{N_3}$  initiation are discussed first, followed by the data for am-I and  $\nu_{C=O}$  initiations.

#### 5.3.1. Energy transport from $\nu_{N_3}$ to the amide moiety

The energy transport initiated by the  $\nu_{N_3}$  tag excitation was recorded by am-I and am-II reporters. Figure 5.2A shows the 2DIR spectrum of Am7-4 focusing on the  $\nu_{N_3}$  / am-II,  $\nu_{N_3}$  / am-I, and  $\nu_{N_3}$  /  $\nu_{C=O}$  cross peaks at the waiting time,  $T$ , of 4.3 ps. Figure 5.2 B shows the projection of the 2DIR spectra onto the  $\omega_t$  axis as a function of  $T$ ; it is apparent that the three cross-peak traces reach the maxima at different waiting times. After the maximum, each trace decays due to dissipation of the excess energy into the solvent.

Examples of the one dimensional waiting-time kinetics, constructed by integrating over the cross-peak area as a function of the waiting time, are shown in Figures 5.2C and 5.2D for  $\nu_{N_3}$  / am-I, and  $\nu_{N_3}$  / am-II, respectively. The waiting time at which the cross-peak amplitude reaches its maximum, denoted as  $T_{\max}$ , was evaluated by a double-exponential fit of the waiting-time kinetics (Figure 5.2C,D, red lines). Each experiment was repeated at least three times and the averaged  $T_{\max}$  values were plotted as a function of the tag-

reporter distance (Figure 5.2E). Both dependences can be fitted well with a linear function (Figure 5.2E); the inverse slope of the fit results in the energy transport speeds of  $13.8 \pm 0.4$  and  $13.9 \pm 0.5$  Å/ps for  $\nu_{N3}$  / am-I and  $\nu_{N3}$  / am-II, respectively (Figure 5.2E). Satisfyingly, the same speed was obtained using both reporters and the speeds match that observed previously for the transport initiated by the  $\nu_{N3}$  mode in alkane chains.<sup>22</sup> Note that the  $T_{\max}$  for the  $\nu_{N3}$  / am-II are offset by ca. 1.6 ps from those for  $\nu_{N3}$  / am-I (Figure 5.2E) for any given compound, suggesting that additional IVR steps at the amide group are required for the excess energy to reach the modes coupled the most to the am-II mode.

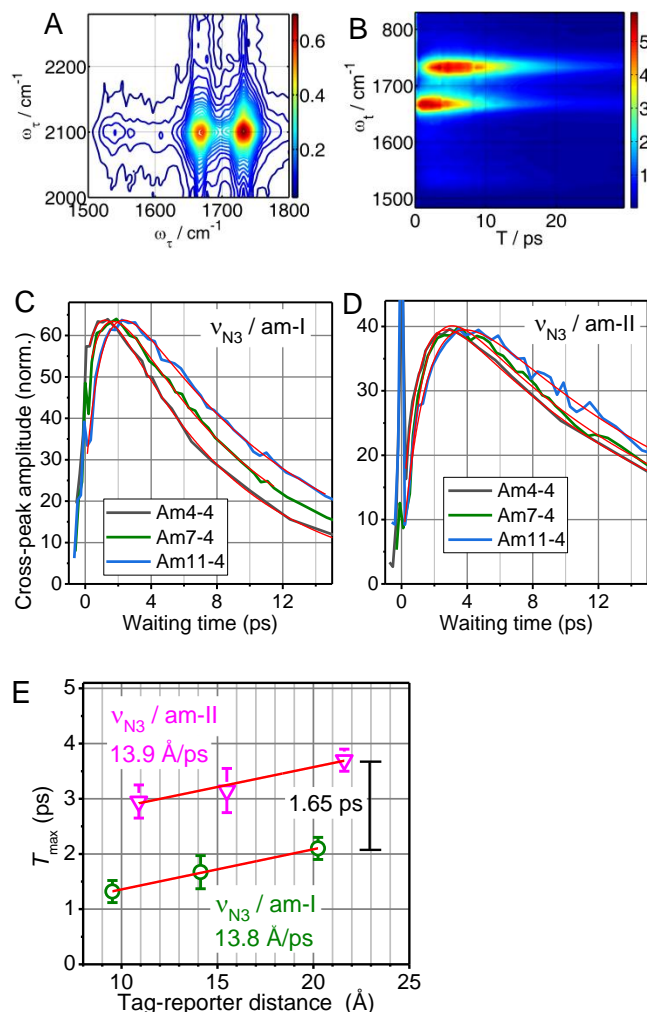


**Figure 5.2.** (A) 2DIR magnitude spectrum of Am7-4 at  $T = 4.3$  ps. From left to right:  $v_{N3}$  / am-II,  $v_{N3}$  / am-I, and  $v_{N3}$  /  $\nu_{C=O}$  cross peaks are seen. (B) 2D waiting time dependence of  $v_{N3}$  / am-II,  $v_{N3}$  / am-I, and  $v_{N3}$  /  $\nu_{C=O}$  (bottom to top) obtained by integrating  $\omega_t$  from 2080 to 2120  $\text{cm}^{-1}$ . (C) Waiting time dependence of the  $v_{N3}$  / am-I cross-peak amplitude for Am4-4 (black line), Am7-4 (green line), and Am11-4 (blue line). The 1-D kinetic traces were fitted with a double exponential function (red lines). The area of integration over the cross peak consisted of  $\omega_t$  from 1650 – 1685  $\text{cm}^{-1}$  and  $\omega_r$  from 2090 – 2110  $\text{cm}^{-1}$ . The  $T_{max}$  is determined for each trace from the fitting. (D) Waiting time dependence of the  $v_{N3}$  / am-II cross-peak amplitude for Am4-4, Am7-4, and Am11-4. The area of integration over the cross peak consisted of  $\omega_t$  from 1520 – 1540  $\text{cm}^{-1}$  and  $\omega_r$  from 2090 – 2110  $\text{cm}^{-1}$ . The fitting of the kinetic traces and  $T_{max}$  consideration is the same as that for panel C. (E)  $T_{max}$  values plotted as a function of tag-reporter distance for the Amn-4 compounds for the transport initiated by  $v_{N3}$  and detected at am-I (green circles) and am-II (magenta triangles). The energy transport speed was calculated as 1/slope of the linear fit (red lines) and resulted in speeds of 13.8 and 13.9 Å/ps for the am-I and am-II reporters, respectively.

### 5.3.2. Energy transport from $\nu_{N3}$ to the ester moiety.

To characterize how rapidly the excess energy absorbed by  $\nu_{N3}$  arrives to another end of the molecule, the  $\nu_{C=O}$  mode of the ester was used as a reporter. The example of 2DIR spectrum featuring the  $\nu_{N3} / \nu_{C=O}$  cross peak and its waiting time dynamics are shown in Figures 5.2A and 5.2B. Figure 5.3A shows the waiting-time traces for the  $\nu_{N3} / \nu_{C=O}$  cross peaks for the three compounds and the fits with double exponential functions (red lines), used to determine the  $T_{max}$  values. The  $T_{max}$  dependence on the tag-reporter distance cannot be well approximated as linear (Figure 5.3B). The  $T_{max}$  obtained for the Am4-4 compound is particularly surprising as the transport time ( $T_{max}$ ) to reach the ester group (3.04 ps) is only slightly larger than the time for arriving to the vicinity of the am-II mode (2.95 ps) (Figure 5.2E). Note that for both longer compounds these two transport times are differing by ca. 1.5 ps.

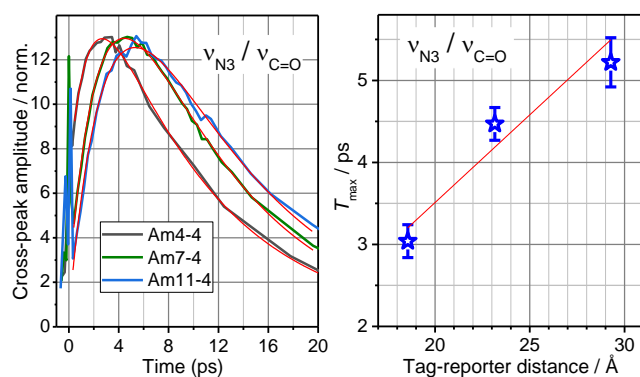


**Figure 5.3.** (A) Waiting time dependence of the  $\nu_{N3} / \nu_{C=O}$  cross-peak amplitude for Amn-4 compounds. The area of integration over the cross peak consisted of  $\omega_t$  from 1725 - 1755  $\text{cm}^{-1}$  and  $\omega_r$  from 2090 - 2110  $\text{cm}^{-1}$  (see Figure 5.2A). (B) The averaged over three or more measurements  $T_{max}$  values for  $\nu_{N3} / \nu_{C=O}$  all Amn-4 compounds and plotted as a function of tag-reporter distance (blue stars). The linear dependence (red line) poorly describes the data.

### 5.3.3. Energy transport from $\nu_{\text{C=O}}$ to the amide group

Energy transport initiated at the ester site with  $\nu_{\text{C=O}}$  excitation was studied with three reporters, am-I, am-II, and  $\nu_{\text{N3}}$ . When the am-I mode was used as a reporter, no rise was found for the  $\nu_{\text{C=O}}$  / am-I cross peak for all three compounds (Figure 5.4), suggesting significant interaction among the involved modes. Such affect was observed previously in various compounds, even for spatially remote groups.<sup>17, 37, 41</sup> The direct interaction of the  $\nu_{\text{C=O}}$  and am-I modes is significant enough that the energy transport from the tag to the amide produces only a slight increase of the  $\nu_{\text{C=O}}$  / am-I cross peak at later times, resulting in a slightly longer  $\nu_{\text{C=O}}$  / am-I cross peak decay dynamics compared to the decay of the diagonal  $\nu_{\text{C=O}}$  peak (1.2 vs. 1,06 ps). The  $\nu_{\text{C=O}}$  / am-II cross peak kinetics (Figure 5.4, blue) also shows a strong direct coupling contribution at  $T = 0$ , although the excess energy arrival does make the cross peak larger. The respective  $T_{\text{max}}$  values for all three compounds appeared to be essentially the same at ca.  $1.33 \pm 0.2$  ps.

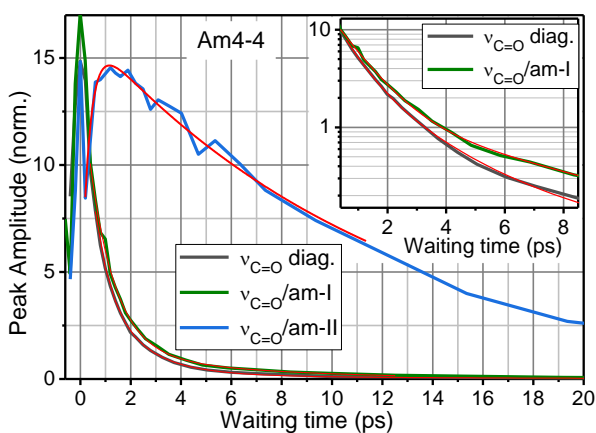


**Figure 5.4.** Waiting time traces of the  $\nu_{\text{C=O}}$  / am-I (green) and  $\nu_{\text{C=O}}$  / am-II (blue) cross and  $\nu_{\text{C=O}}$  diagonal (grey) peaks in Am4-4. The inset zooms in on the early portion of the dynamics. The decay times found from the fit of both the  $\nu_{\text{C=O}}$  diagonal and  $\nu_{\text{C=O}}$  / am-I cross peaks is  $1.0 \pm 0.1$  ps; the slows components of 11 ps (1.4%) and 5.2 ps (10%) were involved in the fit of the respective traces.

**5.3.4. Energy Transport from  $\nu_{\text{C=O}}$  to the azido group** The waiting time dependences of the  $\nu_{\text{C=O}} / \nu_{\text{N}_3}$  cross peak for the three compounds are shown in Figure 5.5A. The  $T_{\text{max}}$  values vary by almost 4 ps between the shortest and the longest compounds; the  $T_{\text{max}}$  time reaches 8 ps for Am11-4. The dependence of  $T_{\text{max}}$  on the tag-reporter distance is strongly non-linear (Figure 5.5B). It is apparent that the shortest compound, Am4-4, behaves drastically different from the other two compounds.

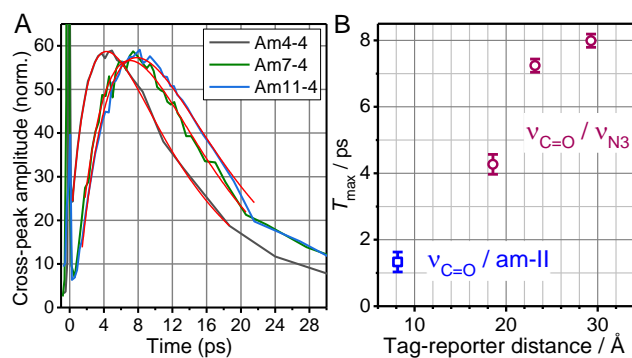


**Figure 5.5.** (A) Waiting time traces of the  $\nu_{\text{C=O}} / \nu_{\text{N}_3}$  cross-peak. The area of integration over the cross peak consisted of  $\omega_t$  from  $1725 - 1745 \text{ cm}^{-1}$  and  $\omega_r$  from  $2090 - 2110 \text{ cm}^{-1}$  (see Figure 5.6A). (B) Tag-reporter distance dependence of the  $\nu_{\text{C=O}} / \nu_{\text{N}_3}$  cross-peaks Amn-4 (mauve circles) and the  $\nu_{\text{C=O}} / \text{am-II}$  cross-peak (blue square).

### 5.3.5. Energy transport from am-I to the azido group

The energy transport in alkane chains initiated by several end groups,  $\text{N}_3$  and  $\text{C=O}$ , resulted in ballistic transport with different speeds to substantial distances.<sup>22, 49-50</sup> However, the transport initiated in alkane chains by an am-I mode is interrogated here for the first time. Examples of the am-I /  $\nu_{\text{N}_3}$  cross peak and the waiting time dependence traces are shown in Figures 5.6A,B. Surprisingly, much larger  $T_{\text{max}}$  values were obtained for the am-

I /  $\nu_{N3}$  cross peak at 4.72, 5.62 and 7.22 ps for the Am4-4, Am7-4, and Am11-4 compounds, respectively (Figure 5.6B,C). The distance dependence of  $T_{\max}$  is found to be linear, resulting in the transport speed of  $4.2 \pm 0.3$  Å/ps (Figure 5.6C).

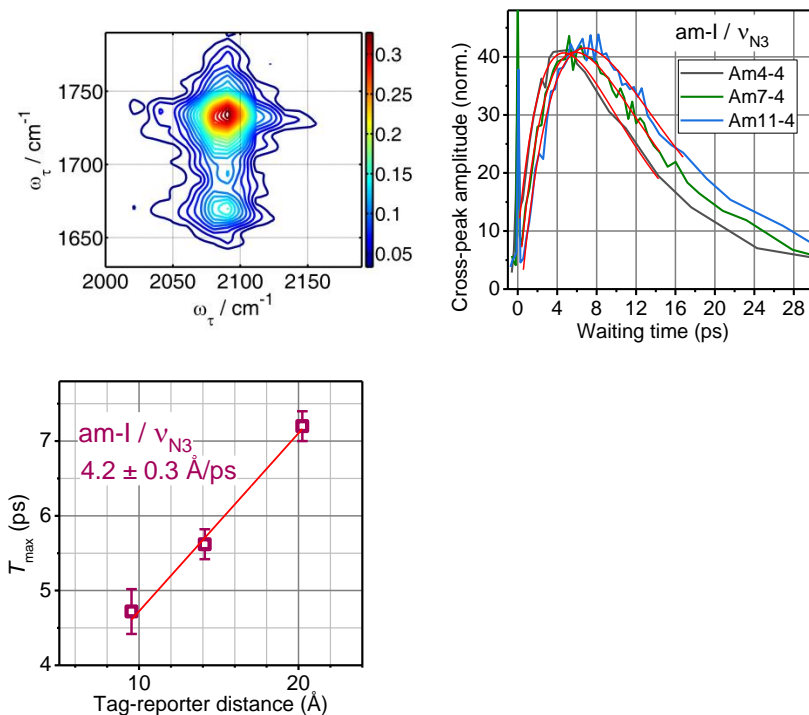


**Figure 5.6.** (A) 2DIR spectrum of Am4-4 at  $T = 6.0$  ps focusing on the am-I /  $\nu_{N3}$  ( $\omega_{\tau} = 1660 \text{ cm}^{-1}$ ) and  $\nu_{C=O} / \nu_{N3}$  ( $\omega_{\tau} = 1750 \text{ cm}^{-1}$ ) cross peaks. The 1D waiting time kinetics in (B) were constructed from the am-I /  $\nu_{N3}$  cross peaks RA2DIR spectra. The  $T_{\max}$  plotted as a function of tag-reporter distance yielded a speed of  $4.2 \pm 0.3$  Å/ps (C) and is described well by a linear fit.

### 5.3.6. Lifetimes of the involved modes

The lifetimes of the  $\nu_{C=O}$  and am-I modes were determined from the waiting dependences of the respective diagonal peaks. An example of the waiting time dependence trace for  $\nu_{C=O}$  is shown in Figure 5.4. The lifetimes of the  $\nu_{C=O}$  and am-I modes were determined at  $1.1 \pm 0.1$  and  $1.04 \pm 0.1$  ps, respectively.

## 5.4. Discussion

The complicated structure of the Amn-4 compounds, in comparison to other fully uninterrupted molecular chains, makes it difficult to describe the transport using the previously developed theoretical methods, including the Fermi's Golden Rule based model for the IVR process<sup>65</sup> and the model involving solution of the Liouville equation for a density matrix<sup>22</sup>, which is applied only to ballistic transport. Our experimental observations suggest that we observe a switch in the energy transport regime at the amide site. Therefore, we have treated different segments of the transport using different theoretical approaches and combined them using the transport time additivity observed previously.<sup>36, 38</sup> Before considering more complex end-to-end energy transport we first discuss the transport between the end groups to the amide group in the Amn-4 compounds, which occurs via uninterrupted alkane chains.

### 5.4.1. Energy transport through a homogeneous alkane chain

#### 5.4.1.1. Transport from the azido group to the amide

The energy transport initiated with  $\nu_{N3}$  in the alkane portions of the molecules with 4, 7, and 11  $\text{CH}_2$  units is detected at the amide moiety using am-I and am-II reporters resulted in a constant speed regime with the speeds of  $13.8 \pm 0.6$  and  $13.9 \pm 0.6$  Å/ps, respectively (Figure 5.2C). The speeds match well the speed of  $14.4 \pm 2$  Å/ps, determined previously for different reporters, the carbonyl stretching mode of the carboxylic acid and asymmetric C=O stretch of the succinimide ester ( $\nu_{\text{as(C=O)}}$ ).<sup>22</sup> The offset in  $T_{\text{max}}$  values of 1.65 ps, found for the am-II reporter, is attributed to additional IVR steps at the amide moiety needed for the energy arrival to the am-II mode vicinity. Indeed, the am-II mode, localized at C-N-H atoms, is farther away from  $\nu_{N3}$  than the am-I mode, localized mostly

at the C=O group. Importantly, the transport does not result in exciting the am-I and am-II modes, but populates the modes coupled strongly to them, thus affecting these reporters via anharmonic interactions. Similar connectivity effects were observed previously for the succinimide ester reporter, where the reporting  $\nu_{\text{as(C=O)}}$  group was ca. 3-4 bonds deep into the end group, away from the alkyl chain end resulting in ca. 3 ps offset for  $T_{\text{max}}$ .<sup>36</sup> An additivity of the transport times via different parts of the molecule was previously observed for several compounds, including the azido-alkyl-succinimide esters.<sup>36, 38</sup> The am-II (and am-I) detection in this study also shows additivity of the transport times. For example, the  $T_{\text{max}}$  of 2.1 ps for the  $\nu_{\text{N3}}$  / am-I cross peak in Am11-4 (Figure 5.2E) involves ca. 1 ps lifetime of the  $\nu_{\text{N3}}$  tag, transport time via the chain of 11 carbons,  $(11 \times 1.5 \text{ \AA}) / 14 \text{ \AA/ps} = 1.2 \text{ ps}$ , resulting in 2.2 ps total time, which is in agreement with the experiment. For the am-II detection an additional time of 1.65 ps have to be added, which corresponds to the energy transport within the amide. This additional time needed for a single IVR step is characteristic and has been observed in other compounds.<sup>24</sup> Note that every point in Figure 5.2E follows the same additivity rules. Similar additivity analysis will help to understand the  $T_{\text{max}}$  values for other results reported in this study.

The transport speeds via  $\nu_{\text{N3}}$  initiation match previously reported studies, indicating the same transport mechanism, which was characterized as the ballistic transport via  $\text{CH}_2$  wagging and twisting bands of the alkyl chain.<sup>22</sup> The alkane band structure, computed using semiempirical force field methods, is shown in Figure 5.7. The initial step of  $\nu_{\text{N3}}$  relaxation populates the  $\nu_{\text{N=N}}$  ( $1340 \text{ cm}^{-1}$ ) and  $\nu_{\text{N-C}}$  ( $943 \text{ cm}^{-1}$ ) modes localized at the azido moiety (Figure 5.7 orange lines). The  $\nu_{\text{N=N}}$  mode is coupled to the twisting and wagging bands supporting the transport with the speed of ca.  $14 \text{ \AA/ps}$ , while  $\nu_{\text{N-C}}$  is coupled to the rocking

modes, potentially supporting a much higher speed of up to 62 Å/ps, which however has not been observed experimentally (Figure 5.7, orange boxes). The suggested reason is a small density of states in the middle of the rocking band for short tested alkyl chains of up to 15 methylene groups.<sup>22</sup>

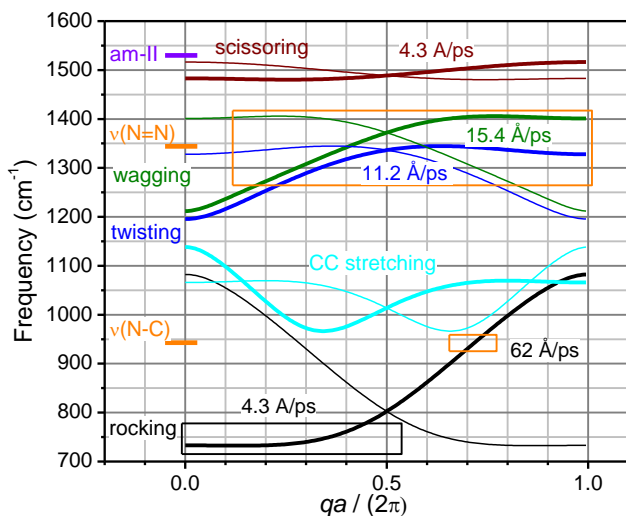


**Figure 5.7.** The dispersion relations of the CH<sub>2</sub> rocking, twisting, wagging, scissoring, and C-C stretching bands for an alkane chain. The orange boxes match the width of the  $\nu_{N=N}$  and  $\nu_{N-C}$  modes of the azide. The group velocity for a narrow range of frequencies centered at  $\nu_0(q_0)$  is determined as  $V_{gr.}(q_0) = (\partial\omega/\partial q)|_{q=q_0}$ , and the mean group velocity over a selected range of wavevectors from  $q_1$  to  $q_2$  was computed as  $\langle V_{box} \rangle = (q_2 - q_1)^{-1} \int_{q_1}^{q_2} |V(q)| dq$ . The transport speeds supported by different portions of the dispersion curves are indicated as insets.

#### 5.4.1.2. Transport from am-I to the azido group

The transport in the alkyl chain initiated by the am-I mode and recorded by  $\nu_{N3}$  occurs with a constant speed of  $4.2 \pm 0.3$  Å/ps (Figure 5.6C). Such transport can be described as ballistic or directed diffusion.<sup>23, 81</sup> The distinction between the two regimes can be made based on the relation of the transport time and the dephasing time of the band states involved in the transport. The transport times can be evaluated simply by dividing

the chain length by the transport speed, resulting in ca. 1.4, 2.5, and 3.9 ps times for Am4-4, Am7-4, and Am11-4, respectively. The dephasing times of the chain states responsible for the transport are unknown, but likely do not exceed 2-3 ps. Assuming it is so, the transport falls into an intermediate regime, which is ballistic at shorter distances and likely diffusive for 16.5 Å chain length of Am11-4. The additivity analysis works well for these  $T_{\max}$  times. For example, the transport time of 5.62 ps for am-I /  $\nu_{N3}$  for Am7-4 (Figure 5.6C) involves the am-I lifetime of ca. 1.04 ps, the transport time of  $(7 \times 1.5 \text{ Å}) / 4.2 \text{ Å/ps} = 2.5 \text{ ps}$ , and the time of 2.2 ps needed to populate the NNN bending modes at the azido end group, population of which results in the strongest perturbation of the  $\nu_{N3}$  reporter.<sup>22, 38 108</sup>

<sup>108</sup> The sum of 5.7 ps matches well the experimental value of 5.62 ps.

An examination of the dispersion relations in Figure 5.7 for the bands supporting such slow speed reveals two candidates. The  $\text{CH}_2$  scissoring band at ca. 1500  $\text{cm}^{-1}$  (unscaled DFT frequencies) supports the speed of 4.3 Å/ps. The bottom portion of the rocking band is also very flat and can support even slower speeds, depending on the frequency range of the band modes involved in the transport. To understand which band of the two is involved, the am-I mode relaxation channels were computed using the previously developed approach based on Fermi's Golden rule and generalized Marcus equation applied to the IVR process, referred here as IVR program.<sup>41, 65, 109</sup> Note that the am-I mode relaxation in *N*-methylacetamide was investigated previously. It was found that when solvated in  $\text{D}_2\text{O}$ , the am-I relaxation is mostly an IVR process (80%) with am-II only participating ca. 7%.<sup>110-111</sup>

Unlike the case for  $\nu_{N3}$  relaxation with a single dominating pathway, numerous relaxation pathways with sizable rates were found for the am-I mode in Am4-4 (Figure

5.9A). Apparent from the graph, no sizable direct population of the CH<sub>2</sub> scissoring band states is found. A large number of pathways, amounting at ca. 31% of all pathway rates, involve the rocking modes of the chain. We will consider the relaxation channels in Section 5.4.3 in greater detail. The relaxation analysis showed a high likelihood of exciting a wavepacket within the low-energy portion of the CH<sub>2</sub> rocking band, which supports small group velocities.

#### 5.4.1.3. Transport from $\nu_{\text{C=O}}$ to the amide.

The transport via alkyl chains, initiated by C=O stretching mode of a carboxylic acid end group, was studied previously and the speed of 8.0 Å/ps was obtained.<sup>22</sup> The same speed is expected for  $\nu_{\text{C=O}}$  initiation in Am $n$ -4, but the situation is complicated by a direct coupling of the  $\nu_{\text{C=O}}$  and am-I modes. While the direct coupling is weak, nonetheless it leads to difficulties of accurately isolating the  $\nu_{\text{C=O}}$  / am-I and am-I /  $\nu_{\text{C=O}}$  cross peaks in the presence of very strong diagonal  $\nu_{\text{C=O}}$  and am-I peaks, their presence is apparent from the slower waiting time dynamics of the cross peak (Figure 5.4). The off-diagonal  $\nu_{\text{C=O}}$  / am-I anharmonicity,  $\Delta(\nu_{\text{C=O}}/\text{am-I})$ , taken from the DFT-computed X-matrix, is 0.011 cm<sup>-1</sup>, which is small, but significant. Notice that no coherent oscillations at the  $\omega_{\text{C=O}} - \omega_{\text{am-I}}$  frequency (70 cm<sup>-1</sup>, expected period 480 fs) were observed, indicating that the coherent transfer between  $\nu_{\text{C=O}}$  and am-I is negligible. An incoherent energy transfer between the modes is also possible, but expected to be slow due to a large energy gap and weak coupling (interaction energy ca. 0.5 – 1 cm<sup>-1</sup>).<sup>29</sup> Nevertheless, such coupling may affect some of the waiting time dependences. For example, the coupling among the  $\nu_{\text{C=O}}$  and am-II modes is also non-negligible with  $\Delta(\nu_{\text{C=O}}/\text{am-II}) = 0.045$  cm<sup>-1</sup>; its influence on the cross peak is

apparent from the non-zero  $\nu_{\text{C=O}}$  / am-II cross peak amplitude at  $T \sim 0$  (Figure 5.4, blue line). The measured  $T_{\text{max}}$  value of 1.33 ps is shorter than the expectation of 1.85 ps ( $= 1.1 \text{ ps} + 6 \text{ \AA} / 8 \text{ \AA/ps}$ ), likely due to the influence of the direct coupling, sizable for short distances. Next we discuss the energy transport across the amide group.

## 5.4.2. Transport across the amide

### 5.4.2.1. Transport from $\nu_{\text{N3}}$ to the ester group

The pathway between the end groups consists of different portions which take different times for energy to pass with, in general, different speeds. Using the transport times determined for the end-group tag to the amide transport, the transport times via the second alkyl portion of the molecule can be determined using the additivity principle. By subtracting the  $T_{\text{max}}$  values for  $\nu_{\text{N3}}$  / am-I from those for  $\nu_{\text{N3}}$  /  $\nu_{\text{C=O}}$  for each compound, the values of 1.7, 2.8 and 3.1 ps result for Am4-4, Am7-4, and Am11-4, respectively. These values are expected to correspond to the time to pass the same fragment in all compounds, the  $\text{C}_4$  alkyl chain. While the values for the two longer compounds are the same within the error bars, the time is very short for Am4-4. Similar analysis, but subtracting  $T_{\text{max}}$  values for  $\nu_{\text{N3}}$  / am-II from those for  $\nu_{\text{N3}}$  /  $\nu_{\text{C=O}}$ , results in 0.1, 1.4 and 1.5 ps for Am4-4, Am7-4, and Am11-4, respectively. The same tendency is apparent: the times for the two longer compounds are the same at ca. 1.45 ps, while apparently no additional time is needed in Am4-4 to pass the  $\text{C}_4$  alkyl chain. Such “instantaneous” signal appearance at  $\nu_{\text{C=O}}$  for the Am4-4 compound suggests that the coupling of some mode(s) at the amide with the  $\nu_{\text{C=O}}$  mode is the source of the signal, not the energy passage. Surprisingly, this coupling appears to dominate the signal only in the Am4-4 compound. We offer two possible reasons to

explain the observation, the  $\nu_{\text{C=O}}$  / am-I coupling and the chain-state coupling in the Am4-4 compound with the alkyl chains of the same length on each side of the amide (C<sub>4</sub>).

The  $\nu_{\text{C=O}}$  / am-I coupling is apparent from the waiting time dependence at the  $\nu_{\text{C=O}}$  / am-I cross peak position and the evaluated off-diagonal anharmonicity of 0.012 cm<sup>-1</sup>. Because of this coupling, any perturbation of the am-I mode affects, essentially instantaneously, the  $\nu_{\text{C=O}}$  mode. This perturbation can occur via anharmonic coupling with the modes at the amide excited via the energy transport, or even due to excitation of the am-I mode via the energy transport.

Note that the  $\nu_{\text{N3}}$  relaxation involves the wave packet formation at the wagging and twisting CH<sub>2</sub> bands at ca. 1270 cm<sup>-1</sup> energy (experimental value), propagating at ca. 14 Å/ps speed, as well as simultaneous excitation of the  $\nu_{\text{N-C}}$  mode, which is in resonance with the rocking band of the chain (Figure 5.7) and is also expected to transport energy towards the amide. If the second wavepacket at the rocking band is indeed formed, it will propagate with the speed of ca. 62 Å/ps, either ballistically or via directed diffusion. In the compound with a short chain, Am4-4, the two portions of energy will arrive to the amide almost simultaneously, while there will be a significant delay between their arrival to the amide for the compounds with longer chains. Indeed, the calculated time mismatch between arrival of the two portions of energy, propagating with 14 and 62 Å/ps speeds, is the shortest for Am4-4 at 0.33 ps, compared to those of 0.58 and 0.93 ps for the two longer compounds. Simultaneous arrival of the two portions of energies to the amide results in much stronger perturbation of the am-I mode and can even facilitate excitation of the am-I or am-II mode. Due to mismatch of the arrival times of the two portions of energy to the amide in Am7-4 and Am11-4, the amount of excess energy there will be much smaller than

that for Am4-4. The larger number of degrees of freedom available for energy dissipation in compounds with longer chains, Am7-4 and Am11-4, and longer path lengths from the azido group, further reduce the amount of excess energy at the amide. As a result, the observed  $\nu_{\text{C=O}}$  / am-I coupling affects the transport time mostly in Am4-4, and possibly slightly in Am7-4.

Furthermore, it is expected that the probability of the am-I, am-II excitation via the transport from  $\nu_{\text{N}_3}$  can be sizable only in Am4-4, particularly due to much faster thermalization in bigger molecules Am4-7 and Am4-11.<sup>112</sup> While the importance of such excitation can only be addressed via sophisticated modeling, the arrival of the two portions of the excess energy to the amide is certainly much more simultaneous in the shorter compound, producing a qualitatively different effect onto  $\nu_{\text{C=O}}$ . A simple kinetic modeling, involving two propagating wave packets in the alkyl chain attached to the azido group and the am-I /  $\nu_{\text{C=O}}$  coupling, is capable of reproducing the observed  $T_{\text{max}}$  values for all three compounds (Figure 5.11).

Another effect that may influence the transport through the amide in Am4-4 is the equality of the chain lengths of the two alkyl chain attached to the amide, which may result in a frequency match of all chain states at both sides. In reality, the frequency match is only approximate, as the states are affected by the end groups and by the amide, which is facing one alkyl chain with the carbonyl group and another with the N-H group. This energy match may facilitate the transport across the amide, which will be discussed more in the next section.

The transport speed at the portion from the amide to the ester can be evaluated based on the transport time of ca. 1.45 ps, which results in the speed of ca. 4.2 Å/ps.

Interestingly, this speed matches that found for the am-I initiation (Section 5.4.1.2). It is conceivable that the CH<sub>2</sub> rocking band portion close to the bottom of the band (< 800 cm<sup>-1</sup>) is involved in the transport.

#### 5.4.2.2. Transport from $\nu_{C=O}$ to the azido group

The energy transport time from  $\nu_{C=O}$  to the azido group can be treated as a sum of transport times in the four portions of the overall path, which includes the transport times from  $\nu_{C=O}$  to the amide, within the amide, from the amide to the azido group, and within the azido group. The goal of this treatment is to isolate the transport time between the amide and the azido group. Because the transport in Am4-4 is clearly affected by the am-I /  $\nu_{C=O}$  coupling, we consider first the transport in the Am7-4 and Am11-4 compounds. The first portion of the transport, is known to occur with the speed of 8.0 Å/ps.<sup>22</sup> Addition of the lifetime of  $\nu_{C=O}$  of ca. 1.1 ps, results in the arrival time to the amide of ca. 1.9 ps. The energy arrives at the N-H side of the amide and it takes ca. 1.65 ps to pass the amide, although in the opposite direction (Figure 5.2E). Thermalization at the azide group requires an additional 2.2 ps, which is needed to populate the two NNN bending modes of the amide.<sup>108</sup> By subtracting these times from the 7.24 and 7.99 ps  $T_{\max}$  values for Am7-4 and Am11-4, respectively, the transport times via the C<sub>7</sub> and C<sub>11</sub> alkyl portions are obtained at 1.49 and 2.24 ps, respectively. The transport speed can be calculated using these two points as 6Å / (2.34-1.59) ps = 8.0 Å/ps. Interestingly, the transport speed matches the speed observed previously for the carbonyl mode initiation.<sup>22</sup> Notice that the consideration of the transport components serves to explain the absolute values of the observed  $T_{\max}$  values, but is not essential for computing the speed through the second alkyl portion of the path as the difference in the  $T_{\max}$  values for the overall transport, of course, results in the same speed.

The analysis of the transport components is necessary to test if the transport times spent within the second alkyl chain are meaningful for the obtained speed. The resulting times match well the times for the transport with the speed of 8 Å/ps via C<sub>7</sub> and C<sub>11</sub> chains, which are ca. 1.3 and 2.1 ps, respectively. The transport times obtained are short enough to support the ballistic transport mechanism. This is the first observation that a wavepacket is reformed at the perturber group and continues propagating ballistically.

Is this observation surprising or expected? Whenever there is a coupling of a mostly localized transition and the chain band states, a wavepacket can be formed, which is represented as a linear combination of the chain states, such that at the time of formation it involves motion at the beginning of the chain. A free, *coherent* evolution of the wavepacket makes the energy to propagate with the group velocity supported by the involved chain band (see Figure 5.7 caption). Note however, that the wavepacket formation is an *incoherent* process for the ensemble of molecules, so is the detection style of the energy arrival to the reporter site via RA 2DIR. In fact, the process of reformation of the wavepacket, after one or more IVR steps at the amide, is not very different from the initial wavepacket formation process at the tag where relaxation process initiates a wavepacket. Nevertheless, this is the first observation of ballistic transport through the group perturbing the chain state delocalization.

The shortest compound, Am4-4, again shows an anomalous waiting time. If the same calculations, based on the time additivity, are applied to  $T_{\max}$  value for the  $\nu_{\text{C=O}} / \nu_{\text{N3}}$  cross peak of 4.27 ps, the transport time of -1.4 ps is obtained for the transport via the alkyl chain between the amide and azido groups. Moreover, the  $T_{\max}$  for the  $\nu_{\text{C=O}} / \nu_{\text{N3}}$  cross peak is even shorter than that for  $\nu_{\text{am-I}} / \nu_{\text{N3}}$  cross peak of 4.72 ps. The origin of such small  $T_{\max}$

times is likely linked to some energy matching of the two alkyl chains of the same length. In this case, the cross peak increase could be described as relaxation of fully delocalized chain states, rather than the transport. To describe the effect in more details a symmetric Am7-7 and Am11-11 compounds need to be interrogated. There is also a possibility of an accidental frequency match for Fermi resonances supporting the C=O decay. Preliminary measurements of the Am4-4 molecules with a deuterated amide group show a drastic increase of the transport time from  $\nu_{\text{C=O}}$  to  $\nu_{\text{N3}}$ , which became longer than that from am-I to  $\nu_{\text{N3}}$ .

### 5.4.3. Mode delocalization.

For the ballistic transport to occur, the delocalization of the energy transporting modes must be maintained throughout the entire length of the transport. Pure alkane chains offer essentially full delocalization, as shown for the chain with ten  $\text{CH}_2$  units, terminated with an azide and methyl ester groups in Figure 5.8A. However, the optical bands of Am4-4 and Am7-4 (Figures 5.8B, C) show strong localization on either side of the amide group. There are a few fully delocalized states found, especially within the C-C stretching band, but the number of delocalized states and the extent of their delocalization are limited. The results of these calculations suggest that neither of these bands will be capable of transferring energy ballistically with a single wavepacket passing through the amide group. An expectation that in Am4-4 the chain states are more delocalized due to a better resonance of two chains of the same length did not result in some increase of delocalization, but the effect is marginal. The reason of localization is in inhomogeneity introduced by the end and central groups, which differently affects the state energies of the two chains – the interaction of the chain states across the amide is too weak to overcome the inhomogeneity

of the chain states. These calculations are in agreement with the experimental observation, which shows that IVR steps occur at the amide, resulting in a delay of the transport by ca. 1.65 ps.

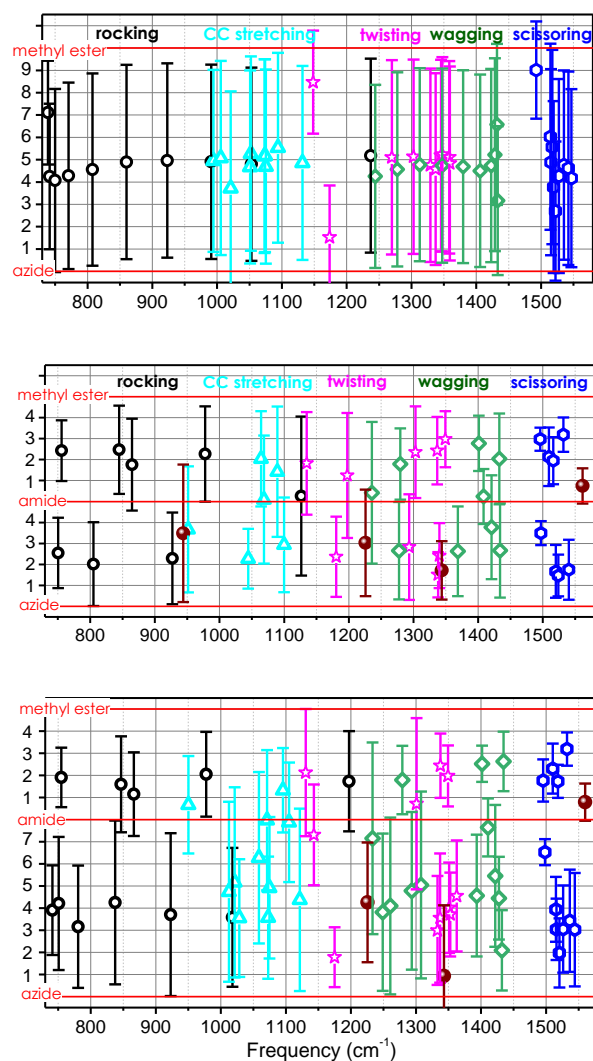


**Figure 5.8.** Extent of delocalization for the DFT computed chain-states in (A) methyl 11-azidoundecanoate (CH10-ester), (B) Am4-4 and (C) Am7-4. The state shown are of the CH<sub>2</sub> rocking (black circle), twisting (magenta stars), wagging (green diamonds), scissoring (blue hexagons), and C-C stretching (cyan triangles) states. The positions of the azide, amide, and methyl ester functional groups are shown by the orange dotted lines. The center of amplitude for each state is plotted with error bars as  $\pm(PN-1)/2$  length, where PN is the participation number, showing the extent of mode amplitude delocalization within the molecule.<sup>23</sup>

#### 5.4.4. Ballistic transport initiation

To identify the chain bands contributing the most to the transporting bands under different initiation conditions the relaxations pathways of the key vibrational modes were computed using the IVR program. To simplify the analysis, smaller molecules were often used in the computations. A side-by-side comparison of the am-I and  $\nu_{\text{C=O}}$  relaxation pathways is shown in Figure 5.9 and discussed below.

**Am-I relaxation.** To explain the speed of 4.2 Å/ps obtained for the transport from am-I towards the azido group the pathways of am-I relaxation were computed. For simplicity of the analysis, the frequencies and anharmonicities were computed for a simplified molecule shown in Figure 5.9A. Each normal mode of the molecule, identified by its frequency at the Y-axis in Figure 5.9, is assigned a bar with the length equal to the sum of all relaxation rates populating this mode in  $\text{ps}^{-1}$ . The bar length for each mode indicates the relative population of this mode via the am-I relaxation. There are many channels of the am-I relaxation and many types of modes are populated, colored differently in Figure 5.9. The orange color is used for high-frequency amide-localized modes, with most important contributors as am-II at ca.  $1600\text{ cm}^{-1}$ , am-III at  $1200\text{ cm}^{-1}$ , the N-C-C stretch of the amide at ca.  $970\text{ cm}^{-1}$ , and the low frequency modes, including the amide-localized out-of-plane deformation mode at  $613\text{ cm}^{-1}$ . The overall relaxation rate of am-I was computed at  $0.759\text{ ps}^{-1}$ , giving the am-I lifetime of 1.3 ps, which is only slightly longer than the experimental lifetime of 1.05 ps. The initial relaxation step of am-I results in populating high-frequency modes above  $700\text{ cm}^{-1}$  (66%) and lower-frequency modes (34%), so that 78% of energy stays within the high-frequency modes. Among those modes, 39% of population goes into amide localized modes (orange bars above  $700\text{ cm}^{-1}$ ), most notably to am-II and am-III,

both involving motion at the nitrogen atom side of the amide, including NH bending, which will more likely be involved in the energy transport towards the ester group in Am $n$ -4. The next largest energy receiver is the rocking band of the chain (cyan color) amounting in 31% of all high-frequency populations. The states of other chain bands got populated as well, but in a significantly smaller amounts, including less than 0.1% for scissoring, 8.0% for wagging, 8.4 % for twisting, and 13.3% for CC stretching bands.

The calculations suggest that the transport via the rocking band will be dominant. The rocking band, however, is very broad and can support a wide variety of speeds. The calculations show that the majority of the rates (75% of all rates to the rocking modes) go to the rocking modes which are less than 810 cm<sup>-1</sup> in frequency. The low frequency portion of the rocking band is rather flat, supporting a small group velocity, in agreement with the experiment. Therefore, we conclude that the transport initiated by an am-I mode in the alkyl chain attached to the CO side of the amide occurs predominantly via the states of the bottom of the rocking band, resulting in the speed of 4.2 Å/ps.

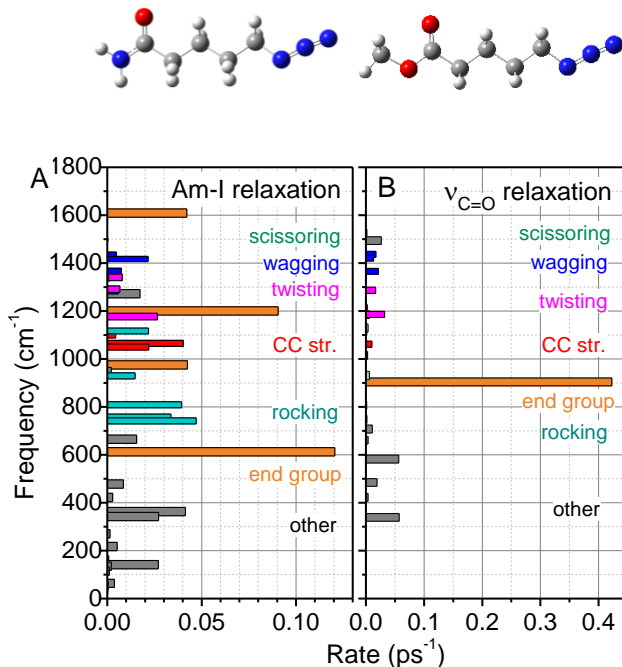


**Figure 5.9.** Rates of all relaxation channels for am-I (A) and ν<sub>C=O</sub> (B). The DFT calculated structures used for the analysis is shown above their respective graphs. The relaxation channels into the optical bands for am-I (A) are 0.1% in scissoring, 8.0% in wagging, 8.4% into twisting, and 13.3% into CC stretching bands. There is a single dominating IVR channel for ν<sub>C=O</sub> (B) into the O-C-CH<sub>2</sub> mode on the ester at 911 cm<sup>-1</sup>.

**ν<sub>C=O</sub> relaxation.** The relaxation rates of the 3<sup>rd</sup>-order IVR pathways for ν<sub>C=O</sub> relaxation are shown in Figure 5.9B, computed for the molecule shown in the inset. A single relaxation channel dominates the relaxation dynamics populating an overtone of the 911 cm<sup>-1</sup> mode and taking ca. 62 - 75% of all relaxation channels, when computed in different compounds. The normal mode at 911 cm<sup>-1</sup> involves an O-C-C stretching motion at the ester. Because this mode receives a substantial majority of population from the tag mode, and because it substantially involves the first CH<sub>2</sub> unit in the chain (O-C-CH<sub>2</sub>-chain), it is likely that this mode is the one which delivers energy to the chain. This mode is within the frequency range of the CC stretching and CH<sub>2</sub> rocking bands, so the coupling between this mode and the CC stretching and CH<sub>2</sub> rocking states of a simplified molecule (ethylacetimide) was

evaluated. To evaluate the coupling, a previously developed method was employed, which relies on bringing the two states in resonance (O-C-C stretching of the ester with CC stretching and CH<sub>2</sub> rocking of the chain atoms) by changing atomic masses of one of the groups and observing a frequency jump of  $2\beta$  when the frequencies pass the resonance; here  $\beta$  is the interaction energy of the two states.<sup>22, 89</sup> The coupling was evaluated by simultaneously scanning the masses of C and O atoms making up the C-O single bond of the methylester. This molecule has two CH<sub>2</sub> rocking motions and two CC stretching states; one CC stretching mode is mostly localized on the two carbon groups of the chain (1089 cm<sup>-1</sup>) while the other one is delocalized throughout the molecular backbone (1016 cm<sup>-1</sup>). The coupling to the CC stretching states at 1089 and 1016 cm<sup>-1</sup> are significant at 3 and 11 cm<sup>-1</sup>, respectively, while the CH<sub>2</sub> rocking states show negligible coupling, smaller than 0.01 cm<sup>-1</sup>. This analysis demonstrates that the CC stretching is strongly coupled to the O-C-C mode and is populated through it, supporting that the energy transport occurs within the CC stretching band. This result is not surprising as the character of the O-C-C stretching is similar to the CC stretching, while the CH<sub>2</sub> rocking motion is orthogonal to it.

The transport across the whole Am11-4 molecule can be compared to the transport across pure alkyl chain in CH15a, featuring the N<sub>3</sub> and carboxylic acid end groups.<sup>22</sup> Notice that two chains are approximately of the same length. The transport from C=O to N<sub>3</sub> takes 6.2 ps in CH15a but ca. 2.2 ps longer in Am11-4 (7.99 ps). The transport initiated by  $\nu_{N3}$  takes 2.7 ps in CH15a, but ca. 2.5 ps longer in Am11-4 (5.2 ps). This time increase is not too drastic, permitting efficient transport via the amide group to be efficient. Indeed, the transport efficiency determined from the cross peak amplitudes for the compounds

prepared under equivalent conditions resulted in a large exponential distance decay factor,  $L_0$ , of  $19.0 \pm 2.0$  Å (Figure 5.10).

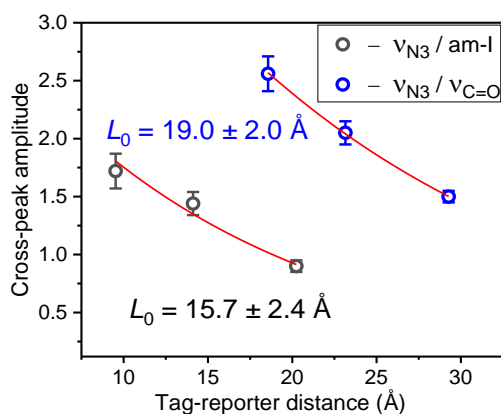


**Figure 5.10.** Dependences of the  $\nu_{N3} / \nu_{C=O}$  and  $\nu_{N3} / \text{am-I}$  cross-peak amplitudes in the Amn-4 compounds. The amplitudes were fitted with an exponential decay function resulting in a characteristic decay distances,  $L_0$ , indicated in the figure.

## 5.5 Conclusions

The study of the energy transport in molecules consisting of two alkyl chains of different lengths linked by an amide group was performed. The transport was initiated by a variety of tags, located at the end groups of the whole molecule, as a well as at the amide group. While the transport dynamics was found to be complex, many interesting conclusions were made. The transport initiated by the am-I mode in the alkyl chain attached to C=O side of the amide was associated with the low-frequency portion of the  $\text{CH}_2$  rocking band of the chain, supporting the speed of  $4.2$  Å/ps. The transport initiated by the C=O mode was complicated by a coupling of  $\nu_{C=O}$  and am-I modes, which was significant enough to affect the reporters at the amide, but too weak to cause any significant energy transfer between the modes. The end-to-end group energy transport patterns for compounds with uneven alkyl chain length fragments on the two sides of the amide appears to be fully

additive, in agreement with previously reported data on additivity. The transport from either end-group to the molecules was described as ballistic. The passage through the amide in both directions was found to be governed by IVR steps. Nevertheless, after the amide group, the transport was found to occur with a constant speed, although the speeds were different when passed in different directions. The transport towards the ester was found to occur with the speed of 4.2 Å/ps, similar to that initiated by am-I and supported by the CH<sub>2</sub> rocking band. The transport towards the azido group occurred with the speed of 8.0 Å/ps, which matched the speed supported by the CC stretching band. Using the transport time additivity, the overall time to pass the C<sub>7</sub> and C<sub>11</sub> alkyl chains was calculated at 1.39 and 2.14 ps, respectively, suggesting that the transport is ballistic for the alkyl chains including the C<sub>11</sub> chain length. Interestingly, the excess energy reaches the amide ballistically, redistributes at the amide, and reforms a wavepacket which propagates further with the high speed of 8 Å/ps. This is the first observation that the wavepacket is reformed at the perturber group and continues propagating ballistically. A possibility of having ballistic transport across a group alien to the chain structure opens opportunities of controlling the energy transport process in molecules by affecting the alien group using specific interactions, including hydrogen bonding.

## 5.6 Kinetic modeling

A kinetic model was implemented to describe the observed signals after  $\nu_{N3}$  initiation. The compounds studied are represented by sites which can transfer energy between them. Each alkyl chain is represented by having two states per methylene site, while the portion between the amide and ester is represented by two states per site. The

amide and end group are represented by three and two states, respectively. The states can transfer energy with different rates of  $k_1$ ,  $k_2$ , and  $k_3$  in the forward direction, and energy can transfer between the states with rates of  $k_{r1}$ ,  $k_{r2}$ , and  $k_r$ . Initial conditions were set as 1 for each state of the first site. The kinetic scheme was solved, and the reporter states which contribute to the signal were introduced (am-I, am-II, and  $\nu_{C=O}$ ). The results can be seen in Figure 5.11 where the open symbols represent the experimental data for the am-I detection (red), am-II detection (blue), and  $\nu_{C=O}$  detection (green), whereas the computed  $T_{\max}$  values (3 points for each cross peaks) are connected with lines of corresponding colors. One of the chain bands was set to transfer energy with the experimentally observed speed of 14 Å/ps ( $k_1$ ) towards the states at the amide, making the latter serve as the effective reporters for the am-I detection. The am-II kinetics were modeled by assigning an additional state at the amide. To describe the results of the  $\nu_{C=O}$  reporter, a direct coupling between the amide states and the  $\nu_{C=O}$  states was introduced. A competition of the direct coupling with the transport dynamics permitted the description of all experimental points quantitatively. At smaller chain length between  $N_3$  and the amide, the direct coupling contributes significantly to determination of the  $T_{\max}$ . With longer chains, the direct coupling makes a smaller impact as the mode influencing both modes (am-I and C=O) is populated later in time and is not competing efficiently with the energy transport process, which determines the  $T_{\max}$  values.

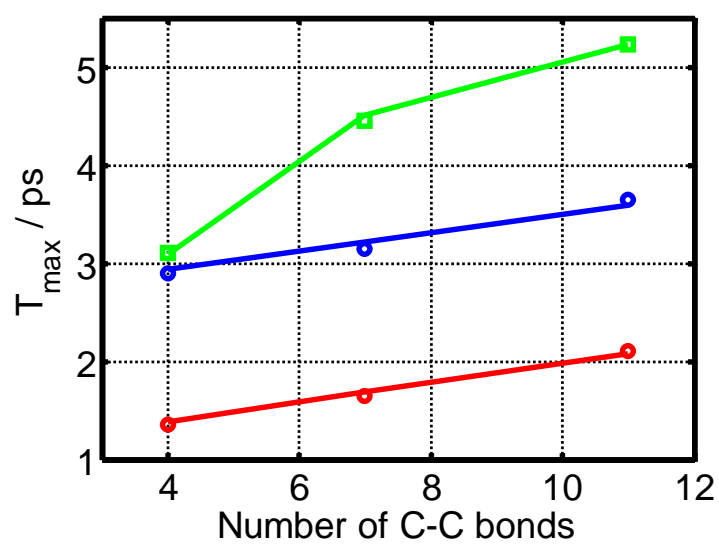


**Figure 5.11.** Experimental points from Figures 5.2E (red and blue) and 5.3B (green) are shown with symbols. The lines represent the results of the kinetic modeling.

## Chapter 6.

### Vibrational energy transport in electronically conjugated systems

#### 6.1. Introduction

The efficient conversion of light into other forms of energy can be achieved through the use of complex electronically conjugated chromophores.<sup>113-114</sup> Molecular systems which feature high levels of electronic conjugation, such as graphene ribbons and carbon nanotubes, have exhibited impressive electronic ballistic conduction with mean free paths exceeding 20  $\mu\text{m}$ .<sup>115-117</sup> Such systems also feature high thermal conductivity. For example, the thermal conductivity of graphene at room temperature is between 2000 – 4000  $\text{Wm}^{-1}\text{K}^{-1}$ .<sup>118</sup> The transverse and longitudinal acoustic modes of graphene support group velocities of ca. 13.6 and 21.3 km/s (136 and 213  $\text{\AA}/\text{ps}$ ), respectively, due to the strong in-plane  $\text{sp}^2$  bonds of the graphene.<sup>118</sup> Such systems also feature significant electron-phonon coupling.<sup>119-120</sup>

The goal of this study is to interrogate the vibrational energy transport in electronically delocalized systems. Specifically, the systems studied were 4-nitrobenzoic acid (BA) and 4'-nitro[1,1'-biphenyl]-4-carboxylic acid] (DBA) (Figure 6.1(a,b)). The energy transport was studied via RA 2DIR spectroscopy by initiating and detecting energy transport through high-frequency vibrational modes. Aside from studying the energy transport, the initial coupling between the tag and reporter was studied as a function of the chain length. This chapter presents the results for the BA and DBA molecules, featuring

one and two phenyl groups in their bridges, while the study of similar compounds with longer chain lengths is planned for the near future.

## **6.2. Experimental details**

### **6.2.1. Experimental method**

A detailed accounting of the fully-automated 2DIR spectrometer is presented in Chapter 2.7.

### **6.2.2. Sample preparation**

The BA and DBA complexes were purchased from TCI and Matrix Scientific, respectively, and were used as received. For spectroscopic measurements, the BA and DBA complexes were dissolved in dimethyl sulfoxide at 30 mM concentrations and placed into a 100  $\mu\text{m}$  thick optical cell with  $\text{CaF}_2$  windows for spectroscopic measurements.

### **6.2.3. Quantum-chemistry calculations**

The ground state structures of the compounds, their normal modes, and anharmonicities were calculated using density functional theory (DFT) with B3LYP hybrid functional and 6-311G(d,p) basis sets, as implemented in a Gaussian 09 software package.<sup>64</sup>

## **6.3. Results and discussion**

The molecular structures of the BA and DBA compounds and their absorption spectra in DMSO are shown in Figure 6.1. The carbonyl stretching mode of the carboxylic acid ( $\nu(\text{C=O})$ ) and the asymmetric stretching mode of the  $\text{NO}_2$  ( $\nu_{\text{as}}(\text{NO}_2)$ ) were used as tags and reporters (Figure 6.1.c). The relaxation dynamics of both modes is described first.

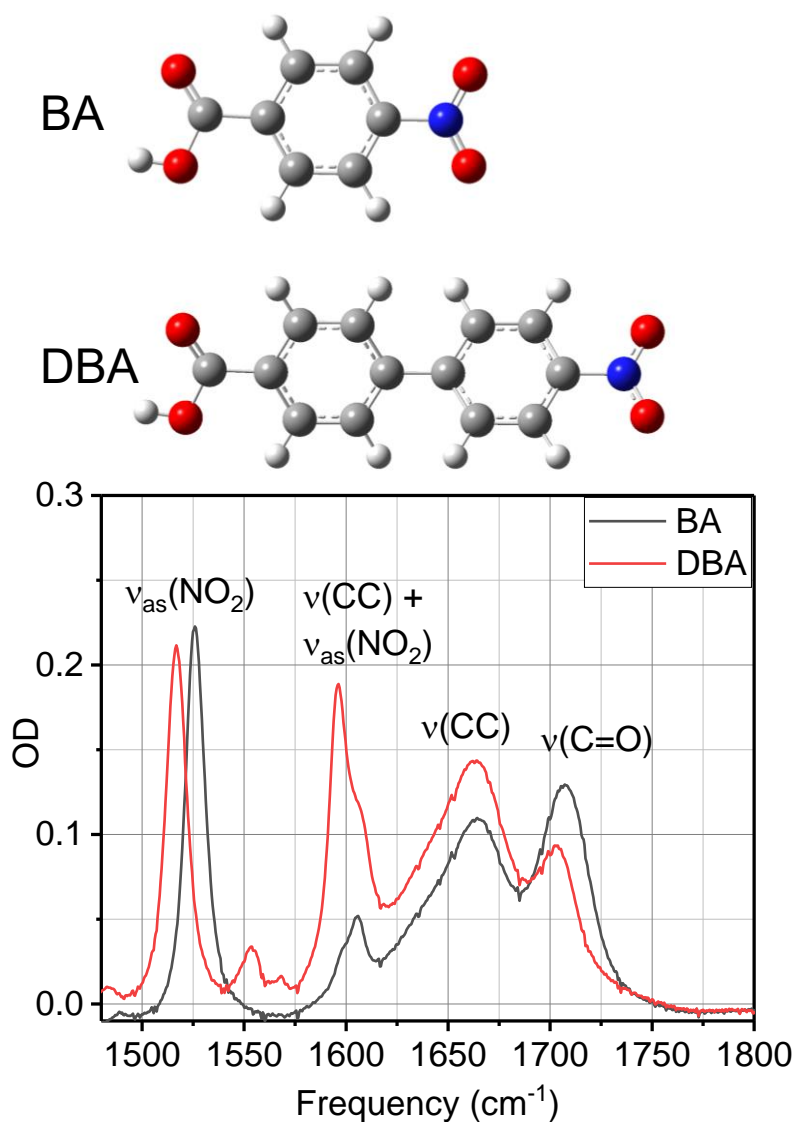


**Figure 6.1.** Structures of (a) BA and (b) DBA. (c) Solvent-subtracted infrared absorption spectra of BA and DBA in DMSO.

**$\nu_{\text{as}}(\text{NO}_2)$  relaxation.** The  $\nu_{\text{as}}(\text{NO}_2)$  relaxation dynamics was studied in both complexes via 2DIR spectroscopy, by exciting and probing the  $\nu_{\text{as}}(\text{NO}_2)$  transition, which involves the asymmetric motion of the two nitroso groups, with short m-IR laser pulses centered at 1550  $\text{cm}^{-1}$  (diagonal peak at 1530  $\text{cm}^{-1}$  in Figure 6.2.a) The one-dimensional waiting-time kinetics were constructed from the 2DIR spectra by integrating over the  $\nu_{\text{as}}(\text{NO}_2)$  diagonal peak and averaging over three measurements for each compound (Fig. 6.2b). Interestingly,

the two traces differ significantly. To describe the difference, a fit with a double-exponential function was performed, resulting in a similar fast component of ca. 1 ps (6.1), but different second component, varying from 4.4 ps for BA to 3.0 ps for DBA (Table 6.1). The fast component of approximately 1 ps is attributed to the lifetime of the excited mode, whereas the slower component reflects the coupling of the tag mode with other modes in the compound, which are populated by the relaxation of  $\nu_{\text{as}}(\text{NO}_2)$ . The slow component in DBA and BA is 3.0 and 4.4 ps has substantial amplitudes of 33 and 38%, respectively, indicating that the coupling is strong. Note that the tag mode (diagonal) dynamics in PEG and alkane chains did not depend on the chain length.<sup>22-23, 49</sup>

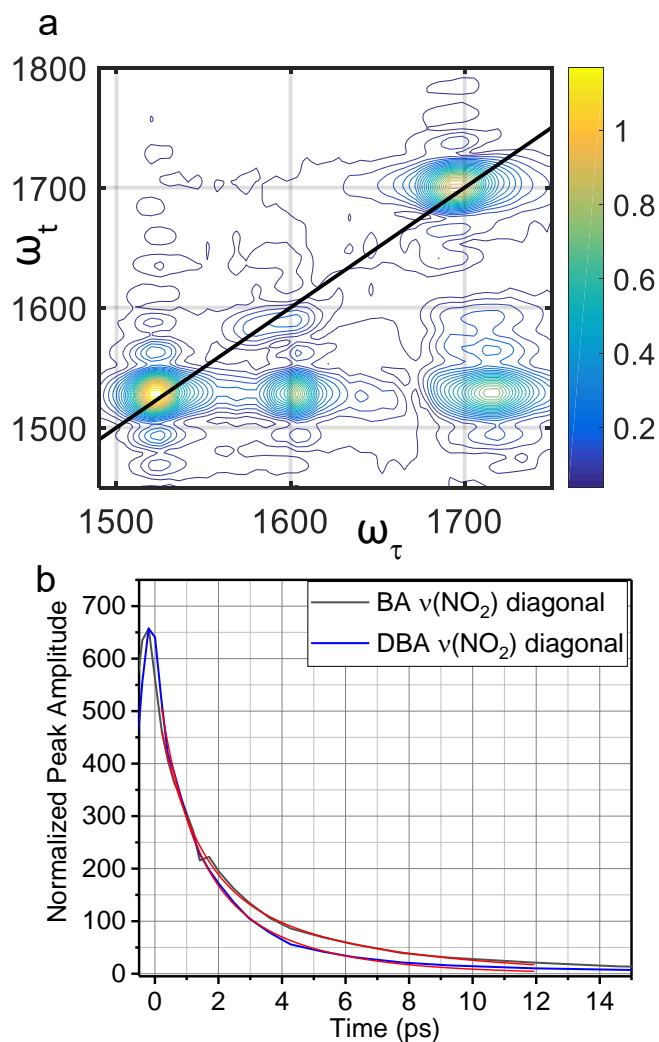


**Figure 6.2.** (b) Waiting time dependence of the  $\nu_{\text{as}}(\text{NO}_2)$  diagonal-peak amplitude for BA and DBA. The fit with a double-exponential function is shown (red lines). (a) 2DIR spectrum at  $T = 3$  ps of the  $\nu_{\text{as}}(\text{NO}_2)$  diagonal ( $1530 \text{ cm}^{-1}$  diagonal),  $\nu(\text{C}=\text{O})$  diagonal ( $1700 \text{ cm}^{-1}$  diagonal), and the  $\nu_{\text{as}}(\text{NO}_2)/\nu(\text{C}=\text{O})$  cross peak ( $1710 \text{ cm}^{-1}$ ,  $1530 \text{ cm}^{-1}$ )

**Table 6.1.** Results of the fit of the diagonal  $\nu_{\text{as}}(\text{NO}_2)$  waiting-time dependences with a double exponential function,  $S(T) = A_1 \exp(-T/\tau_1) + A_2 \exp(-T/\tau_2)$ . The relative contribution of the slowly decaying component ( $\tau_2$ ) is given in parentheses ( $\gamma = A_2/(A_1 + A_2) \times 100\%$ ).

	$\tau_1$ / ps	$\tau_2$ / ps	$\gamma$ , %
BA	1.1 +/- 0.2	4.4 +/- 0.5	33 +/- 7
DBA	1.0 +/- 0.2	3.0 +/- 0.3	38 +/- 6

To better understand these differences, IVR modeling of the  $\nu_{\text{as}}(\text{NO}_2)$  relaxation dynamics for BA and DBA was performed using the recently developed approach employing a Marcus-type Fermi-golden rule treatment of vibrational transitions (see Chapter 3.5.3).<sup>41, 65</sup> The computed IVR rates between modes  $i, j$ , and  $k$ ,  $i \rightarrow j + k$ , were used to follow the energy relaxation and dissipation. Two types of dependences are plotted for each compound; one is the population of the excited  $\nu_{\text{as}}(\text{NO}_2)$  mode and another is the observed signal in 2DIR, which also involves contributions from the coupling of the daughter modes of  $\nu_{\text{as}}(\text{NO}_2)$  relaxation to the  $\nu_{\text{as}}(\text{NO}_2)$  mode. The modeling shows the trends which are similarly to the experimental results (Figure 6.3(a,b), Table 6.2). The results of the modeling show that with a fixed fast component of 1 ps and with a fixed amplitude of about 33 and 37%, the slow components for BA and DBA are 1.95 and 0.95 ps, respectively, roughly matching the observed trend. The faster decaying  $\nu_{\text{as}}(\text{NO}_2)$  diagonal signal in DBA can be attributed to the higher density of energy accepting states of the two phenyl rings. The relaxation channels of  $\nu_{\text{as}}(\text{NO}_2)$  in BA and DBA were computed (Figure 6.3(b,c)) and the relaxation channels into optical vibrational modes delocalized on the phenyl bridge groups were identified ( $> 720 \text{ cm}^{-1}$ ). The percentage of the rates into these modes were calculated as  $\frac{\sum \text{rates into ring modes}}{\sum \text{total rates}}$ . The result was that 9.5% and 18.5% of the total decay rates of  $\nu_{\text{as}}(\text{NO}_2)$  lead into optical ring modes for BA and DBA, respectively (Figure 6.3(b,c)). This result suggests that the abundance of optical ring-modes in DBA gives a faster decaying slow component. The faster decaying dynamics in DBA versus BA can be attributed to the higher density of vibrational states offered by the biphenyl group.

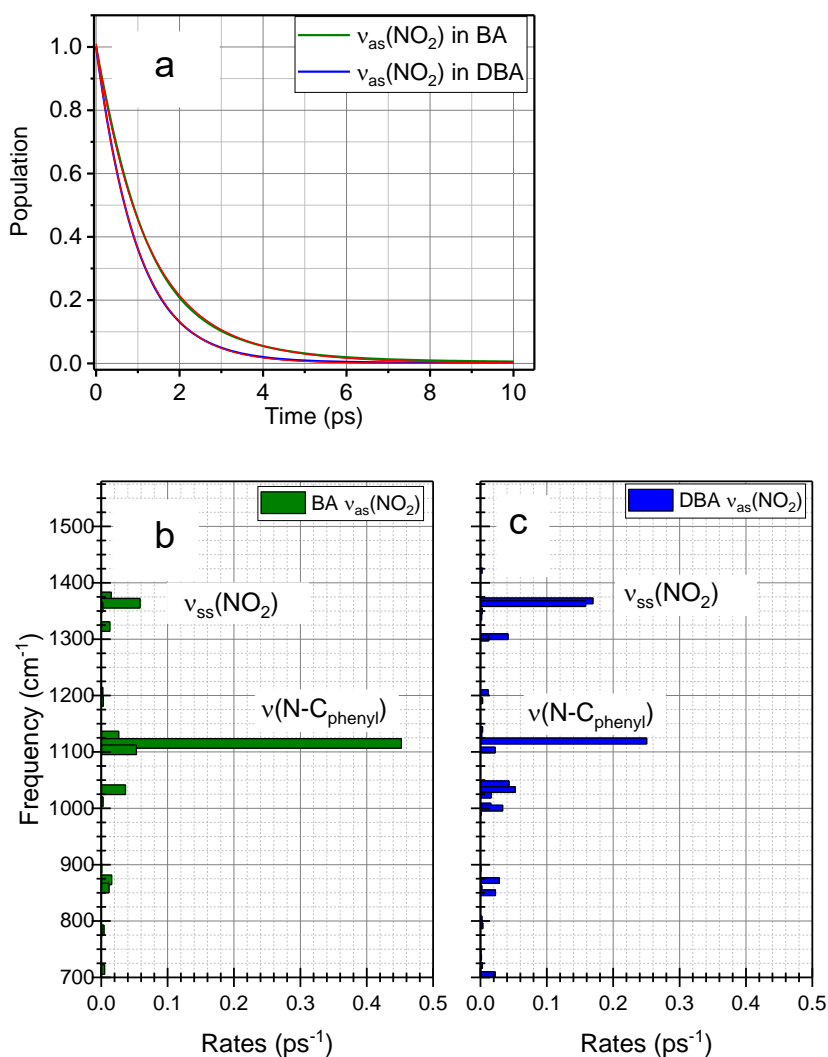


**Figure 6.3.** (a) Relaxation dynamics in BA and DBA of  $v_{as}(\text{NO}_2)$  with harmonic frequencies of 1584 and 1572 cm<sup>-1</sup>, respectively. The decay is fit with a double-exponential function (red lines). (b,c) Graphically presented relaxation pathways for the  $v_{as}(\text{NO}_2)$  normal mode in (b) BA and (c) DBA.

**Table 6.2.** Parameters of the IVR computed lifetimes of the  $v_{as}(\text{NO}_2)$  mode (Figure 6.3(a,b)). The decays were fit with a double exponential function,  $S(T) = A_1 \exp(-T/\tau_1) + A_2 \exp(-T/\tau_2)$ . The relative contribution of the slowly decaying component ( $\tau_2$ ) is given in parentheses ( $\gamma = A_2/(A_1 + A_2) \times 100\%$ ).

	$\tau_1$ / ps	$\tau_2$ / ps	$\gamma$ , %
BA	1.0	1.95	33
DBA	1.0	0.95	37

**$\nu(\text{C}=\text{O})$  relaxation.** The  $\nu(\text{C}=\text{O})$  relaxation dynamics were studied similarly by exciting and probing the  $\nu(\text{C}=\text{O})$  transition with laser pulses centered at  $1720\text{ cm}^{-1}$  and following the waiting-time dependence of the  $\nu(\text{C}=\text{O})$  diagonal peak (Fig. 6.2.a). Interestingly, the  $\nu(\text{C}=\text{O})$  mode did not show a difference between the two compounds, unlike the  $\nu_{\text{as}}(\text{NO}_2)$  transition. The lifetime of the  $\nu(\text{C}=\text{O})$  mode was found to be  $1.0 \pm 0.2$  and  $1.1 \pm 0.1$  ps in BA and DBA, respectively (Figure 6.4). Note that there is no significant slow component to the decay, as was observed in the case of  $\nu_{\text{as}}(\text{NO}_2)$ .

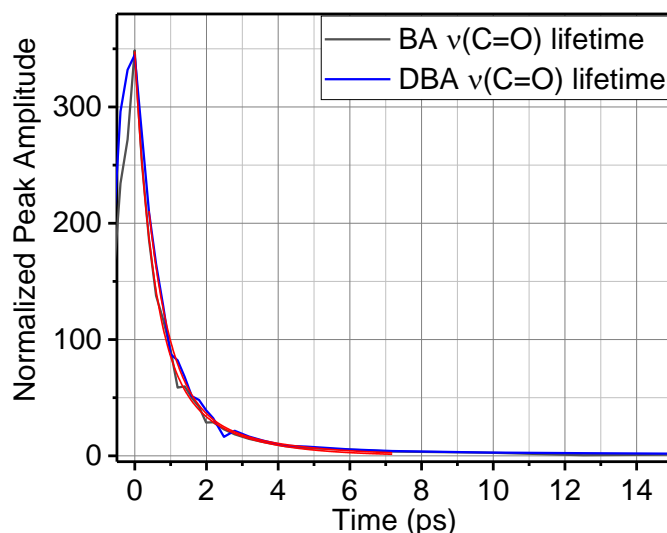


**Figure 6.4.** Waiting time dependence of the  $\nu_{\text{as}}(\text{NO}_2)$  diagonal-peak amplitude for BA and DBA. The fit with a double-exponential function is shown (red lines). The 2DIR spectrum of the  $\nu(\text{C}=\text{O})$  diagonal can be seen in Figure 6.2(a).

It is possible that the lack of dependence of the  $\nu(\text{C}=\text{O})$  lifetime to the structure is related to the energy of the mode. The energy of the  $\nu_{\text{as}}(\text{NO}_2)$  transition is approximately  $1515\text{ cm}^{-1}$ , which close in energy with the CH bending and CC stretching modes of the ring(s) that appears between  $1450$  and  $1550\text{ cm}^{-1}$  (Figure 6.5.) The  $\nu_{\text{as}}(\text{NO}_2)$  also appears

to be coupled well to the ring modes, as a substantial amplitude of motion is observed on both the nitro and phenyl groups for some modes in the 1450 – 1550  $\text{cm}^{-1}$  frequency range (Figure 6.5). Since the  $\nu_{\text{as}}(\text{NO}_2)$  is in resonance with the ring modes, their density of states can affect the  $\nu_{\text{as}}(\text{NO}_2)$  dynamics. The  $\nu(\text{C}=\text{O})$  mode, on the other hand, is over 100  $\text{cm}^{-1}$  higher in energy than any modes associated with the phenyl groups and seemingly uncoupled to the phenyl bridge (Figure 6.5), so it is unaffected by the density of the ring states.

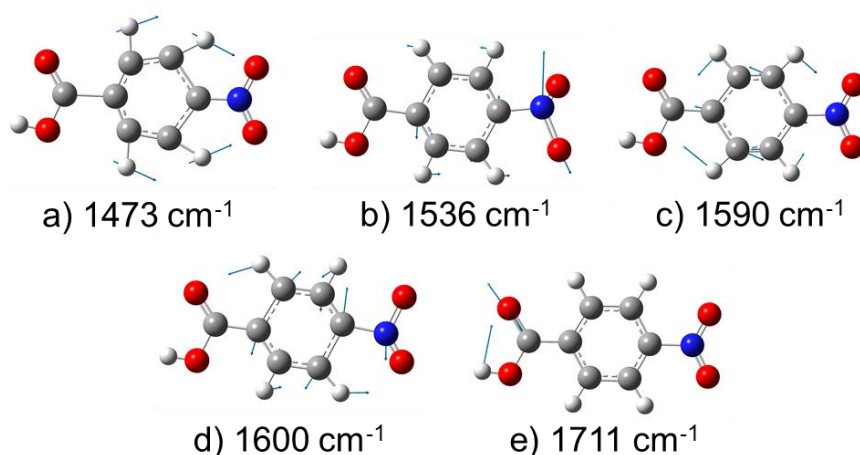


**Figure 6.5.** DFT computed harmonic frequencies and atomic displacements in BA for (a) the  $\text{CH}_2$  wagging mode at 1473  $\text{cm}^{-1}$ , (b)  $\nu_{\text{as}}(\text{NO}_2)$  at 1536  $\text{cm}^{-1}$ , (c)  $\nu(\text{C}=\text{C})$  at 1590  $\text{cm}^{-1}$ , (d)  $\nu(\text{C}=\text{C})$  at 1600  $\text{cm}^{-1}$ , and (e)  $\nu(\text{C}=\text{O})$  at 1711  $\text{cm}^{-1}$ . All DFT computed harmonic frequencies are scaled by 0.97. All vibrational modes between 1470 and 1711  $\text{cm}^{-1}$  are presented here.

It can be seen that the  $\text{NO}_2$  and ring modes are mixed in Figure 6.5(b,d). By examining the displacement vectors, one can see that the mixtures are in phase and out of phase in 6.5(b) and 6.5(d). The mixture is not evenly split between the  $\text{NO}_2$  and ring modes: the amplitude of the displacement vectors show that the lower frequency mode is mostly attributed to the  $\nu_{\text{as}}(\text{NO}_2)$  while the higher frequency mode has most of the

amplitude on the ring. The  $\nu(\text{C}=\text{O})$  mode, however, is completely localized to the carboxylic acid group.

**$\nu_{\text{as}}(\text{NO}_2)$  to  $\nu(\text{C}=\text{O})$  energy transport.** The vibrational energy transport from the nitro group to the carboxylic acid was studied in both complexes via RA 2DIR, by initiating energy transport via the  $\nu_{\text{as}}(\text{NO}_2)$  transition and detecting at  $\nu(\text{C}=\text{O})$ . The one-dimensional waiting time kinetics of the  $\nu_{\text{as}}(\text{NO}_2)$  /  $\nu(\text{C}=\text{O})$  cross peak are shown in Figure 6.6(c). Averaged over three measurements, the  $T_{\text{max}}$  values are  $2.62 \pm 0.3$  and  $3.98 \pm 0.2$  ps for BA and DBA, respectively. The inverse slope of the line connecting the points in the distance dependence of  $T_{\text{max}}$  is  $3.1 \text{ \AA/ps}$  (Figure 6.6(e)). The tag-reporter distance was taken to be the shortest distance between the nitrogen atom of the  $\text{NO}_2$  group and the carbon atom of the carboxylic acid. Such a slow transport is likely diffusive already in DBA. Interestingly, the cross-peak decay is much slower in the DBA complex (Fig. 6.6a). Such an observation will require more investigation by studying complexes with longer bridges.

**$\nu(\text{C}=\text{O})$  to  $\nu_{\text{as}}(\text{NO}_2)$  energy transport.** The vibrational energy transport from the carboxylic acid to the nitro group was studied in both complexes by initiating the energy transport via the  $\nu(\text{C}=\text{O})$  transition and detecting the  $\nu_{\text{as}}(\text{NO}_2)$  transition. The one-dimensional waiting time traces of the  $\nu(\text{C}=\text{O})$  /  $\nu_{\text{as}}(\text{NO}_2)$  cross peak are shown in Figure 6.6(d). Averaged over three measurements, the  $T_{\text{max}}$  values are  $1.2 \pm 0.2$  and  $1.78 \pm 0.2$  ps for BA and DBA, respectively. The resulting speed was calculated to be  $7.4 \text{ \AA/ps}$  (Figure 6.6(e)). Interestingly, this speed of transport is similar to the speed of energy transport observed in alkanes. The speed in this case is fast and likely ballistic. The band structure analysis for a

poly(*p*-phenylene) chain and experiments performed on complexes with longer bridges are required for detailed assessment.

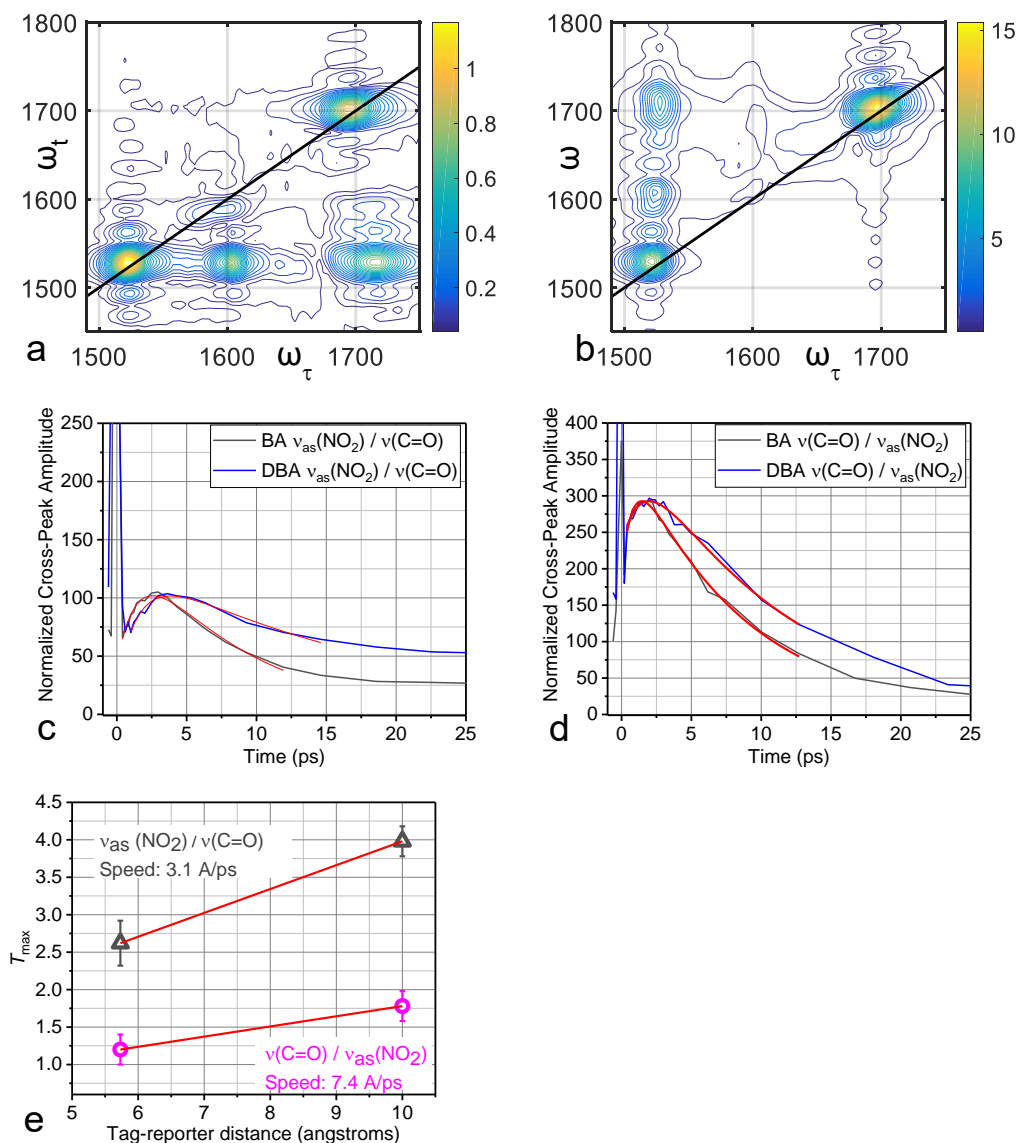


**Figure 6.6.** 2DIR spectrum showing the (a)  $\nu_{\text{as}}(\text{NO}_2) / \nu(\text{C}=\text{O})$  and (b)  $\nu(\text{C}=\text{O}) / \nu_{\text{as}}(\text{NO}_2)$  cross peaks in BA at  $T = 3$  ps. (c) Waiting time dependence of the  $\nu_{\text{as}}(\text{NO}_2) / \nu(\text{C}=\text{O})$  and (d)  $\nu(\text{C}=\text{O}) / \nu_{\text{as}}(\text{NO}_2)$  cross-peak amplitude for the BA and DBA compounds. The fit with a two-exponential fit is shown (red lines). (e)  $T_{\text{max}}$  values plotted as a function of the tag-reporter distance for the BA and DBA compounds for the transport initiated by  $\nu(\text{C}=\text{O})$  (magenta) and  $\nu_{\text{as}}(\text{NO}_2)$  (gray). The DFT computed tag-reporter distances for BA and DBA are 5.73 and 10.0 Å, respectively.

**Tag-reporter initial coupling.** It was investigated via DFT whether electronic delocalization would result in a substantial initial coupling between the tag and reporter modes. The DFT computed anharmonicity for  $\nu(\text{C=O}) / \nu_{\text{as}}(\text{NO}_2)$ ,  $\Delta_{\nu(\text{C=O})/\nu_{\text{as}}(\text{NO}_2)}$ , is 0.249 and 0.06  $\text{cm}^{-1}$ , respectively. These anharmonicities are large considering the substantial tag-reporter distances. To compare these bridges with a bridge that does not feature electronic delocalization, the geometry and anharmonicities of 6-nitrohexanoic acid was computed (Figure 6.7(b)). The tag-reporter distance of 6-nitrohexanoic acid was calculated to be 9.15 Å, somewhat shorter than the 10.0 Å distance in DBA (Table 6.3.). The calculated  $\nu(\text{C=O}) / \nu_{\text{as}}(\text{NO}_2)$  anharmonicity in 6-nitrohexanoic acid is 0.008  $\text{cm}^{-1}$ , almost an order of magnitude smaller for the anharmonicity in DBA. It appears that the phenyl bridge provides greater tag-reporter coupling than the alkane bridge. Detailed RA 2DIR experiments on alkane chains terminated by  $\text{NO}_2$  and carboxylic acid groups are needed to further investigate the reasons behind this observation.

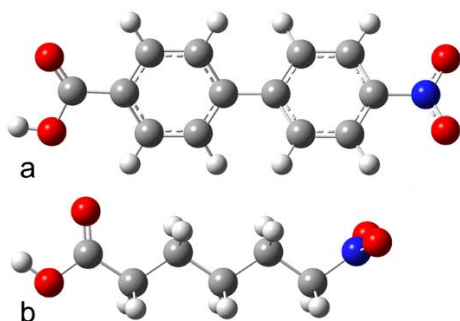


**Figure 6.7.** DFT calculated structures of (a) DBA and (b) 6-nitrohexanoic acid.

**Table 6.3.** DFT computed tag-reporter distances and coupling constants in DBA and 6-nitrohexanoic acid.

	Tag – reporter distance (Å)	$\Delta_{\nu(\text{C=O})/\nu_{\text{as}}(\text{NO}_2)}$
BA	5.73	0.249
DBA	10.0	0.06
6-nitrohexanoic acid	9.145	0.008

## 6.4. Conclusions

An experimental and theoretical investigation of the vibrational energy transport in two molecules with phenyl bridges of different length was performed. The speed of energy transport from  $\nu_{\text{as}}(\text{NO}_2)$  to  $\nu_{\text{as}}(\text{C=O})$  was slow 3.1 Å/ps and is likely diffusive in DBA. The speed of transport from  $\nu_{\text{as}}(\text{C=O})$  to  $\nu_{\text{as}}(\text{NO}_2)$  was 7.4 Å/ps, which is likely ballistic in both compounds. To complete this study, the band structure of poly(*p*-phenylene) need to be computed and the compounds with longer *p*-phenylene bridges are required. The synthesis of 4''-nitro-[1,1':4,1''-terphenyl]-4-carboxylic acid via collaboration with Professor Robert Pascal (Tulane University) is under consideration.

### List of References

1. Davydov, A. S., *Solitons in molecular systems*. . Kluwer Acad.: Dordrecht, Holland, 1985.
2. Rose, G. D.; Fleming, P. J.; Banavar, J. R.; Maritan, A., A backbone-based theory of protein folding. *Proceedings of the National Academy of Sciences* **2006**, *103* (45), 16623-16633.
3. Fujisaki, H.; Straub, J. E., Vibrational energy relaxation in proteins. *Proc. Natl. Acad. Sci. U.S.A.* **2005**, *102* (19), 6726-31.
4. Glowacki, D. R.; Rose, R. A.; Greaves, S. J.; Orr-Ewing, A. J.; Harvey, J. N., Ultrafast energy flow in the wake of solution-phase bimolecular reactions. *Nature Chem.* **2011**, *3*, 850-855.
5. Gruebele, M.; Wolynes, P. G., Vibrational energy flow and chemical reactions. *Acc. Chem. Res.* **2004**, *37* (4), 261-7.
6. Stratt, R. M., Chemistry-nonlinear thinking about molecular energy transfer. *Science* **2008**, *321*, 1789-1790.
7. Sobczynski, R.; Setser, D. W.; Slagle, A. R., Vibrational energy and bimolecular reactions: Enhancement of the electron transfer derived product channels for quenching of Xe(3P<sub>2</sub>) and Kr(3P<sub>2</sub>) atoms by CF<sub>n</sub>Cl<sub>4-n</sub>, C<sub>2</sub>F<sub>n</sub>Cl<sub>6-n</sub>, and CF<sub>3</sub>CFC<sub>1</sub>CF<sub>2</sub>Cl. *The Journal of Chemical Physics* **1990**, *92* (2), 1132-1144.

8. Yavatkar, R.; Tirumala, M., Platform wide innovations to overcome thermal challenges. *Microelectron. J.* **2008**, *39* (7), 930-941.
9. Moore, A. L.; Shi, L., Emerging challenges and materials for thermal management of electronics. *Mater. Today* **2014**, *17* (4), 163-174.
10. Cahill, D. G.; Ford, W. K.; Goodson, K. E.; Mahan, G. D.; Majumdar, A.; Maris, H. J.; Merlin, R.; S.R., P., Nanoscale thermal transport. *J. Appl. Phys.* **2003**, *93* (2), 793-818.
11. Minnich, A. J.; Johnson, J. A.; Schmidt, A. J.; Esfarjani, K.; Dresselhaus, M. S.; Nelson, K. A.; Chen, G., Thermal conductivity spectroscopy technique to measure phonon mean free paths. *Phys. Rev. Lett.* **2011**, *107*, 095901(1-4).
12. Siemens, M. E.; Li, Q.; Yang, R.; Nelson, K. A.; Anderson, E. H.; Murnane, M. M.; Kapteyn, H. C., Quasi-ballistic thermal transport from nanoscale interfaces observed using ultrafast coherent soft X-ray beams. *Nature Mater.* **2009**, *9*, 26-30.
13. Maire, J.; Anufriev, R.; Nomura, M., Ballistic thermal transport in silicon nanowires. *Scientific Reports* **2017**, *7*, 41794.
14. Carter, J. A.; Wang, Z.; Dlott, D. D., Ultrafast nonlinear coherent vibrational sum-frequency spectroscopy methods to study thermal conductance of molecules at interfaces. *Acc. Chem. Res.* **2009**, *42* (9), 1343-1351.
15. Wang, Z.; Carter, J. A.; Lagutchev, A.; Koh, Y. K.; Seong, N.-H.; Cahill, D. G.; Dlott, D. D., Ultrafast flash thermal conductance of molecular chains. *Science* **2007**, *317*, 787-790.
16. Pein, B. C.; Sun, Y.; Dlott, D. D., Unidirectional Vibrational Energy Flow in Nitrobenzene. *The Journal of Physical Chemistry A* **2013**, *117* (29), 6066-6072.

17. Kasyanenko, V. M.; Lin, Z.; Rubtsov, G. I.; Donahue, J. P.; Rubtsov, I. V., Energy transport via coordination bonds. *J. Chem. Phys.* **2009**, *131*, 154508.
18. Mueller-Werkmeister, H. M.; Bredenbeck, J., A donor-acceptor pair for the real time study of vibrational energy transfer in proteins. *Phys. Chem. Chem. Phys.* **2014**, *16* (7), 3261-3266.
19. Schwarzer, D.; Kutne, P.; Schroeder, C.; Troe, J., Intramolecular vibrational energy redistribution in bridged azulene-anthracene compounds: Ballistic energy transport through molecular chains. *J. Chem. Phys.* **2004**, *121* (4), 1754-1764.
20. Botan, V.; Backus, E. H.; Pfister, R.; Moretto, A.; Crisma, M.; Toniolo, C.; Nguyen, P. H.; Stock, G.; Hamm, P., Energy transport in peptide helices. *Proc. Natl. Acad. Sci. U.S.A.* **2007**, *104* (31), 12749-54.
21. Delor, M.; Sazanovich, I. V.; Towrie, M.; Spall, S. J.; Keane, T.; Blake, A. J.; Wilson, C.; Meijer, A. J. H. M.; Weinstein, J. A., Dynamics of Ground and Excited State Vibrational Relaxation and Energy Transfer in Transition Metal Carbonyls. *J. Phys. Chem. B* **2014**, *118* (40), 11781-11791.
22. Yue, Y.; Qasim, L. N.; Kurnosov, A. A.; Rubtsova, N. I.; Mackin, R. T.; Zhang, H.; Zhang, B.; Zhou, X.; Jayawickramarajah, J.; Burin, A. L.; Rubtsov, I. V., Band-Selective Ballistic Energy Transport in Alkane Oligomers: Towards Controlling the Transport Speed. *J. Phys. Chem. B* **2015**, *119* (21), 6448-6456.
23. Qasim, L. N.; Kurnosov, A.; Yue, Y.; Lin, Z.; Burin, A. L.; Rubtsov, I. V., Energy Transport in PEG Oligomers: Contributions of Different Optical Bands. *J Phys Chem C* **2016**, *120* (47), 26663-26677.

24. Rubtsova, N. I.; Rubtsov, I. V., Vibrational Energy Transport in Molecules Studied by Relaxation-Assisted Two-Dimensional Infrared Spectroscopy. *Ann. Rev. Phys. Chem.* **2015**, *66*, 717-738.
25. Narasimhan, T., Fourier's heat conduction equation: History, influence, and connections. *Reviews of Geophysics* **1999**, *37* (1), 151-172.
26. Chen, G., Thermal conductivity and ballistic-phonon transport in the cross-plane direction of superlattices. *Physical Review B* **1998**, *57* (23), 14958-14973.
27. Davydov, A. S., *Theory of molecular excitons*. McGraw-Hill Book Co.: New York, 1962; p 174.
28. Namboodiri, M.; Kazemi, M. M.; Zeb Khan, T.; Materny, A.; Kiefer, J., Ultrafast Vibrational Dynamics and Energy Transfer in Imidazolium Ionic Liquids. *J. Am. Chem. Soc.* **2014**, *136* (16), 6136-6141.
29. Chen, H.; Bian, H.; Li, J.; Wen, X.; Zhang, Q.; Zhuang, W.; Zheng, J., Vibrational Energy Transfer: An Angstrom Molecular Ruler in Studies of Ion Pairing and Clustering in Aqueous Solutions. *The Journal of Physical Chemistry B* **2015**, *119* (12), 4333-4349.
30. Schade, M.; Moretto, A.; Crisma, M.; Toniolo, C.; Hamm, P., Vibrational energy transport in peptide helices after excitation of C-D modes in Leu-d10. *J. Phys. Chem. B* **2009**, *113* (40), 13393-13397.
31. Backus, E. H. G.; Nguyen, P. H.; Botan, V.; Pfister, R.; Moretto, A.; Crisma, M.; Toniolo, C.; Stock, G.; Hamm, P., Energy Transport in Peptide Helices: A Comparison between High- and Low-Energy excitation. *J. Phys. Chem.* **2008**, *112*, 9091-9099.

32. Hithell, G.; Donaldson, P. M.; Greetham, G. M.; Towrie, M.; Parker, A. W.; Burley, G. A.; Hunt, N. T., Effect of oligomer length on vibrational coupling and energy relaxation in double-stranded DNA. *Chem. Phys.* **2018**, *512*, 154-164.
33. Hithell, G.; Shaw, D. J.; Donaldson, P. M.; Greetham, G. M.; Towrie, M.; Burley, G. A.; Parker, A. W.; Hunt, N. T., Long-range vibrational dynamics are directed by Watson–Crick base pairing in duplex DNA. *The Journal of Physical Chemistry B* **2016**, *120* (17), 4009-4018.
34. Naraharisetty, S. G.; Kasyanenko, V. M.; Zimmermann, J.; Thielges, M.; Romesberg, F. E.; Rubtsov, I. V., 2DIR spectroscopy on C-D modes of leucine-d10 side chain. In *Springer Ser. Chem. Phys.*, Corkum, P.; Silvestri, S. D.; Nelson, K., Eds. Springer: 2009; Vol. 92, pp 592-594.
35. Mueller-Werkmeister, M., H.; Li, Y.-L.; Lerch, E.-B. W.; Bigourd, D.; Bredenbeck, J., Ultrafast Hopping from Band to Band: Assigning Infrared Spectra based on Vibrational Energy Transfer. *Angewandte Chemie, Intern. Ed.* **2013**, *52* (24), 6214-6217.
36. Rubtsova, N. I.; Nyby, C. M.; Zhang, H.; Zhang, B.; Zhou, X.; Jayawickramarajah, J.; Burin, A. L.; Rubtsov, I. V., Room-temperature ballistic energy transport in molecules with repeating units *J. Chem. Phys.* **2015**, *142*, 212412.
37. Kasyanenko, V. M.; Tesar, S. L.; Rubtsov, G. I.; Burin, A. L.; Rubtsov, I. V., Structure dependent energy transport: Relaxation-assisted 2DIR and theoretical studies. *J. Phys. Chem. B* **2011**, *115* (38), 11063-11073.
38. Rubtsova, N. I.; Qasim, L., N.; Kurnosov, A. A.; Burin, A. L.; Rubtsov, I. V., Ballistic energy transport in oligomers. *Acc. Chem.Res.* **2015**, *48*, 2547-2555.

39. Kim, G.-H.; Lee, D.; Shanker, A.; Shao, L.; Kwon, M. S.; Gidley, D.; Kim, J.; Pipe, K. P., High thermal conductivity in amorphous polymer blends by engineered interchain interactions. *Nature Mater.* **2014**, *14*, 295.
40. Jiji, L. M., *Heat Conduction*. Springer: Berlin, Heidelberg, New York, 2009; p 418.
41. Tesar, S. L.; Kasyanenko, V. M.; Rubtsov, I. V.; Rubtsov, G. I.; Burin, A. L., Theoretical study of internal vibrational relaxation and energy transport in polyatomic molecules. *J Phys. Chem. A* **2013**, *117* (2), 315-323.
42. Majumdar, A., Microscale Heat Conduction in Dielectric Thin Films. *J. Heat Transfer* **1993**, *115* (1), 7-16.
43. Sistani, M.; Staudinger, P.; Greil, J.; Holzbauer, M.; Detz, H.; Bertagnolli, E.; Lugstein, A., Room-Temperature Quantum Ballistic Transport in Monolithic Ultrascaled Al–Ge–Al Nanowire Heterostructures. *Nano Lett.* **2017**, *17* (8), 4556-4561.
44. Hsiao, T.-K.; Chang, H.-K.; Liou, S.-C.; Chu, M.-W.; Lee, S.-C.; Chang, C.-W., Observation of room-temperature ballistic thermal conduction persisting over 8.3  $\mu\text{m}$  in SiGe nanowires. *Nature Nanotechnology* **2013**, *8*, 534.
45. Maldovan, M., Transition between ballistic and diffusive heat transport regimes in silicon materials. *Appl. Phys. Lett.* **2012**, *101* (11), 113110.
46. Sandner, A.; Preis, T.; Schell, C.; Giudici, P.; Watanabe, K.; Taniguchi, T.; Weiss, D.; Eroms, J., Ballistic Transport in Graphene Antidot Lattices. *Nano Lett.* **2015**, *15* (12), 8402-8406.

47. Chen, H.; Heremans, J. J.; Peters, J. A.; Goel, N.; Chung, S. J.; Santos, M. B., Ballistic transport in InSb/InAlSb antidot lattices. *Appl. Phys. Lett.* **2004**, *84* (26), 5380-5382.
48. Mingo, N.; Broido, D. A., Carbon Nanotube Ballistic Thermal Conductance and Its Limits. *Phys. Rev. Lett.* **2005**, *95* (9), 096105.
49. Lin, Z.; Rubtsov, I. V., Constant-speed vibrational signaling along polyethyleneglycol chain up to 60-Å distance. *Proc. Natl. Acad. Sci. U.S.A.* **2012**, *109* (5), 1413-1418.
50. Lin, Z.; Zhang, N.; Jayawickramarajah, J.; Rubtsov, I. V., Ballistic energy transport along PEG chains: distance dependence of the transport efficiency. *Phys. Chem. Chem. Phys.* **2012**, *14* (30), 10445-54.
51. Rubtsova, N. I.; Kurnosov, A. A.; Burin, A. L.; Rubtsov, I. V., Temperature dependence of the ballistic energy transport in perfluoroalkanes. *J. Phys. Chem. B* **2014**, *118* (28), 8381-8387.
52. Rubtsova, N. I.; Rubtsov, I. V., Ballistic energy transport via perfluoroalkane linkers. *Chem. Phys.* **2013**, *422*, 16-21.
53. The Infracord double-beam spectrophotometer. *Clinical Science* *16* (2).
54. Griffiths, P. R.; De Haseth, J. A., *Fourier transform infrared spectrometry*. John Wiley & Sons: 2007; Vol. 171.
55. Spence, D. E.; Kean, P. N.; Sibbett, W., 60-fsec pulse generation from a self-mode-locked Ti: sapphire laser. *Opt. Lett.* **1991**, *16* (1), 42-44.
56. Leger, J.; Nyby, C.; Varner, C.; Tang, J.; Rubtsova, N. I.; Yue, Y.; Kireev, V.; Burtsev, V.; Qasim, L.; Rubtsov, G. I.; Rubtsov, I. V., Fully automated dual-frequency

three-pulse-echo 2DIR spectrometer accessing spectral range from 800 to 4000 wavenumbers. *Rev. Sci. Instr.* **2014**, *85*, 083109.

57. Garrett-Roe, S.; Hamm, P., Purely absorptive three-dimensional infrared spectroscopy. *J. Chem. Phys.* **2009**, *130* (16), 164510.
58. Shen, S.; Henry, A.; Tong, J.; Zheng, R.; Chen, G., Polyethylene nanofibres with very high thermal conductivities. *Nat Nanotechnol* **2010**, *5* (4), 251-5.
59. Meier, T.; Menges, F.; Nirmalraj, P.; Hölscher, H.; Riel, H.; Gotsmann, B., Length-Dependent Thermal Transport along Molecular Chains. *Phys. Rev. Lett.* **2014**, *113*, 060801(1-6).
60. Losego, M. D.; Grady, M. E.; Sottos, N. R.; Cahill, D. G.; Braun, P. V., Effects of chemical bonding on heat transport across interfaces. *Nature Mater.* **2012**, *11*, 502-506.
61. Segal, D.; Nitzan, A.; Hanggi, P., Thermal conductance through molecular wires. *J. Chem. Phys.* **2003**, *119* (13), 6840-6855.
62. Nitzan, A., Molecules take the heat. *Science* **2007**, *317*, 759-760.
63. Davydov, A. S., Solitons in molecular systems. *Phys. Scr.* **1979**, *20* (3-4), 387.
64. Frisch, M. J.; Trucks, G. W.; Schlegel, H. B.; Scuseria, G. E.; Robb, M. A.; Cheeseman, J. R.; Montgomery, J. A.; Jr., T. V.; Kudin, K. N.; Burant, J. C.; Millam, J. M.; Iyengar, S. S.; Tomasi, J.; Barone, V.; Mennucci, B.; Cossi, M.; Scalmani, G.; Rega, N.; Petersson, G. A.; Nakatsuji, H.; Hada, M.; Ehara, M.; Toyota, K.; Fukuda, R.; Hasegawa, J.; Ishida, M.; Nakajima, T.; Honda, Y.; Kitao, O.; Nakai, H.; Klene, M.; Li, X.; Knox, J. E.; Hratchian, H. P.; Cross, J. B.; Bakken, V.; Adamo, C.; Jaramillo, J.; Gomperts, R.; Stratmann, R. E.; Yazyev, O.; Austin, A. J.; Cammi, R.; Pomelli, C.; Ochterski, J. W.; Ayala, P. Y.; Morokuma, K.; Voth, G. A.; Salvador, P.; Dannenberg, J.

- J.; Zakrzewski, V. G.; Dapprich, S.; Daniels, A. D.; Strain, M. C.; Farkas, O.; Malick, D. K.; Rabuck, A. D.; Raghavachari, K.; Foresman, J. B.; Ortiz, J. V.; Cui, Q.; Baboul, A. G.; Clifford, S.; Cioslowski, J.; Stefanov, B. B.; Liu, G.; Liashenko, A.; Piskorz, P.; I. Komaromi, R. L. M., D. J. Fox, T. Keith, M. A. Al-Laham, ; C. Y. Peng, A. N., M. Challacombe, P. M. W. Gill, ; B. Johnson, W. C., M. W. Wong, C. Gonzalez, and J. A. Pople, *Gaussian 03, Revision D.02, Gaussian, Inc., Wallingford CT* **2004**.
65. Burin, A. L.; Tesar, S. L.; Kasyanenko, V. M.; Rubtsov, I. V.; Rubtsov, G. I., Semiclassical model for vibrational dynamics of polyatomic molecules: Investigation of Internal Vibrational Relaxation. *J. Phys. Chem. C* **2010**, *114* (48), 20510-20517.
66. Tasumi, M.; Shimanouchi, T.; Miyazawa, T., Normal Vibrations and Force Constants of Polymethylene Chain. *J. Mol. Spectr.* **1962**, *9*, 261-287.
67. Bower, D. I.; Maddams, W. F., *The Vibrational Spectroscopy of Polymers*. . Cambridge University Press: Cambridge, U.K., 1989; p 163-165.
68. Benderskii, V. A.; Kats, E. I., Propagating vibrational excitations in molecular chains. *JETP Lett.* **2011**, *94*, 459-464.
69. Benderskii, V. A.; Kotkin, A. S.; Rubtsov, I. V.; Kats, E. I., Vibrational energy transport in molecular wires *JETP Letters* **2013**, *98* (4), 219-222.
70. Holstein, T., Studies of polaron motion. *Ann. Phys.* **1959**, *8*, 343-389.
71. Barone, V., Anharmonic vibrational properties by a fully automated second-order perturbative approach. *J. Chem. Phys.* **2005**, *122*, 014108.
72. Lin, Z.; Keiffer, P.; Rubtsov, I. V., A method for determining small anharmonicity values from 2DIR spectra using thermally induced shifts of frequencies of high-frequency modes. *J. Phys. Chem. B* **2011**, *115* (18), 5347-5353.

73. Sarabi, B.; Ramanayaka, A. N.; Burin, A. L.; Wellstood, F. C.; Osborn, K. D., Spectroscopy of random two-level systems in insulating films. *arXiv:1501.05865* </abs/1501.05865> [*cond-mat.supr-con*] **2015**.
74. Matsuura, H.; Miyazawa, T., Optical and acoustic branches and frequency distribution of polyethylene glycol chain. *Bull. Chem. Soc. Jpn.* **1969**, 42 (2), 372-378.
75. Rubtsov, I. V., Relaxation-assisted 2DIR: Accessing distances over 10 Å and measuring bond connectivity patterns. *Acc. Chem. Res.* **2009**, 42 (9), 1385-1394.
76. Yang, R.; Yang, X.; Evans, D.; Hendrickson, W.; Baker, J., Scanning tunneling microscopy images of poly (ethylene oxide) polymers: evidence for helical and superhelical structures. *J. Phys. Chem.* **1990**, 94 (15), 6123-6125.
77. Takahashi, Y.; Tadokoro, H., Structural studies of polyethers,  $-(\text{CH}_2)_m\text{O}-$  n. X. Crystal structure of poly (ethylene oxide). *Macromolecules* **1973**, 6 (5), 672-675.
78. Miyazawa, T.; Fukushima, K.; Ideguchi, Y., Molecular vibrations and structure of high polymers. III. Polarized infrared spectra, normal vibrations, and helical conformation of polyethylene glycol. *The Journal of Chemical Physics* **1962**, 37 (12), 2764-2776.
79. Alessi, M. L.; Norman, A. I.; Knowlton, S. E.; Ho, D. L.; Greer, S. C., Helical and Coil Conformations of Poly(ethylene glycol) in Isobutyric Acid and Water. *Macromol.* **2005**, 38 (22), 9333-9340.
80. Barone, V., Anharmonic vibrational properties by a fully automated second-order perturbative approach. *J. Chem. Phys.* **2005**, 122 (1), 14108.
81. Kurnosov, A. A.; Rubtsov, I. V.; Burin, A. L., Fast transport and relaxation of vibrational energy in polymer chains. *J. Chem. Phys.* **2015**, 142 (1), 011101/1-011101/4.

82. Skinner, J. L.; Hsu, D., Pure dephasing of a two-level system. *J. Phys. Chem.* **1986**, *90* (21), 4931-4938.
83. Fayer, M. D., *Elements of quantum mechanics*. Oxford University Press New York: 2001.
84. Abrahams, E.; Anderson, P.; Licciardello, D.; Ramakrishnan, T., Scaling theory of localization: Absence of quantum diffusion in two dimensions. *Phys. Rev. Lett.* **1979**, *42* (10), 673.
85. Botan, V.; Hamm, P., Intramolecular vibrational energy relaxation in nitrous acid (HONO). *J. Chem. Phys.* **2008**, *129* (16), 164506/1-164506/7.
86. Yu, X.; Leitner, D. M., Vibrational energy Transfer and Heat Conduction in a Protein. *J. Phys. Chem. B* **2003**, *107*, 1698-1707.
87. Backus, E. H. G.; Bloem, R.; Pfister, R.; Moretto, A.; Crisma, M.; Toniolo, C.; Hamm, P., Dynamical Transition in a Small Helical Peptide and Its Implication for Vibrational Energy Transport. *J. Phys. Chem. B* **2009**, *113*, 13405-13409.
88. Yue, Y.; Qasim, L. N.; Kurnosov, A. A.; Rubtsova, N. I.; Mackin, R. T.; Zhang, H.; Zhang, B.; Zhou, X.; Jayawickramarajah, J.; Burin, A. L.; Rubtsov, I. V., Band-Selective Ballistic Energy Transport in Alkane Oligomers: Toward Controlling the Transport Speed. *J. Phys. Chem. B* **2015**, *119* (21), 6448-6456.
89. Sarabi, B.; Ramanayaka, A. N.; Burin, A. L.; Wellstood, F. C.; Osborn, K. D., Spectroscopy of random two-level systems in insulating films. *arXiv.org, e-Print Arch., Condens. Matter* **2015**, 1-4.
90. Hush, N. S., An overview of the first half-century of molecular electronics. *Ann. N.Y. Acad. Sci.* **2003**, *1006* (1), 1-20.

91. Tour, J. M., *Molecular electronics: commercial insights, chemistry, devices, architecture and programming*. World Scientific: 2003.
92. Song, S.-h.; Katagi, H.; Takezawa, Y., Study on high thermal conductivity of mesogenic epoxy resin with spherulite structure. *Polymer* **2012**, *53* (20), 4489-4492.
93. Prasher, R. S.; Chang, J.-Y.; Sauciuc, I.; Narasimhan, S.; Chau, D.; Chrysler, G.; Myers, A.; Prstic, S.; Hu, C., Nano and Micro Technology-Based Next-Generation Package-Level Cooling Solutions. *Intel Technology Journal* **2005**, *9* (4).
94. Ganguli, S.; Roy, A. K.; Anderson, D. P., Improved thermal conductivity for chemically functionalized exfoliated graphite/epoxy composites. *Carbon* **2008**, *46* (5), 806-817.
95. Chung, S.; Lee, J.-H.; Jeong, J.; Kim, J.-J.; Hong, Y., Substrate thermal conductivity effect on heat dissipation and lifetime improvement of organic light-emitting diodes. *Appl. Phys. Lett.* **2009**, *94* (25), 168.
96. Duda, J. C.; Hopkins, P. E.; Shen, Y.; Gupta, M. C., Thermal transport in organic semiconducting polymers. *Appl. Phys. Lett.* **2013**, *102* (25), 251912.
97. Kim, N.; Domercq, B.; Yoo, S.; Christensen, A.; Kippelen, B.; Graham, S., Thermal transport properties of thin films of small molecule organic semiconductors. *Appl. Phys. Lett.* **2005**, *87* (24), 241908.
98. Jin, Y.; Nola, S.; Pipe, K. P.; Shtein, M., Improving thermoelectric efficiency in organic-metal nanocomposites via extra-low thermal boundary conductance. *J. Appl. Phys.* **2013**, *114* (19), 194303.
99. Wang, X.; Liman, C. D.; Treat, N. D.; Chabinyk, M. L.; Cahill, D. G., Ultralow thermal conductivity of fullerene derivatives. *Physical Review B* **2013**, *88* (7), 075310.

100. Shen, S.; Henry, A.; Tong, J.; Zheng, R.; Chen, G., Polyethylene nanofibres with very high thermal conductivities. *Nature Nanotech.* **2010**, *5*, 251-255.
101. Henry, A.; Chen, G., High thermal conductivity of single polyethylene chains using molecular dynamics simulations. *Phys. Rev. Lett.* **2008**, *101*, 235502(1-4).
102. Kimura, S.; Yasuda, E.; Tanabe, Y., Structural Dependence of Thermal Conductivity and Electrical Resistivity on Carbon Fiber/Glass-Like Carbon Composites. *Journal of the Ceramic Association, Japan* **1985**, *93* (1074), 89-95.
103. Xu, Y.; Wang, X.; Zhou, J.; Song, B.; Jiang, Z.; Lee, E. M. Y.; Huberman, S.; Gleason, K. K.; Chen, G., Molecular engineered conjugated polymer with high thermal conductivity. *Science Advances* **2018**, *4* (3).
104. Kang, D.-G.; Park, M.; Kim, D.-Y.; Goh, M.; Kim, N.; Jeong, K.-U., Heat transfer organic materials: robust polymer films with the outstanding thermal conductivity fabricated by the photopolymerization of uniaxially oriented reactive discogens. *ACS applied materials & interfaces* **2016**, *8* (44), 30492-30501.
105. Keith, J. M.; King, J. A.; Lenhart, K. M.; Zimny, B., Thermal conductivity models for carbon/liquid crystal polymer composites. *J. Appl. Polym. Sci.* **2007**, *105* (6), 3309-3316.
106. Kato, T.; Nakamura, T.; Agari, Y.; Ochi, M., Relation between thermal conductivity and network formation with polymerizable liquid crystals. *J. Appl. Polym. Sci.* **2007**, *103* (5), 3169-3174.
107. Naraharisetty, S. G.; Kasyanenko, V. M.; Rubtsov, I. V., Bond connectivity measured via relaxation-assisted two-dimensional infrared spectroscopy. *J. Chem. Phys.* **2008**, *128*, 104502/1-104502/7.

108. Varner, C.; Zhou, X.; Saxman, Z. K.; Leger, J. D.; Jayawickramarajah, J.; Rubtsov, I. V., Azido alkanes as convenient reporters for mobility within lipid membranes. *Chem. Phys.* **2018**.
109. Tesar, S. L.; III, J. M. L.; Kurnosov, A. K.; Burin, A. L., Temperature dependence for the rate of hole transfer in DNA: Nonadiabatic regime. *Chem. Phys.* **2012**, *393*, 13-18.
110. Piatkowski, L.; Bakker, H., Vibrational relaxation pathways of amide I and amide II modes in N-methylacetamide. *The Journal of chemical physics* **2012**, *136* (16), 04B622.
111. Farag, M. H.; Bastida, A.; Ruiz-López, M. F.; Monard, G. r.; Ingrosso, F., Vibrational energy relaxation of the amide I mode of N-methylacetamide in D2O studied through Born–Oppenheimer molecular dynamics. *The Journal of Physical Chemistry B* **2014**, *118* (23), 6186-6197.
112. Yu, X.; Leitner, D. M., Heat flow in proteins: Computation of thermal transport coefficient. *J. Chem. Phys.* **2005**, *122*, 054902.
113. Fidler, A. F.; Singh, V. P.; Long, P. D.; Dahlberg, P. D.; Engel, G. S., Dynamic localization of electronic excitation in photosynthetic complexes revealed with chiral two-dimensional spectroscopy. *Nature communications* **2014**, *5*, 3286.
114. Scholes, G. D.; Fleming, G. R., On the mechanism of light harvesting in photosynthetic purple bacteria: B800 to B850 energy transfer. *The Journal of Physical Chemistry B* **2000**, *104* (8), 1854-1868.
115. Calado, V.; Zhu, S.-E.; Goswami, S.; Xu, Q.; Watanabe, K.; Taniguchi, T.; Janssen, G. C.; Vandersypen, L., Ballistic transport in graphene grown by chemical vapor deposition. *Appl. Phys. Lett.* **2014**, *104* (2), 023103.

116. Koch, M.; Ample, F.; Joachim, C.; Grill, L., Voltage-dependent conductance of a single graphene nanoribbon. *Nature nanotechnology* **2012**, 7 (11), 713.
117. Banszerus, L.; Schmitz, M.; Engels, S.; Goldsche, M.; Watanabe, K.; Taniguchi, T.; Beschoten, B.; Stampfer, C., Ballistic transport exceeding 28  $\mu\text{m}$  in CVD grown graphene. *Nano Lett.* **2016**, 16 (2), 1387-1391.
118. Pop, E.; Varshney, V.; Roy, A. K., Thermal properties of graphene: Fundamentals and applications. *MRS Bull.* **2012**, 37 (12), 1273-1281.
119. Mazzola, F.; Frederiksen, T.; Balasubramanian, T.; Hofmann, P.; Hellsing, B.; Wells, J. W., Strong electron-phonon coupling in the  $\sigma$  band of graphene. *Physical Review B* **2017**, 95 (7), 075430.
120. Pomarico, E.; Mitrano, M.; Bromberger, H.; Sentef, M. A.; Al-Temimy, A.; Coletti, C.; Stöhr, A.; Link, S.; Starke, U.; Cacho, C., Enhanced electron-phonon coupling in graphene with periodically distorted lattice. *Physical Review B* **2017**, 95 (2), 024304.